Abrasive Water Jet Perforation and Multi-Stage Fracturing

Zhongwei Huang | Gensheng Li
Shouceng Tian | Xianzhi Song
Mao Sheng | Subhash Shah

ABRASIVE WATER JET PERFORATION AND MULTI-STAGE FRACTURING

ZHONGWEI HUANG, GENSHENG LI,
SHOUCENG TIAN, XIANZHI SONG,
MAO SHENG, SUBHASH SHAH

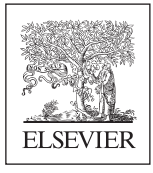

Gulf Professional Publishing
An imprint of Elsevier

Gulf Professional Publishing is an imprint of Elsevier
50 Hampshire Street, 5th Floor, Cambridge, MA 02139, United States
The Boulevard, Langford Lane, Kidlington, Oxford, OX5 1GB, United Kingdom

Notices
Knowledge and best practice in this field are constantly changing. As new research and experience broaden our understanding, changes in research methods, professional practices, or medical treatment may become necessary.

Practitioners and researchers must always rely on their own experience and knowledge in evaluating and using any information, methods, compounds, or experiments described herein. In using such information or methods they should be mindful of their own safety and the safety of others, including parties for whom they have a professional responsibility.

To the fullest extent of the law, neither the Publisher nor the authors, contributors, or editors, assume any liability for any injury and/or damage to persons or property as a matter of products liability, negligence or otherwise, or from any use or operation of any methods, products, instructions, or ideas contained in the material herein.

Library of Congress Cataloging-in-Publication Data
A catalog record for this book is available from the Library of Congress

British Library Cataloguing-in-Publication Data
A catalogue record for this book is available from the British Library

ISBN: 978-0-12-812807-7

Publisher: Joseph P. Hayton
Acquisition Editor: Katie Hammon
Editorial Project Manager: Katie Washington
Production Project Manager: Mohanapriyan Rajendran
Designer: Christian J. Bilbow

Typeset by TNQ Books and Journals

CONTENTS

PREFACE

Fracturing technology was first applied in the United States in 1947. Since then, significant progress has been made in fracturing equipment, fluid, proppant, and down-hole assembly. However, many problems still exist, such as fluid leakage and damage, higher initial pressure, difficulties to control both initial position and fractures height, lack of effective methods to monitor and measure the practical parameters of the fracture, and others. The above problems increase fracturing cost and negatively stimulate its effectiveness. To resolve these problems, researchers have developed many types of fracturing technologies, such as dual-packer, limited entry, ball-off, temporary plugging or sans-plug, among others, to realize comparatively "accurate" fracturing. Although they all have different shortcomings, these technologies enabled significant achievement in stimulating studies.

This book presents a hydra-jet multi-stage fracturing technology, integrating abrasive water jet (AWJ) perforation and hydraulic isolating with a pinpoint fracturing job. To some extent, this technology avoids the weaknesses of the above fracturing technologies, while offering a wide feasibility for conventional or unconventional wells, completed with open-hole, liner, or cemented casing well with damaged cement sheaths. The book includes nine chapters: Chapter 1 introduces the fundamentals of AWJ; Chapter 2 presents the experimental results of AWJ perforation, analyzing the influence of eight parameters on the perforation tunnel; Chapter 3 describes experimentally investigated mechanisms and numerical simulations; Chapter 4 provides the effect law of AWJ perforation parameters on the formation of initial and propagation pressures; Chapter 5 investigates the flow characteristics and pressure drop in coiled tubing; Chapter 6 describes how to calculate fracturing parameters and how to program the fracturing procedure, compiling a software based on the calculation results; Chapter 7 shows down-hole assembly structures; Chapter 8 lists some field cases, utilizing tubing and coiled tubing, and provides a detailed risk analysis and counter measures; Chapter 9 briefly introduces several new types of "fluids" possible to be utilized as fracturing fluids, thus providing a forecast for future technology.

As a novel technology during recent years, hydra-jet fracturing has not yet been investigated thoroughly or completely. Many factors influence its performance and fracturing effectiveness. Therefore, we still have a

long way to go to perfect this technology. If the reader finds flaws or remedies, please do not hesitate to let us know. With common effort, we are convinced that the promising hydra-jet fracturing technology will reach a new milestone.

CHAPTER ONE

Theoretical Basis of Abrasive Jet

Contents

Abrasive Water Jet Perforation and Multi-Stage Fracturing
ISBN: 978-0-12-812807-7
https://doi.org/10.1016/B978-0-12-812807-7.00001-7

Abstract

Water jet with high pressure can successfully cut rock, steel, and even reinforced concrete. However, at lower pressure, mixing a certain amount of abrasive particles in the water jet can also greatly improve the jet ability and effectively cut materials. High-pressure water jet blended with abrasives is known as an abrasive jet.

This chapter provides a detailed overview of the literature related to abrasive jet, the theoretical basis, and the cutting mechanism utilized. The review in this chapter specifically addresses three types of abrasive jet. According to the nature of the fluid, abrasive jets can be divided into abrasive water and abrasive suspension jets. Furthermore, depending on the mixing method, abrasive water jets can be divided into post- and premixed abrasive water jets. Different types of abrasive jets have different jet characteristics, and their uses are not identical.

Keywords: Abrasive suspension jet; Abrasive water jet; High pressure; Postmixed; Premixed.

1.1 INTRODUCTION

1.1.1 Development History of High-Pressure Water Jet Technology

Water jet technology originated during the first half of 19th century. As early as 1830, The Russians used a large-diameter water jet to excavate unconsolidated sand gravel gold and to flush the gold. This technology had been applied and developed in California of the United States from 1853 to 1886. At that time, the pressure utilized was very low ranging from a few to 12 atmospheres. In the 1930s, water jet technology had been used for hydraulic coal mining and other metal mining in Russia and China (Zhonghou, Gensheng, & Zhiming, 1991).

In the 1950s, based on the experience of hydraulic coal mining and rain erosion of high-speed aircraft, it was established that the improvement of jetting pressure and velocity could wash out hard materials and significantly increase the coal mining effect. Then the development of higher pressure equipment and experiments began. In the 1960s, with the advent of high-pressure plunger pumps and boosters, the study of jet dynamics and nozzle structure began.

At the end of the 1960s, the National Science Foundation of the United States supported a large research project aimed at seeking an efficient method for rock cutting. The researchers introduced and tested 25 new methods, such as electric spark, electron beam, laser, flame, and plasma and high-pressure water jet. Ultimately, the experts recognized that the

most feasible and effective method of rock breaking is high-pressure water jetting, and consequently, only this method has achieved practical application (Shengxiong et al., 1998). In the 1970s, various countries began to study this high-pressure water jet technology, which propelled the technology into a new stage of rapid development. During this period, studies focused on the rock breaking mechanism by water jet, pulsed jet characteristics and application of water jet in cutting, as well as rock breaking and cleaning. The new technologies included hydraulic auxiliary rock breaking, cavitating jet, abrasive jet, and intermittent jet. Since the 1980s, with the appearance of advanced testing and study means such as laser velocity measurements, high-speed photography, fluid visualization, and numerical simulation, the high-pressure water jet technology has developed more rapidly (Zhonghou, 1998). With further research on the technologies of abrasive jet, cavitating jet, pulse jet, hydraulic auxiliary rock breaking and basic theories, and cutting mechanisms and their influencing factors, special jet technologies with steam water, liquid metal, liquid gas (air, nitrogen, or carbon dioxide gas), and ice particles has emerged. The application range was extended from original mining, rock breaking, drilling, cleaning, and scale removing to metal or superhard material cutting, surface treatment, and grinding (Junwei, Xiyong, & Dajun, 2012). Application areas involved coal, oil, metallurgy, chemical engineering, and other industrial sectors as well as nuclear waste, marine, and other hazardous working environment. The degree of automation and cutting accuracy has significantly improved. In recent years, high-pressure water jet technology has been rapidly developed and the application field has been widened (Qinggang, 2014). Due to its unique characteristics and advantages, high-pressure water jet has been considered as a new processing tool for the new century. The study of water jet technology in China has developed in the 1970s. The technology expanded beyond its coal domain into petroleum, metallurgy, aviation, chemical, construction, machinery, municipal construction, and transportation fields (Zhonghou, Gensheng, & Ruihe, 2002). After more than 30 years of research and practice, great progress has been made and a number of new technologies and products have been developed, and some of them have reached a globally advanced level.

1.1.2 Introduction of Abrasive Jet

High-pressure water jet can successfully cut brittle materials such as rock; however, it requires a much higher pressure of about 700−1000 MPa to cut steel and reinforced concrete, etc. It is difficult to get and utilize such

high pressures. However, at lower pressure, mixing a certain amount of abrasive particles in the water jet will greatly improve the jet ability and effectively cut steel plates and reinforced concrete. A high-pressure water jet blended with abrasives is known as an abrasive jet. Due to a certain amount of abrasive particles mixed into the water flowing at high speed, the kinetic energy of the high-pressure water is transferred to the abrasive, transferring the action mode of the jet on the targets. The sustained action of the water jet on targets is transformed into an impact and grinding effect of the abrasive on targets. The particle flow deals high-frequency erosion to the targets, which greatly improves the quality and work efficiency of jetting (Summers, 1987).

The abrasive jet was for the first time applied in the United States. In the early 1960s, Bobo was the first to use an abrasive jet for oil well drilling, which substantially improved the drilling speed. In 1963, Bobo had obtained a patent for the equipment of oil well drilling via abrasive jet. In 1966, the Atlantic Richfield and the Gulf Oil in the United States obtained the patent for drilling rigs and bit nozzle of oil well drilling via abrasive jet, respectively. Due to the severe abrasion of abrasive jet on drilling tools and bit nozzle, this technology had not widely been used in petroleum drilling (Zhonghou & Gensheng, 1992).

Large-scale research and application of abrasive jet began in the early 1980s throughout the world. Dr. Mohamed of Hashish has been recognized as the father of abrasive jet. He conceived a new type of jet in 1979 to improve the cutting ability of pure water jet. In 1980, he added garnet into the water jet to form abrasive jets, which could successfully cut steel, glass, and concrete. In 1983, the first commercial abrasive cutting machine was introduced and used for glass cutting. With the continuous development of computers and artificial intelligence, the current cutting equipment of abrasive jet has been developed from mechanization to intelligence. Ingersoll-Rand, a world leader in the development of abrasive jet cutting, has achieved a mechatronic abrasive water cutting system. Currently, more than 2500 sets of mechanical—electrical integrated abrasive cutting devices have been installed globally, and the annual growth rate is 20%. Abrasive jet technology will become the industry's fastest growing technology according to the market research firm Frost & Sullivan (Labus, 1995).

In 1989, the abrasive suspension jet, which was first proposed by R. H. Hollinger and W.D. Perry, featured new advantages over abrasive water jet. Since then, cutting and flowing characteristics were taken into consideration by many scholars (Xiaomin et al., 1992).

Studies on the abrasive jet by Chinese scholars were basically synchronized with those in foreign countries. In 1986, the Chengdu Institute of Aircraft Manufacturing Company first completed the packaging, commissioning, and trial cutting processing of abrasive jet cutting devices, filling a gap in the domestic market (Gensheng & Zhonhou, 2005).

The classification of abrasive jet is based on two factors. According to the different nature of the fluid, abrasive jets can be divided into abrasive water and abrasive suspension jets. Abrasive water jet is a solid—liquid two-phase medium flow, mixing abrasive grains and high-pressure water, which still belongs to the Newtonian fluids. The abrasive suspension jet prepares the abrasives and various additives into slurries in advance and uses a high-pressure pump to pressurize and create the abrasive suspension jet through the nozzle. This type of jetting is called non-Newtonian fluid. Depending on the mixing method, abrasive water jets can be divided into post- and a premixed abrasive water jets. Different types of abrasive jets have different jet characteristics, and their uses are not identical.

1.2 POSTMIXED ABRASIVE JETTING

The working principle of postmixed abrasive water jet is shown in Fig. 1.1. Under the high-pressure pump, water medium passes through the first nozzle (i.e., water nozzle), high-speed water jet is created, and a certain degree of vacuum is produced in the mixing chamber. Due to the pressure difference between the abrasive box and mixing chamber, abrasive

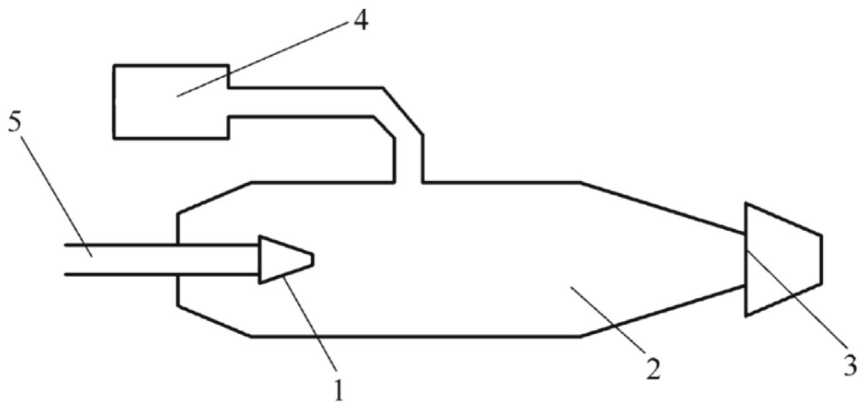

Figure 1.1 Working principle diagram of the postmixed abrasive water jet. 1, Water nozzle; 2, mix chamber; 3, abrasive jets; 4, abrasive box; 5, high-pressure water pipe.

grains enter into the mixing chamber via pneumatic transportation with the action of dead weight and pressure difference and produce turbulent diffusion and blending with the water jet. Then it enters through the second nozzle (i.e., abrasive nozzle), thus generating abrasive water jets (Moshen & Jiajun, 1993).

A postmixed abrasive jet was applied at the birth of abrasive jetting. However, it has since been found that the abrasive sucked by swabbing is difficult to introduce into the central part of the jet and most of the abrasive particles accumulate in the surface of jet; consequently, the abrasive does not sufficiently mix with water and accelerate, thus reducing the energy transfer efficiency of the water medium to the abrasive. To improve the mixing effect of the abrasive and water, a series of abrasive jets appeared successively, such as jetting with collimator and extended mixing tube.

1.2.1 Postmixed Abrasive Jet Nozzle

1.2.1.1 Nozzle Classifications

There are many types of postmixed abrasive jet nozzles. According to the jetting number, the nozzles can be classified into single-jet and multijet nozzles. According to the input direction of the abrasive, nozzles can be classified into side entry, midentry, and tangential feed types. Some common abrasive jet nozzles are as follows.

1.2.1.1.1 Single-Jet Nozzle With Side Entry Supply

Single-jet nozzles with side entry supply are the most typical and common abrasive jet nozzle. A schematic diagram is illustrated as Fig. 1.2. High-pressure water spurts out of the high-pressure water nozzle as it passes through the central pipeline and creates the high-pressure water jet. Due to the entrainment effect produced by the high-pressure water jet in the mixing chamber, the atmosphere in the chamber with high-pressure water spurts to the air jet by the abrasive jet nozzle and a partial vacuum in the mixing chamber is created, thus sucking the abrasive into the chamber or blowing compressed air into the chamber by which the abrasive is pushed into the water jet. At last, the material is squirted through the nozzle to form an abrasive jet. The role of the mixing chamber is to mix the abrasive with the water jet.

It is well known that the velocity of the water jet in the central part is high, the involved abrasive from outside the jetting is difficult to introduce into the central part, and most of the abrasive is gathered in the external layer

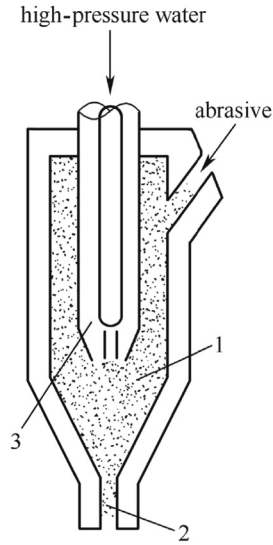

Figure 1.2 Single jetting nozzle with side entry supply. 1, Mixing chamber; 2, abrasive jet nozzle; 3, high-pressure water jets.

of water jets. Therefore the velocity of the abrasive is lower than that of the potential core of jet water. A large number of test results show that the cutting ability of the abrasive jet will be much higher than that of a water jet under the same pressure. When the pressure ranges between 200 and 400 MPa, the abrasive jet can cut any hard material.

A key feature of the nozzle is its simple structure and favorable jetting density and stability; however, the mixing efficiency of the abrasive and water jet is barely satisfactory.

1.2.1.1.2 Single-Jet Nozzle With Tangential Feed

Fig. 1.3 illustrates a single-jet nozzle with tangential feed. This nozzle is spindle shaped, the abrasive inlet is arranged along the tangential direction of the mixing chamber, and a parallel air inlet is set at the abrasive inlet. The abrasive suspension is injected via slurry pump from the abrasive inlet to the nozzle.

Due to the injection of high-pressure water jets, the abrasive suspension and air simultaneously enter into the mixing chamber along the tangential direction of the chamber, rotate, and move forward, fully mixing the abrasive and water jets and reducing intercollision of abrasive particles. Therefore the cutting ability of the abrasive jet can be improved.

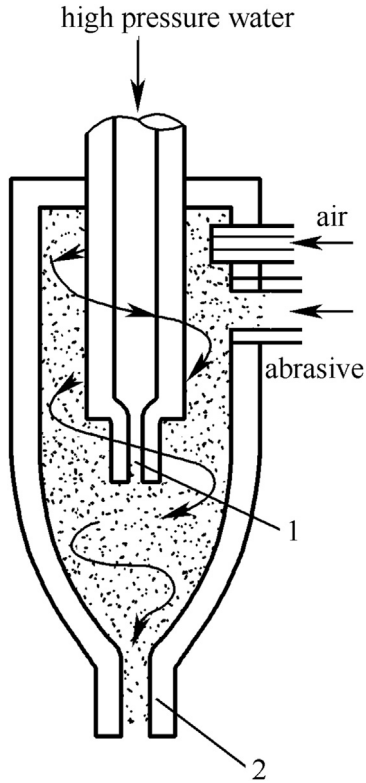

Figure 1.3 Single-jet nozzle with tangential feed. 1, Water jet nozzle; 2, abrasive jet nozzle.

1.2.1.1.3 Multijet Nozzle With Side Entry Supply

Multiple water jet nozzles are arranged in this type of nozzle. The nozzles can be divided into parallel and converging multiple jets with side entry supply according to the arrangement of the water jet nozzle.

Fig. 1.4 is a schematic diagram of a parallel multiple jet nozzle with side entry type supply. Multiple water jet nozzles are distributed in parallel in a circle on the top of the nozzle. Due to the restriction of hole spacing, the abrasive jet diameter is large, the entrainment ability and mixing effect are good, and the cutting ability is greatly improved; however, the width of the grooving is wide.

To reduce the diameter of jets, the axis arrangement of various nozzles, which are distributed in a circle, is changed from parallel to convergent along the center of the nozzle. Therefore many water jets can be converged into a single water jet, which is shown in Fig. 1.5.

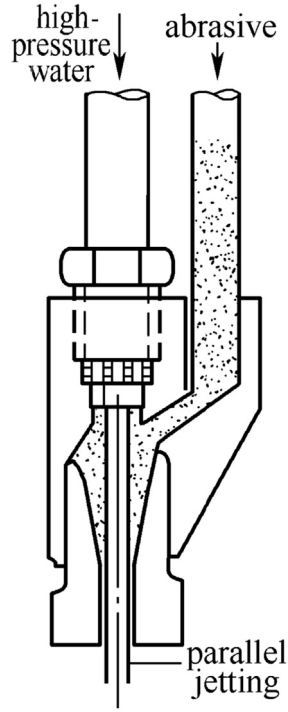

Figure 1.4 Parallel multijet nozzle with side entry supply.

1.2.1.1.4 Multijet Central Entry Nozzle

Fig. 1.6 is a schematic diagram of the nozzle. Under the entrainment effect of various converged jets, the abrasive enters the mixing chamber through midway and is mixed into water jets to improve the mixing efficiency of the abrasive and water jet. The experiment shows that the mixing effect is not obvious and radial dimension is large; therefore it is rarely used.

1.2.1.1.5 External Mixed Abrasive Nozzle

Fig. 1.7 is a schematic diagram of an external mixed abrasive nozzle. This type of nozzle has no mixing chamber or abrasive nozzle. The abrasive suspension is ejected from the middle of the nozzle and mixed into the water jet to obtain the kinetic energy under the entrainment of multiple converging jets. Due to the absence of the mixing chamber, the free water jet ejected from the water nozzle has a weak ability to suck abrasive. Therefore a significant proportion of the abrasive suspension is scattered outside the water jet.

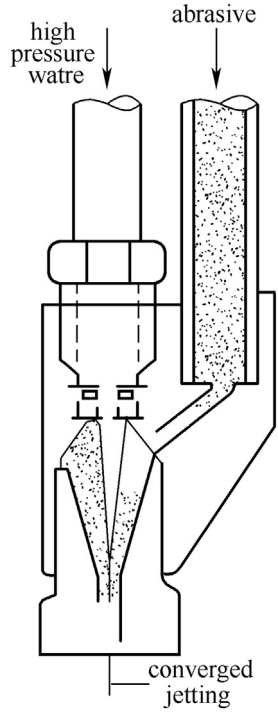

Figure 1.5 Converged multijet nozzle with side entry supply.

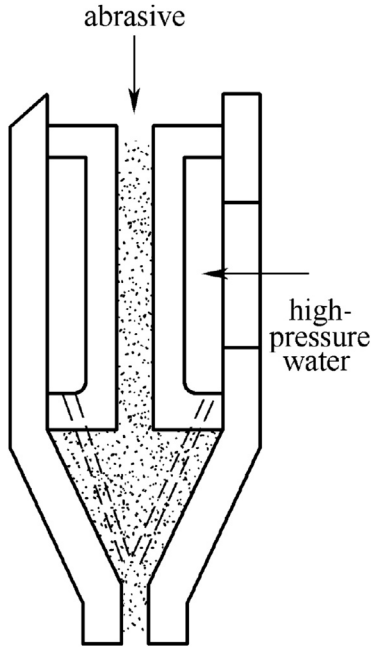

Figure 1.6 Multijet central entry nozzle.

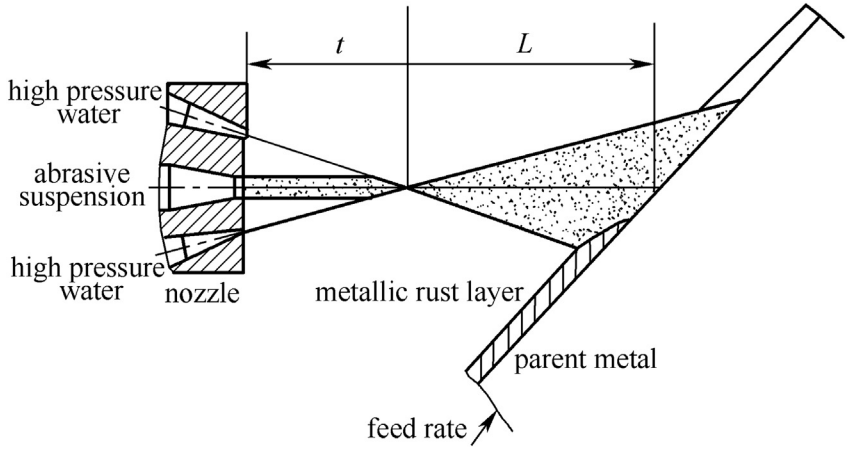

Figure 1.7 External mixed abrasive nozzle.

This type of nozzle has a simple structure and no abrasion issues. However, the mixing effect of the abrasive and water jet is poor and the abrasive jet quality is not satisfactory. The nozzle can only be used for large-scale rust removal. It is the exact object that has been adopted for steel descaling machinery in the Kunming Institute of Technology.

1.2.1.1.6 Rotary Injected Abrasive Jet Nozzle

The abrasive jet nozzle is equipped with a swirl device mounted on a single jet nozzle of the side entry type, which can cause the high-pressure water jet to generate rotational kinetic energy. Fig. 1.8 shows that the high-pressure water rotates under the function of a rotating device and generates a rotary water jet through the water nozzle. The rotary water jet has a large spread angle and strong entrainment, mixing the abrasive more easily into the water jet to enhance the erosion ability. This type of nozzle can improve the efficiency of scale removal; however, it is inappropriate for cutting due to the large jetting spread angle.

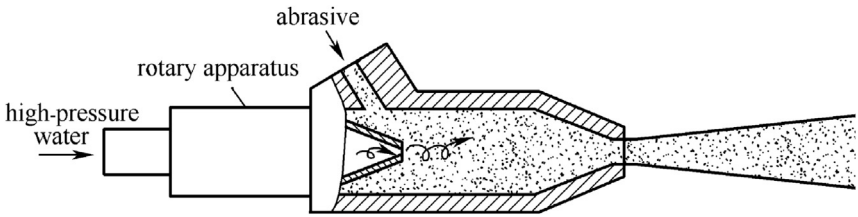

Figure 1.8 Rotary injected abrasive jet nozzle.

1.2.1.1.7 Abrasive Jet Nozzle Equipped With Straightening Pipe

This nozzle was also developed from a single jet nozzle type with side entry. As shown in Fig. 1.9, after the water jet produced by the water jet nozzle entraps the abrasive within the mixing chamber, it is directly injected into the straightening pipe and jet along the axis of the pipe. The abrasive jet can be further mixed and accelerated in the long straightening pipe, which improves the impact capability and range of the abrasive jet.

There are two forms of straightening pipe: straight pipe and straight pipe with a contraction section at the front end. The contraction enables a denser abrasive jet but increases its erosion. The abrasive jet nozzle equipped with straightening pipe is easy to produce due to its simple structure. It has been widely used in cutting operations for abrasive jet, especially in cutting narrow grooves.

1.2.1.2 Nozzle Design

The design of the abrasive jet nozzle not only affects the quality of the abrasive jet but also directly affects the life of the abrasive jet nozzle. The main dimensions of the abrasive jet nozzle include the diameter of the water jet nozzle, the diameter of the abrasive jet nozzle, the size of the mixing chamber, and both the diameter and length of the straightening pipe. A lot of research on abrasive jet nozzle has been conducted by domestic and foreign scholars. Being subject to many factors, it is difficult to arrive at an accurate formula. Therefore several empirical formulas are recommended based on a large number of experimental results.

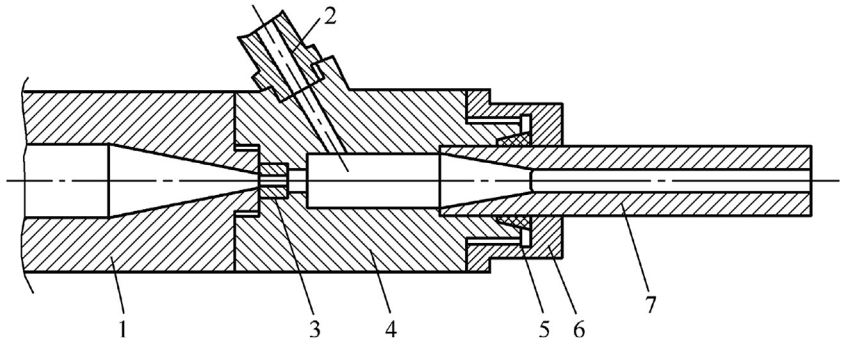

Figure 1.9 Abrasive jet nozzle equipped with straightening pipe. 1, Nozzle body; 2, abrasive inlet; 3, nozzle core; 4, nozzle seat; 5, sealing; 6, locknut; 7, collimated pipe.

1.2.1.2.1 Diameter of Water Jet Nozzle

The diameter of a water jet nozzle is mainly determined by the job demand, pump pressure, and rated flow rate. When both the pump pressure and rated flow rate are constant, the diameter of the nozzle can be expressed by the following equation:

$$d = \sqrt{\frac{4Q}{pu}} = \sqrt{\frac{4Q}{pC\sqrt{2p/\rho}}} \tag{1.1}$$

where d is the nozzle diameter, Q is the rated flow rate, p is the pumping pressure, and ρ is the fluid density.

1.2.1.2.2 Diameter of the Abrasive Jet Nozzle

The diameter of the abrasive jet nozzle is related to the diameter of the water jet nozzle and the distance between the abrasive jet nozzle and the water jet nozzle. A large number of tests show that the diameter of the abrasive jet nozzle should be slightly larger than that of the water jet. Undersized abrasive jet nozzles will create more severe abrasion and less effective self-priming ability of the nozzle and result in abrasive blockage. This is the reason for stuffing of the water jet at the abrasive jet nozzle. However, overdimensioned abrasive jet nozzles can reduce abrasion. The air may move into the mixing chamber through the nozzle inlet, which can reduce the self-priming ability of the nozzle and accelerate the diffusion of the abrasive jet. Experience shows that the diameter of the abrasive jet nozzle shall be two to three times larger than that of the water jet nozzle and more than three times larger than the particle size of the abrasive.

1.2.1.2.3 Dimension of the Mixing Chamber

The dimension of the mixing chamber has a direct effect on the mixing effect of abrasive and water jet. Large-sized chambers can improve the mixing effect of abrasive and water jet, while increasing the resistance of the water jet. This will reduce the dynamic pressure and consequently the cutting ability. Therefore the dimension of the mixing chamber should not be too large. Generally, the dimension of the mixing chamber should be determined by the structure of the water jet nozzle and cannot be deliberately increased. The mixing chamber is generally 30—40 times the diameter of the water jet nozzle.

1.2.1.2.4 Diameter and Length of the Straightening Pipe

The straightening pipe can promote further mixing of the abrasive and water jet, thus improving the cutting ability of the abrasive jet. The diameter of the straightening pipe should be the same as that of the abrasive jet nozzle and the length of the pipe should not be too long. A long pipe will reduce the cutting ability of the abrasive jet and shall be designed to be 15—20 times the diameter.

1.2.2 Abrasive and Its Supply Method

1.2.2.1 Summary of Abrasive

Abrasive is an essential medium of any abrasive jet. The variety and nature of the abrasive has a great impact on the working efficiency of an abrasive jet.

1.2.2.1.1 Classification of Abrasives

Generally speaking, abrasives can be divided into three categories: mineral, metal, and artificial mineral. The physical features of several common abrasives are illustrated in Table 1.1.

The requirements for abrasive selection are favorable cutting effect, sufficient supply, and economic price. The hardness, particle size, shape, and density of the abrasive greatly influence the cutting ability of abrasive jet. Abrasive jets with emery as the abrasive have the best cutting effect. However, this is expensive and cannot be widely used. Garnet, which is also selected as the abrasive, has favorable cutting effects and is rich in China. The price of garnet is much lower than that of emery; therefore, it has been widely used in China and abroad. As a commonly used abrasive, silica sand has the worst cutting effect, but it is cheap and also the most commonly used material.

1.2.2.1.2 Particle Size of the Abrasive

The particle size is the most important parameter of an abrasive and the probability dimension of abrasive particle is generally called the particle

Table 1.1 Natural properties of common abrasives

Name	Symbol	Hardness	Specific gravity	Cost
Silica sand	S.S	1100	3.0	Low
Granet	G.	1300	3.8	Medium
Alumina	A.U	1500	3.4	Medium
Emery	S.C	2500	3.2	Expensive
Iron residue	I.S	500	3.2	Low
Iron sand	I.G	800	7.3	Medium

size. The nominal dimension range of particle diameter of specific abrasives can be concluded from the particle size. The abrasive particle that is smaller or larger than the specific diameter occupies a certain proportion in each size class of abrasives.

There are two standards of classifying and two symbols for abrasive particles: one is represented by the nominal dimension (μm), whereas the other is represented by the mesh number of screen per inch. The symbol of the size number is to add "#" on the upper corner of the number. A large number of tests show that an abrasive jet with abrasive number 60# and 80# is better suited for cutting metal.

The new national standard (GB 2481-83) for abrasives stipulates that R40/3 in international standard ISO3310/1982 (E) must be adopted for checking mesh size. The mesh size L is a sequence with a common ratio of $10^{3/40}$, which is shown in the following formula:

$$l = 45 \times \left(10^{3/40}\right)^n \tag{1.2}$$

where n is 0, 1, 2, …, 30.

This dimension series for the inspection of mesh is completely consistent with the specifications in international standard ISO/DI S8486 and American standard (ANSIB 74.12-R1982) and is identical to the Japanese standard (JISR 6001-1973) and the European abrasive manufacturing association standard (FEPA 32GB 1971).

The mesh inspection, which is specified on old GB for abrasive (GB 2481-81), uses R10 dimension series. The mesh size is a sequence with the common ratio of $10^{1/10}$, which is shown in the following equation:

$$l = 45 \times \left(10^{1/10}\right)^n \tag{1.3}$$

where n is 0, 1, 2, …, 19.

This dimension series is completely consistent with the specifications of the national standard of the Soviet Union (OCT 1971 - 3647). A comparison of mesh size series in new and old international standards is given in Table 1.2. The table also shows particle sizes of the abrasives.

1.2.2.1.3 Reusability of Abrasives

In an abrasive jet cutting system, the flow rate of the abrasive is generally about 3 kg/min, and sometimes it even reaches 6 kg/min. Thus the cost of abrasive consumption cannot be ignored. It is necessary to study the reusability of the abrasive to reduce costs.

Table 1.2 Comparison of mesh dimension series of old and new international standard

	New international standard		Old international standard	
No. n	Mesh number (particle size)	Basic dimension (μm)	Mesh number (particle size)	Basic dimension (μm)
0	325	45	320	40
1	270	53	280	50
2	230	63	240	63
3	200	75	180	80
4	170	90	150	100
5	140	106	120	125
6	120	125	100	160
7	100	150	80	200
8	80	180	70	250
9	70	212	60	315
10	60	250	46	400
11	50	300	36	500
12	45	355	30	630
13	40	425	24	800
14	35	500	20	1000
15	30	600	16	1250
16	25	710	14	1600
17	20	850	12	2000
18	18	1000	10	2500
19	16	1180	8	3150
20	14	1400	/	/
21	12	1700	/	/
22	10	2000	/	/
23	8	2360	/	/
24	7	2800	/	/
25	6	3350	/	/
26	5	4000	/	/
27	4	4750	/	/
28	31/2	5600	/	/
29	0.265	6700	/	/
30	5/16	8000	/	/

Grinding and collision will be created during the process of acceleration and material impaction for the abrasive. The particle size of the used abrasive will decrease. The degree of grinding is related to the nature of the abrasive.

If the average particle size of abrasive after usage remains close to the original size, the reusability of the abrasive is good. The particle size of

the abrasive, such as steel grit, has little change before and after usage, which represents good reusability. Brittle materials, such as silica sand and garnet, have significant variations in particle size before and after usage, which represents poor reusability and limited possibility for recycling. After cutting concrete and steel, the weight percentage of abrasives with original particle size can be used as an indicator for abrasive recycling. Experiments show that the reusability of steel grit is about 90%, whereas the reusabilities of silica sand and garnet are both about 10%. The cutting capacity of reused garnet has been reduced by 40%–60% if other conditions remain unchanged. The garnet used for cutting has little reusability. During cleaning and scale removal, the reusability of the abrasive will be significantly improved by low jetting operation pressure.

1.2.2.1.4 Recycling of Abrasive

Abrasives are generally able to precipitate in a short period of time due to their high specific gravity. Experiments show that the wastewater produced by cutting concrete with garnet, silica sand, and steel grit has rapid settling velocity. The abrasive water in the three cases can be completely settled within 1.0–1.5 min even without coagulant. Among these abrasives, garnet has the fasted settling velocity and the slurry after cutting will be completely settled in 1.0 min.

The abrasive has high settling velocity in water and hence can be recovered via multiplexed settling pit. The open cross-sectional area of the pit should be large enough to lower the water velocity, than settle the velocity of the abrasive. When the abrasive is sufficiently settled in the pit, the water–abrasive mixture can be introduced into another pit. The recovered abrasive must be screened and treated for recycling. In addition, a centrifugal cyclone can also be used for the rapid recovery of abrasive. However, it is only to be used in the automation system for continuous recovery of abrasive.

1.2.2.2 Supply System of Abrasive

The abrasive supply system is divided into dry abrasive and wet abrasive suspension supply system.

1.2.2.2.1 Dry Abrasive Supply System

The dry abrasive has very poor flow performance and cannot flow in a horizontal way. Therefore pneumatic transportation is required for dry abrasive.

In the pneumatic transportation, the most important parameter is the critical velocity produced via settlement of abrasive particles. When the particle size "d" is equal to 0.1—1.0 mm, the critical velocity "u" is:

$$u = 0.261\left(\frac{\rho_a - \rho_g}{\rho_g} \times \frac{g}{\upsilon^{-\frac{1}{2}}}\right)^{\frac{2}{3}} d \tag{1.4}$$

where u is the critical velocity (m/s), ρ_a is the abrasive density (kg/m^3), ρ_g is the gas density (kg/m^3), υ is the air viscosity (Pa s), and d is the abrasive particle size (mm).

When the abrasive density is 2500 kg/m^3, then $u = 6.51\ d$.

In the actual pneumatic transportation device, due to the collision and friction between particles or between particles and pipe walls, the presence of a boundary layer near the pipe wall, and nonuniform distribution of air speed in the elbow, much higher air velocity than the settling velocity of particles is required. The results of experiments indicate that the critical conveying air velocity is 18—22 m/s and the practical air velocity is 30—40 m/s.

Dry abrasive supply systems can also be divided into pressurized and self-priming forms.

- Pressurized abrasive supply system: The abrasive is pressurized into the abrasive tank via an air compressor and enters the mixing chamber of the abrasive nozzle via the transmission pipe. The pressure of compressed air is generally 0.2—0.4 MPa.

A pressurized abrasive tank is shown in Fig. 1.10. It is mainly composed of a pressurized abrasive sealed abrasive tank, a gas—water separator, an air valve, a sand valve, and other components. The compressed air is divided into two branches via the gas—water separator, one can lead to the upper of abrasive feeder and the other can lead to the bottom of the pressurized abrasive tank. The gas flow is controlled by the gas valve. Abrasive will leak into the bottom of the air conduit under both air effect and its own weight and will then be conveyed to the nozzle via high-speed air flow.

A gas—water separator is a type of accessory used to remove water, oil, and dust in gas sources, which has to be installed vertically.

- Self-priming dry abrasive supply system: The system depends on the swabbing generated in the mixing chamber of the abrasive jet nozzle by water injection to produce the airflow, which can be used to supply

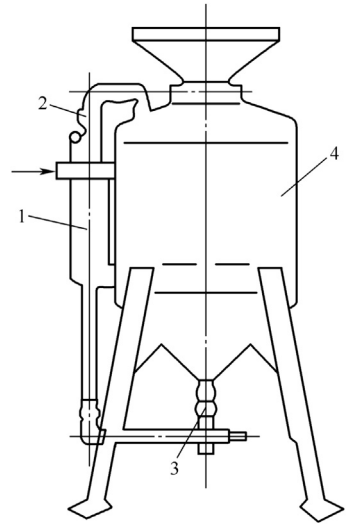

Figure 1.10 Pressurized abrasive tank. 1, Gas—water separator; 2, gas valve; 3, sand valve; 4, pneumatic abrasive tank.

abrasive to the sand supply pipeline. The system adopts double hoppers: the upper one is the main hopper, which will be used to store abrasives, whereas the lower one is the collecting hopper which will collect the leaky abrasive by self-weight (Fig. 1.11). The control valve at the bottom of the storage hopper can adjust the supply amount of abrasives. There are certain distances between collecting and storage hopper, so that the abrasive can produce sufficient initial kinetic energy during free falling. In addition, the air is sucked into the sand delivery pipe through the gap between two hoppers, creating high-speed water flow. The supply amount of abrasive is only related to the hopper structure and abrasive properties, but not to the amount of abrasive in the hopper. Therefore the system can continuously and uniformly supply the abrasive. Moreover, the system has a simple structure, costs less, requires no driving force, and can consequently be widely used.

When the air velocity is too low in the sand delivery pipe, the abrasive will not be suspended in the pipe, but produce mass flow instead, resulting in uneven sand supply. Furthermore, pipes near the abrasive jet nozzle are

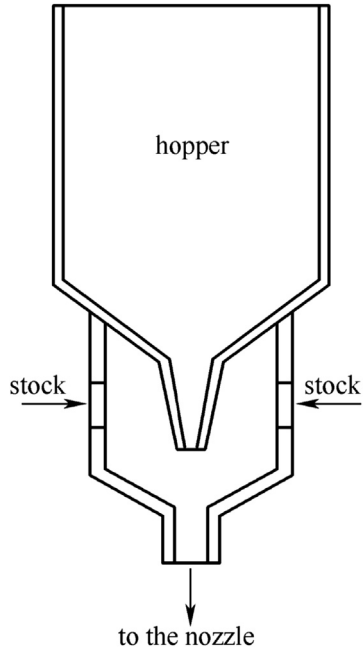

Figure 1.11 Dry abrasive supply system.

easily moisturized, which will result in the agglomeration of the abrasive, even blocking the sand delivery pipeline from supplying sand. These are the disadvantages of the system.

1.2.2.2.2 Wet Supply System

In the generation device of the abrasive jet, the dry abrasive supply system is more frequently used due to its simple process and high efficiency. However, there are also some disadvantages such as wide kerfs and susceptibility to produce cracks, burrs, and debris. The abrasive used in the system can hardly be recycled, which greatly increases the overall cost.

A wet supply system is shown in Fig. 1.12. The system uses the tangential-feed nozzle and two parallel high-pressure pumps to supply high-pressure water. The feeding material is an abrasive suspension. First, the abrasive suspension is prepared by mixing abrasive, clay, and water in a specific proportion. Clay can prevent the abrasive from precipitation and hardening. The formulated abrasive suspension has good fluidity and is easy to control. The abrasive suspension will be conveyed to the abrasive nozzle via mud pump, and the used slurry will be collected in a

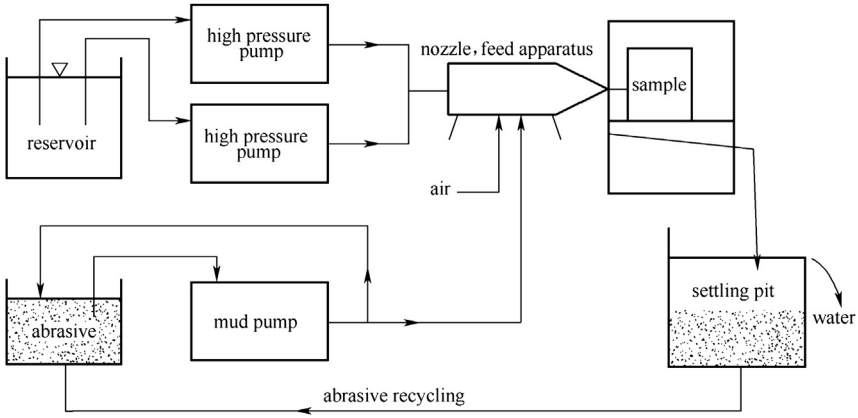

Figure 1.12 Wet supply system.

sedimentation tank for recycling after treatment. The slurry feed jet can produce narrow cuts and higher surface smoothness than a common abrasive jet in metal cutting.

1.2.3 Mixing Mechanism of Abrasive for Postmixed Abrasive Jet

1.2.3.1 Movement of Abrasive Jet Along the Axial Line

When the abrasive enters the water jet, due to the velocity difference between the abrasive and water, the abrasive will be subjected to a force, which is the reason for the acceleration. The force can be expressed with the following equation:

$$F = C_D \frac{1}{2} \rho_\omega (V_\omega - V_\alpha)^2 \frac{\pi}{4} d_\alpha^2 \tag{1.5}$$

where C_D is a dimensionless parameter R_{ep}, which is determined by the Reynolds number of the particle, R_{ep}. Generally, the R_{ep} value for abrasive jet is located in the transitional zone, therefore C_D can be set at 0.44. ρ_ω and V_ω are the density and velocity of water, respectively. V_α and d_α are the velocity and particle size of the abrasive particles, respectively.

First, a special case will be discussed. A stationary spherical particle, which is added to the uniform flow field at a speed of V_o, will be accelerated by the force of fluid on the particle. The law of motion is described by Newton's second law.

$$(m' + m_\alpha) \frac{dV_\alpha}{dt} = C_D \frac{1}{2} \rho_\omega (V_o - V_\alpha)^2 \frac{\pi}{4} d_\alpha^2 \tag{1.6}$$

where m' is the virtue mass or added mass. Since the acceleration movement of the particle will help other surrounding particles to accelerate. This effect is equivalent to an additional mass m'. The spherical particle can be expressed by:

$$m' = \frac{1}{2} \cdot \frac{\pi}{6} q_\alpha^3 \rho_\omega \tag{1.7}$$

Eq. (1.6) can be rewritten as

$$\left(\frac{\rho_\alpha}{\rho_\omega} + \frac{1}{2}\right) \frac{dN_\alpha}{dt} = \frac{3C_D}{4d_\alpha}(V_o - V_\alpha)^2 \tag{1.8}$$

$$\eta = \frac{V_\alpha}{V_o}, \quad \zeta = \frac{4}{3C_D}\left(\frac{\rho_\alpha}{\rho_\omega} + \frac{1}{2}\right), \quad \alpha = \frac{V_o t}{\zeta d_\alpha}$$

where η, ζ, and α are dimensionless.

The equation is simplified to:

$$\frac{d\eta}{d\alpha} = (1 - \eta)^2 \tag{1.9}$$

$$\eta = \frac{\alpha}{1 + \alpha} \tag{1.10}$$

The mixing effect is expressed by the equation $1 + \eta = 1/(1 + \alpha)$. The higher the value of α, the better the mixing effect will be.

In fact, when studying the mixing effect, the velocity of particles at different distances has to be calculated. Therefore, t in the equation η (that is α) is eliminated and replaced by the distance of particles in time t. The distance l is expressed by:

$$l = \int_0^t V_\alpha d\tau = \zeta d_\alpha [\alpha - \ln(1 + \alpha)] \quad \text{or} \quad \frac{l}{\zeta d_\alpha} = \alpha - \ln(1 + \alpha) \tag{1.11}$$

The relationship between V_α / V_o and $l/\zeta d_\alpha$ can be calculated via Eqs. (1.10) and (1.11).

This will provide a number of figures that illustrate the mechanism.

If $\eta = 0.9$, $\alpha = 9$, $l/\zeta d_\alpha = 6.70$

1. $\rho_\alpha/\rho_\omega = 3$, $\zeta = 10.60$, $l/d_\alpha = 71$
2. $\rho_\alpha/\rho_\omega = 7.3$, $\zeta = 25.15$, $l/d_\alpha = 168$

When the flow field does not consist of single particles, C_D is also related to the position of particles.

In general, C_D will either be reduced, or the time and distance, which are required to achieve the same mixing effect, have to be extended.

From the aforementioned analysis, we learn that:

1. The mixing process of particles and fluids or the accelerations of particles require both time and space. Their relationships cannot be described via simple laws of conservation momentum.
2. A higher value of α, i.e., a higher value of $l/\zeta d_\alpha$, indicates a better mixing effect and faster particle acceleration. When l is a constant, the density and particle size of abrasive particles should be as small as possible. However, density and particle size are related to the erosion process and the particle size should be used within an appropriate range.

The velocity of the water jet has decreased in the direction of axial line. Therefore an analysis of the motion of particles in the flow field with velocity gradient is necessary.

The fluid particle has an accelerated velocity dV_ω/dt in the flow field, which is equivalent to a "pressure gradient" within the flow field.

$$\frac{\partial P}{\partial n} = -\rho_\omega \frac{dV_\omega}{dt} \tag{1.12}$$

Under the pressure gradient, the particles are subjected to "buoyancy" $\Omega\rho_\omega \frac{dV_\omega}{dt}$, where Ω_i is the volume of the particle.

Therefore the motion equation of the particle can be illustrated as:

$$\Omega\rho_\alpha \frac{dV_\alpha}{dt} = \Omega\rho_\omega \frac{dV_\omega}{dt} - \rho_\omega \frac{\Omega}{2}\left(\frac{dV_\alpha}{dt} - \frac{dV_\omega}{dt}\right) + \theta(V_\omega - V_\alpha) \times C_D \times \frac{1}{2}\rho_\omega (V_\omega - V_\alpha)^2 \times S_D \tag{1.13}$$

where θ is the sign function and S_D is the incident flow area.

The flow field of the water jet is constant; the velocity of the fluid particle is only the function of location. This can be illustrated as:

$$\frac{dV_\omega}{dt} = V_\omega \frac{dV_\omega}{dX} = \frac{1}{2}\frac{dV_\omega^2}{dt} \tag{1.14}$$

Imagine that the particle arrived at location X at time t, velocity $V_\alpha = \frac{dX}{dt}$, and acceleration $\frac{dV_\alpha}{dt} = \frac{d^2X}{dt^2}$; Eq. (1.13) can be rewritten as:

$$\left(-\frac{\rho_\alpha}{\rho_\omega} + \frac{1}{2}\right)\frac{d^2X}{dt^2} = \frac{3}{4}\frac{dV_\omega^2}{dX^2} + \theta\frac{3C_D}{4d_\alpha}\left(\frac{dX}{dt} - V_\omega\right)^2 \tag{1.15}$$

The definite condition of the equation is $X|_{t=0} = X_o$, $\left.\frac{dX}{dt}\right|_{t=0} = 0$

This makes Eq. (1.15) dimensionless.

$$X = \frac{X'}{D}, \quad V_\alpha = \frac{V'_\alpha}{V_\alpha}, \quad V_\omega = \frac{V'_\omega}{V_o}, \quad d_\alpha = \frac{d'_\alpha}{D}$$

$$X_o = \frac{X'_t}{D}, \quad t = V_o \frac{t'}{D}, \quad \rho = \frac{\rho_\alpha}{\rho_\omega} + \frac{1}{2}$$

where D is the diameter of the water jet nozzle, V_o is the exit velocity, d' is the diameter of abrasive particle, and d is the dimensionless diameter.

Consequently, the equation is shown as follows:

$$\rho \frac{d^2X}{dt^2} = \frac{3}{4} \frac{dV_\omega^2}{dt^2} + \theta \frac{3C_D}{4d} \left(\frac{dX}{dt} - V_\omega \right)^2 \tag{1.16}$$

Eq. (1.16) has the same form as Eq. (1.15), but Eq. (1.16) is nondimensional. This is an equation that describes longitudinal motion (acceleration process) of abrasive particles.

In the same cross-section of the water jet, the jet velocity, which is related to the distance to axial line, is not the same. Only the location of particles in the jet can determine V_ω in the equation.

1.2.3.2 Lateral Movement of Abrasive Particle

The lateral movement of the particle can be divided into two parts. The first is the preparation of the abrasive for jetting and the second is the movement of the abrasive in the direction of the axial line.

When the abrasive particle reaches the jet surface at a certain speed, a number of particles collide with jets and rebound, thus hindering injection. The collision phenomenon is not obvious when the velocity of the added particles is low. The abrasive jet nozzle is used to force the particles to enter the jet via collision with rebounded particles. The inner diameter of the nozzle must not be too large to ensure abrasive suspension within the nozzle. Pinpoint erosion experiments show that the shape of the erosion pit is determined by the water jet structure and has nothing to do with the feed location.

There is a further entry mode of the abrasive (see Fig. 1.13). Since the internal velocity distribution of water jet is not uniform, the exit of the nozzle will average the internal velocity when the outlet diameter of the nozzle is less than the diameter of the jetting at the exits. At the same time, the abrasives in area A are well prepared for jetting and the mixing effect is favorable at that moment (but erosion is severe at the nozzle outlet).

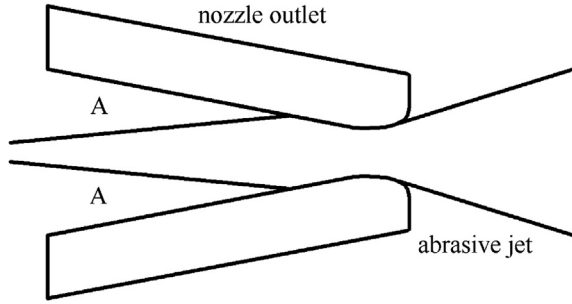

Figure 1.13 Abrasive jet nozzle scheme.

The particles will accelerate along the axis line when they are optimally prepared for jetting. As the particle moves into the boundary layer (shear flow field), it will be subjected to lift force, which will force particles to move toward the axial line of the jet with lateral motion.

When spherical particles move steadily within the flow field and automatically rotate with the angular velocity of ω, particles will be subjected to a lift force (Magnus lift). Rubinow and Keller have calculated the lift force as follows:

$$L_\omega = \pi\left(\frac{d_\alpha}{2}\right)^3 \rho_\omega \omega (V_\alpha - V_\omega) \tag{1.17}$$

If shear flow dominates the field, the particles will be subjected to another lift force (Saffman lift), which is caused by interaction of shear and slippage. Saffman has calculated this lift force under certain conditions:

$$L_S = 6.64\mu\left(\frac{d_\alpha}{2}\right)^2 \left|\frac{S}{V}\right|^{\frac{1}{2}} (V_\alpha - V_\omega) \tag{1.18}$$

Rubinow experiments show that the aforementioned equation works when the Reynolds number of particles R_{ep} is below 2. However, R_{ep} in the abrasive jet has a magnitude of 10^4, and therefore there is no reason to suggest that the Saffman formula can still work. Magnus and Saffman indicated that the particles move toward the axis line after entering the jet.

Abrasive particles in the abrasive jet are not in a single state; the particles are subjected to a lift that is similar to the normal stress of Bagnold. The collision effect in the mixing process between all abrasive jet particles is analyzed according to the thinking of Bagnold. During the process of abrasive jetting, particle B will be closer to the axis line than particle A; therefore u_B is considered to be larger than u_A. When two particles collide with each other,

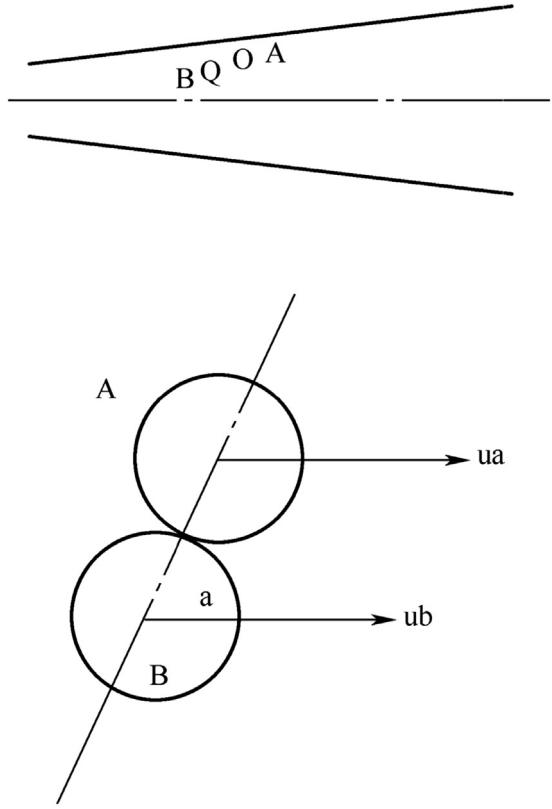

Figure 1.14 Collision structure diagram of abrasive particles.

the angle α between the center line and the taxis line of particles ranges between 0 to $\pi/2$ (Fig. 1.14).

The collision is not in alignment, and the collision velocities are $u_A \cos \alpha$ and $u_B \cos \alpha$. The velocity in the direction of the central line after collision is as follows:

$$V'_A n = u_A \cos \alpha + \frac{(1+e)m_B}{m_A + m_B}(u_B - u_A)\cos \alpha \tag{1.19}$$

$$V'_B n = u_B \cos \alpha + \frac{(1+e)m_A}{m_A + m_B}(u_A - u_B)\cos \alpha \tag{1.20}$$

$$u_B > u_A,$$

So

$$V'_A n > u_A \cos \alpha,\ V'_B n > u_B \cos \alpha$$

This means that particle *B* will move toward the central line, but particle *A* moves in the opposite direction.

When the abrasive enters into the jet, the distribution of abrasives in the jet has become increasingly scarce as it moves toward the central line. Therefore the total effect of collision between particles is to enable the particle to move toward the axis line of jet. This is the same phenomenon as described in Bagnold's findings, where particles move upward under shear action.

1.3 PREMIXED ABRASIVE JET

1.3.1 Development of Premixed Abrasive Jet

The aforementioned abrasive jet has been developed early and is widely used. However, due to the poor mixing performance of the abrasive material and water, the abrasive material has not been fully utilized, leading to the need for higher water pressure. For cutting steel, the water pressure should normally be above 200 MPa.

To fundamentally improve the mixing jet performance of abrasive material and water, the premixed abrasive jet technique has been developed in recent years. Unlike the previous method that adds the abrasive material after the water jet started, the premixed abrasive jet involves mixing the abrasive with water into an abrasive slurry water in a high-pressure water pipe and jet via abrasive nozzle. Therefore abrasives in a premixed abrasive jet have a very high kinetic energy, which greatly improves the effect of material erosion. In the same cutting condition, the working pressure of a premixed abrasive jet is much lower. A working pressure of 10 MPa is sufficient to cut hard materials such as steel (Qingwen, 2001).

Fig. 1.15 describes a device that utilizes a premixed abrasive jet, which is composed of a high-pressure pump station, an abrasive supplier, and a spray gun. The high-pressure pump station is exactly the same as a pure water jet, except that the pressure level is much lower. Abrasive jet nozzle of the premixed abrasive jet is broadly similar the pure water jet nozzle, except that the issue of nozzle wear is even more highlighted. Therefore the key of premixed abrasive jet technology is to add the abrasive to the high-pressure pipe and to mix it evenly with water. High-pressure water comes from a pumping station: one stream vent leads to the top of the abrasive tank and the other directs to the mixing cell. The high-pressure water basically puts a form of static pressure on the abrasive after reaching the upper abrasive tank due to the very slow abrasive flow rate. Therefore abrasives enter the mixing cell through the feed valve under a combination force of

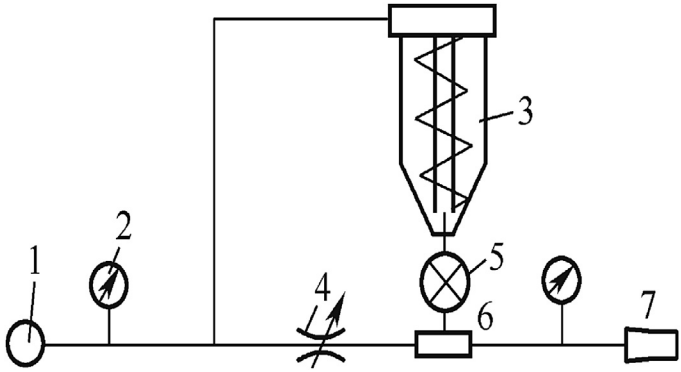

Figure 1.15 Premixed abrasive jet. 1, High-pressure pump; 2, pressure gauge; 3, abrasive tank; 4, throttle valve; 5, feed valve; 6, mixing cell; 7, nozzle.

hydrostatic pressure and gravity. The high-pressure water flows into the mixing cell through the throttle valve jet from the nozzle after uniformly mixing the abrasives. Abrasive supply can be adjusted by the feed valve.

According to the liquid–solid two-phase flow theory, abrasive particles will not be deposited when the pressure of the abrasive slurry in the pipeline is higher than the critical speed.

A high-pressure abrasive tank is a high-pressure vessel, the pressure of which is equal to the working pressure of the high-pressure water system, which is supposed to be able to accommodate abrasive amounts during 20–30 min. To improve the stress condition of the pressure vessel, a thin container of small diameter is recommended. A composite wall structure should be adopted in case of a big-diameter container. The abrasive can be loaded in dry form as slurry into the pressure vessel. When using artificial feeding, the upper container should be installed with a mobile seal. Since forces on the seal are associated with the seal section, the charging caliber should not be too wide. The seal should be convenient to open or close and provide good sealing performance.

The feed valve is responsible for opening, closing, and adjusting the abrasive supply. Ball valves and reciprocating sliding valves can be used as feed valve plug valves. When selecting the valve type, flow characteristics of the liquid–solid two phase should be fully considered to avoid valve failure due to abrasives being stuck between the valve core and valve seat. The mixing cell is actually a cavity. An orifice upstream of the mixing chamber can generate a pressure drop and produce a local vortex to enable uniform mixing of the abrasive in the water when high-pressure water flows through.

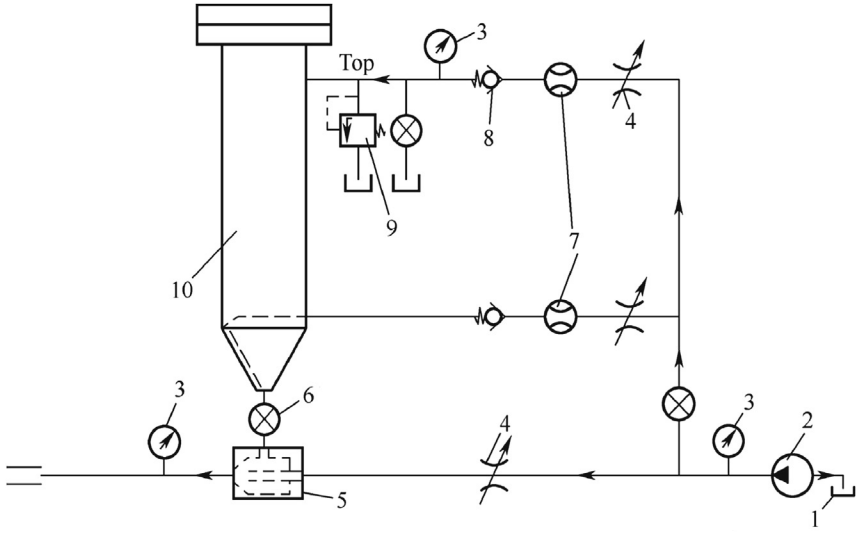

Figure 1.16 Ejector injection of a premixed abrasive jet system. 1, Water tank; 2, high-pressure pump; 3, pressure gauge; 4, throttle valve; 5, ejector; 6, gate; 7, flow meter; 8, check valve; 9, relief valve; 10, abrasive tank.

Fig. 1.16 shows a diagram for ejector injection of a premixed abrasive jet system. Its abrasive supply device is mainly composed of high-pressure abrasive cans, an ejector device, a control valve, and a water supply system.

High-pressure water from a high-pressure pump station is divided into three streams. The first stream flows though the water gate and is then throttled and directed to the top of the high-pressure abrasive tank, applying a positive pressure to the abrasives. The second stream of water flows though the water gate and is then throttled and vented to the cone bottom of the high-pressure abrasive tank for the purpose of abrasive fluidization and easy injection into the high-pressure water pipe. The third stream of water flows through the throttle valve to the ejector. All three ways of flow can be adjusted via throttle valves.

Jetting of high-pressure water through the ejector device results in pressure reduction of the mixing cell. At the same time, the fluidized abrasive at the bottom of the abrasive tank is injected into the mixing cell under pressure from the upper part and is involved in high-speed water flow and even mixing with water. The high-speed water carrying the abrasives is ejected from the nozzle via pipelines.

Plenty of tests show that both the premixed abrasive jet techniques suffer from problems of uneven abrasive supply.

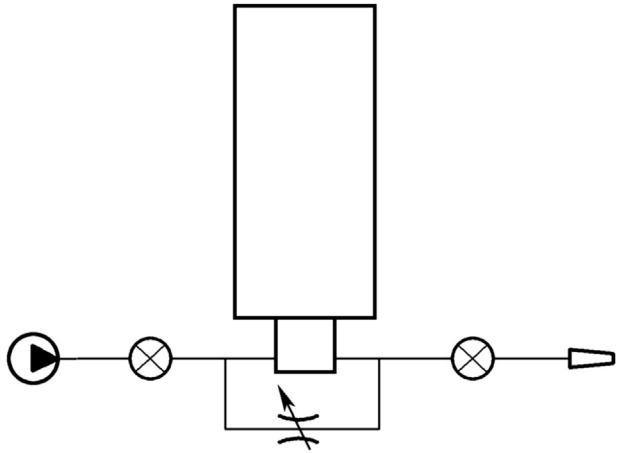

Figure 1.17 Novel abrasive feed system.

Fig. 1.17 shows a novel type of abrasive supply system. High-pressure water flows into the abrasive tank at the bottom of the mixing cell to transport abrasives. At the same time and due to high gravity, abrasive particles follow a settlement downward movement in the abrasive tank, whereas water presents seepage flow upward through the space between the abrasive particles. The volume flow of both are the same. The aforementioned flow state can be directly observed within the abrasive tank via transparent organic glass.

In this type of feeder system, the abrasive tank is independent of the flow path. The pressure difference at every point of the system is a static hydraulic pressure difference only caused by height, i.e., the pressure gradient of the fluid in the abrasive clearance is constant and does not depend on the height of the abrasives in the tank. The amount of abrasives in the tank will not affect the feeding either.

1.3.2 The Abrasive Accelerating Mechanism of Premixed Abrasive Jet

1.3.2.1 Abrasive Accelerating Mechanism

In premixed abrasive jets, abrasives enter the high-pressure pipeline first and are then accelerated for the first time. However, due to the low flow velocity in the conveying tube, the acceleration of the abrasive process is mainly finished at the nozzle contraction, cylindrical section, and the jet core section.

At the entrance of the nozzle, the speeds of abrasive and water are in balance and the two-phase velocity difference is zero. Within the nozzle

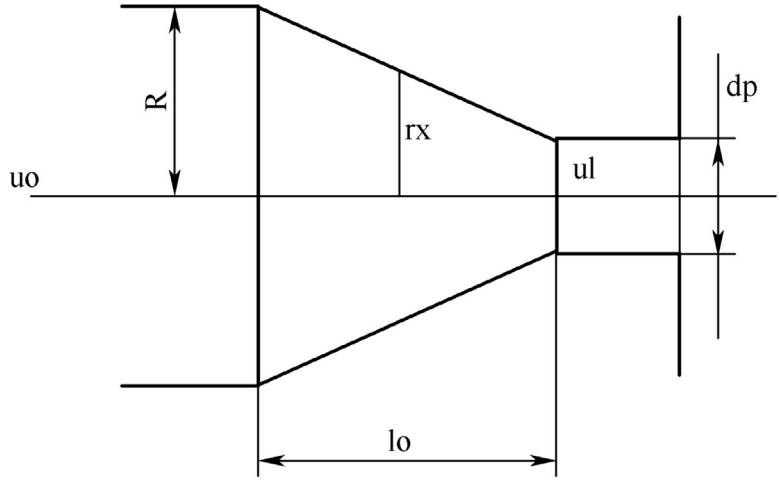

Figure 1.18 Nozzle structure for a premixed abrasive jet.

contraction, the velocity distribution curve of the abrasive and water are similar except for the abrasive speed, which always lags behind the speed of the water, and the gap steadily increases. In the following instances of the calculation model, the speed difference of both phases at contraction is about 25%.

The curves in Fig. 1.18 show that when the particles go into the nozzle contraction, their speed slowly increases. However, with the increase of distance *X*, particle velocity increases faster.

The acceleration of the abrasive in the cylindrical section of the nozzle is opposite to that in the contraction segment. The initial speed of particles in the cylindrical section quickly increases at the early stage, but when the particle speed increased to a certain degree, the speed increment was limited. Since nozzle contraction is generally short, the speed of particles that are injected out of the nozzle has a large difference compared with water velocity. The core section of the jet is a uniform flow field; particularly the core section at the front is very similar to that of the cylindrical section. Therefore the speed will continually accelerate in the core section of the jet and will reach the highest value in the middle or at the back.

1.3.2.2 Water Flow Velocity Distribution Within the Nozzle

For the premixed abrasive jet technique, abrasive and water are ejected from the same nozzle; therefore the nozzle shape is almost the same as that of a pure water jet nozzle. The structure is as shown in Fig. 1.18.

In premixed abrasive jet, abrasives are directly added to high-pressure pipeline and mixed with high-pressure water to achieve a speed balance. However, due to the slow water flow in the high-pressure pipeline, the acceleration of the abrasive particle is mainly finished in the nozzle contraction, cylindrical section, and the core segment of the jet.

The velocity distribution of the turbulent flow in the pipeline with circular section is as follows:

$$u = u_m \left(\frac{r}{R}\right)^n \tag{1.21}$$

where the empirical index is related to the flow Reynolds number; the larger the Reynolds number, the smaller will n be; R is the pipe radius and u_m is the maximum speed at the axis.

The average speed of velocity distribution is represented in Eq. (1.21):

$$\overline{u} = \frac{1}{R}\int_0^R u_m \left(\frac{r}{R}\right)^n dr$$

Then,

$$\overline{u} = \frac{1}{n+1} u_m \tag{1.22}$$

To qualitatively explain the flow state within the nozzle contraction, the velocity distribution on the contraction of the arbitrary cross-section is assumed in the same form as Eq. (1.21). As a result, the average speed of each section and the maximum speed at the axis is consistent with Eq. (1.22). Furthermore, if the contraction flow rate increases with decreasing n, the section average speed consequently aligns more and more with the maximum speed at the axis, i.e., the sectional velocity distribution moves more and more toward an average; therefore the average speed of each section can be used as the velocity distribution at the contraction section. Water flow rate at the contraction section can be obtained by the continuity equation as follows:

$$u = u_o \left(\frac{R}{r_X}\right)^2 \tag{1.23}$$

where u_o is the flow velocity at the nozzle entrance.

Due to the small diameter of the nozzle exit, the water flow speed is basically evenly distributed within the cylindrical section.

1.3.2.3 Solution of the Model

1.3.2.3.1 The Solution for the Equation of Particle Motion in Contraction Section

Abrasive particles are assumed to be even spheres with the same diameter d_p. Therefore we can conclude that very little direct collision would occur between abrasive particles for the following two reasons: the volume fraction of the abrasives is very low and particles with the same size have the same dynamic characteristics. Thus we can ignore the interaction between abrasives and only consider the acceleration process of a single particle inside the nozzle.

Within the nozzle contraction, the particles are subjected to resistance caused by different velocity and acceleration between the two phases. This can be described with the following equation:

$$\rho_p V \frac{du_p}{dt} = \frac{1}{2}\rho V\left(\frac{du}{dt} - \frac{du_p}{dt}\right) + \rho V \frac{du}{dt} + C_D \frac{1}{2}\rho(u - u_p)^2 \frac{\pi}{4} d_p^2 \tag{1.24}$$

where the resistance factor C_D has a value of 0.42 because the Reynolds number of the particles will soon maximize upon entry into the nozzle.

Setting $\beta = \rho/\rho_p$ and $\alpha = 1 + \beta/2$, Eq. (1.24) can be simplified as follows:

$$\frac{du_p}{dt} = \frac{3C_D\beta}{4\alpha d_p}(u - u_p)^2 + \frac{3\beta}{2\alpha}\frac{du}{dt} \tag{1.25}$$

When examining the speed of all particles in the flow field at a certain moment, the particle speed u_p is just a function of the position x as it is in stationary flow. In this way, the velocity distribution of a certain particle in different positions across the flow field can be calculated as long as the velocity distribution of the particles at a certain moment in the flow field can be obtained. At this time, the speed at different positions can still match Eq. (1.25), where u_p is no longer the velocity of a particular particle, but instead is the speed of particles at different positions. At the same time, Eq. (1.25) can be turned into the following:

$$u\frac{du_p}{dX} = a(u - u_p)^2 + bu\frac{du}{dX} \tag{1.26}$$

where $a = \frac{3C_D\beta}{4\alpha d_p}$, $b = \frac{3\beta}{2\alpha}$

According to the spline function approximation method, the function $u^0 e^{AX+B}$ is used to gradually approach the flow velocity distribution of u in the contraction section. A general solution can be obtained as follows after substitution into Eq. (1.26):

$$u_p = \frac{u_o}{2a}(A + 2a + G)e^{AX+B} + \frac{u_o G}{Ku_o G e^{-Gx} - ae^{-AX-B}} \tag{1.27}$$

where $G = \sqrt{A^2 + 4Aa(1-b)}$; K is the integral constant and can be determined via the boundary conditions between each district. Constants A and B according to function $u_o e^{AX+B}$ can be numerically calculated using Eq. (1.23).

To make the general solution (1.27) that represents the particle velocity distribution more clearly, a detailed numerical calculation is conducted. The structure parameters of the nozzle in Fig. 1.18 are as follows:

$R = 9.5$ mm, $d_o = 3$ mm, $l_o = 70$ mm.

According to Eq. (1.23), the distribution of flow velocity in the nozzle contraction can be obtained as follows (Table 1.3).

According to the aforementioned changing trend of logarithmic dimensionless velocity, the interval [0, 70] is divided into six small intervals and the piecewise approximate function of speed u via numerical calculation is:

$$u = \begin{cases} u_o e^{0.029X-0.03} & [0, 25] \\ u_o e^{0.044X-0.446} & [25, 45] \\ u_o e^{0.058X-1.07} & [45, 52] \\ u_o e^{0.07X-1.689} & [52, 58] \\ u_o e^{0.096X-3.215} & [58, 65] \\ u_o e^{0.132X-5.58} & [65, 70] \end{cases} \tag{1.28}$$

Table 1.3 Water flow velocity distribution in nozzle contraction section

x	0	10	20	25	30	35	40	42	45	48
u/u_o	1	1.29	1.73	2.04	2.44	2.97	3.69	4.06	4.72	5.55
ln (u/u_o)	0	0.26	0.55	0.713	0.89	1.09	1.31	1.4	1.6	1.71
x	50	52	55	58	60	63	65	68	69	70
u/u_o	6.24	7.06	8.63	10.79	12.72	16.74	20.58	29.39	33.6	40
ln (u/u_o)	1.83	1.95	2.16	2.16	2.54	2.54	3.02	3.38	3.52	3.69

Setting the abrasive density as $\rho_p/\rho = 2.4$, particle size $d_p = 0.65$ mm. Feeding the specific data and Eq. (1.28) into the general solution (1.27) results in the following:

$$u_p = \begin{cases} 1.35u_o e^{0.029X} - \dfrac{u_o}{1.16e^{-0.101X} + 1.7e^{-0.029X}} & [0, 25] \\ 0.97u_o e^{0.044X} - \dfrac{u_o}{3.38e^{-0.127X} + 2.05e^{-0.044X}} & [25, 45] \\ 0.56u_o e^{0.058X} - \dfrac{u_o}{7.4e^{-0.149X} + 3.27e^{-0.058X}} & [45, 52] \\ 0.32u_o e^{0.07X} - \dfrac{u_o}{12e^{-0.166X} + 1.7e^{-0.07X}} & [52, 58] \\ 0.08u_o e^{0.096X} - \dfrac{u_o}{239e^{-0.2X} + 20.8e^{-0.096X}} & [58, 65] \\ 0.008u_o e^{0.132X} - \dfrac{u_o}{30207e^{-0.245X} + 180.7e^{-0.132X}} & [65, 70] \end{cases} \tag{1.29}$$

According to Eq. (1.29), the velocity distribution of particles is as follows (Table 1.4).

The velocity distribution curve of water and abrasive particle in the contraction segment of the nozzle is shown in Fig. 1.19.

1.3.2.3.2 The Solution of the Particle Motion Equation in the Cylindrical Section

In the cylindrical section of the nozzle, water flow speed is the constant u_1. Then the particle motion Eq. (1.25) is simplified to (1.30):

$$\frac{du_p}{dt} = a(u_1 - u_p)^2 \tag{1.30}$$

This equation of motion is simple and can be solved directly. In the Euler coordinate, $u_p = dX/dt$; therefore, Eq. (1.30) can be turned into

Table 1.4 Velocity distribution of particles

x	0	10	20	25	30	35	40	42	45	48
u_p/u_o	1	1.21	1.5	1.7	2	2.4	3.2	3.2	3.6	4.3
x	50	52	55	58	60	63	65	68	69	70
u_p/u_o	4.7	5.3	6.5	8	9.8	13.2	16	22.6	25.5	28.7

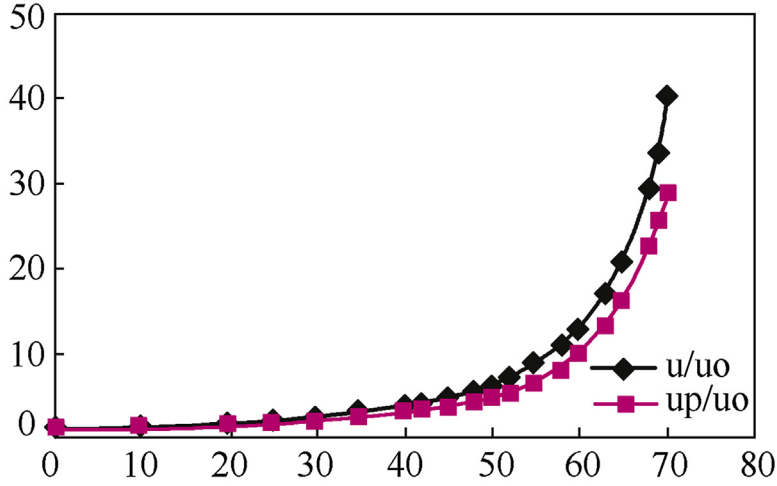

Figure 1.19 Comparison of two-phase flow velocity in the nozzle contraction.

$$u_p \frac{du_p}{dX} = a(u_1 - u_p)^2 \tag{1.31}$$

The general solution is

$$X = \frac{1}{a}\left[\ln(u_1 - u_p) + \frac{u_1}{u_1 - u_p}\right] + C \tag{1.32}$$

where the integral constant C can be determined via initial conditions.

First, the special case $u_p|_{x>0} = 0$ is calculated. Then the integral constants should be

$$C = -\frac{1}{a}(\ln u_1 + 1) \tag{1.33}$$

Combining Eqs. (1.32) and (1.33):

$$X = X(u') = \frac{1}{a}\left[\ln(1 - u') + \frac{u'}{1 - u'}\right] \tag{1.34}$$

where $u' = u_p/u_1$ is the dimensionless velocity of particles.

Then the integral constant can be calculated when the initial particle velocity $u_p|_{x=0} = 0$

$$C = -\frac{1}{a}\left[\ln(u_1 - u_{po}) + \frac{u_1}{u_1 - u_{po}}\right] \tag{1.35}$$

Table 1.5 Relationship between the dimensionless velocity of particles and the uniform flow field of the distance function

u'	0.1	0.2	0.3	0.4	0.5	0.6	0.7	0.75	0.8	0.85	0.9	0.95
$x(u')$	0.03	0.12	0.31	0.68	1.33	2.53	4.89	7	10.35	16.35	29	69.28

Combining Eqs. (1.32) and (1.35):

$$X = \frac{1}{a}\left[\ln(1-u') + \frac{u'}{1-u'} - \ln\left(1-u'_o\right) - \frac{u'_o}{1-u'_o}\right] \tag{1.36}$$

where $u'_o = u_{po}/u_1$ is the dimensionless velocity of particles.

Comparing Eqs. (1.36) and (1.34), we find that the distance required for a particle to accelerate in a uniform flow field from u'_o to u' is equal to the distance required for the value of that particle in the same flow field to accelerate from zero to u' minus the distance required to accelerate from zero to u'_o, i.e.,

$$X = X(u') - X\left(u'_o\right) \tag{1.37}$$

In a uniform flow field, the acceleration distance of the particle is only associated with the initial dimensionless velocity and can be determined via the dimensionless function $X(u')$. Since $X(u')$ is only related with the dimensionless velocity, it can be universal used. This is called the distance function of uniform flow field. Its specific value is listed in Table 1.5.

Table 1.5 shows that the higher the dimensionless velocity of particles, the longer the distance needed to accelerate with the same increment of velocity. In a uniform flow field, the lower the particle velocity, the easier it is to accelerate the particles.

1.4 ABRASIVE SUSPENSION JET

The abrasive suspension jet (or abrasive slurry jet) was once named the H-P-S technology, which is how it was first known to the public (Maurer, 1980). Abrasive suspension is a type of non-Newton fluid that uses viscous polymer solutions as carrier and is mixed with the appropriate amount of abrasive particles. Instead of a two-phase medium of mixed fluids and solids, it is a single fluid and hence does not suffer from slippage between solid and liquid phases.

1.4.1 Preparation of Abrasive Suspensions and Their Rheological Behaviors

The rheological pattern of the abrasive suspension has received considerable focus; however, the insights have not yet been as thorough as for the drilling fluid, and the shear-thinning rheological model is often used for abrasive suspension. Three abrasive suspension formulas are listed as examples:

Formula 1: Methylcellulose polymers are used as additive at a concentration of 2×10^4 ppm, dissolved in water to form a solution with an apparent viscosity of 12,700 cP. Garnets with diameters of 53−75 μm (280-200 Tyler mesh) or 75−106 μm (200-150 Tyler mesh) are typically utilized as an abrasive at a weight concentration of 105.7 g/L.

Formula 2: The adopted polymer additive is polyacrylamide at a concentration of 1.5×10^3 ppm, and the produced solution has an apparent viscosity that ranges from 1730 to 9300 cP. An abrasive of the same type, grain sizes, and weight concentrations as those in Formula 1 is used.

Formula 3: The formula and the rheological properties of the polymer solution are identical to that in Formula 2. However, corundum with higher hardness is used as abrasive, which is made into ultrafine particles (powders) with a grain size of 10 μm. This formula is applicable for microcutting with a very narrow kerf.

The additives mentioned in the previous discussion are all linear, long-chain polymers; therefore, their aqueous solutions are viscoelastic fluids that present both viscosity and elasticity. The main difference between such fluids and viscous fluids is that they are capable of local strain recovery while external forces are unloaded. However, the main difference from elastic solids is their creep behavior. In addition, it is distinguished from Newton fluids mainly by normal stress difference effect presented in shear flow. For instance, Wessenberg first reported the Wessenberg effect, namely, the "stick climbing" phenomenon, in 1946. These rheological properties served the abrasive suspension jet well. The polymers can form flocculation networks, thus enhancing the bonding between the polymer and the solid particle and endow the abrasive suspension with the excellent property of shear thinning. Hence abrasive suspension has a small friction loss as it flows through the jet nozzle, whereas the shear rate is high, which also shows significant intensity as it forms a high-speed nonsubmerged jet. Similarly, since the Deborah number (De) $>> 1$, as the abrasive suspension jet hits the target surface, it shows instantaneous solidlike rigidity, with which more hydraulic energy can be transformed into the jet impact force. The

Table 1.6 Abrasive suspension jet versus conventional abrasive jet

Jet type technical parameter	Conventional abrasive jet	Abrasive suspension jet
Pressure, MPa	206.9	51.7
Traverse rate, cm/min	10.2	5.1
Power, KW	4.6	0.66
Energy consumed to cut 1 cm, J	26.8	7.54
Abrasive required to cut 1 cm, g/cm	26	16
Type and grain sizes of the abrasive	Garnets of 60# and 80#	Garnets of 150# and 200#
Abrasive material flow rate, g/min	271	81.6
Water flow rate, L/min	0.13	0.15

aforementioned analysis reveals that combined with the following experimental data of the abrasive suspension jet, and compared with the conventional abrasive jet, this possesses incomparably extraordinary dynamic properties. The main parameters are listed in Table 1.6.

1.4.2 Slurry Pressurization and Delivery

The pressurization and delivery process of the abrasive suspension is shown in Fig. 1.20. To avoid wear of the high-pressure pump (or the pressure intensifier) caused by the slurry, the basic principle has been set that the abrasive suspension should not pass through the high-pressure pump. Low-pressure mud pumps (centrifuge pumps, plunger pumps, or diaphragm pumps) or compressed air are used to transfer the abrasive suspension to the lower part of the floating piston cylinder. The operation pressure of discharge valve 4 as shown in Fig. 1.20 is set between the working pressures of the mud pump and those of the high-pressure pump. Normally, the pressure of the low-pressure mud pump is only 0.3 MPa, which cannot open valve 4. When the filled abrasive suspension reaches the top dead position of the floating piston, pressurized water will be fed via the high-pressure pump, thus pushing the floating piston to drive the abrasive suspension to pass through the jet nozzle, forming the jet. When the floating piston reaches its bottom dead position, the jet material in the cylinder will have run out, and the high-pressure water should then be cut off. Next, the water within the cylinder is replaced by the abrasive suspension driven by the mud pump and flows out from valve 1, which ends a working cycle. Given that all mechanical equipment are in normal operation, the keys to this system are as follows: strict grain size control of the abrasive and, selection and

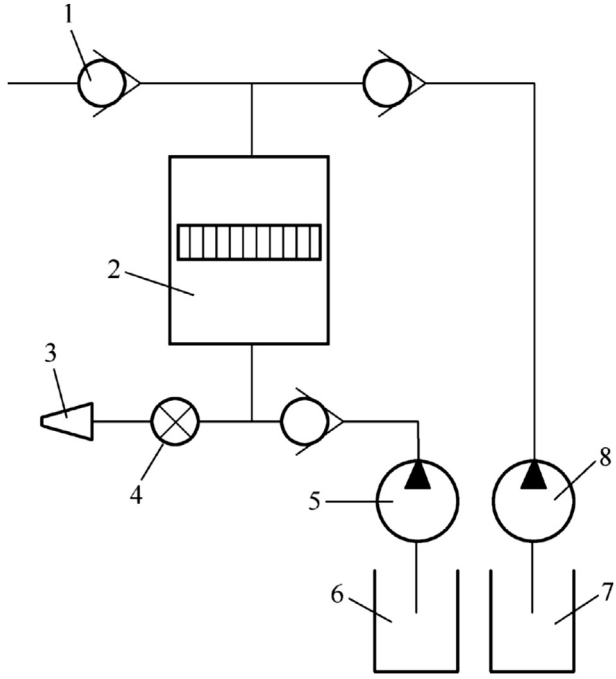

Figure 1.20 Schematic of the principle of the abrasive suspension jet. (1) one-way valve, (2) floating piston cylinder, (3) nozzle, (4) discharge valve, (5) mud pump, (6) mud cylinder, (7) water cylinder, and (8) pressure source.

preparation of polymers, which should ensure no separation or precipitation between the liquid and solid phases. In addition, with three to five cylinders in parallel and corresponding control valves, the system can realize the continuous supply of abrasive suspensions.

1.5 CUTTING MECHANISM AND MODELS OF ABRASIVE SUSPENSION JETS

The cutting mechanism of the abrasive jet has become a research topic that attracted tremendous attention from experts and scholars of various countries over the past few years. The US scholar Mazurkiewicz analyzed the particle microcutting process on ductile materials on the basis of the particle erosion theory for ductile materials. Prof. Bayashi, a Japanese scholar, has systematically studied the section shape of aluminum alloys that have been cut by abrasive jets. In China, Xu Jing has analyzed the cutting process of brittle materials, using the pseudostatic elastic theory, whereas Duan

Xiong has qualitatively discussed the cutting mechanism of brittle and ductile materials on the basis of electronic scanning and X-ray energy spectrum analyses. Moreover, Song Yongzheng studied the cutting mechanism using abrasive jets with pressures from 100 to 300 MPa in the context of industrial cutting. Both the hardness and flow speed of the abrasive microparticle are high, and the cutting of the abrasive jet mainly depends on the erosion effect of the abrasive (Qingwen, 1997).

1.5.1 Principles of Erosion

Erosion refers to the damage on the material surface caused by the impact of the particle. In a broad sense, the particle can include solids, liquids, and gas bubbles. The energy exchange occurs as the particle hits the solid surface. In other words, energy will be redistributed between both objects, and the impacted surface may suffer from elastic or plastic deformation (Jiajun, 1992). Grant, Head, Harry, and Hutchings have discussed the energy exchange that occurs as the spheres or cubes hit the surface at an incident angle of either 30 or 90 degrees, to estimate the initial kinetic energy dissipation of the particles at the moment of the impact (Dick et al., 1995). An energy distribution schematic is shown in Fig. 1.21. After vertically hitting the target, the sphere maintains only 1%—10% of its initial energy, and the rest is dissipated over the material surface, including a significant loss due to elastic waves (1%—5%) and plastic indentation (about 90%), which has nothing to do with erosion. Almost 80% of the total energy consumed by the material is thermally dissipated, whereas about 10% is stored in the material with the generation of dislocation and other crystal defects. Different energy distribution patterns are seen in spheres or cubes, hitting the target surface obliquely, because more energy has left with the particles and the distribution proportion has been changed.

Two phenomena occur as the high-speed droplet impacts the solid surface, namely, high pressures are generated at the point of impact and fluids flow radially along the solid surface from the impact point (the center). So far, no mature theory has been proposed to describe the compressive pressure distribution caused by sphere droplets hitting solid surfaces. However, from experimental observations and educated guesses, it has been argued that the peak pressure occurs at the impact point as the solid surface is being hit. The peak pressure can reach 6300 N, with high-speed water jets hitting the surface of steel at rates of 720 m/s. Moreover, the peak pressure occurs within 2—3 μs after the impact of the water droplet, and afterward water immediately starts to flow radially at an initial rate up to 9 times that of

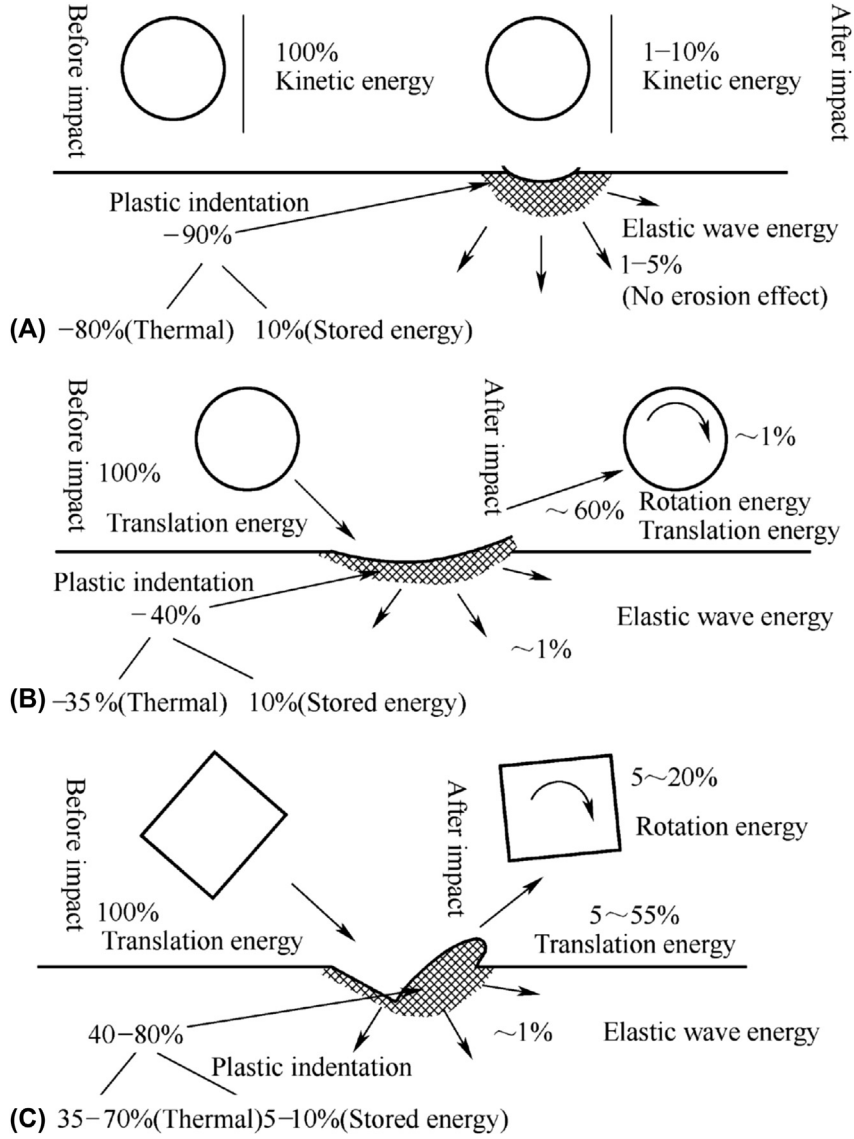

Figure 1.21 Energy distribution of particles hitting target surfaces. (A) Energy balance of spheres vertically hitting target surfaces. (B) Energy distribution of spheres hitting target surfaces at an incident angle of 30 degrees. (C) Energy distribution of cubes hitting target surfaces at an incident angle of 30 degrees.

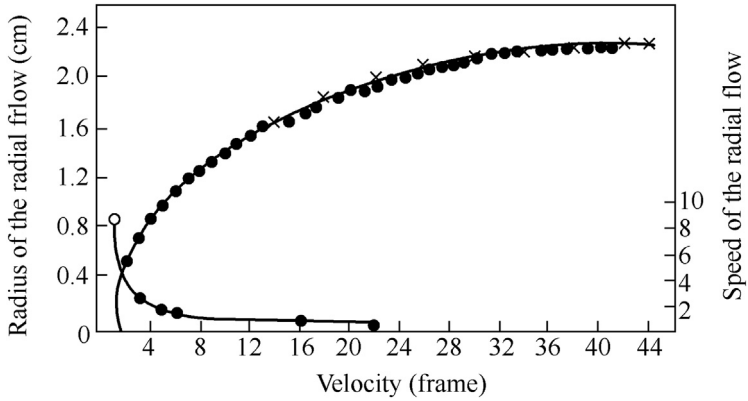

Figure 1.22 Speed and radius of the radial flow versus time × radius of the radial flow; ○, speed.

the impact speed, declining rapidly after about 1 ms. The radial flow that occurs as droplets hit glass at a rate of 8.2 m/s was captured via Schlieren photography and high-speed camera, and the results are shown in Fig. 1.22.

Erosion occurs as soon as the impact rate of the particle that hits the material surface reaches a critical threshold value, regardless of whether it is a solid particle or high-speed droplets. In terms of the erosion caused by sand blasting, the erosion rate of the material is defined as the weight or volume of the material that is lost by particles per unit mass. In addition to being characterized by the weight loss per unit time, droplet erosion or cavitation erosion can also be measured via average damage depth, namely, the average erosion depth in a given area. The erosion rate is a parameter that is affected by system factors, instead of the intrinsic property of the material. The three main control aspects are (1) environmental factors such as speed, concentration, and incident angle of particles and the temperature of the environment; (2) the properties of the abrasive material such as hardness, diameter, and destructibility; and (3) material properties such as the thermophysical characteristics and material strength. The main factors that affect the erosion are listed in the following paragraphs.

1.5.1.1 Incident Angle

The incident angle refers to the angle between the impact direction and the solid surface. For a vertical impact, this angle is 90 degrees. A number of experimental results have shown that the erosion rate of the material changes with the incident angle. For ductile materials, the erosion rate reaches its

peak with incident angles of 20–30 degrees, whereas the top erosion rate typically occurred with incident angles of about 90 degrees for brittle materials.

1.5.1.2 Particle Speed

The effect of particle speed on the erosion rate is an important part of the erosion mechanism study. From massive observations on materials that have been eroded by various particles, it can be concluded that

$$\varepsilon = Kv^n$$

where v stands for the particle speed and n and K are both constants.

A linear correlation, with a slope of n, can be illustrated by taking the logarithm of ε versus v. The relationship between erosion rate and particle speed shown from a group of typical engineering materials impacted by silicon sands and SiC particles is shown in Fig. 1.23. The slope of the straight line is 2.3.

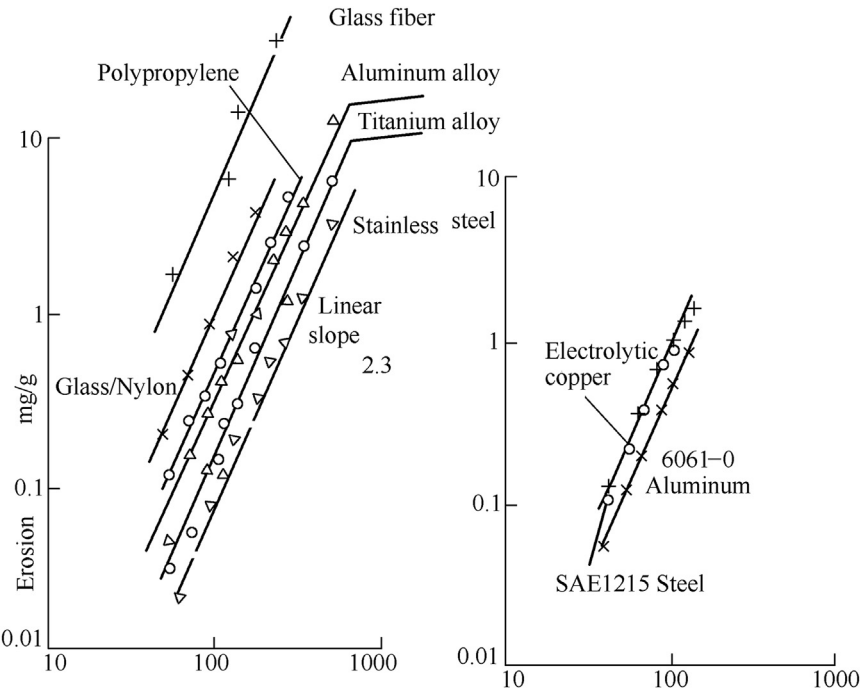

Figure 1.23 Erosion rate versus particle speed. (A) Silica, 125–150 μm, 90 degrees; (B) SiC, 250 μm, 20 degrees.

An exponential correlation exists between the erosion rate and particle speed, regardless of the particle type, material type, or incident angle, which suggests that the kinetic energy of the particle is the main reason for material erosion. The early experimental results show that $n = 2.0$ (Xiaohong et al., 2000), and yet, n changes from 2.1−2.4 to 6.5 as the erosion target expands from ductile to brittle materials. It has been proved through careful experiments that n also slightly grows with increasing incident angle. These divided experimental observations are hard to explain in view of the particle kinetic energy only.

As the particle speed decreases to a certain lower limit, only elastic deformation occurs without any loss of material as the particle impacts on its target. This lower speed limit is called the threshold velocity, which changes with the type and shape of the particle as well as with the material properties. With regard to sand blast erosion, the threshold velocity for cast iron spheres with diameters of 0.3 mm on glass is 9.9 m/s; however, the threshold velocity for silica sands with diameters of 0.23 mm on Cr-11 steel is only 2.7 m/s.

For droplet erosion, the aforementioned correlation is still applicable, and attention should be paid to the characteristics of water droplets, for selecting n and the threshold velocity; the latter is very high. A threshold velocity of 125 m/s has been reported for a 215,000 times impact on high-strength Cr-12 steel. Therefore the relationship between the weight loss caused by droplet erosion and particle velocity can be expressed as:

$$W \propto (v - v_c)^n$$

where $v_c \approx 120$ m/s and n is related to the experimental apparatus utilized and the material property of the erosion target.

It should be noted that n also relates to the water jet velocity. For relatively low water jet velocity, $n \approx 2.5$ and the term v_c adds a relatively large contribution to the expression. In terms of a very high jet velocity $n \approx 5$, especially for brittle materials, which indicates catastrophic damage.

1.5.1.3 Erosion Time

Erosion wear is different from adhesive wear and abrasive wear and has a relatively long latency or incubation stage, especially for droplet or cavitation erosion. When the particle first starts to impact the solid surface, the cases are mainly work hardening and surface roughening, instead of the necessary immediate material loss. The process does not enter the stage of stable erosion, until damage accumulates to a certain degree. For sand blast type erosion during the initial erosion stage, the material probably "gains

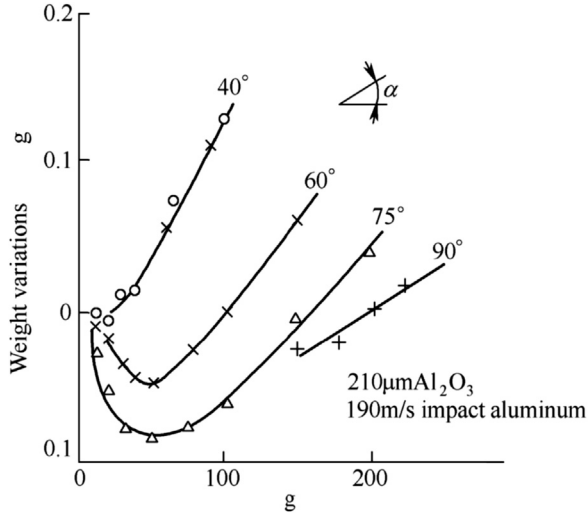

Figure 1.24 Weight variations of materials eroded with varied incident angles.

weight" due to the embedded particle. The weight gain that occurs with small incident angles is far lower than that with large incident angles. Fig. 1.24 shows the relationship between particle consumption and material weight variation with aluminum materials eroded by Al_2O_3 particles at different incident angles.

Experiments of droplet erosion and cavitation erosion have shown that a curve of the weight loss variation of typical ductile materials plotted against time can be divided into three stages: the latent stage (I), the maximum erosion rate stage (II), and the stable erosion stage (III). A typical curve is shown in Fig. 1.25. The length of the latent stage indicates the outside energy that the material can bear as the elastic deformation evolves into plastic damage. This is important with regard to characterizing the cavitation erosion resistance of the respective material. In the maximum erosion rate stage many pits occur on the material surface, and these pits gradually combine. Afterward, the erosion rate decreases and reaches its stable stage. The magnitude of the stable erosion rate is also an indicator of the cavitation erosion resistance of the material. One explanation for decline and final stabilization of the erosion rate is that the surface roughened by erosion can maintain a water cushion layer, which to some extent offsets the direct erosion of droplets or bubbles on the material surface.

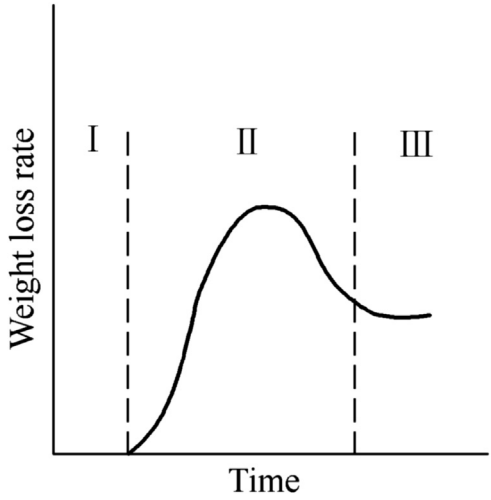

Figure 1.25 Weight loss rate of ductile materials under cavitation erosion versus time.

1.5.1.4 Environmental Temperature

The effects of environmental temperature on material erosion are hard to be condensed into simple patterns. Some results suggest that the erosion rate of the material grows with increasing temperature and yet, the material surface may be oxidized as the temperature increases too far. Generally speaking, the material erosion rate or damage rate increases as the temperature of the liquid medium increases. However, it begins to decrease as the temperature reaches a specific and high value, and is close to zero as the temperature approaches the boiling point. One explanation for this is that under lower temperatures, both activity and erosion effect of the liquid intensify with increasing temperature, thus accelerating erosion; the vapor pressure of the liquid rises as the temperature reaches a specific threshold, which leads to the increase of naturally occurring bubbles within the liquid or significant gas cushion effects and therefore lower impact effects. In summary, for gas-driven sand blast erosion, the effects of environmental temperature are mainly rooted in the high-temperature property of the material, because the melting point or strength of the particle is far beyond that of the target material; for droplet or cavitation erosion, the temperature is often below the boiling point of the jet medium. Therefore the dominant factor is the medium environment instead of the target material.

1.5.1.5 Properties of Impact Particles

Erosion derives from the impact of jet particles on the solid surface, including droplets and bubbles. Since significant differences exist between the properties of solids and fluids, both cases are separately discussed.

The shape and size of a solid particle have a great influence on erosion. So far, no satisfactory explanation has been proposed for the grain size effect that has been observed years ago. When the particle size exceeds a critical size, the erosion rate starts to reach equilibrium. The damage caused by sharp particles is more severe than that caused by spheres, and that by hard particles is severe than damage caused by soft particles; this has been understood and accepted. A further factor that should be noted is the crushability of the particle, i.e. the tendency of particles to break into fragments during impact. In any discussion about the effects of the incident angle on material erosion, only the condition of the smooth original surface and intact particles with uniform sizes has to be considered. However, as the incident angle increases, the odds of brittle particles breaking after impact grow, and the fragments of the broken particle can lead to secondary erosion on the rugged material surface. This is part of the explanation for why some ductile materials can still maintain a relatively high erosion rate in the case that their incident angle is close to 90 degrees. This hypothesis has been experimentally proven.

1.5.2 Video Observation of the Cutting Process of Abrasive Jet

For abrasive water jets, water is used as the carrier and a water jet accelerates abrasive microparticles. Since the abrasive microparticle is much heavier than water and although it has sharp edges and corners, the cutting effectivity of materials mainly depends on the grinding effect of the abrasive microparticles on the material. In addition, the abrasive supply is not continuous in the water jet, and the high-speed particle flow composed of abrasive materials can thus impose a high-frequency impact effect on the target material. Therefore the impact and grinding forces imposed on the material by the abrasive jet are much larger than those imposed by the water jet under identical conditions, which consequently leads to higher cutting efficiency.

Mazurkiewicz, a US scholar, used an abrasive jet to cut a rectangular plexiglass specimen and filmed the cutting and penetrating process using a camera with film speeds of 64 and 1000 frames/s. The action points in the early penetration of the plexiglass sheet are captured and shown in Fig. 1.26. The cutting velocity during the whole process could be determined according to the time interval between each frame, which was 0.0156 s.

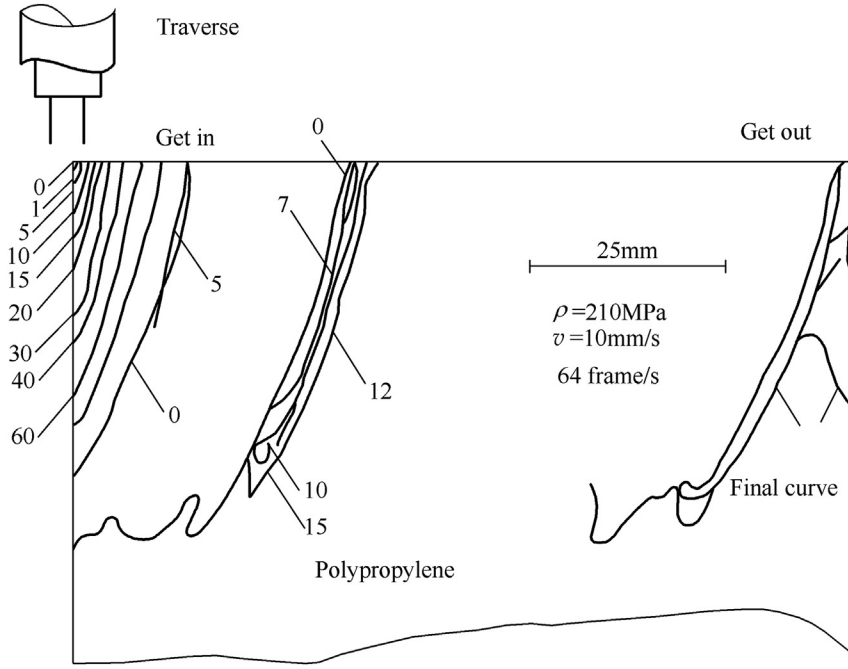

Figure 1.26 Jet/solid converged interface traces and entrance and exit locations of jets.

Fig. 1.27 shows two penetration cycles after the cutting process started to repeat. It can be seen that the penetration depth was 25 mm for a jet velocity of 210 m/s. During cutting of the rectangular specimen, the cutting process can be divided into three stages, as shown in Fig. 1.28.

Stage 1: The cutting process initiates with various cutting behaviors. This stage lasts until the maximum depth has been reached.

Stage 2: The cutting process is repeated until the jet starts to penetrate the specimen.

Stage 3: This stage is the late stage of cutting, where the jet has penetrated through both the specimen and cutting ends.

Fig. 1.28 shows that with horizontal displacement of x_1, the cutting depth is equal to h_1 (x_1 equals the jet diameter at the impact point). Then as the horizontal displacement reaches x_2, and the cutting depth h_2, the cutting is mainly realized by erosion with lower incident angles. When the horizontal displacement changes from x_2 to x_3, the cutting depth increases from h_2 to h_3, which is accomplished by the combined erosion with both lower and higher incident angles under continuous action. The penetration process is completed, as the horizontal displacement

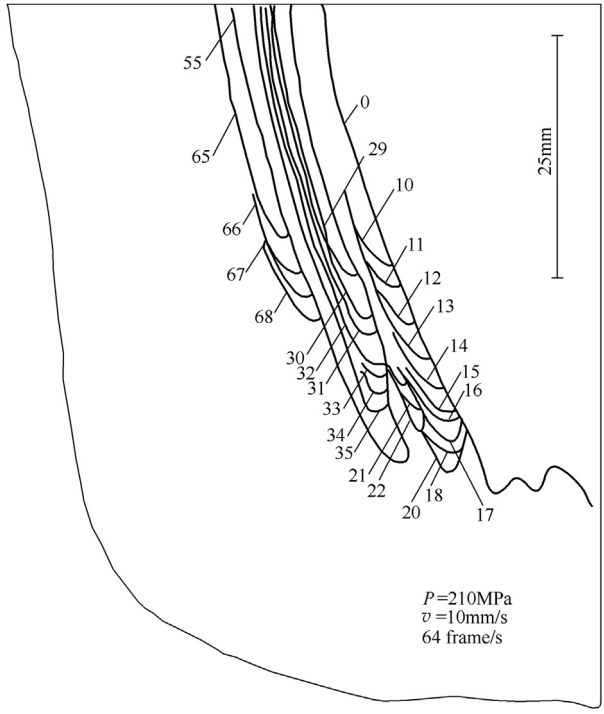

Figure 1.27 Two cycles of jet/solid converged interface traces penetrating through the specimen.

reaches x_4. The penetration depth from h_3 to h_4 is completely dominated by erosion with higher incident angles. The wear before the cutting depth of h_2 is often called cutting wear, as it mainly happens at the top of the kerf and abrasive particles impact on the material with lower incident angles. The wear from the cutting depth h_2 to h_4 is called deformation wear, which occurs in the depth of the kerf where abrasive particles hit the material with higher angles.

1.5.3 Erosion Theory for Brittle Materials

Brittle materials include glass, ceramic, graphite, and some alloys with extremely low plasticity, in which cracks can initiate without plastic deformation and can soon evolve into brittle breakage. Apparently, the microcutting model is not suitable for such materials. It has been experimentally shown that as a single particle impacts the brittle material, cracks generally occur at those impact positions that are flawed, as the particle impact velocity reached a certain value, the threshold velocity. The shape of the particle has a tremendous effect on crack initiation. Normally, two types of cracks

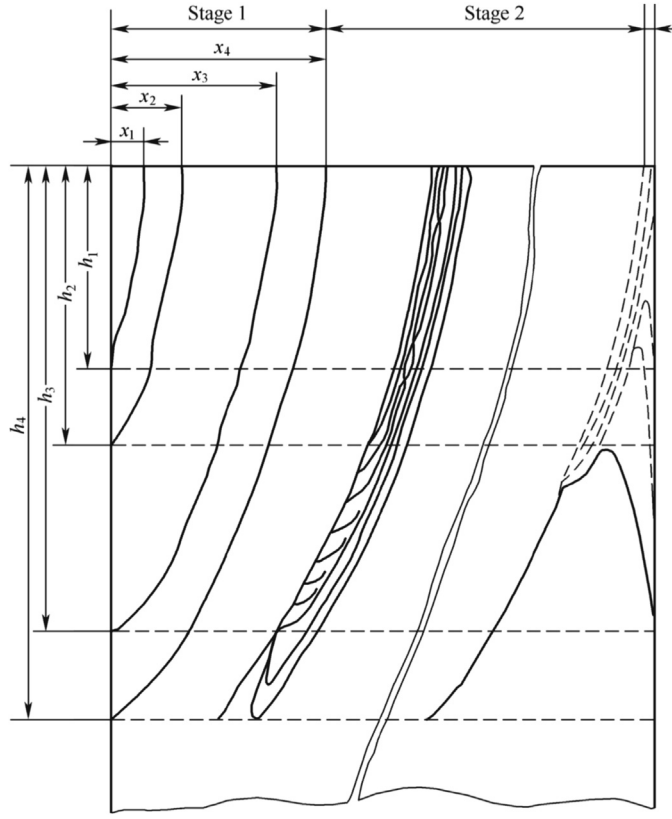

Figure 1.28 Three stages of the cutting process. Stage 1, initial cutting; stage 2, stable periodic penetration; stage 3, jet penetrating through the specimen boundary.

(traverse and radial) appear on the surface (Xiaohe & Jing, 1984). Fig. 1.29 shows the crack propagation model.

The key to the development of an erosion model for brittle materials lies in establishing a correlation between crack initiation and propagation, particle impact velocity, and the material property. Evans et al. suggested that the erosion rate is in direct proportion to the material loss for each impact. Since the erosion volume V and the generated traverse crack are directly proportional to the radial crack c_r, $V \approx \pi c_r^2 h$. Moreover, c_r relates to the critical stress intensity factor K_c and to the hardness H of the material as well as to the particle impact velocity v_0, the grain size r, and the density ρ. Calculations reveal that

$$V \propto v_0^{3.2} \cdot r^{3.7} \cdot \rho^{1.58} \cdot K_c^{-1.3} \cdot H^{-0.25}$$

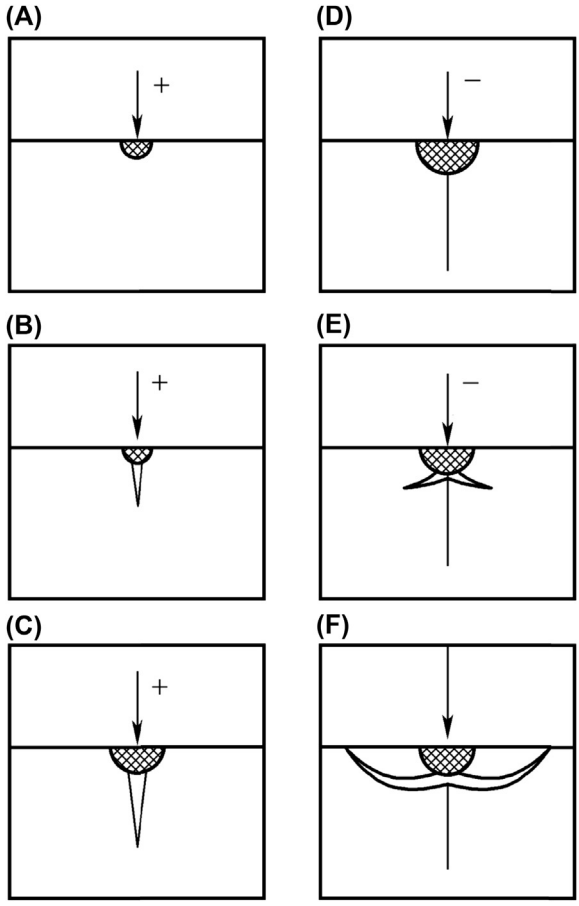

Figure 1.29 Propagation of cracks caused by impacts of sharp particles; "+," loading; "−," unloading.

This equation indicates the existence of an exponential correlation between the erosion rate and the particle speed. With K_c, H, and ρ set as variables, the erosion test has been conducted using materials such as Si_3N_4. As shown in Fig. 1.30, the results directly prove the theory proposed by Evans.

1.5.4 Mathematical Model of Abrasive Jet Cutting

1.5.4.1 Crow's Rock Cutting Model

In 1973, Crow proposed a jet cutting theory that considered the jet parameter, traverse rate, and rock property. The theory has been further modified by Crow to include the effects of rock porosity on jet cutting effect. The model of this theory is shown in Fig. 1.31.

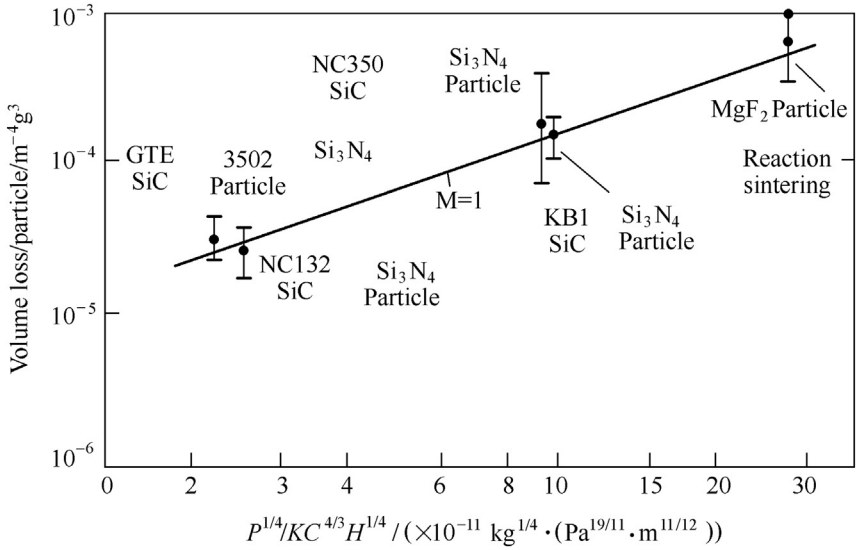

Figure 1.30 Erosion of Si_3N_4 and MgF_2 manufactured using different methods and hit by SiC particles.

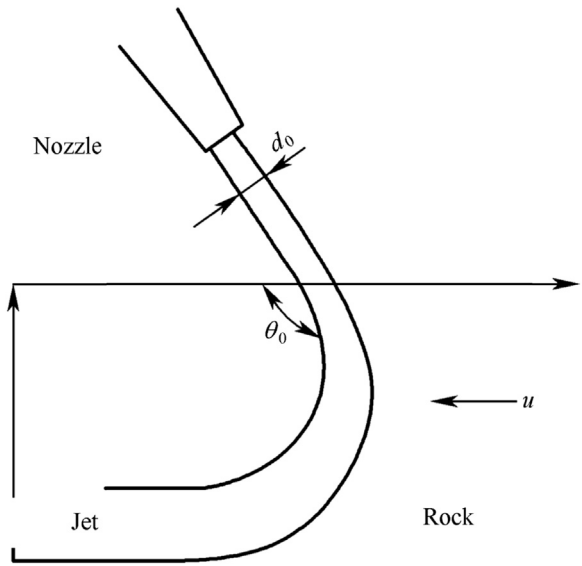

Figure 1.31 Jet cutting model (Crow, 1973).

It has been argued that when the traverse rate of the jet is infinite, the forming rate of the cutting area will reach its peak value $(hu)_{\max}$, which can be calculated as:

$$(hu)_{\max} = \frac{2Kd_o p_o}{\eta f \mu_T d_r}\left(1 - e^{-\mu_W \cdot \theta_0}\right) \tag{1.38}$$

where d_o is the nozzle diameter in mm; d is the grain size of the rock in mm; f is the porosity of the rock, which is dimensionless; K is the permeability coefficient, which is dimensionless; P_o is the jet pressure in MPa; u is the jet traverse rate in m/s; μ is the viscosity of the fluid in Pa s; μ_T is the internal friction coefficient, which is dimensionless; μ_W is Coulomb's friction coefficient, which is dimensionless; and θ_0 is the incident angle in degrees.

Eq. (1.38) shows that the cutting rate increases with increasing rock permeability, nozzle diameter, and jet pressure, whereas it decreases with increasing fluid viscosity, rock porosity, and particle size of the rock. The optimal impact angle θ, which ranges from $\pi/2$ to π, depends on μ_W and the traverse rate, u.

Crow noted that contradiction existed between cutting theory and test results, and hence he proposed a "universal rule for hydraulic rock cutting." The rule is based on experiments, and in the new theory, the kerf depth variation can be described as

$$h = \frac{n \cdot (p_o - p_c)}{\tau_o} d_o F(u/c_e) \tag{1.39}$$

where h is the kerf depth in m; n is the number of the movement times, which is dimensionless; p_c is the critical jet pressure in MPa; τ_o is the shear strength of the rock in MPa; and c_e is the theoretical rock cutting rate $c_e = \frac{K\tau_o}{\eta f \mu_T d_r}$ in m/s.

Eq. (1.39) is the common expression of Crow's cutting theory.

1.5.4.2 Rehbinder's Rock Cutting Model

In 1977, Rehbinder proposed a second jet-based rock cutting theory, under the assumption that stagnation pressure exists at the bottom of the kerf. The stagnation pressure can be calculated as

$$p_o = p_r e^{-\beta h/D} \tag{1.40}$$

where β is an empirical constant, which is dimensionless; D is the kerf width in cm; h is the kerf depth in cm; and p_r is the jet stagnation pressure in MPa.

This theory predicts that as the jet stagnation pressure surpasses a critical pressure ($p_o > p_{th}$), the kerf depth variation can be described as

$$\frac{h}{D} = 100 \ln\left(1 + \frac{\beta K p_o t}{\mu l D}\right) \tag{1.41}$$

where l is the average grain size of the rock in cm, t is the action time of the jet in s, μ is the dynamic viscosity of water in Pa s, and K is the rock permeability in m^2.

The action time of the jet on the rock can be calculated as:

$$t = nd/u \tag{1.42}$$

where n is the number of the movement times, and is dimensionless; d is the nozzle diameter in mm; and u is the traverse rate in m/s.

The theory also predicts the potential maximum kerf depth to be

$$\left(\frac{h}{D}\right)_{\max} = 100 \ln\left(\frac{p_o}{p_{th}}\right) \tag{1.43}$$

Fig. 1.32 shows the dimensionless kerf depth curve predicted on the basis of the aforementioned theory.

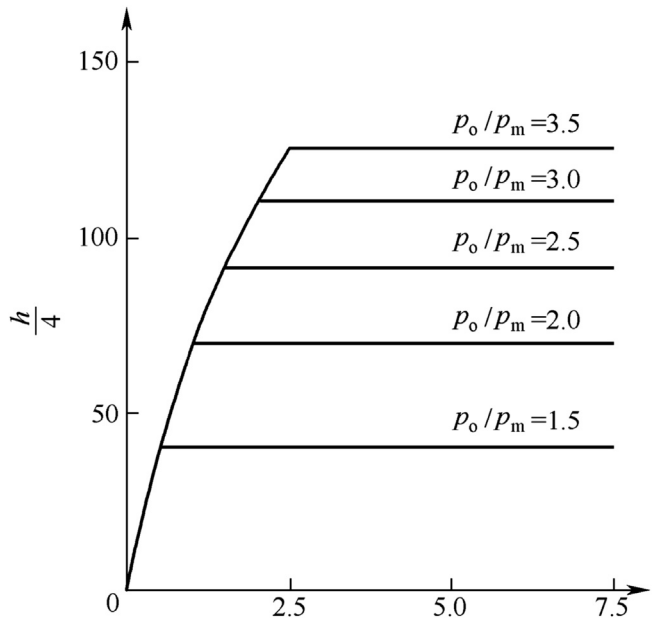

Figure 1.32 Theoretical kerf depth.

A series of jet cutting experiments conducted by Rehbinder revealed that the curves of kerf depth versus action time of the jet are similar to the theoretical prediction.

1.5.4.3 Hashish's Cutting Model

As mentioned earlier, Crow's rock cutting theory includes many jet parameters and improves special target properties. However, limitations still exist in his theory, and since formulation, the theory has become hard to apply to general designs and applications. The penetrability, grain size, and tensile strength of the rock are regarded as important influential factors for erosion-based cutting in a theory similar to Crow's, proposed by Rehbinder. As with Crow's theory, this theory too cannot be applied to general designs and applications. In 1978, Hashish established a universal cutting formula applicable to many materials. The prediction process of the cutting depth under the cutting wear mode is shown now discussed.

First, it is assumed that the jet impacts on the inclined surface at an inclination angle of α_0. The distributions of the impact parameters on the surface are then determined, mainly including the local impact angle, particle speed, and local mass flow rate. Based on these parameters, the local volumetric erosion rate can be determined, which equals the material loss rate during stable cutting. Due to jet deviation, the particle gradually changes its direction toward being parallel to the surface and the stable cutting ends, which means that the volumetric erosion rate drops to zero. At this point, only part of the jet is in a stable cutting status and the rest of the abrasive impacts the target at relatively higher angles. Then the distribution of the volumetric erosion rate can be obtained. Next, another surface was chosen for particle impacts, and the aforementioned process repeats until the calculated area equals the assumed surface.

For cutting dominated by deformation wear, the process is as follows.

The particle speed at the moment when the cutting wear mode ends should first be determined. If the jet only causes cutting wear, the particle reflected from the surface will reenter the jet and affect the cutting effect of the deformation wear. If only part of the jet caused cutting wear, the remaining particle will affect the deformation-based cutting and penetration, similar to the reflected particle.

The penetrating rate can then be calculated based on the volumetric erosion rate, and the cutting depth generated by the deformation wear can by determined with the integral of the penetration rate equation on the jet action time, obtained from both traverse rate and jet diameter.

For simplicity, the following assumptions have been made:

The decrease in particle speed is ignored, which is more appropriate for cutting with relatively shallow depth.

The flow rate of the abrasive jet participating in the cutting wear is assumed to be $C\dot{m}$, where C is a constant and $\dot{m}$ is the mass flow rate of the abrasive particle.

The flow rate distribution of the abrasive on the jet cross-section is assumed to be even.

It is, furthermore, assumed that the particle speed v can be calculated using the simple momentum equation $\dot{m}_w v_j = (\dot{m}_w + \dot{m})v$, where $\dot{m}_w$ is the mass flow rate of water. The effects of the hydraulic loading during the microcutting process are neglected.

The motion trail of the particle hitting the surface at speed v and angle α is as follows:

$$x = \frac{v \sin \alpha}{\beta\phi} \sin \beta t + \left(v \cos \alpha - \frac{v \sin \alpha}{\phi} \right) t \tag{1.44}$$

$$y = \frac{v \sin \alpha}{\beta} \sin \beta t \tag{1.45}$$

$$\theta = \frac{mrv \sin \alpha}{\beta\phi I} (\sin \beta t - \beta t) \tag{1.46}$$

where

$$\beta = (\phi\psi b\sigma/m)^{\frac{1}{2}}. \tag{1.47}$$

It is assumed that the mass center of the particle m suffers displacements of x and y, as it rotates for an angle θ. The trail coordinates of the particle end are x_t and y_t, $x_t \approx x + r\theta$ and $y_t \approx y$. The resistance in x-direction is $R_x = \sigma y \psi b$, where σ is the dynamic yield stress and ψ is a coefficient that indicates a large impact area in the edge. The resistance in y-direction is assumed to be ϕR_x, where ϕ is a further coefficient that can be determined from similar microcutting processes. The assumption suggests that the resistance vector remains constant during penetration through the material. These equations are based on the motion equations of the particle in the direction of x, y, and θ. The erosion volume of the material δV can be determined via the integral of $y_t dx_t$ on the penetration time. When the particle leaves the target, i.e., $y = 0$, the cutting time is $t^* = \pi/\beta$ according to Eq. (1.45). Therefore

$$\delta V = \frac{mv^2}{\sigma\psi\phi}\left(\sin 2\alpha - \frac{2}{K}\sin^2\alpha\right) \tag{1.48}$$

where

$$K = \frac{\phi}{1 + \dfrac{mr^2}{I}} \tag{1.49}$$

I is the rotational inertia.

In cases in which the particle impacts ductile materials at small angles, δV in Eq. (1.48) can be replaced with $\delta \dot{V}$, and m with $d\dot{m}$; then, the volumetric erosion rate can be determined. However, this is not applicable for high-speed abrasives, because during the erosion, the "real" impact angle is constantly changing. For simplicity, it is assumed that Eq. (1.48) can be further applied to the repeated impact. With $\psi = \phi = 2$, $I = ½mr^2$, $\delta \dot{V}$ can be expressed as

$$\delta \dot{V} = \frac{d\dot{m}v^2}{4\sigma}\left(\sin 2\alpha - 3\sin^2\alpha\right) \tag{1.50}$$

For small-angle impacts, $\sin 2\alpha \approx 2\alpha$, and the second term can be neglected, compared with the first term. Therefore

$$\delta \dot{V} = \frac{d\dot{m}v^2}{2\sigma}\alpha \tag{1.51}$$

For stable cutting, the volumetric erosion rate of the material should equal the material damage rate in areas where this type of wear mode is dominant. Hence,

$$\delta \dot{V} = dhud_j \tag{1.52}$$

where d stands for the grain size, h is the cutting depth, u represents the traverse rate, and d_j is the jet diameter.

It is assumed that the cutting depth equals the jet diameter, since both parameters are similar as soon as the standoff distance is small. Given that the abrasive in the jet has an even distribution, $d\dot{m}$ in Eq. (1.51) can be expressed as $\dot{m}dx/d_j$.

The next step is to describe the angle α as a function of kerf depth. At the top of the kerf, the impact angle is α_o. Due to the cutting wear that results from particle reflection, the angle changes to zero at the bottom of the kerf. It has been assumed that the variation along the interface of the jet participating in the cutting mode is linear; therefore

$$\frac{d\alpha}{dx} = -\frac{\alpha_o}{cd_j} \tag{1.53}$$

With the integral of $\frac{dh}{dx} = \frac{dh}{d\alpha}\frac{d\alpha}{dx}$ as well as Eqs. (1.51)−(1.53), the cutting depth in cutting wear mode can be expressed as

$$h_c = \frac{c\dot{m}v^2\alpha_o}{4d_j u\sigma} \tag{1.54}$$

The angle d_o is the angle of the kerf on the surface, which can be determined from Eqs. (1.51) and (1.52). When $h = 0$, then

$$\frac{dh}{dx}|_{h=0} = \frac{c\dot{m}v^2\alpha_o}{4d_j u\sigma} \tag{1.55}$$

Because

$$\alpha_o \approx \left.\frac{dh}{dx}\right|_{h=0} \tag{1.56}$$

it can be found that

$$\alpha_o = \sqrt{\frac{2\sigma u d_j^2}{\dot{m}v^2}} \tag{1.57}$$

Substituting Eq. (1.57) into Eq. (1.54) yields

$$h_c = C\sqrt{\frac{\dot{m}v^2}{8\sigma u}} \tag{1.58}$$

Before calculating the cutting depth of the deformation wear mode, Eqs. (1.57) and (1.58) need to be discussed.

Eq. (1.57) can be used to confirm that only deformation wear (not cutting wear) exists in the cutting process. From Eqs. (1.44) and (1.47), and the assumption that the horizontal velocity of the particle ends $\dot{x}_t = 0$, it can be directly concluded that

$$\alpha_c = \tan^{-1}\frac{d}{6} \approx \frac{\pi}{10} \quad (\phi = 2\,\text{时}) \tag{1.59}$$

It should be noted that Eqs. (1.57) and (1.58) assumed the existence of the critical traverse rate u_c. For water jets, it should be considered that the cutting mechanism relies on the traverse rate during the selection of the appropriate prediction model. By solving Eqs. (1.57) and (1.59), u_c can be expressed as

$$u_c \approx \frac{\pi^2 \dot{m} v^2}{200 \sigma d_j^2} \tag{1.60}$$

The cutting depth that resulted from Eq. (1.58) is independent of the jet diameter d_j, which can be directly seen from the cutting caused by the jet edge. Another reason why Eq. (1.58) is not affected by d_j is the assumption that no decline happens to the velocity along the direction of the cutting depth. However, C is likely related to the jet diameter. If the jet medium is solid water, instead of droplets, the relatively large jet will suppress particle deviation, which still requires further studies.

To calculate the cutting depth of the deformation wear, the following energy balance equation can be used:

$$\delta V = \frac{m(v \sin \alpha - v_c)^2}{2\varepsilon} \tag{1.61}$$

where ε stands for the energy required for the deformation wear to destruct one unit volume of the target material and v_c is the critical particle speed (the threshold velocity).

With δV replaced by $\delta \dot{V}$; m, by $(1 - C)\dot{m}$; v_c neglected; and compared with $v \sin \alpha$, α assumed to be 90 degrees, Eq. (1.61) can be written as

$$\delta \dot{V} = \frac{\dot{m}(1 - C)v^2}{2\varepsilon} \tag{1.62}$$

Under these circumstances, the volumetric erosion rate can be described as

$$\delta \dot{V} = \frac{\pi}{4} d_j^2 \frac{dh}{dt} \tag{1.63}$$

The integral of simultaneous equations composed of Eqs. (1.62) and (1.63) on time can be written as

$$\int_0^{h_d} dh = \frac{m(1 - C)v^2}{2\varepsilon} \int_0^{d_j/u} \frac{4}{\pi d_j^2} dt \tag{1.64}$$

The solution of Eq. (1.64) is as follows.

$$h_d = \frac{2\dot{m}(1 - C)v^2}{\pi u \varepsilon d_j} \tag{1.65}$$

According to Eqs. (1.58) and (1.65), the total cutting depth h can be determined as

$$h = h_c + h_d = C\sqrt{\frac{mv^2}{8\sigma u}} + \frac{2m(1 - C)v^2}{\pi u \varepsilon d_j} \tag{1.66}$$

The equation is only applicable when u is below u_c, calculated from Eq. (1.60). If $u > u_c$, only the second term in Eq. (1.66) would be applicable.

If v in Eq. (1.22) were to be replaced with v_j in the simple momentum equation, and $p \approx \frac{1}{2}\rho v^2$ would correspondingly be substituted, Eq. (1.66) can then be written as

$$h = \frac{C}{2 + (1 + R)\sqrt{\frac{\dot{m}p}{\rho\sigma u}}} + \frac{4(1 - C)\dot{m}p}{\pi\rho\varepsilon u d_j (1 + R)^2} \tag{1.67}$$

This formula qualitatively agrees with the experimental results. The first term is the cutting depth caused by cutting wear, whereas the second term is attributed to deformation wear. To simplify the analysis, the proportional factor C is used. However, C is not constant. Since flaws exist in this formula, which require modification, no quantitative comparison between experimental data and the prediction results using this formula can be made here. The limitations of this formula are as follows:

- Effects of the particle size are not considered, since the microcutting model does not include this parameter. Grain size relates to the erosion resistance of the material during the erosion, although differences exist regarding this topic. For small particles, the erosion resistance of the material grows with increasing yield stress, which explains why a grain size smaller than a particular range can lead to a decrease in cutting depth. However, this does not offer insights into the declining depth as grain sizes exceed this range. In such cases, there are two possible explanations: one is that the particle increases in size, sphericity, and circumference, i.e., the particle is not that sharp during microcutting; the other explanation is the acceleration process within the mixing nozzle. The formula mentioned earlier can be modified to use the sphericity and circumference to characterize the effects of grain size. Efforts on such research topics are now making progress.
- It has been observed that the effects of the traverse rate are far more complicated than suggested by Eq. (1.67). In fact, such effects are intensified with the increase of the traverse rate in exponential form. Ignorance of the decline of the particle velocity along the cutting depth is also part of the limitations. However, to utilize the simplified formula, the power function of the traverse rate u can be modified into a different function, which is always smaller than a certain limit.
- For the mixing of abrasive and water, a simplified momentum equation is used. Hence the effects of nozzle length are not obvious.
- The formula does not consider the threshold conditions.

REFERENCES

Crow, S. C. (1973). A theory of hydraulic rock cutting. *International Journal of Rock Mechanics & Mining Sciences & Geomechanics Abstracts, 10*(6), 567–584.

Dick, R. A., Shengxiong, X., et al. (1995). *Fluidics and cutting applications(in Chinese)*. Hefei: Machinery Industry Jet Technology Information Network.

Gensheng, L., & Zhonhou, S. (2005). Advances in researches and applications of water jet theory in petroleum engineering. *Petroleum Exploration and Development, 32*(1), 96–99.

Jiajun, S. (1992). *Water jet cutting technology (in Chinese)*. Xuzhou: China University of Mining and Technology Press.

Junwei, Z., Xiyong, X., & Dajun, R. (2012). Analysis of high pressure jet theory and application in petroleum engineering (in Chinese). *Chinese Science and Technology Expo, 30*, 32.

Labus, T. J. (1995). *Fluid jet technology fundamentals & applications*. USA: American Waterjet Technology Association.

Maurer, W. C. (1980). *Advanced drilling techniques*. Tulsa: Petroleum Publishing Co.

Moshen, C., & Jiajun, S. (1993). *High pressure water jet technology (in Chinese)*. Beijing: Coal Industry Press.

Qinggang, X. (2014). Research review of high pressure jet theory and application in petroleum engineering (in Chinese). *Chemical Engineering Management, 32*(26), 270.

Qingwen, Y. (1997). Abrasive waterjet cutting technology and application prospect (in Chinese). *Machine Building, 1*, 8–9.

Qingwen, Y. (2001). Forecast and study evolution on water jet technology. *Coal Mine Machinery, 11*, 4–6.

Shengxiong, X., et al. (1998). *High pressure water jet technology and application (in Chinese). Beijing*. China Machine Press.

Summers, D. A. (1987). Development of high pressure water jet drilling technology (in Chinese). *High Pressure Water Jet, 1*, 47–51.

Xiaohe, X., & Jing, Y. (1984). *Theory of rock breaking*. Beijing: China Coal Industry Press.

Xiaohong, L., et al. (2000). Experimental investigation of hard rock cutting with collimated abrasive water jets. *International Journal of Rock Mechanics and Mining Sciences, 37*, 1143–1148.

Xiaomin, W., et al. (1992). *High pressure jet technology translation (in Chinese)*. Beijing: China Coal Industry Press.

Zhonghou, S. (1998). *Theory and technology of water jet (in Chinese)*. Dongying: Petroleum University Press.

Zhonghou, S., & Gensheng, L. (1992). Application and prospect of high pressure water jet technology in drilling (in Chinese). In *Proceedings of the drilling basic theory symposium on Chinese Petroleum Society*.

Zhonghou, S., Gensheng, L., & Ruihe, W. (2002). Application and prospects of water jet technology in petroleum engineering. *Engineering Science, 4*(12), 60–65.

Zhonghou, S., Gensheng, L., & Zhiming, W. (1991). New jet theory and prospects of application in petroleum engineering. In *Proceedings of the 13th World Petroleum Congress*.

CHAPTER TWO

Mechanism and Parameter Optimization of Abrasive Water Jet Perforation

Contents

Abstract

This chapter investigates the mechanisms of abrasive water jet (AWJ) perforation, and the results of laboratory experiments and field cases on abrasive AWJ perforation are presented. AWJ perforation is a two-stage process: the ductile casing erosion stage and the brittle rock penetration stage. Each stage follows different failure mechanisms. Experiments were conducted to reveal the effect of pressure, flow rate, abrasive material, particle size, abrasive concentration, ambient pressure, rock material, exposure time, etc., on penetration performance. The conclusions derived from the laboratory experiments were supported by field tests. Further simulation experiments of AWJ perforation are illustrated in the third section.

Abrasive Water Jet Perforation and Multi-Stage Fracturing
ISBN: 978-0-12-812807-7
https://doi.org/10.1016/B978-0-12-812807-7.00002-9

Keywords: Experiment; Fracture initiation; Hydra-jet perforating; Mechanism.

2.1 MECHANISTIC INVESTIGATION OF ABRASIVE WATER JET PERFORATION

2.1.1 Introduction to Abrasive Water Jet Perforation

Abrasive water jet (AWJ) perforation or sand jet perforation is a process that uses a high-pressure fluid slurry to perforate oil or gas wells, and simultaneously extend a cavity into the reservoir. AWJ perforation has its origins in the 1960s with many large-scale commercial successes in several international venues. While the AWJ perforation process was a technical success at that time, it was not an economic success. A few advances in the technology were reported until the late 1990s. Advances in metallurgy have allowed major redesigns of sand jet perforating tools and jet orifices. These advances coupled to improvements in pump pressures and higher pressure limits make the AWJ perforation process even more effective. Newer modular AWJ perforation tool designs ensure near limitless reconfiguration of the coiled tubing-conveyed plugs, packers, hold-down tools, perforation, and fracturing tools for simultaneous use during the completion and workover operations.

The applications for AWJ perforation technology include perforation and reperforation of vertical and horizontal oil and gas wells, and perforation and treatment of coalbed methane wells. AWJ perforation can also be used in conjunction with other technologies such as freshwater and foam fracturing, and for enhanced performance resulting from chemical injection and acidizing. It provides an alternative to widely accepted wire-line or tubing-conveyed explosive methods used in most fields today. Hundreds of documented successes are available to confirm that AWJ perforation increases the communication between the wellbore and reservoir more effectively with less formation damage and is accomplished in fewer round trips in and out of the wellbore than the more widely used perforating methods. Added benefits are realized because perforating and fracturing can be accomplished nearly simultaneously using a common work string (Dotson, Farr, & Findley, 2009).

2.1.2 Theoretical Analysis of the Particle Acceleration Process in Abrasive Water Jet Perforation

Knowledge of particle velocity is of great importance because the material is cut by wear due to the kinetic energy of each abrasive particle. In this spirit,

Hashish (1984) developed a cutting model in which the depth of the cut depends on the velocity of the abrasive particle. In his model, the velocity of the particle is estimated by means of a conservation law of momentum at equilibrium corresponding to velocity, which the particle would have at impact if the mixing tube were sufficiently long. In practice, that situation is not attainable; therefore the present theoretical analysis of the particle acceleration process has been developed to estimate the velocity of the abrasive particle at practical distances of impact, which are usually used in systems for cutting with an AWJ.

The most important existing models of the acceleration process encountered in the literature are those of Drew (1983), Abudaka and Crofton (1989), and Nadeau, Stubley, and Burns (1991). Drew et al. presented more complete equations of momentum for the phases involved in the mixture flowing within a nozzle; however, the analytical resolution of such equations is impossible because they are differential and nonlinear. Abudaka et al. presented a simple equation of the motion of a particle within the jet in the mixing tube under the action of the interfacial drag force. However, he considered that fluid jet velocity is held constant during the acceleration process. In addition, his model has two constants, which are determined in an ad hoc fashion. Using the approximate method of Runge-Kutta, Nadeau et al. numerically resolved the differential and nonlinear equation of the motion of a particle within the water jet in the mixing tube. As a result, he plotted the acceleration of particles and the deceleration of the water phase as a function of distance within the mixing tube. The results are most interesting; however, the numerical solution method considered only the effect of the interfacial drag force and neglected the effect of air on the particle velocity.

Thus there is no simple and analytical solution to the differential and nonlinear equation of the motion of a particle, describing the mechanical phenomena as a whole equation of momentum (Tazibt, Parsy, & Abriak, 1996).

2.1.3 Mechanism of Abrasive Water Jet Perforating

The mechanistic investigation showed that AWJ perforation is a two-stage process, the ductile casing erosion stage and the brittle rock penetration stage, and each stage follows different failure mechanisms.

2.1.3.1 Mechanism of Abrasive Water Jet Perforating Casing

Material removal in ductile materials takes place by abrasive wear (microcutting by the abrasive particles) and plastic deformation (Hashish, 1988).

Microcutting by the abrasive particles takes place at the top of the kerf, whereas plastic deformation occurs at the bottom of the kerf. Microcutting occurs at a low impact angle (local impact angle), irrespective of the global impact angle of the jet with respect to the workpiece (Paul, Hoogstrate, Van Luttervelt, & Kals, 1998).

In AWJ perforation, an inclined kerf, as shown in Fig. 2.1, is generated as the jet traverses over the workpiece at a particular speed. The kerf is gradually displaced in the traverse direction as the machining continues. In the upper part of the kerf, the abrasive particles are at a shallow inclination angle with respect to the local kerf geometry. Material removal by microcutting in this zone can be modeled after Finnie's suggestions (Engel, 1978, chap. 4). As material removal progresses along the depth of the kerf, the inclination angle between the abrasive particles and the local kerf geometry becomes

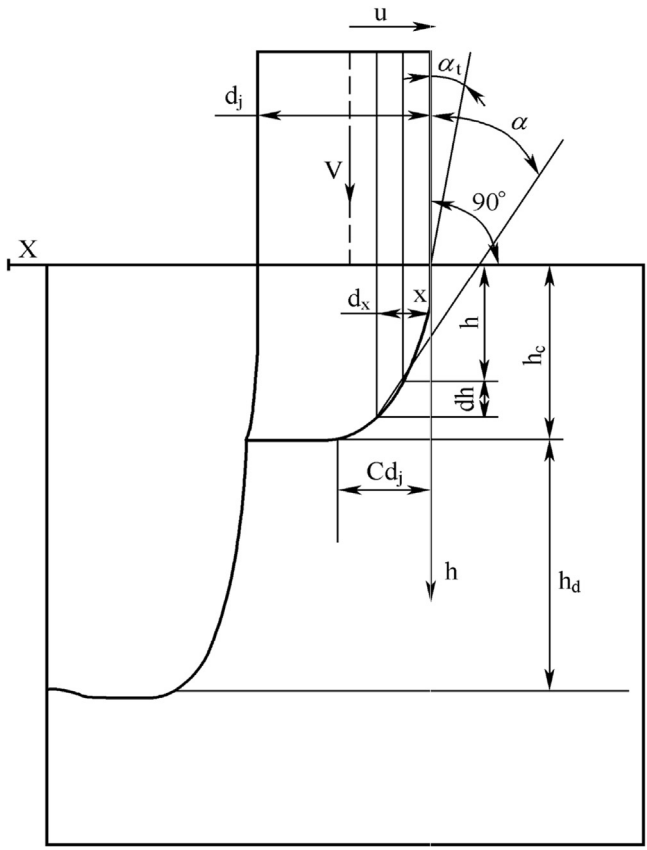

Figure 2.1 Development of the geometry of the kerf.

zero. At zero inclination or impact angle, the material is not removed, as modeled by Finnie and supported by the experimental data. However, due to the continuous traverse of the AWJ, small steps are formed, and such step formation leads to a sudden change in the curvature of the kerf and the impact angle. At the step, the particles impact the site orthogonally, and thus material removal at such sites can be modeled as plastic deformation, as conceived by Bitter (1963). Finnie's earlier model cannot be used for near-orthogonal impact (such as at the site of step formation) because it fails to correlate with the experimental data on erosion.

The basic model of microcutting as developed by Finnie et al. does not account for the effect of particle size and shape, leading to a conservative estimate of a velocity index of 2, whereas the experimental data indicate a velocity index of 2.5 for ductile materials. Hashish (1987) incorporated particle size and shape in the erosion model and presented an analytical model to predict the total depth of the cut in the AWJ machining of a ductile material, but neglected any variation in the width of the kerf along the depth of the cut. However, the experimental investigations indicate that the kerf width generally decreases along the depth of the kerf. Broersen (1993) further indicates that there seems to be a minimum kerf width, and that the location of such minimum kerf width is in the transition zone (between the microcutting zone and the plastic deformation zone). The minimum kerf width is practically independent of the AWJ machining parameters and the characteristics of the workpiece. Preliminary experiments and analysis of the experimental data suggest that the effects of the different parameters and the work material cannot be neglected.

2.1.3.2 Mechanism of Abrasive Water Jet Perforating Cement and Rock

The mechanical behavior of a rock depends on the shape and distribution of its constituents, as well as on the presence of discontinuities such as pores and cracks. The latter factors play an important role in the observed nonlinear stress–strain curve due to the crack closing under the elastic regime or sliding along crystal boundaries or crack surfaces. Material removal in the rock is much more complex than that in casing. Rock mineralogical composition and crystal size, as well as rock permeability, are the most relevant rock parameters when describing the erosion of stones under high-pressure water jets. The role of porosity was seen to be significant for contents >2%.

Several authors studied the fracture behavior of rocks subjected to high-pressure water jet impacts and verified that the compressive strength exerted

by the jet produces a stress concentration, leading to the nucleation of microcracks in locations of possible nucleation. Nucleation sites are preferentially the cleavage planes, faults in crystals, pores, and the boundaries between the crystals and between the crystals and the matrix. When the exerted force exceeds the tensile strength of the material, cracks propagate under a quasistatic regime depending on rock propagation resistance and its permeability, or generically on the rock structure, constituents' behavior, and loading conditions of the targeted area. Nucleated cracks lead to the outbreak of large particles washed out by the water jet effect. Brittle erosion models have been classified by Zeng, Kim, and Wallace (1993) into three types: conical crack model, lateral crack model, and intergranular crack model. When abrasive particles are entrained into a high-pressure water jet, they erode the target rapidly, removing the material (Momber & Kovacevic, 1997).

2.2 PARAMETER OPTIMIZATION EXPERIMENT OF ABRASIVE WATER JET PERFORATION

2.2.1 Laboratory Experiment Study on Abrasive Water Jet Perforating Parameters

By conducting a series laboratory experiments, researchers made a systematic study of the seven key parameters of AWJ as follows: pressure, flow rate, abrasive material, abrasive flow rate, abrasive particle size, rock property, and ambient pressure (Li et al., 2004).

The equipment of the experiment is shown in Fig. 2.2.

All the nozzle experiments used were made of hard alloy, and the nozzle structure is shown in Fig. 2.3.

To simulate the true underhole working situation, two types of rock specimen were experimented: both were a mixture of cement and silica sand, but at different proportions, 1:2 and 1:3 (cement volume vs. silica sand volume). The main physical characteristics of the two types of rock specimens are listed in Table 2.1.

For the purpose of convenient experimental result observation, the rock specimens were made in multisegments. The size was $20 \times 16.5\ cm^2$, and altogether 60 segments were produced.

The analysis of the experimental results is as follows.

1. Water jet pressure

   The effect of water jet pressure is shown in Fig. 2.4, indicating that increasing the water jet pressure could create a deeper hole in the

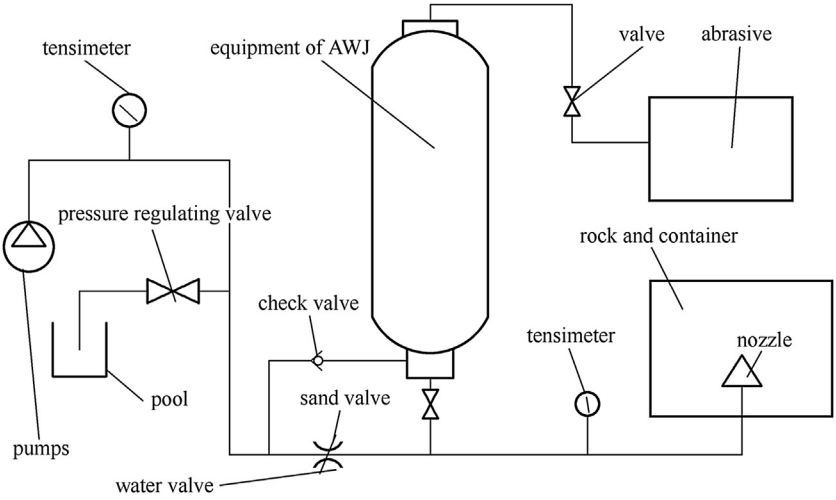

Figure 2.2 The equipment of the experiments.

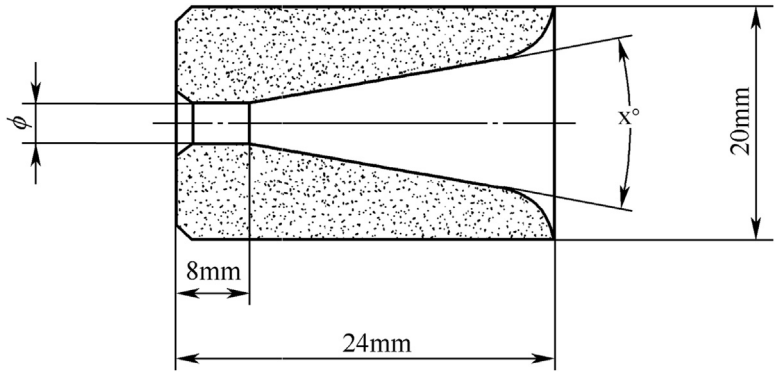

Figure 2.3 Nozzle structure.

Table 2.1 Physical characteristics of the rock specimen

Specimen	Compression strength (MPa)	Elastic modulus (MPa)	Porosity (%)	Permeability (μm^{-3})
1:2	18.19	818.55	20.23	0.61
1:3	11.51	585.35	27.77	0.45

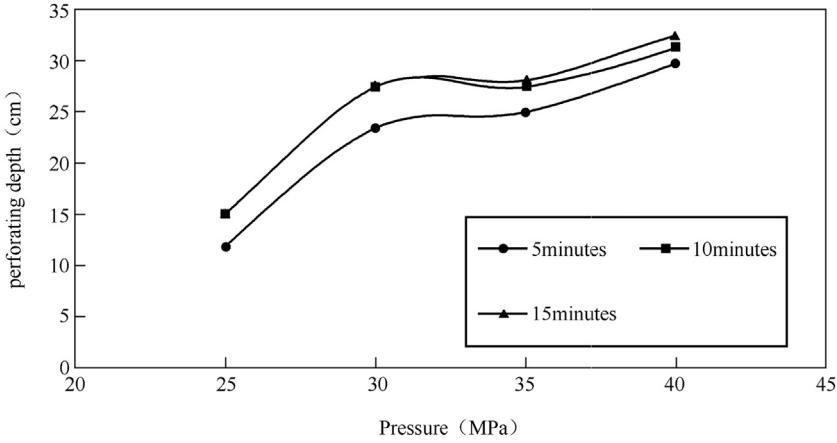

Figure 2.4 Effect of perforating pressure. Silica sand dn = 0.3–0.6 mm.

specimen. In addition, the observation of the appearance of the hole shows that the diameter also greatly increased. A maximum cutting depth existed as well as an optimal cutting time. Usually, 10–15 min cutting time was enough to reach the maximum depth.

2. Water flow rate

Fig. 2.5 shows that the cutting depth apparently increases with increasing water flow rate. When the water flow rate changed from 153 to 213 L/min, even the water jet pressure dropped to 10 MPa; however, the cutting depth was almost the same.

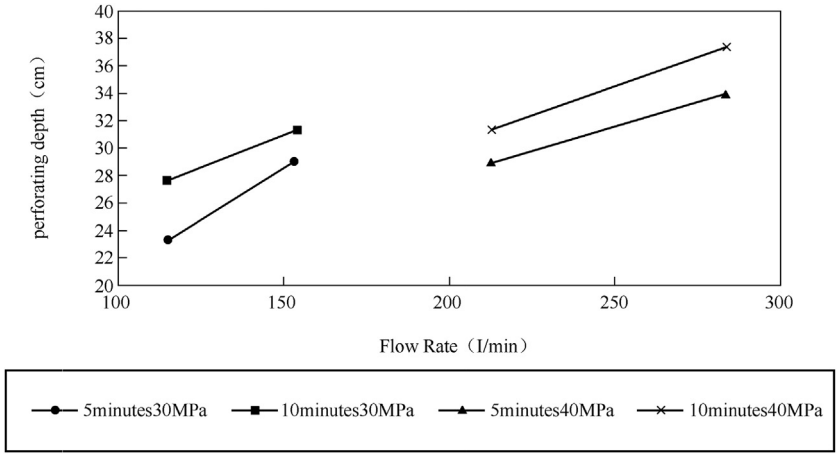

Figure 2.5 Effect of water flow rate. Silica sand dn = 0.3–0.6 mm.

3. Abrasive material

   Fig. 2.6 shows the comparison curve of silica sand cutting depth and garnet. The result is under the same water jet pressure and water jet flow rate, and by using garnet a bigger depth can be achieved. The reason is the greater hardness of garnet than that of silica sand. According to the proved theory, abrasive cutting ability had the same changing trend with its hardness, and with respect to those hard materials such as garnet, the cutting ability of sharp corners is greater than that of smooth corners. By employing garnet sand a deeper perforating depth could be obtained, but for economic and availability reasons, silica sand remained the recommended material, and thus the laboratory experiments mainly used silica sand.

4. Abrasive concentration

   Increasing the abrasive concentration will lift the number of impacts on the target material, which would in turn increase the depth of cutting or cutting speed. However, under constant hydraulic conditions, the velocity of the particles at a higher abrasive flow rate would be slower than the velocity at a reduced abrasive flow rate. Fig. 2.7 shows the existence of an optimal abrasive concentration. Under laboratory conditions, the optimal value is 6%—8%.

   The effect of abrasive particle size cutting is illustrated in Fig. 2.8, showing the existence of an optimum particle size. The medium size abrasive (diameter 0.4—0.6 mm) was found to be more effective than both fine and coarse abrasives.

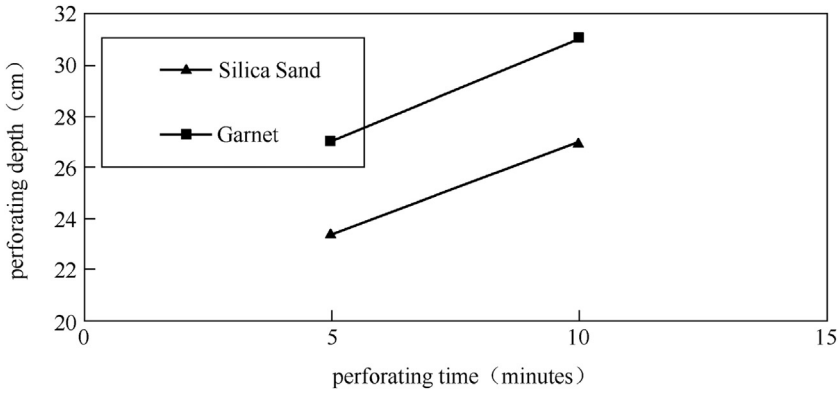

Figure 2.6 Effect of abrasive materials. Silica sand dn = 0.3—0.6 mm, $P = 30$ MPa.

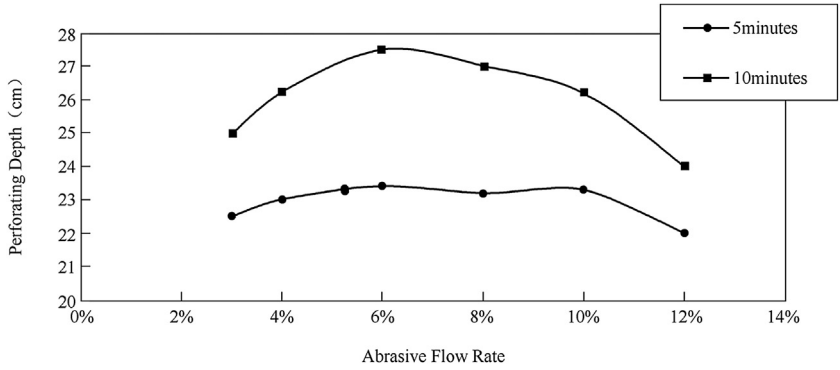

Figure 2.7 Effect of abrasive concentration. Silica sand dn = 0.3—0.6 mm, pressure = 30 MPa.

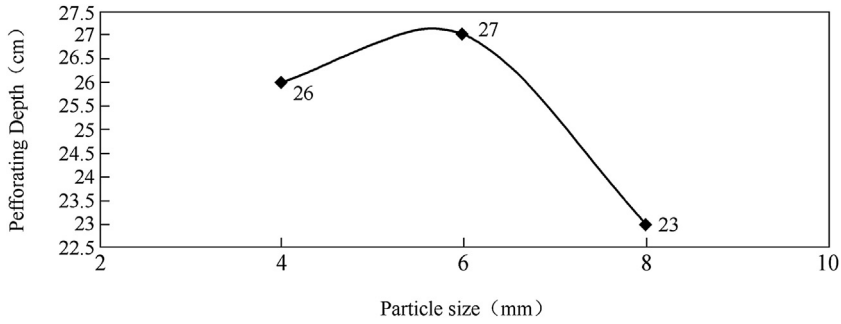

Figure 2.8 Effect of material particle size. Silica sand dn = 0.3—0.6 mm, pressure = 30 MPa.

5. Ambient pressure
   Fig. 2.9 shows that the depth of cut almost had a linear decreasing trend with ambient pressure. Therefore when this technology was adopted at the deep well, the effect of ambient pressure must be considered. The following field experiment showed that at a depth of 4840 m, the AWJ could still satisfy the need for perforation.
6. Rock properties
   Fig. 2.10 illustrates that rock hardness could affect the cutting depth of AWJ. The depth would increase with decreasing rock hardness.

2.2.2 Surface Experiment Study on Abrasive Water Jet Perforating Parameters

AWJ perforation has been extensively investigated in several laboratories (Jilei, Gensheng, & Jian, 2003; Li, Niu, & Liu, 2002). Based on the

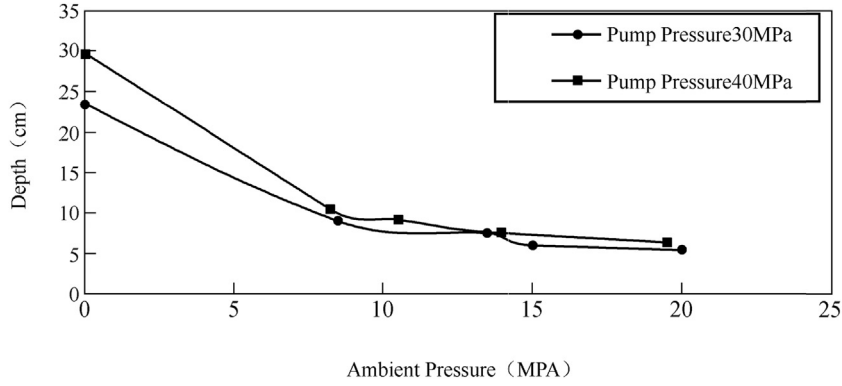

Figure 2.9 Effect of ambient pressure at different pressures. Time = 5 min.

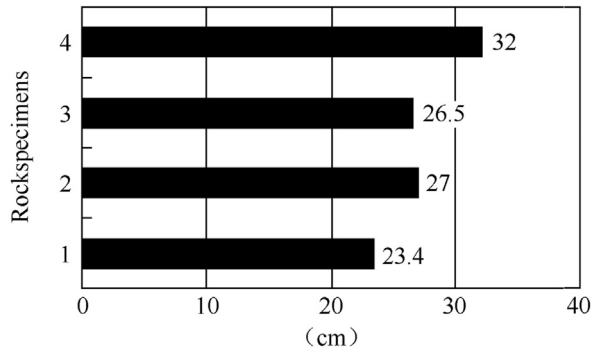

Figure 2.10 Effect of rock property. Pressure = 30 MPa, time = 5 min. 1—1:2 (cement: sand). 2—red sandstone. 3—brown sandstone. 4—1:3 (cement:sand).

experimental results in this article, Huang Zhongwei et al. made two larger cement samples. Simulating practical field conditions, including casing sizes, wellhead, pumps, pressure, flow rate, etc., two unit experiments, one in 139.7 mm casing and another in 178 mm casing, were carried out at the Xinjiang oilfield, Kalamayi, China, in October 2004 (Huang, Niu, Li, Yuan, & Liu, 2008).

The two cylinder samples in the experiment were mainly made of common Portland cement and sands (diameter 0.5−2.5 mm), both with a diameter and height of 2.4 and 1.2 m, respectively. Every sample was surrounded by a steel plate, 4 mm thick, and buried underground. At the center of the two samples, two sizes of casing, 139.7 and 177.8 mm diameter, were put inside vertically. At the bottom of the samples, a cross girder was placed to support the weight when lifting it out of the ground.

For the two sizes of casing, two types of blasting tools with diameters of 108 and 140 mm and a length of 480 mm were used. On every tool, a total of four nozzles were installed with a phase difference—the exit diameter being 4, 5, 6, and 8 mm. The body of the tool was made of common steel, whereas at the surface of the tool, around the nozzles, a layer of hard alloy was welded to resist the impact of the returned fluid (slurry). In addition, at the end of the tool, a check valve was connected. Before adding abrasives, the valve was kept open to pump in clean water to flush the tubing and the tool clear of solid purities. Therefore the nozzles could not be plugged anymore. After this, by throwing a steel ball to the valve seat to close it, the slurry could then be pumped to the required pressure.

According to previous experimental results (Li et al., 2002), the pressure, flow rate, and blasting time were set at ~50 MPa, 2.2 m^3/min, and 24 min, respectively, at every perforation point. The abrasive was silicon sand of 0.45–0.9 mm diameter. The slurry was pressured by three pumps used in fracturing jobs and the field test situation was shown in Fig. 2.11.

2.2.2.1 In 177.8 mm Casing

In this unit, the pressure was adjusted in the range 45–50 MPa. After 24 min blasting time, it consumed 55 m^3 water and 7.5 m^3 sand. The proportion of

Figure 2.11 Pressure test on a cement sample.

sand to water was controlled in the range 5%–7%. The tool was positioned at one place in the sample. At the completion of the experiment, the cement sample was lifted up to the surface and separated by traversing just at the blasting position, making it very convenient to measure the tunnels.

Fig. 2.12A shows that the hole diameter on the casing wall increased approximately linearly with the nozzle's diameter. Under a standoff distance of 11.2 mm, the hole diameter was approximately two times the nozzle orifice. In addition, the hole edge was much more uniform and smoother than that in the explosive perforation, as shown in Fig. 2.12B. Fig. 2.12C and D show the relationship curves between the tunnel depth and average tunnel diameter with different nozzle diameters. It was obvious that these two parameters also increased with increasing nozzle diameter.

Another important parameter was nozzle diameter reaming. Compared to the change before and after the experiment, four nozzles were found to increase less than 2% of their original diameters. This proved that the selected nozzle material could resist the AWJs grind and satisfy the tough field job.

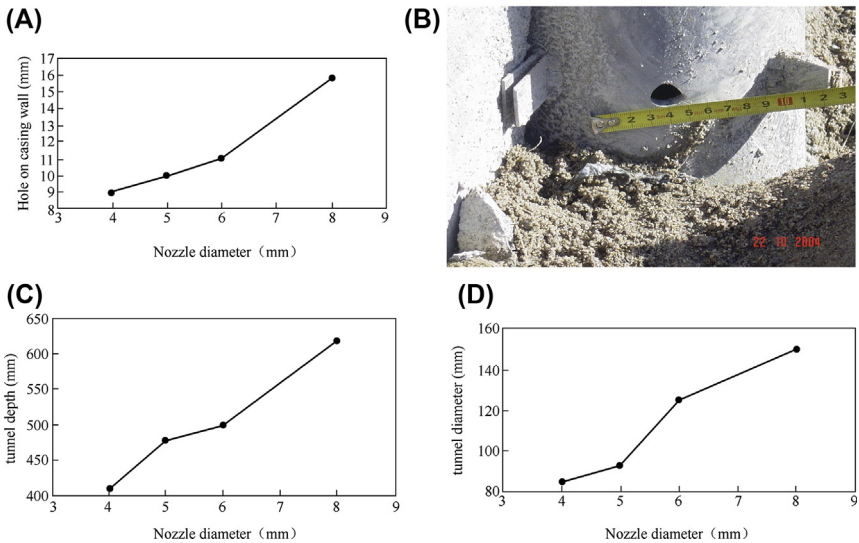

Figure 2.12 Hole diameter and tunnel parameters versus nozzle diameter and blasting time on 177.8 mm casings: (A) hole diameter on the casing wall versus nozzle diameter, (B) hole on the casing wall, (C) tunnel depth versus nozzle diameter, and (D) average tunnel diameter versus nozzle diameter.

2.2.2.2 In 139.7 mm Casing

In this sample, the blasting tool was moved three times. At every position, the pressure was controlled in the range 37–41 MPa and the sand proportion was in the range 5%–7%, with different blasting times of 16, 17, and 24 min. Fig. 2.13A–C show the curves obtained at a blasting time and standoff distance of 16 min and 8.5 mm, respectively. These three curves had similar trends to those obtained from 177.8 mm casing. The obvious difference exists, as shown in Fig. 2.13A, i.e., compared to the hole on the 177.8 mm casing wall, these were smaller because of the smaller standoff distance.

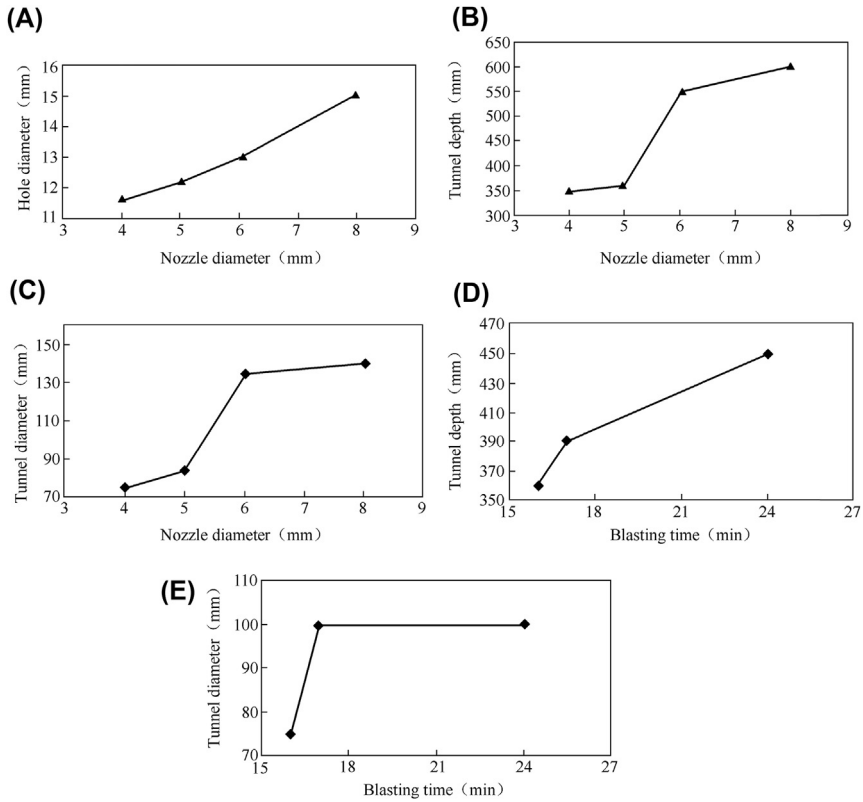

Figure 2.13 Hole diameter and tunnel parameters versus nozzle diameter and blasting time on 139.7 mm casings: (A) hole diameter on casing wall versus nozzle diameter, (B) tunnel depth versus nozzle diameter, (C) average tunnel diameter versus nozzle diameter, (D) tunnel depth versus blasting time, and (E) average tunnel diameter versus blasting time.

Fig. 2.13B and C show the relationship curves between the tunnel depth and diameter with the blasting time (nozzle diameter 5 mm). Fig. 2.13B shows that the tunnel depth increased with increasing blasting time, whereas the curve became smooth after 17 min. Fig. 2.13E shows a similar trend, and the tunnel diameter did not increase after 17 min.

2.3 FIELD EXPERIMENT OF ABRASIVE WATER JET PERFORATION

To further research hydra-jet fracturing in a low permeability reservoir, a large number of ground simulation experiments on sand jet perforating have been performed since the 1990s. These experiments were carried out to study the depth and diameter of the perforation channels and the parameters affecting them.

Hu, Zhu, and Lv (2012) from Jianghan Machinery Research Institute, DR, CNPC, performed a sand jet perforating simulation experiment. In this experiment, field jetting tools, parameters, and equipment were used. In addition, the core samples corresponded to the main target formation and were used to completely simulate the structure of the real boreholes, including the main compositions such as the casing pipe, cement sheath, formations, etc.

2.3.1 Preparation and Procedures of Experiment

The target formation of this experiment was Chang 6 formation of Pangu Liangxi Wu 420 area. The Chang 6 rock sample was gathered in the area of Sishilipu, north of Suide County. Eight samples were gathered by the combined methods of hydraulic cutting and explosion, and six of them were made into a cubic type with a size of $500 \times 500 \times 1000\ mm^3$; the other two samples had a size of $1500 \times 1500 \times 1000\ mm^3$ (Fig. 2.14).

Figure 2.14 Sampling location and completed rock sample of Chang 6 stratum.

In addition, a number of small samples were gathered for a sample physical parameter test and hydra-jet performance test. The physical parameters of Chang 6 sample were shown in Table 2.2.

The experiments were conducted at a dedicated experimental drilling site, where the wellhead assembly was installed, the manifold was joined, and fracturing trucks were arranged (Fig. 2.15). The equipment mainly included a set of wellheads, three fracturing trucks of 2000-type, a measuring truck, a manifold truck, a fracturing blender truck, and three fracturing tanks with a volume of 40 m^3. In addition, eight tank trucks, two filtering tanks, and a cementing truck of 400-type were also required on the site to transport the liquid waste.

Each experiment proceeded as follows: first, the target was hung above the wellhead and fixed on the test fixture; second, some related connection work was performed; and third, the target was replaced by another one after one experiment. The operating liquid flowed successively through the equipment in the following order: fracturing vehicles, high-pressure manifold, tubing string, jetting tool, annulus, wellhead cross joint, valve, discharge lines, and filter tank.

Table 2.2 Physical parameters of Chang 6 sample

Porosity (%)	Permeability ($\times 10^{-3}$ μm^2)	Apparent density (g/cm^3)	Elastic modulus (GPa)	Poisson ratio	Compressive strength (MPa)
11.66	0.64	2.29	15.3	0.31	64.5

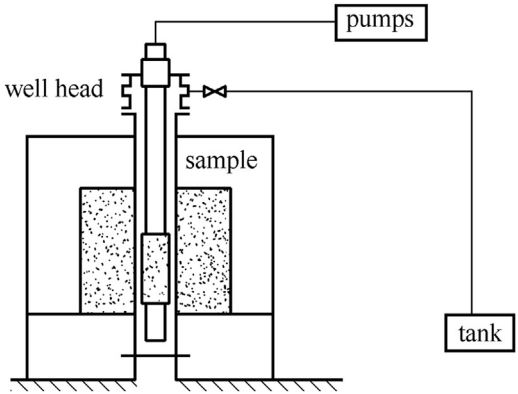

Figure 2.15 Sketch of test equipment.

The structure of the jet nozzle in the experiments was a combination of streamline inlet and straight hole section. The jetting tools in the experiments had two structures (Fig. 2.16). The jets with symmetrical double nozzles were used for the single abrasive perforation test, whereas those with symmetrical six nozzles were used for the fracture initiation test.

Three types of test target were prepared for these two tests (Fig. 2.17): one was a symmetrical double-nozzle abrasive perforating test, requiring six cement targets and two rock sample targets; the other was a symmetrical six-nozzle fracture initiation test, which needed a large-scale rock sample target. In all the tests, N80 casing had an outer diameter, wall thickness, and cement sheath thickness of 139.7, 7.72, and 50 mm, respectively.

The base solution used in the experiment was guanidine gum fracturing fluid at a concentration of 0.4%; the abrasive was quartz sand of 20—40 meshes with a concentration of 150 kg/m^3. The designed parameters of field test were shown in Table 2.3.

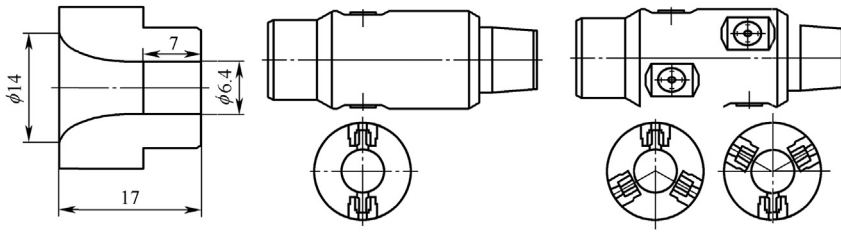

Figure 2.16 Drawings of nozzle structure and jet tools.

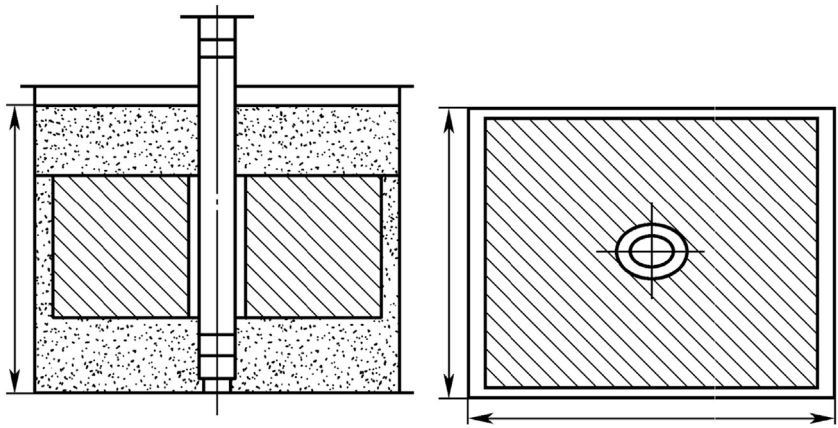

Figure 2.17 Schematic of test assembly.

Table 2.3 Designed parameters of test

Sample	No.	Displacement (m^3/min)	Jetting time (min)	Number of nozzles	Jetting velocity[a] (m/s)	Operating pressure[a] (MPa)
Cement targets	1	0.6	15	2×6.4	158	12.5
	2		20	2×6.4	158	12.5
	3	0.8	15	2×6.4	210	22
	4		20	2×6.4	210	22
	5	0.6	15	2×6.4	158	12.5
	6		15	$2 \times 4 + 2 \times 3.5$	225	25.4
Chang-6 formation rock sample target	7	0.6	15	2×6.4	158	12.5
	8	0.8	20	2×6.4	210	22
	9	2.2	20	6×6.4	200	20

[a]Jetting velocity and operating pressure were all theoretical values.

2.3.2 Dissection of Samples and Data Analysis

Twenty-four channels were made on the nine samples in the experiments. Many tools including a diamond wire saw and disc saw, which could incise large and small samples, respectively, were used, finally resulting in 24 complete channel shapes. The result showed that the shape and parameters of the formation rock targets and cement targets were very similar, indicating that choosing the recipe of cement targets according to the jetting performance was feasible to build simulating experimental conditions.

According to the dissection result and the experiment process, the channels could be divided into three types: a normal cavity created by abrasive perforating at the intended time, a cracked cavity created by abrasive perforating before the intended time, and a fractured cavity created with hydra-jet-assisted fracturing, which would be elaborated and analyzed concretely as follows.

2.3.2.1 Characteristics of Normal Cavity

The experiment on five targets (four cement targets and one formation rock sample target) was finished at the intended time, resulting in 10 normal cavities (Fig. 2.18). Field test parameters and measured data of normal cavities were shown in Table 2.4.

The shape of these cavities showed a common feature: they were basically oval or tear-drop shaped, and the cavities could be divided into four parts:

1. The first part was the casing perforation section, in which the cross-section was oval and the diameter was approximately 3.5 times the individual channels.

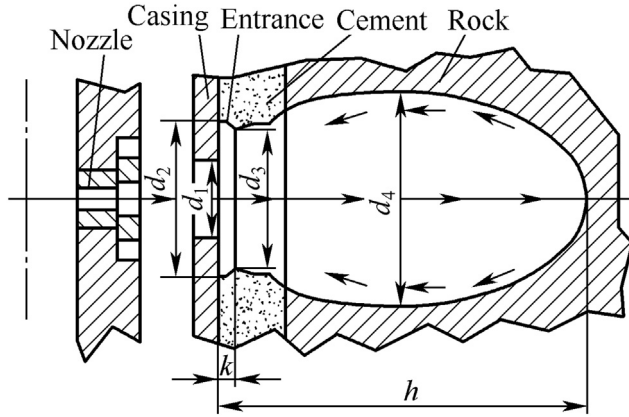

Figure 2.18 Shape of normal cavity created with abrasive perforating at intended time.

Table 2.4 Field test parameters and measured data of normal cavities

	Sequence number	Standoff distance (mm)	Jetting time (min)	Displacement (m^3/min)	Max pump pressure (MPa)	Channel direction	Casing hole diameter (d1)	Entrance sputtering diameter (d2)	Entrance sputtering depth (k)	Cement reduction section diameter (d3)	Max diameter (d4)	Channel depth (h)
Cement targets	1#	21	15	0.6	19.22	East	11.7 × 23	70	7	46	54	103
						West	23 × 23.5	55	5	36	55	105
	2#	21	20	0.6	20.26	East	21 × 19	66	14	50	67	124
						West	24 × 25.5	55	12.5	50	70	120
	3#	21	16	0.72	31.54	A side	22 × 29	95	5	82	87	160
						B side	22 × 27	78	9	65	81	164
	5#	18	15	0.6	14.65	East	19 × 21	48	9	40	55	110
						West	18.6 × 20.5	58	7	43	57	108
Rock sample target	7#	21	15	0.3–0.6	17.75	A side	19.2 × 22	60	7	43	57	121
						B side	22.7 × 24	45	8	40	62	133

2. The second part was the entrance sputtering section. The jet flow blasts the cement sheath and then flashes back the casing to form a short inverted flared cavity in the entrance of the cement sheath. The entrance sputtering depth k for most samples was approximately 10 mm. Moreover, the entrance sputtering depth k widened with increasing jetting time. The diameter of this section was approximately two or three times the casing perforation, where there was a trend of extending with increasing displacement.
3. The third part was a cement reduction section, with relatively smaller diameter in the range 10−15 mm, less than the diameter of the entrance sputtering section with a relatively small curvature.
4. The fourth part was the main section, representing the major structure of the cavity shape. This oval (or tear-drop shaped) cavity was 100−170 mm long, with a maximum diameter of two to three times that of the casing perforation, increasing with the displacement.

The cavity structure was found to be formed by jetting if the target did not break, but it was not the streamlined structure as usually imagined. The reason was the existence of the entrance sputtering section between the casing and cement sheath, forming a large mutation in the whole cavity structure behind the casing perforation. The structure of the entrance sputtering section had not been reported in the literature. However, in retrospect, this structure was found to exist commonly in the case of jetting targets with small parameters (2.5 mm jetting nozzle and 80 L/min displacement) under laboratory conditions. They would be easily ignored because of their small length and diameter with small parameters.

2.3.2.2 Characteristics of Cracked Cavity Created Before Intended Time

After enhancing the displacement and increasing the jetting velocity to 200 m/s as designed, fractures would initiate in the sample within 1 min by jetting perforation. As soon as the fracture is initiated, pumps should be stopped for the sake of safety, thus jetting did not continue as designed. During the experiment, as there was a slight difference between the annular pressures of these cracked cavities and that of the normal cavity, the main reason for the cracked cavity before the intended time was the partial pressurization caused by the enhanced jetting velocity.

In this experiment, a total of eight cavities in three targets formed before the intended time, including four cavities in one sample. Field test parameters and measured data of cracked cavities were shown in Table 2.5. The characteristics of the main section of these cavities were obviously different

Table 2.5 Field test parameters and measured data of cracked cavities

Sequence number	Jetting time (min)	Displacement (m^3/min)	Max pump pressure (MPa)	Channel direction	Casing hole diameter (d1)	Entrance sputtering diameter (d2)	Entrance sputtering depth (k)	Cement reduction section diameter (d3)	Max diameter (d4)	Channel depth (h)	Remarks
4#	1	0.8	31.61	East	14.7 × 17.4	35	2	20	35	360	Fracture along the channel axis; lots of water came in; sword-shaped channel
				West	14.3 × 17.4	40	5	32	47	90.5	Fracture and water seepage along the outer surface of the cement sheath and along the pore axis
6#	—	0.6	29.52	West 1	5 × 7.5			15.3	15.3	32	No jet through the cement sheath; very small bore
				West 2	7 × 9			18.3	20	32	
				East 3	6 × 7.5			17	17	20	
				East 4	7 × 9			17	17	125	Fracture along the channel axis; lots of water came in; sword-shaped channel

8#	0.5	0.8	30.09	East	20 × 16	59	4	45	45	104	Fracture along the channel radical; no crack along axis; carrot-shaped channel
				West	20 × 17	38	4	33	33	160	Fracture along the channel axis; lots of water came in; sword-shaped channel

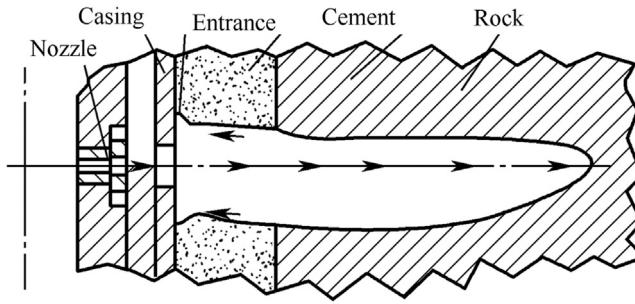

Figure 2.19 Shape of cracked cavity created with abrasive perforating before intended time.

from the normal ones (Fig. 2.19). When the fracture is initiated, high-speed jetting flow jetted along the crack propagate direction and eroded a narrow and sword-shaped channel, whose length was obviously larger than those of the normal ones. The shape of the cement sheath around the pore entrance was cylindrical without obvious necking. In addition, the main section was a flat sword-shaped channel. While the entrance sputtering section could be observed, even though it was quite narrow, the jetting time was very short, about 1 min, the channels did not develop very well, and there was a huge difference among the eight cavities. Some of them just formed 100 mm shallow grooves, whereas others already eroded a flat cavity over 360 mm long along the fracture.

2.3.2.3 Characteristics of the Fractured Cavity Created With Hydra-jet-Assisted Fracturing

In the #6 nozzle jetting test, the displacement increased gradually from 1.5 to 2.34 m^3/min until a fracture initiated in the target, when the pressure reached 32 MPa. Hydra-jet lasted for 20 min and created six fractured cavities (Fig. 2.20). Field test parameters and measured data of fractured cavities were shown in Table 2.6.

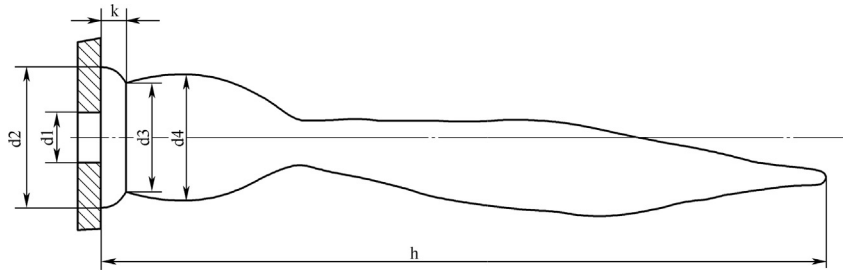

Figure 2.20 Shape of the fractured cavity created with hydra-jet-assisted fracturing.

Table 2.6 Field test parameters and measured data of the fractured cavities

Sequence number	Jetting time (min)	Jetting time (min)	Max pump pressure (MPa)	Channel direction	Casing hole diameter (d1)	Entrance sputtering diameter (d2)	Entrance sputtering depth (k)	Cement reduction section diameter (d3)	Max diameter (d4)	Hole depth (h)
9#	20	1.5−2.4	32.1	N	24 × 27.8	53	9	44	60	181
				NW	21.5 × 27.5	42	6	35	50	354
				SW	22.5 × 25	48	6	43	48	268
				S	23 × 28	68	5	49	53	279
				SE	20 × 27	56	8	44	51	290
				NE	23 × 29	59	9	40	43	230

The shape of the fractured cavity had combined characteristics of normal cavity and cracked cavity. Before fracture initiation, the olivary cavity was due to the jetting flow and backflow. However, once the fracture is initiated, high-velocity jetting flow eroded a slim and flat channel along the crack propagation direction. Therefore the fractured cavity had five parts: (1) casing perforation; (2) entrance sputtering section; (3) cement reduction; (4) olivary main section; and (5) gladiate channel. The shape and size of the first four parts were very similar to that of the normal cavity, whereas the length of the most gladiate channel was in the range 250−300 mm, with a minimum of 180 mm and a maximum of 350 mm.

Since the pumps were turned off immediately after the fracture initiated, the gladiate cavity did not fully develop and extend. Therefore if jetting continued for a period of time, the gladiate cavity would further extend to the edge of the target.

Six nozzles eroded six individual channels, extending along the crack in the propagation direction when the fracture initiated (Fig. 2.21). Six channels were not in the same level, but after fracture initiation, the horizontal crack cohered the six channels and formed into a large successive crack, dividing the target into two pieces. The results show that the jetting holes, created by hydra-jet-assisted fracturing, can guide the fracture initiation and extension near the wellbore. Since this experiment was conducted without confining pressure and triaxial stress, further experimental investigation is needed to confirm the effect of multiple fracture cavities on the fracture initiation near the wellbore with stress.

The dissected process of the No. 9 target is shown in Fig. 2.22.

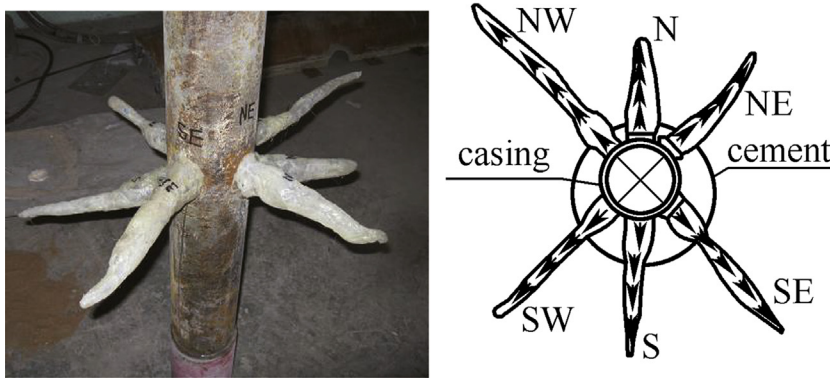

Figure 2.21 Distribution of fractured cavities created with hydra-jet-assisted fracturing.

Figure 2.22 Dissected process of the No. 9 test assembly with rock sample.

REFERENCES

Abudaka, M., & Crofton, P. (1989). Theoretical analysis and preliminary experimental results for an abrasive water jet cutting head. In *Paper presented at the 5th American Water Jet Conference*.

Bitter, J. (1963). A study of erosion phenomena part I and part II. *Wear, 6*(1), 5–21.

Broersen, S. (1993). *Cutting with high pressure water jet* (Masters thesis). The Netherlands: Laboratory for FPA, WbMT-OP, TU Delft. Report No. FPA-93–9013.

Dotson, T., Farr, J., & Findley, E. (2009). Advances in sand jet perforating. In *Paper presented at the SPE Rocky Mountain Petroleum Technology Conference*.

Drew, D. A. (1983). Mathematical modeling of two-phase flow. *Annual Review of Fluid Mechanics, 15*(1), 261–291.

Engel, P. A. (1978). *Impact wear of materials* (Vol. 2). Elsevier.

Hashish, M. (1984). Flow ind. In *Paper presented at the ASME*.

Hashish, M. (1987). An improved model of erosion by solid particle impact. In *Paper presented at the Erosion by Liquid and Solid Impact, Seventh International Conference*.

Hashish, M. (1988). The effect of pressure on the performance of abrasive water jet machining. *The International Journal of Advanced Manufacturing Technology, 1*, 255–263.

Huang, Z., Niu, J., Li, G., Yuan, X., & Liu, Y. (2008). Surface experiment of abrasive water jet perforation. *Petroleum Science and Technology, 26*(6), 726–733.

Hu, Q., Zhu, F., & Lv, W. (2012). Simulating experiments of hydrajet perforating process. In *Paper presented at the IADC/SPE Asia Pacific Drilling Technology Conference and Exhibition*.

Jilei, N., Gensheng, L., & Jian, S. (2003). Investigation and application of abrasive water jet perforation to enhance oil production. *Petroleum Drilling Techniques, 31*(5), 55–57.

Li, G.-S., Niu, J.-l., & Liu, Z.-K. (2002). Experimental study on mechanisms of hydraulic sand blasting perforation for improvement of oil production. *Journal-University of Petroleum China Natural Science Edition, 26*(2), 31–34.

Li, G., Niu, J., Song, J., Huang, Z., Ma, L., Tang, R., et al. (2004). Abrasive water jet perforation—an alternative approach to enhance oil production. *Petroleum Science and Technology, 22*(5–6), 491–504.

Momber, A., & Kovacevic, R. (1997). Test parameter analysis in abrasive water jet cutting of rocklike materials. *International Journal of Rock Mechanics and Mining Sciences, 34*(1), 17–25.

Nadeau, E., Stubley, G., & Burns, D. (1991). Prediction and role of abrasive velocity in abrasive water jet cutting. *International Journal of Water Jet Technology, 1*(3), 12.

Paul, S., Hoogstrate, A., Van Luttervelt, C., & Kals, H. (1998). Analytical and experimental modelling of the abrasive water jet cutting of ductile materials. *Journal of Materials Processing Technology, 73*(1), 189–199.

Tazibt, A., Parsy, F., & Abriak, N. (1996). Theoretical analysis of the particle acceleration process in abrasive water jet cutting. *Computational Materials Science, 5*(1–3), 243–254.

Zeng, J., Kim, T. J., & Wallace, R. J. (1993). *Quantitative evaluation of machinability in abrasive waterjet machining* (Vol. 58, p. 169). ASME-Publications-PED.

CHAPTER THREE

Numerical and Experimental Study of Flow Field in a Hydra-Jet Hole

Contents

Abstract

Understanding the characteristics of a flow field in a hydra-jet hole is crucial to explain why hydra-jets can realize pinpoint fracturing without using a mechanical packer. This chapter reports a numerical simulation and experimental study on flow fields in a hydra-jet hole, involving the modeling, experimental setup and scheme, and results. From laboratory experiments and numerical simulation data, five key factors—confining pressure, nozzle pressure drop, nozzle distance, inlet ratio, and perforation

Abrasive Water Jet Perforation and Multi-Stage Fracturing
ISBN: 978-0-12-812807-7
https://doi.org/10.1016/B978-0-12-812807-7.00003-0

tunnel depth—were utilized to preliminarily calculate the law of pressure distribution of a perforation tunnel and the jetting boost pressure. The results indicated that the nozzle pressure drop and entry ratio significantly affect the pressure distribution of the perforation tunnel and the jetting boost pressure and that the nozzle pressure drop is linearly related to the jetting boost pressure.

Keywords: Experiment; Flow field; Numerical simulation; Pressure distribution.

3.1 NUMERICAL SIMULATION OF FLOW FIELD IN A HYDRA-JET HOLE

Hydra-jet fracturing technology (Tian, Li, Huang, & Shen, 2008; Xia et al., 2009) involves the pumping of a fracturing fluid to perforate and fracture a formation. The first step involves the use of a sand-laden jet stream (Huang, Li, Niu, & Luo, 2008; Li et al., 2010) to penetrate the casing and form a hole in the formation. Then, by maintaining a constant tubing flow rate, the annulus is closed, and the fracturing fluid is pumped from the annulus to facilitate fracturing. Typically, the proppant-laden fluid is pumped through the tubing. According to the Bernoulli equation (Wang et al., 2006), the stagnation pressure at the top of the hole is greater than the annular pressure at the bottom of the hole. When the stagnation pressure is greater than the initiation pressure, the fracture will initiate and propagate smoothly (Huang, Li, Tian, Shen, & Luo, 2008; Li, Huang, Tian, & Shen, 2010). However, for those intervals without jetting and for controlling the annulus pressure such that it is less than the initiation pressure, the formation will not be fractured. Under this mechanism, the so-called pinpoint fracturing (Qu, Li, Huang, & Tian, 2010a, 2010b) can be realized without a conventional packer.

Hence, it is crucial to understand the pressure distribution inside the formation hole formed by abrasive water jet. Because of the complex practical conditions, it is difficult to calculate the actual pressure along the formation hole by analytical methods. Hence, this chapter mainly discusses two methods—commercial computational fluid (Han, Wang, & Lan, 2004; Wang, 2004) dynamics software and experiments, respectively, to obtain the distribution of the pressure and velocity fields with different nozzle and hole parameters for the purpose of verifying the mechanism of hydraulic isolation (Gong, Huang, Li, & Nie, 2007) to reduce the risk of sand-stick.

3.1.1 Flow Field Modeling and Boundary

3.1.1.1 Modeling and Meshing

Hydraulic abrasive water jet perforation ground tests revealed a spindle-shaped perforation hole. Considering that the flow field in the hole is symmetric about the hole axis, the simulated flow field is half the axisymmetric flow field (Fig. 3.1). The hole depth is 700 mm, the entrance diameter is 20 mm, the hole depth at the maximum aperture is 440 mm, and the largest aperture is 60 mm.

As shown in Table 3.1, the numerical simulation scheme includes the distribution of pressure and velocity in the perforating hole under two borehole conditions applied for the hydraulic injection fracturing: casing completion and open hole completion. The perforation geometries corresponding to the two completion methods mainly differ at the perforation entrance: for the casing hole, the abrasive jet must penetrate two materials of steel and rock because of the different damage mechanisms for the two materials, the punching hole diameter of the casing hole caused by water jet is not equal to the root diameter of the hole, and the casing is similar to a baffle at this time. For open hole wells, a casing hole is absent because the jet is directly acting on the rock.

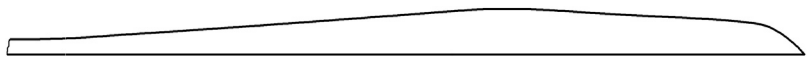

Figure 3.1 Geometrical shape of perforation hole of hydraulic abrasive water jet.

Table 3.1 Numerical simulation—hole geometry parameter scheme

Number	Diameter of casing hole (mm)	Nozzle diameter (mm)	Perforation depth (mm)	Diameter of the hole root (mm)	Type of simulation well
1	10	4.5	700	20	Casing wells
2	10	5.0	700	20	Casing wells
3	15	5.5	700	20	Casing wells
4	15	6.0	700	20	Casing wells
5	/	6.5	700	20	Open hole wells
6	/	7.0	700	20	Open hole wells

Figure 3.2 Schematic diagram of hole area division.

Based on local meshing, the mesh is divided into five regions according to the geometric and flow characteristics of the region (Fig. 3.2). The regions with drastic changes in the flow field are used for mesh encryption, whereas the area with slight changes can appropriately decrease the grid density, which is more targeted. This method can not only very well reflect the distribution of the flow field in the calculation domain but also reduce the number of grids and calculation time.

The total grid number of the numerical model is approximately 54,000, and the equalized skew is 0 for 94.58% of the grid; the minimum grid area is 6.03×10^{-3} mm^2, and the maximum grid area is 0.775 mm^2; these indexes revealed that the grid quality is good and that the numerical simulation results can reflect the actual flow. To better observe the grid structure, the partial enlarged view of the start (Fig. 3.4) and end (Fig. 3.3) of the channel is provided, where the different grid densities can be clearly observed.

3.1.1.2 Boundary Conditions

The boundary condition is the condition that the governing equation should satisfy on the boundary of fluid motion, typically including the inlet, outlet, and wall boundary conditions. For an axisymmetric flow field, symmetric boundary conditions are also applicable.

In this model, the inlet boundary is set as the pressure inlet, the total pressure is the nozzle inlet pressure, and the hydraulic diameter is the nozzle diameter. The outlet boundary is set as the pressure outlet, the total pressure

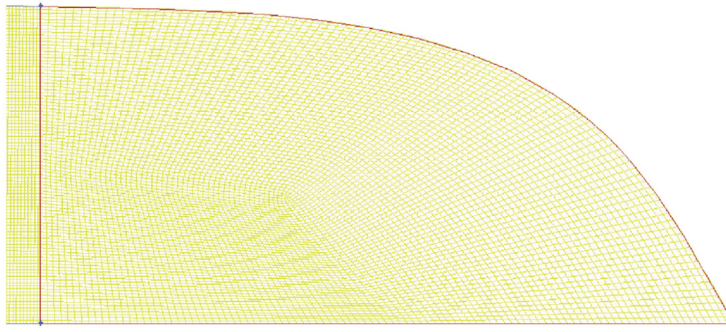

Figure 3.3 Meshing results of the end of the hole.

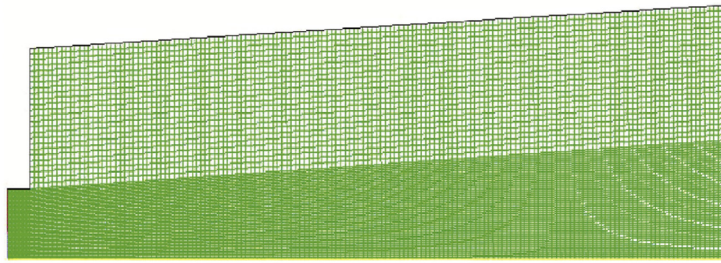

Figure 3.4 Meshing results of the beginning of the hole.

of which is the confining pressure of the annulus; the hydraulic diameter is equal to the inlet diameter of the hole minus the nozzle diameter. No parameters are required in the symmetric boundary conditions; only a reasonable symmetry position must be determined, where it should be specified as the hole axis. All flow boundaries except for the outlet, inlet, and hole axis are set as a smooth wall without slip conditions, i.e., the velocity of the fluid at the wall is zero.

3.1.2 Numerical Simulation Analysis

3.1.2.1 Characteristics of the Pressure and Velocity Distribution of the Hole

The pressure and velocity distribution of the nozzles with six diameters under different nozzle pressures and confining pressures was obtained by numerical simulation, with a total of 44 combination groups of nozzle parameters. From the simulation results, the flow field in the hole (e.g., the pressure and velocity fields) shows the same characteristics. The diameter of Φ4.5-mm nozzle was used to analyze the flow field in the borehole with hydraulic injection fracturing at a hole depth of 700 mm, inlet pressure of 25 MPa, and a confining annular pressure of 5.0 MPa.

3.1.2.2 Pressure Field Analysis

As can be observed from the total pressure cloud in the hole (Figs. 3.5 and 3.6), only the pressure of the root of the hole violently changes, but after a certain distance from the hole inlet, the pressure remains unchanged. The inlet pressure is mainly affected by the high-pressure jet, and its pressure and pressure gradient are large, which is in agreement with the characteristics of free shear flow: the pressure at the outlet of the hole is the lowest, with a bimodal pressure profile.

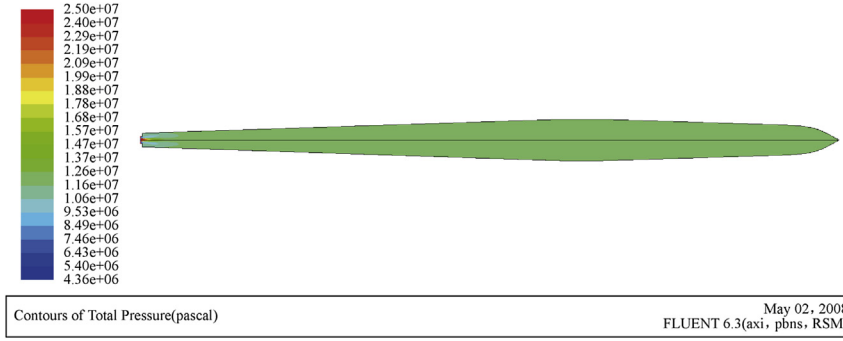

Figure 3.5 Total pressure cloud of the hole.

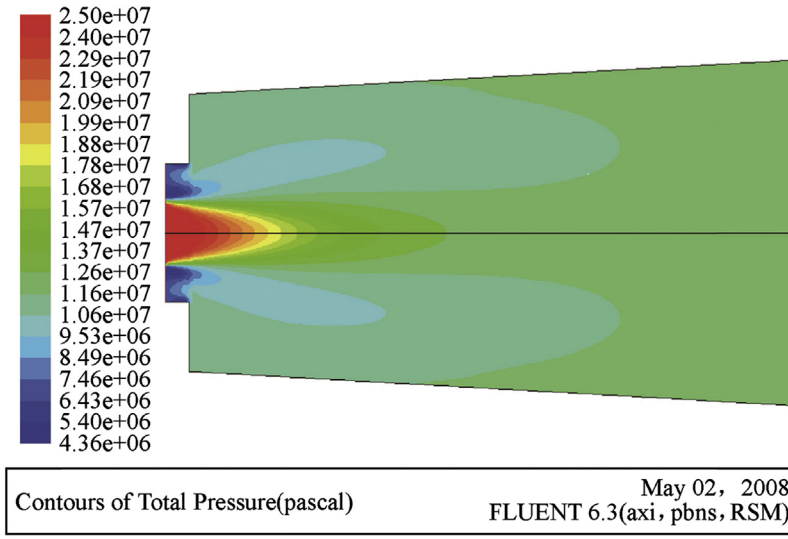

Figure 3.6 Total pressure cloud at the beginning of the hole.

The maximum static pressure in the hole is not at the entrance of the hole, but in the hole depth, with no axial and radial pressure gradients, and all static pressure values are equal to the total pressure (Fig. 3.7).

The change in the axial pressure (axial total pressure) reflects the pressure attenuation characteristic of the high-pressure jet. Combined with the available hole axial pressure curve (Fig. 3.8), the axial pressure rapidly decreases from 25 to 12 MPa, and the same pressure loss is 52% when the jet injection distance reaches 57 mm. The pressure profile is approximately parabolic in nature, with a gradually sharpened shape, indicating that the pressure drop

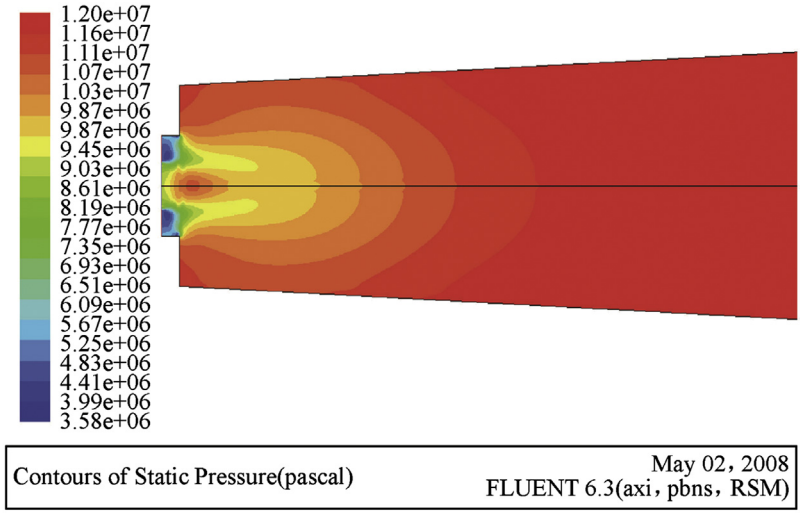

Figure 3.7 Static pressure cloud at the beginning of the hole.

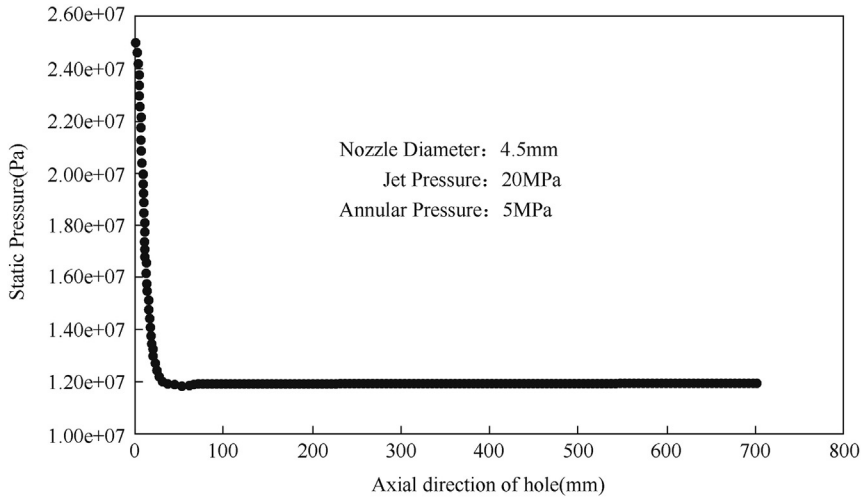

Figure 3.8 Axial pressure of the hole distribution curve along the axis direction.

of the nozzle is squeezed by the surrounding fluid, which limits the spread of pressure waves, thereby rapidly decreasing the axial pressure.

The change in wall pressure reflects the phenomenon of "pressurization inside the hole" in hydraulic jetting. From the wall pressure curve (Fig. 3.9), the maximum wall pressure is observed at 49 mm from the orifice; the maximum pressure reaches 12 MPa, relative to the confining annular

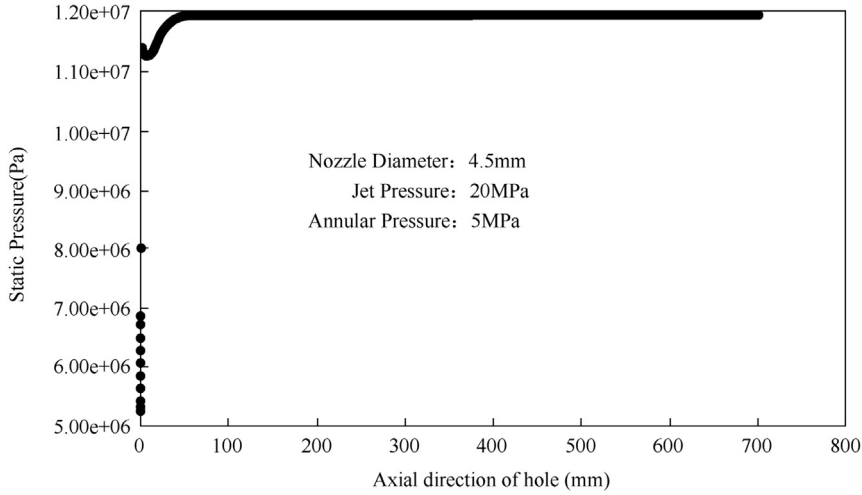

Figure 3.9 Wall pressure of the hole distribution curve along the axis direction.

pressure of 5 MPa, and the pressurization value in the hole reaches 7 MPa. The wall pressure remains constant after reaching the maximum.

3.1.2.3 Velocity Field Analysis

From the velocity cloud and axial velocity vectors (Figs. 3.10 and 3.11), the maximum hole velocity is observed at the hole entrance, indicating that the high-pressure jet has a high initial velocity (200—250 m/s). The fluid velocity at the hole depth is zero, indicating stagnation of fluid at the hole tip.

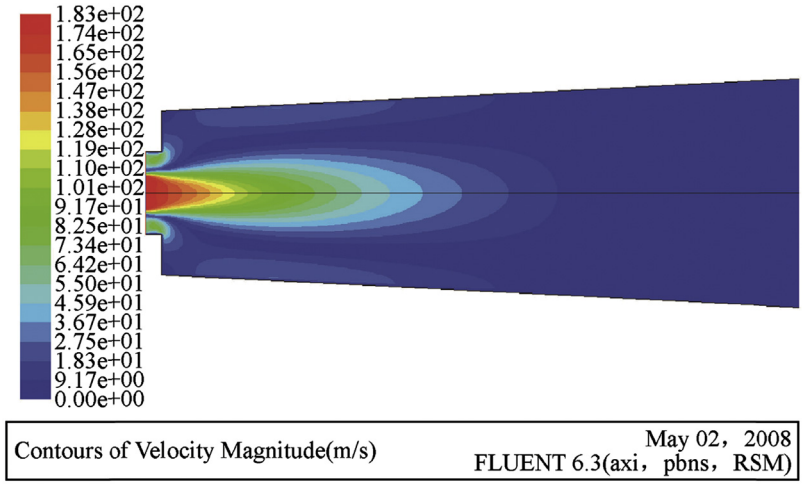

Figure 3.10 Velocity cloud inside the hole.

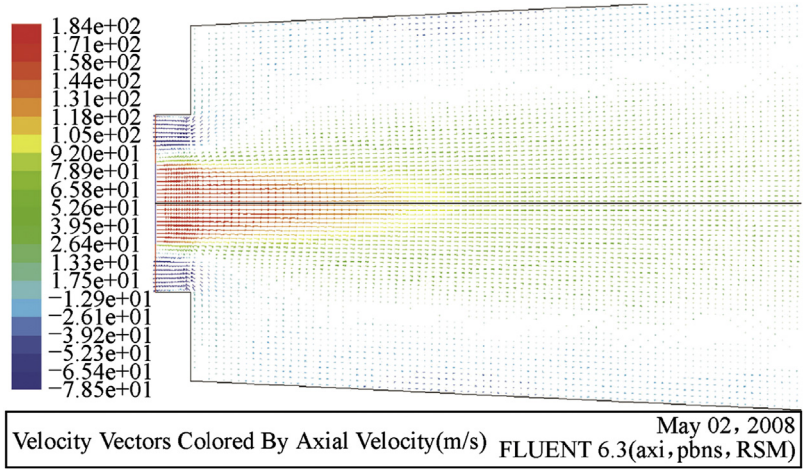

Figure 3.11 Velocity vector diagram at the beginning of the hole.

The attenuation law of the jet axis velocity (Ya & Wang, 2005) can be exploited to measure the working ability of the jet. The jet attenuation law is considerably different from that of the ordinary jet in hydraulic jet fracturing. At this time, the length of the potential core of the jet is extremely small (only 3.2 mm), and its dimensionless spray distance is less than 1, whereas the ordinary jet has a long potential core, and its dimensionless spray distance can reach 5—50. In addition, the jet velocity decreased from 179 to 0 m/s only through a short distance of 57 mm. Irrespective of the jet, the velocity decrease is related to the strong shear and convection effect at the jet boundary, leading to the intense momentum exchange between the water jet and the surrounding fluid and finally jet energy attenuation. This analysis indicates that the jet velocity rapidly decreases because of two reasons. First, because the jet is in a high-confining-pressure state, the surrounding fluid strongly squeezes the jet and accelerates the momentum exchange between the water jet and the surrounding fluid. Second, because of the limited space within the hole, the wall reflection causes severe fluid fluctuations, leading to severe energy dissipation.

Notably, the abrasive water jet is similar to the ordinary jet in that its velocity profile is also similar and parabolic; that is, the central velocity is greater than the small velocity on both sides. From the velocity vector (Fig. 3.11), the core area of the jet only has axial velocity, but no radial velocity. The radial velocity only exists at the outer boundary of the jet; that is, the incident stream begins to turn at the outer boundary, ultimately flowing out in the reverse direction through the outlet hole.

3.1.2.4 Streamline Inside the Hole Chart Analysis

A streamline is a vector line in a velocity field at a certain time. Streamline density represents the absolute velocity, and its tangential flow direction is the direction of speed. The streamline and the trace are coincident in the steady flow. Analysis of the streamline inside the hole chart (Fig. 3.12) shows that the streamline in the hole entrance and the hole wall exhibits a high density, indicating that these areas have increased flow velocity. The streamline is basically parallel to the flow into the hole, and after a certain distance from injection, the outermost streamline of the jet begins to bend, which in turn bends the streamlines from the outside to inside. All streamlines flow out of the hole along the wall all the way to the outlet after bending to 180 degrees, which is a phenomenon typical of "backflow."

This phenomenon indicates that the flow field is affected by the centrifugal force field, and a large shear stress gradient is present. The centrifugal force field is caused by the radial velocity of the fluid, and the shear stress gradient exists in the flow of all viscous fluids under a fixed boundary; hence, the backflow in the hole is normal.

Some areas are only surrounded by streamlines, and no streamlines pass through, indicating that the fluid in these zones is stagnant. This result is the same as that obtained from the velocity vector diagram.

3.1.3 Analysis of the Factors Affecting the Pressure Distribution of the Hole

3.1.3.1 Effect of the Confining Pressure on Pressure Distribution of the Hole

The annular confining pressure is mainly caused by the static liquid column pressure generated by the static liquid column in the annulus, and its value is related to the well depth; the artificial controllability is low.

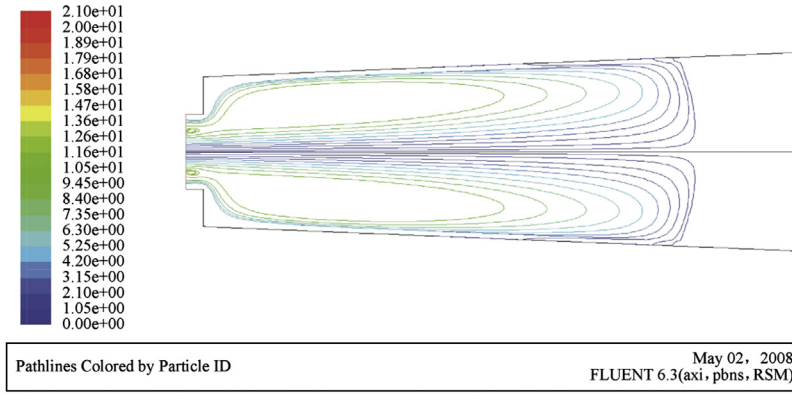

Figure 3.12 Streamline at the beginning of the hole chart.

3.1.3.1.1 Effect of the Confining Pressure on the Pressure Distribution in the Hole of Casing Wells

The pressure distribution in the hole under confining pressures of 5, 10, 15, and 20 MPa was simulated. Figs. 3.13 and 3.14 show the results.

Fig. 3.13 shows the comparison of wall pressure at the same nozzle pressure drop and different confining pressures. With increasing confining pressure, the hole wall pressure increases. This result indicates that the greater the

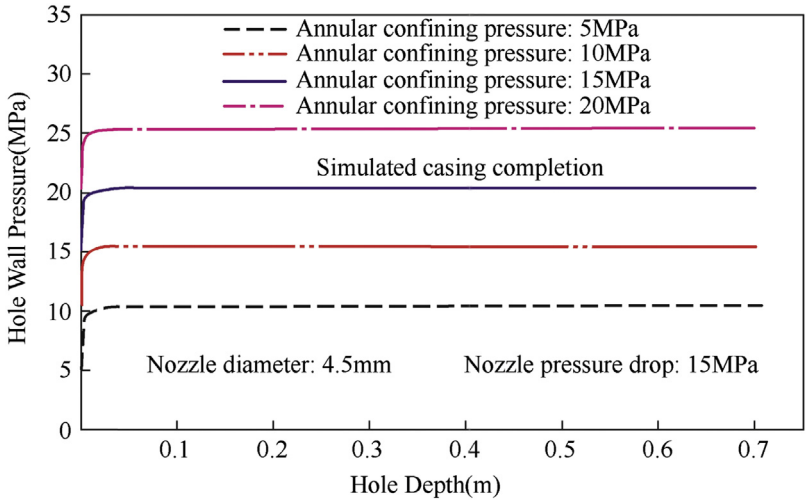

Figure 3.13 Effect of the confining pressure on wall pressure.

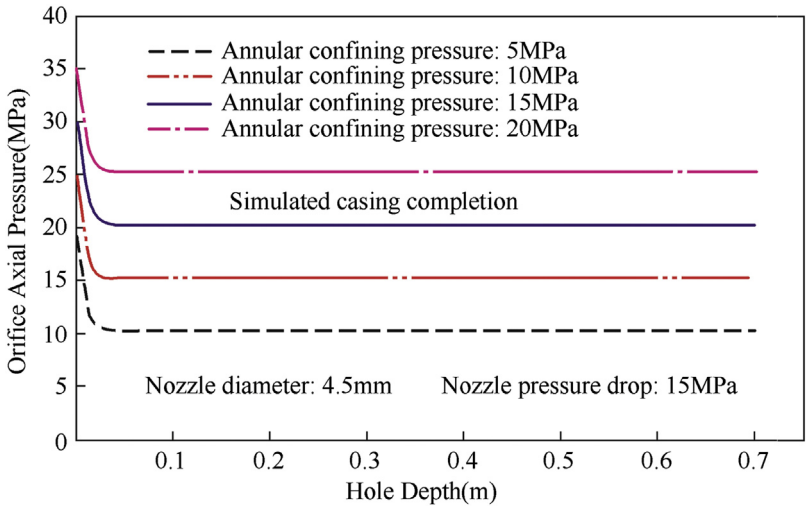

Figure 3.14 Effect of the confining pressure on the axial pressure.

confining pressure, the stronger the squeezing effect on the jet; hence, the momentum exchange velocity between the jet and the surrounding fluid increases, which in turn rapidly converts kinetic energy to static pressure.

According to the aforementioned analysis and combined with the actual process, it is necessary to minimize the confining pressure at the water jet perforation stage, which can reduce the bound to the jet and improve the rock-breaking capacity of water jet to obtain the ideal perforation hole. During fracturing, the annular confining pressure should be increased as much as possible to obtain a high static pressure in the hole, which is helpful to break the formation and maintain the extension of the fracture.

Fig. 3.14 shows the change in the axial pressure of the hole at different confining pressures. The axial pressure sharply decreases regardless of the confining pressure, but the deceleration rate of the axial pressure is different under different confining pressures. The greater the confining pressure, the more rapid is the axial pressure decrease. The axial pressure tends to attain steady values regardless of the confining pressure, and its magnitude is equal to the wall pressure under the same conditions. This result indicates that the impact area of the confining pressure is limited.

Quantitative analysis reveals that hole pressurization is a fixed value regardless of the confining pressure in the same nozzle pressure drop; that is, if the nozzle pressure drop is 15 MPa, the hole pressurization is 5.0 MPa under four confining pressures (Table 3.2).

3.1.3.1.2 Effects of the Confining Pressure on Pressure Distribution of the Hole in Hole Wells

Figs. 3.15 and 3.16 show the changes in the wall pressure and axial pressure caused by the confining pressure change under the open hole condition, respectively. The other rules are the same as those in the casing wells, except

Table 3.2 Statistical table of pressurization in hole with different confining pressures

Nozzle pressure drop (MPa)	15	15	15	15
Confining pressure (MPa)	5	10	15	20
Stagnation zone pressure on hole wall (MPa)	10.13	15.05	20.12	25.12
Pressurization in hole (MPa)	5.13	5.05	5.12	5.12

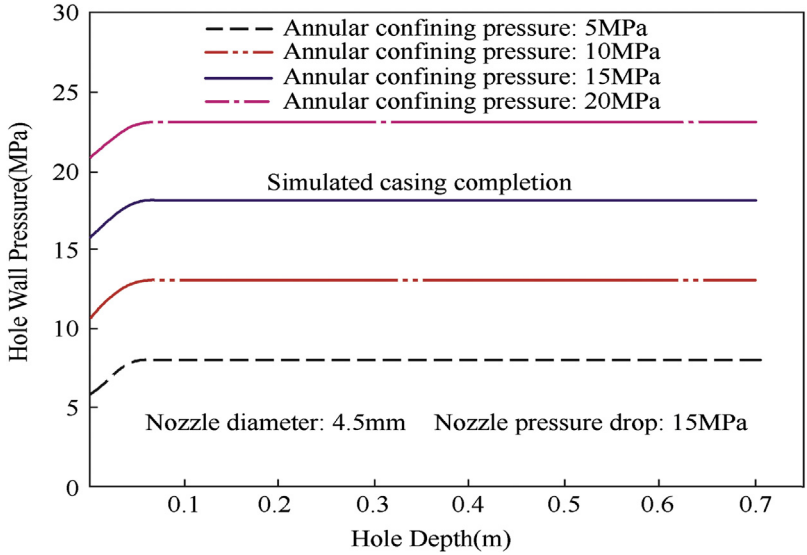

Figure 3.15 Effect of the confining pressure on the wall pressure.

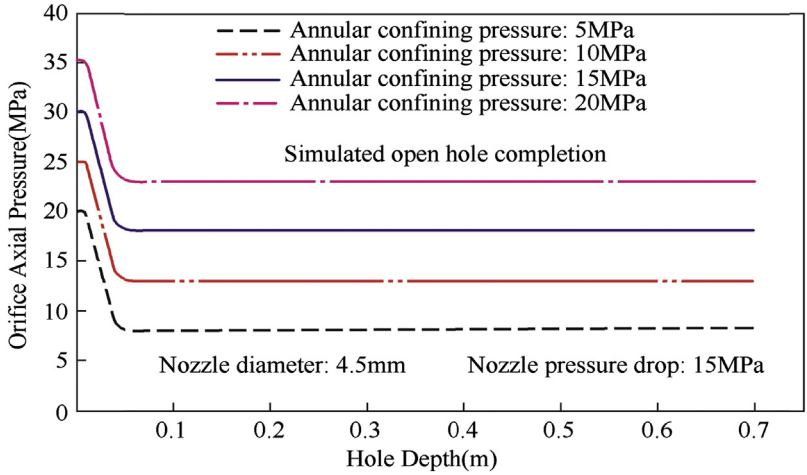

Figure 3.16 Effect of the confining pressure on the axial pressure.

that the axial pressure decrease is slower. By comparing the results obtained from quantitative analysis under different well patterns and nozzle diameters, under the condition of the same nozzle pressure drop, the pressurization value in the hole is not related to the well type and annular confining pressure.

3.1.3.2 *Effect of Nozzle Pressure Drop on Pressure Distribution of the Hole*

The nozzle pressure drop is defined as the difference between the nozzle inlet pressure and the nozzle outlet pressure. Here, the nozzle outlet pressure is the annular confining pressure.

3.1.3.2.1 Effect of the Confining Pressure on the Pressure Distribution of the Hole in Casing Wells

Nozzle pressure drop, respectively, take 15, 20, 25, 30 MPa, which is the nozzle inlet pressure were taken 20, 25, 30, 35 MPa. Figs. 3.17 and 3.18 show the simulation results.

Fig. 3.17 shows the change in the wall pressure at different nozzle pressure drops. With the increase in the nozzle pressure drop, the hole wall stagnation pressure increases; when the nozzle pressure drop increases by a particular value, the pressurization value in the hole also increases by the same value, e.g., if the nozzle pressure drop increases by 5 MPa, the pressurization in the hole increases by 1.74 MPa. The relative increase in the nozzle pressure drop is the same as that of the pressurization in the hole (Table 3.3).

Fig. 3.18 shows the effect of the nozzle pressure drop on the axial pressure of the hole. Regardless of the nozzle pressure drop, the axial pressure decrease rate is quite high, and the axial pressure tends to be stable at 70–80 mm after injection. In addition, quantitative analysis indicates that the increase in axial pressure is consistent with the increase in the nozzle pressure drop by the same value. Comparison of Figs. 3.17 and 3.18 shows

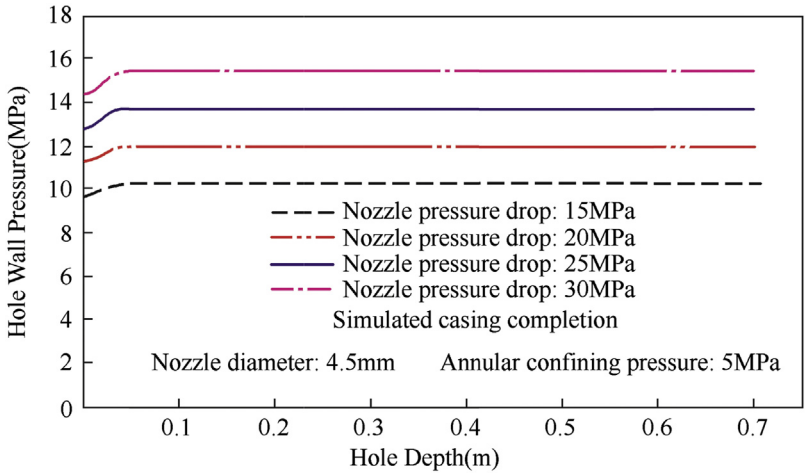

Figure 3.17 Effect of the nozzle pressure drop on the wall pressure.

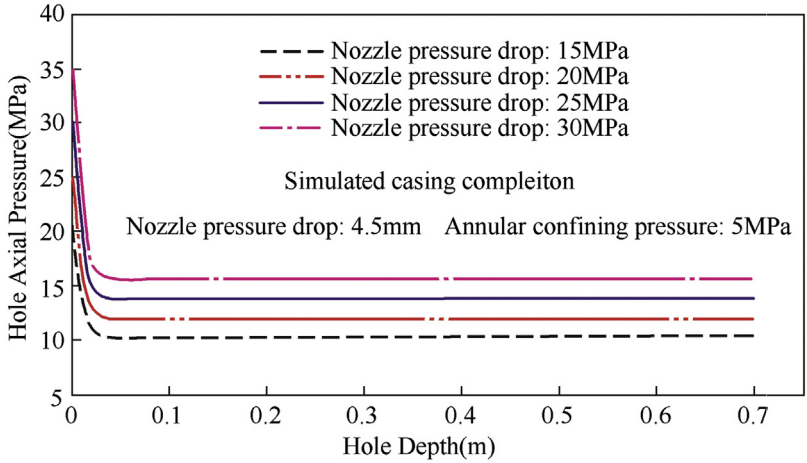

Figure 3.18 Effect of the nozzle pressure drop on the axial pressure.

Table 3.3 Statistical table of pressurization of the hole with different nozzle pressure drops

Nozzle pressure drop (MPa)	15	20	25	30
Stagnation zone pressure on hole wall (MPa)	10.23	11.97	13.71	15.45
Pressurization in hole (MPa)	5.23	6.97	8.71	10.45
Nozzle pressure drop relative increase (%)	/	25	20	16.7
Pressurization relative increase (%)	/	24.97	19.98	16.65

that the hole axial pressure and wall pressure are equal under the same nozzle pressure drop, which also confirms that the pressure of the stagnation zone is constant.

In addition, the decay length of the axial pressure is approximately the same (70—80 mm), indicating that the nozzle pressure drop marginally affects the jet attenuation, and despite the large difference in the nozzle pressure drop, with increasing jet distance, the zone axial pressure difference is significantly reduced. This result also reflects that the confining pressure significantly affects the jet after it leaves the nozzle. As long as the confining pressure is the same, irrespective of the nozzle pressure drop, the final axial pressure is similar.

3.1.3.2.2 Effect of the Confining Pressure on the Pressure Distribution of the Hole in Open Hole Wells

Figs. 3.19 and 3.20 show the variation in the wall pressure and axial pressure of the borehole under different nozzle pressure drop conditions. The same result is observed as in the case of the casing hole: the higher the nozzle pressure drop, the higher the wall pressure of the hole stagnation zone. Quantitative analysis also found that in the open hole, the nozzle pressure drop

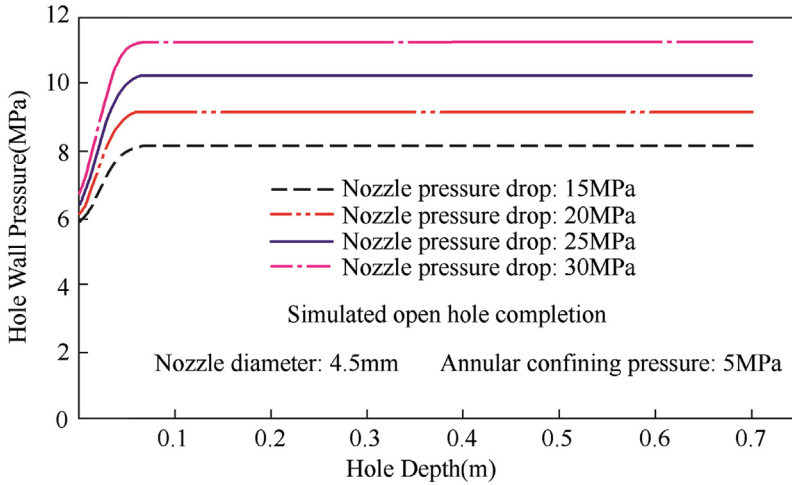

Figure 3.19 Effect of the nozzle pressure drop on the wall pressure.

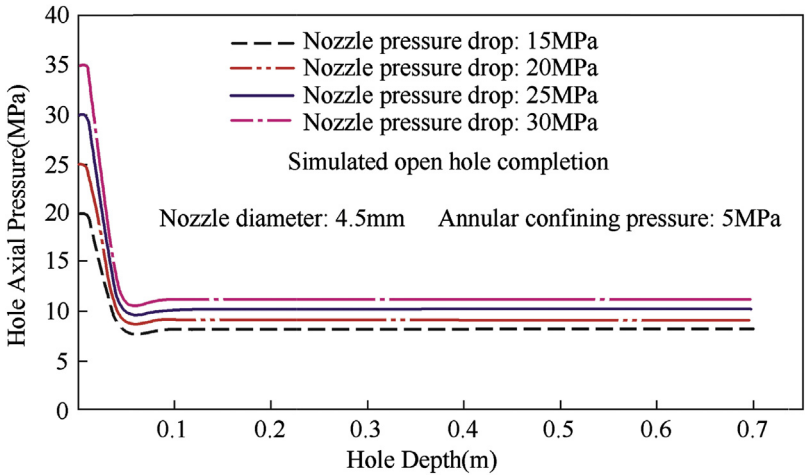

Figure 3.20 Effect of the nozzle pressure drop on the axial pressure.

increases for each additional 5 MPa and the hole pressurization increases to 1.04 MPa; as for the same confining pressure, if the nozzle pressure drop increases by the same value, then the increase of the hole pressurization is also constant.

However, the slope of the axial pressure curve in the open hole is far less than that of the corresponding curve in the casing hole, and the attenuation range of the jet in the open hole is 90—110 mm. This result indicates that under the same nozzle pressure drop, the decay rate of the jet in the open hole is generally less than that of the casing hole, that is, the squeezing of the surrounding fluid to the jet is weakened because the borehole of the open hole well does not exhibit the baffle effect produced by the casing; the exit size of the flow system increases; the fluid is no longer subject to fluid disturbance caused by the casing wall reflection; the energy loss is small, and the squeeze effect of the surrounding fluid to the jet is weakened.

3.1.3.3 Effect of the Inlet Ratio on Pressure Distribution of the Hole

The inlet diameter of the hole is determined by the nozzle diameter and the standoff distance. The larger the nozzle diameter, the larger the inlet diameter of the hole. Therefore the effects exerted by the nozzle diameter and inlet diameter on the pressure distribution in the hole are not independent and must be considered simultaneously.

To simultaneously consider the effect of these two factors, a dimensionless number d/D (the ratio of nozzle diameter and casing hole diameter) is formulated to characterize the effect of these two factors. This dimensionless number represents the ratio of the feature size of the inlet to the feature size of the aperture, which can reflect the relative size of the inlet and outlet cross-sections, defined as the "inlet ratio." The pressure distributions of the hole at six inlet ratios were numerically simulated (Table 3.4).

3.1.3.3.1 Effect of the Confining Pressure on Pressure Distribution of the Hole in Casing Wells

Fig. 3.21 shows the variation in the wall pressure with the inlet ratio. The greater the inlet ratio, the higher the wall pressure, that is, the supercharging

Table 3.4 Relationship between the inlet ratio and nozzle diameter

Nozzle diameter d (mm)	4.5	5.0	5.5	6.0	6.5	7.0
Inlet diameter D (mm)	10	10	15	15	20	20
Inlet ratio (d/D)	0.45	0.50	0.37	0.40	0.325	0.35

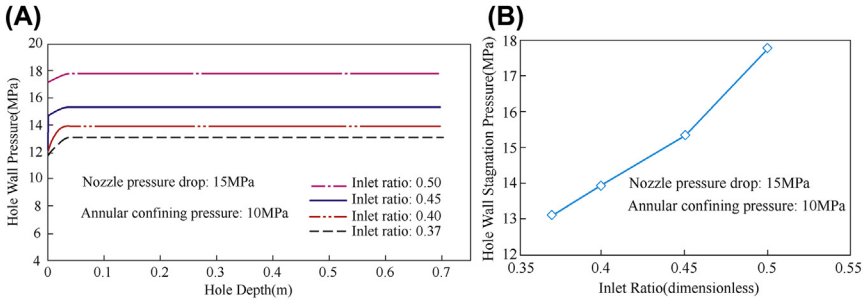

Figure 3.21 (A) Effect of the inlet ratio on the wall pressure. (B) Influence of inlet ratio on the wall pressure.

effect is better. The reason is as follows: for the same nozzle pressure, the greater the inlet cross-section (the nozzle diameter), the greater the inlet flow rate; from the law of the conservation of mass, the exit velocity also increases. A high exit velocity will increase the inertia of the water stagnation effect, thereby increasing the conversion efficiency of kinetic energy to the pressure energy and improving the supercharging effect.

3.1.3.3.2 Effect of the Confining Pressure on the Pressure Distribution of the Hole in Open Hole Wells

Combined with the experimental program, the effect of the inlet ratio on the hole wall pressure was simulated for nozzle diameters of Φ6.5 and Φ7.0 mm in the open hole wells (Fig. 3.22). The hole pressure of the open hole well increases with the increase in the inlet ratio. In addition, the mechanism by which the inlet ratio influences the hole pressure distribution is the same regardless of the well type.

3.1.3.4 Effect of the Hole Depth on the Pressure Distribution of the Hole

The hole depth is determined by the nozzle diameter and nozzle pressure drop irrespective of a casing or open hole well. The greater the nozzle diameter, the higher the nozzle pressure drop, and the stronger the breaking ability of the water jet, the greater the depth of perforation.

In this chapter, we compare and analyze the characteristics of the pressurization for three hole depths of 550, 600, and 700 mm. Fig. 3.23 shows the wall pressure distribution for different hole depths. The three wall pressure curves almost coincide; so long as the depth of the hole is greater than the length of the jet attenuation, the pressurization inside the hole is the same regardless of the hole depth.

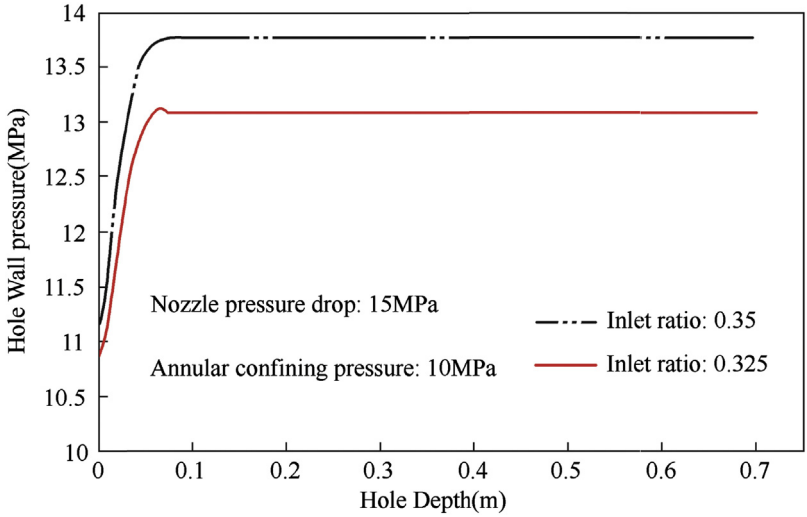

Figure 3.22 Effect of the inlet ratio on the wall pressure.

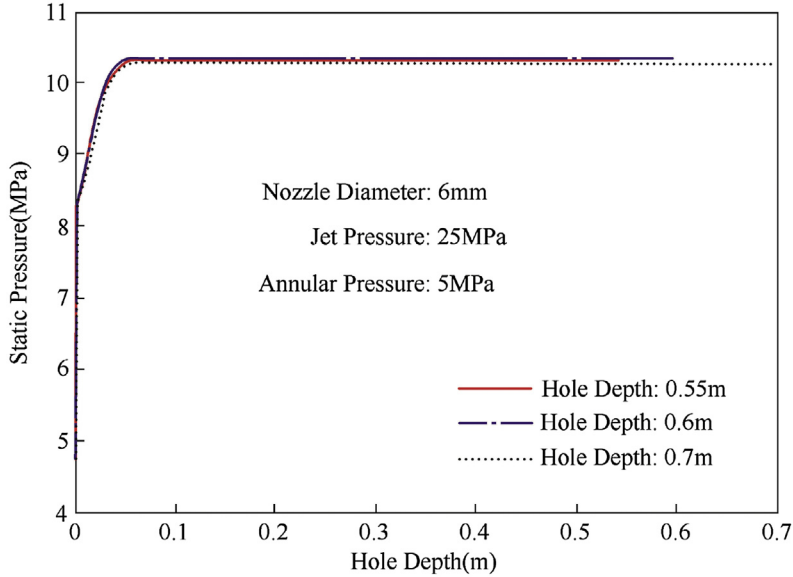

Figure 3.23 Effect of the hole depth on the wall pressure.

However, a deep perforation hole can reduce the formation fracture pressure; hence as far as possible a deep perforation hole must be obtained during the perforation, which is more conducive to crack formation and the extension of fracture.

3.2 EXPERIMENTAL STUDY FOR FLOW FIELD INSIDE THE HYDRA-JET HOLE

The hole pressure along the axis direction can be measured on the basis of the experiments conducted for the flow field of inside a hydraulic jet hole. On one hand, it could be used to validate the numerical simulation results; on the other hand, it can estimate the pressurization value inside the hole under actual flow conditions. In this study, the effect of six factors was examined on the pressure distribution inside the pore, and more than 250 sets of experimental data were obtained. By regression analysis of the experimental data, the empirical formulae of the pressurization in the jet hole corresponding to different nozzles were obtained. The formulae are expected to provide a theoretical reference for the design of hydraulic fracturing and control of the annulus pressure.

3.2.1 Experimental Equipment and Methods

3.2.1.1 Experimental Devices

The main factors affecting the pressure and jet pressurization in the hydraulic injection hole include annular ambient pressure, nozzle pressure drop, spray distance, nozzle diameter, casing wall hole diameter, and perforation hole depth. According to the experimental requirements, a platform for testing the flow field inside the hydraulic jet hole was designed and processed, and experimental devices were assembled (Fig. 3.24).

The experimental frame consists of a support, a nozzle, a pressure-regulating valve, a simulation casing wall, a simulation perforation hole, and a data acquisition/processing system, among others. The experimental frame can realize the following functions. The nozzle inlet pressure and ambient pressure in the central tube can be adjusted to a certain range. Nozzles and the simulated casing wall holes can be altered to change their diameters. The standoff distance can be changed by adjusting the screw. The simulated jetting holes are composed of a series of adjustable subcentering holes, the length and diameter of which can be varied, and pressure sensors are installed at the adjustable nipple, which can be used to measure the pressure of different perforation positions of the simulated jetting holes.

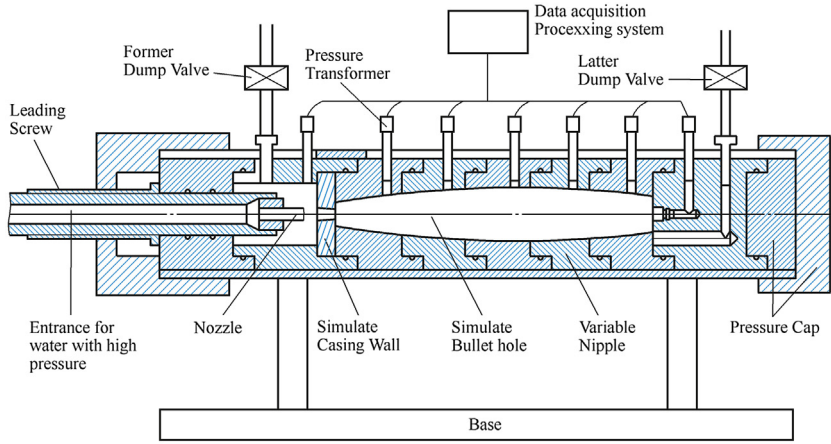

Figure 3.24 Schematic of the physical experimental setup.

Experimental device work capacity:

1. Ambient pressure: 5.0−25.0 MPa;
2. Inlet pressure: 5.0−40.0 MPa;
3. Diameter of the simulated hole: adjustable 20−60 mm;
4. Hole depth: adjustable 0−700 mm;
5. Number of sensors placed: 10−16 (data can be collected synchronously).

3.2.1.2 Experimental Principle

As shown in Fig. 3.25, to simulate hydraulic injection, the working fluid is pressurized by a high-pressure pump and passed to a nozzle through a high-pressure pipe, followed by ejection from the nozzle. Next, it passes through the simulated casing wall hole into the simulated perforation hole.

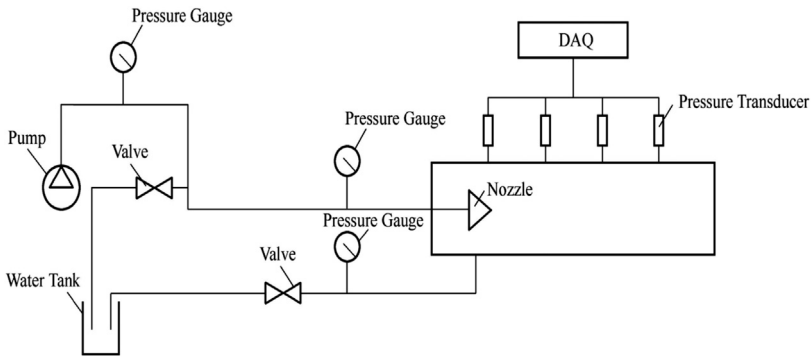

Figure 3.25 Schematic of the experimental system.

By regulating the overflow valve, the inlet pressure of the nozzle can be changed. By adjusting the pressure-regulating valve of the nozzle, the ambient pressure of the nozzle outlet can be changed. By adjusting the screw, the standoff distance (the distance between nozzle and simulated casing wall) can be changed. By combining different adjustable nipples, the different sizes and depths of the simulated perforating holes can be obtained.

3.2.1.3 Experimental Scheme

Laboratory experiments were carried out to examine the hole pressure distribution and the regularity of pressurization under a perforation depth of 500—700 mm. The other parameters that can be changed in the experiment are spray distance, nozzle inlet pressure, nozzle ambient pressure, nozzle diameter, hole diameter of simulated casing wall, and the size and depth of the simulated perforation hole. The detailed experimental scheme is as follows:

The pore pressure distribution was measured at a hole depth of 500 mm. The short section (20, 24, 28, 32, 36, 40, 44, 48, 52, 56, 60, and 56 mm in diameter and 40 mm in length) was installed in turn, followed by a pressure-measuring plug.

1. Nozzle, with a diameter of 4.5 mm, is installed. The simulated casing wall hole is 10 mm. The following experiments are performed:
   a. Standoff distance 15 mm, without ambient pressure. The back valve is completely closed, and the front valve is open.
      Adjust the overflow valve and change the nozzle inlet pressure to 15, 20, 25, 30, and 35 MPa and measure the hole pressure under various cases.
   b. Standoff distance is 15 mm. The ambient pressure is 5, 10, 15, and 20 MPa. The ambient pressure is achieved by adjusting the front valve. The back valve is completely closed. The nozzle inlet pressure is varied under different ambient pressures. The hole pressure is measured under different ambient pressures and nozzle inlet pressures.
   c. Adjust the spraying distance to 20 and 25 mm; repeat steps (1) and (2).
2. Replace the nozzles of 5, 5.5, 6, 6.5, and 7 mm. Repeat step 1, where 5.5- and 6-mm nozzles are replaced with the 15-mm simulated casing wall perforations, and 6.5- and 7-mm nozzles are replaced with 20-mm simulated casing wall perforations.

Measure the hole pressure distribution at a hole depth of 580 mm. After the sub of the last inner diameter of 56 mm in (a), subs of 52 mm diameter and 48 mm diameter are sequentially added, followed by the pressure-measuring plug; the steps 1 and 2 are repeated.

Measure the hole pressure distribution at a hole depth of 660 mm. After the sub of the last inner diameter of 48 mm in (b), subs of 44 mm diameter and 32 mm diameter are sequentially added, followed by the pressure-measuring plug; repeat steps 1 and 2 in (a).

Measure the hole pressure distribution at a hole depth of 700 mm. After the sub of the last inner diameter of 48 mm in (c), sub of 20 mm diameter is added; repeat steps 1 and 2 in (a).

Table 3.5 shows the combination of the parameter selection of this experiment. As a result, the experiment provided more than 250 groups of experimental data for the hole pressure distribution.

3.2.2 Analysis of Experimental Results

The experimental results were analyzed by examining the effects of the ambient pressure, nozzle pressure drop, standoff distance, inlet ratio, and perforation depth. The experiments estimated the pressure distribution of the hole and the law of jet pressurization. The correlation of jet pressurization for different diameter nozzles is obtained by linear regression.

3.2.2.1 Effect of Experimental Parameters on the Hole Pressure Distribution

3.2.2.1.1 Effect of Ambient Pressure on the Pressure Distribution of the Hole

Taking the 5-mm nozzle as an example, Figs. 3.26 and 3.27 show the pressure distribution curve and jet supercharging curve of the 5-mm nozzle under different ambient pressures, respectively.

Table 3.5 Hydraulic jet fracturing experiment scheme parameter table

Nozzle diameter (mm)	Inlet pressure (MPa)	Ambient pressure (MPa)	Jetting pressure (MPa)	Casing wall hole diameter (mm)	Hole depth (mm)
4.5	15—35	0—20	15, 20, 25	10	500—700
5.0	15—30	0—15	15, 20, 25	10	500—700
5.5	15—25	5—10	15, 20, 25	15	500—700
6.0	15—25	5—10	15, 20, 25	15	500—700
6.5	15—20	0—5	15, 20, 25	20	500—700
7.0	15—20	0—5	15, 20, 25	20	500—700

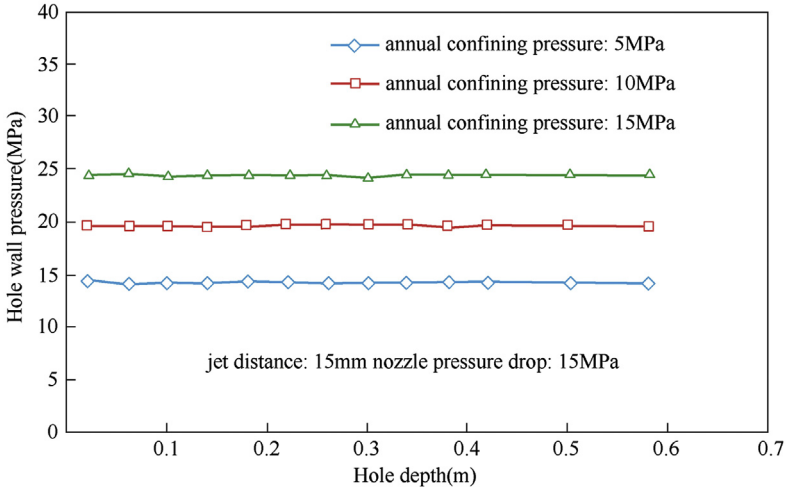

Figure 3.26 Effect of the confining pressure on the wall pressure distribution.

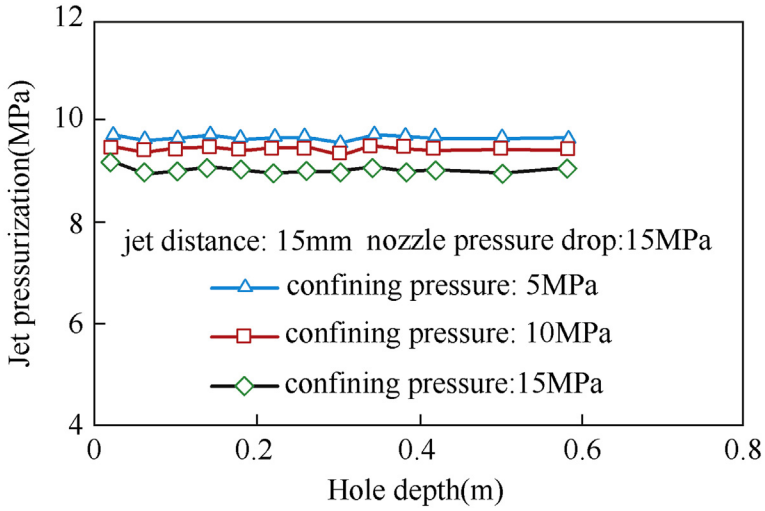

Figure 3.27 Effect of the confining pressure on the jet.

As shown in Fig. 3.26, under the same conditions, with increasing ambient pressure, the hole pressure increases. When the ambient pressure value is 5 MPa, the hole pressure value is 14.31 MPa. When the ambient pressure value is 10 MPa, the hole pressure value is 19.57 MPa. When the ambient pressure value is 15 MPa, the hole pressure reaches 24.56 MPa.

Fig. 3.27 shows the hole supercharging curve for a nozzle diameter of 5 mm and a nozzle pressure drop of 15 MPa. Under the same conditions, with increasing ambient pressure, there is no obvious change in the hole supercharging value. When the ambient pressure is 5 MPa, the hole supercharging value is approximately 9 MPa. When the ambient pressure is 10 MPa, the hole supercharging is approximately 9.3 MPa. When the ambient pressure is 15 MPa, the hole supercharging value is approximately 9.6 MPa. Under the same conditions, with the increasing ambient pressure, the amplitude of jet pressurization is approximately unchanged, which is consistent with the results of numerical simulation. When the nozzle diameter is 5 mm, the nozzle pressure drop is 15 MPa, the standoff distance is 15 mm, and the jet pressurization value under different ambient pressures is approximately 9.4 MPa; hence the ambient pressure marginally affects the jet pressurization.

3.2.2.1.2 Effect of the Nozzle Pressure Drop on the Pressure Distribution of the Hole

Taking the diameter of Φ4.5-mm nozzle as an example, Figs. 3.28 and 3.29 show the pressure distribution curve and jet pressurization curve of the 4.5-mm nozzle under different nozzle pressure drop conditions, respectively.

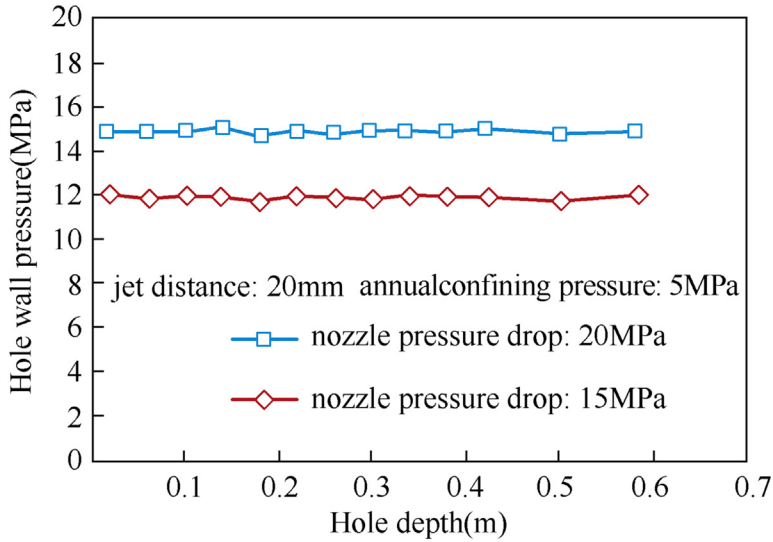

Figure 3.28 Influence of nozzle pressure drop on wall pressure distribution.

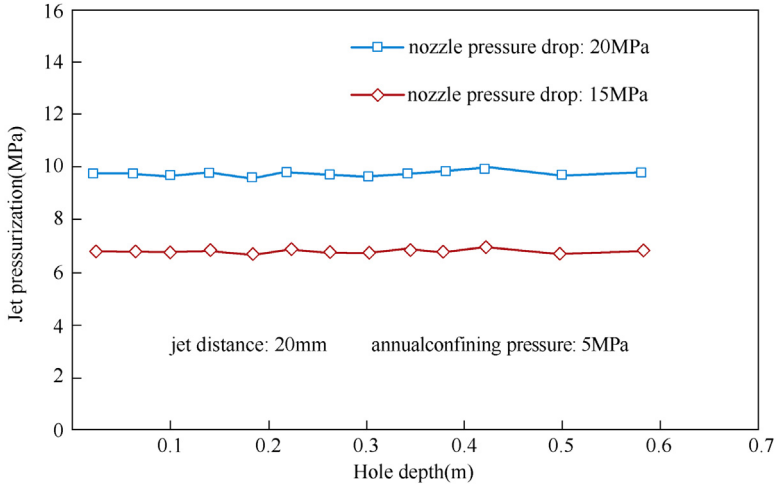

Figure 3.29 Effect of the nozzle pressure drop on jet pressurization.

From the figure, with the increase in the nozzle pressure drop, the hole pressure and jet pressurization also increase. Under the experimental conditions, when the nozzle pressure drop is 15 MPa, the hole pressure is 11.8 MPa and the jet pressurization is approximately 6.8 MPa. When the nozzle pressure drop is 20 MPa, the hole pressure is 14.9 MPa, and the jet pressurization is 9.9 MPa. The nozzle pressure drop considerably affects the jet pressurization. Jet pressurization is essentially the conversion of the kinetic energy of the high-velocity fluid at the nozzle exit to the hydrostatic pressure of the fluid in the perforation channel. The larger the nozzle pressure drop, the larger the kinetic energy of the fluid at the exit, and the larger the hydrostatic pressure of the fluid in the perforation channel; hence jet pressurization is high.

3.2.2.1.3 Effect of Standoff Distance on the Hole Pressure Distribution

Taking the diameter of Φ5.5-mm nozzle as an example, Figs. 3.30 and 3.31 show the pressure distribution curve and the jet pressurization curve using the 5.5-mm nozzle with different standoff distances, respectively.

As can be seen from the figure, under the experimental conditions, although the standoff distance increases, the hole pressure and jet pressurization exhibit negligible changes, the hole pressure is maintained at approximately 8 MPa, and the jet pressurization is 3 MPa. Under the experimental conditions, the jet standoff distance marginally affects the hole pressure distribution and jet pressurization.

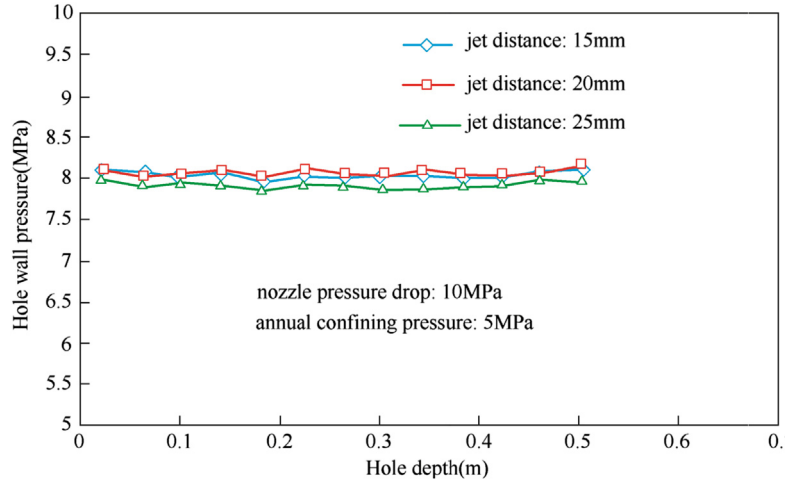

Figure 3.30 Effect of the jet distance on wall pressure distribution.

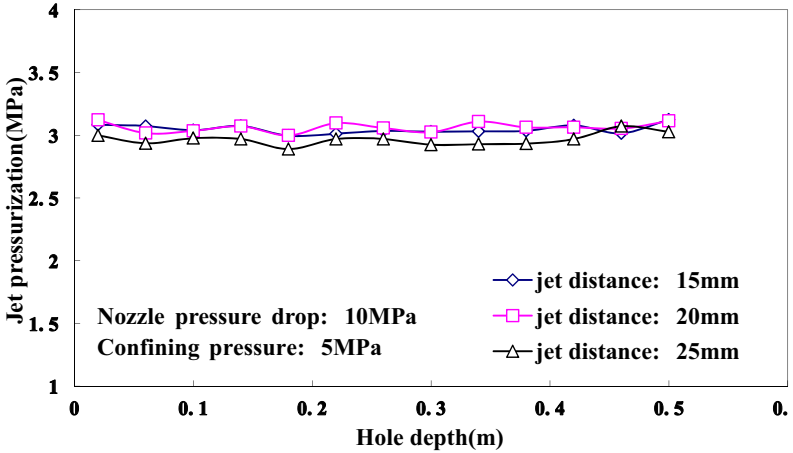

Figure 3.31 Influence of jet distance on jet pressurization.

3.2.2.1.4 Effect of the Inlet Ratio on the Hole Pressure Distribution

Fig. 3.32 shows the hole pressure distribution at different inlet ratios. Under the same conditions of nozzle pressure drop, ambient pressure, and standoff distance, the larger the inlet ratio and wall pressure of the hole, more evident is the supercharging effect. Under the experimental conditions, when the inlet ratio is 0.4, the hole pressure achieves the maximum value of 11.2 MPa. When the inlet ratio is 0.37, the hole pressure is 10.7 MPa.

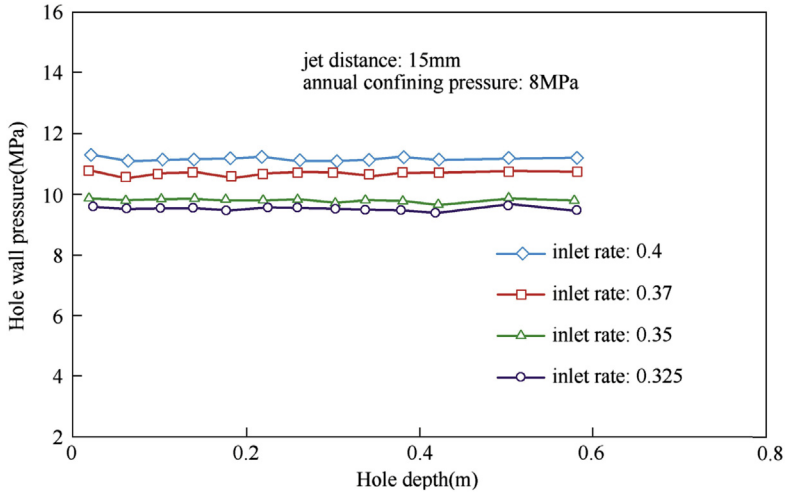

Figure 3.32 Effect of the inlet ratio on the wall pressure distribution.

When the inlet ratio is 0.35, the hole pressure is 9.9 MPa. When the inlet ratio value is 0.325, the minimum hole pressure value is 9.6 MPa.

Figs. 3.33 and 3.34 show the jet pressurization curve at different inlet ratios. When the inlet ratio value is 0.4, the nozzle jet pressurization value achieves the maximum value of 3.2 MPa. When the inlet ratio is 0.325,

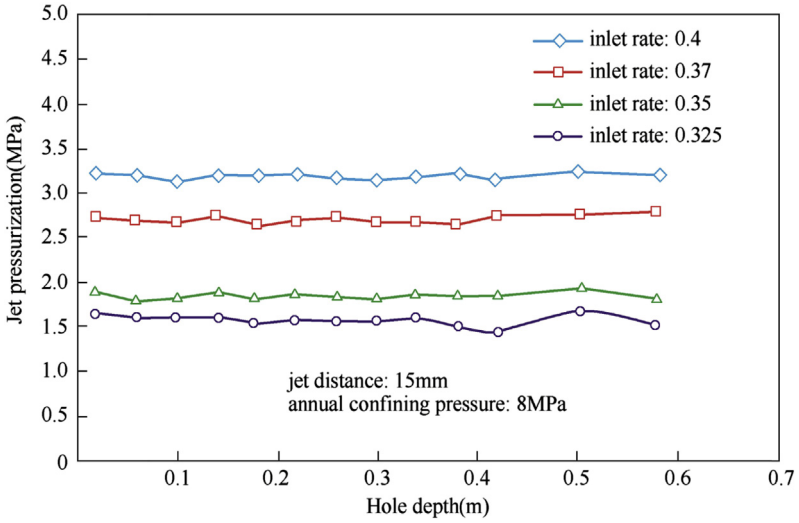

Figure 3.33 Effect of the inlet ratio on jet pressurization.

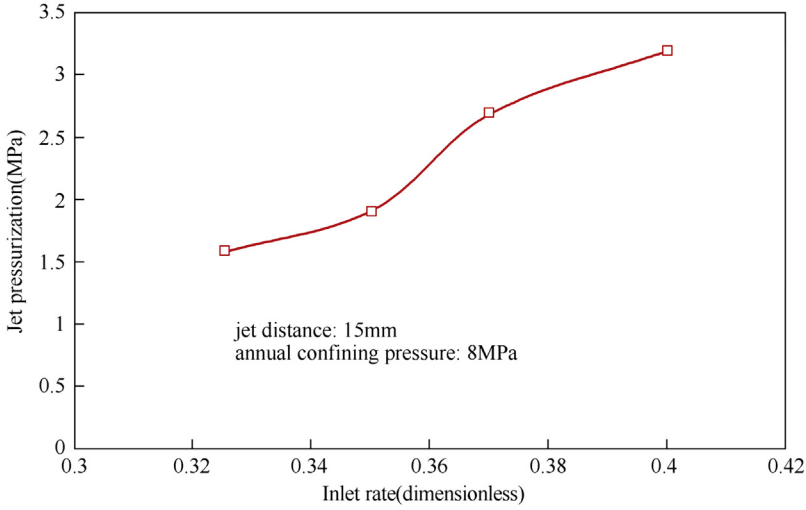

Figure 3.34 Effect of the pressurization at different inlet ratios.

the nozzle pressurization effect is the minimum, 1.6 MPa. Under the same conditions, when the inlet ratio increases, the pressure in the hole increases, the jet supercharging pressure increases, and the supercharging effect becomes more obvious.

3.2.2.1.5 Effect of Hole Depth on Hole Pressure Distribution

Figs. 3.35 and 3.36 show the hole pressure distribution curve and the jet pressurization curve for 5.5-mm nozzle at different perforation hole depths,

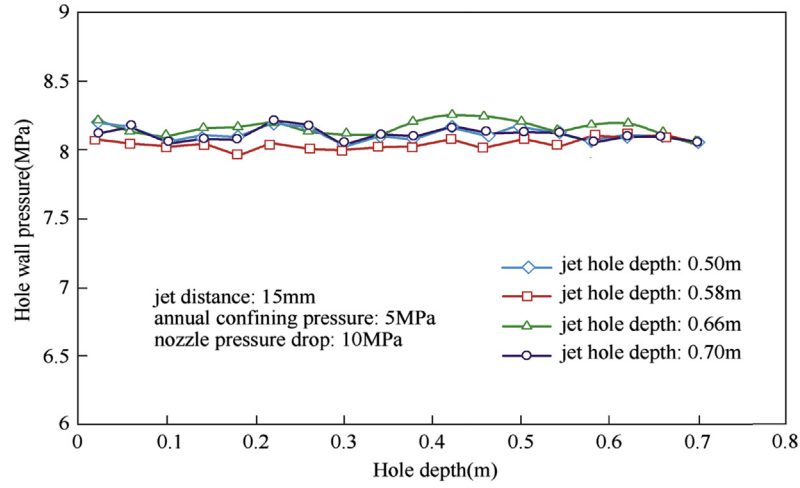

Figure 3.35 Effect of the hole depth on the wall pressure distribution.

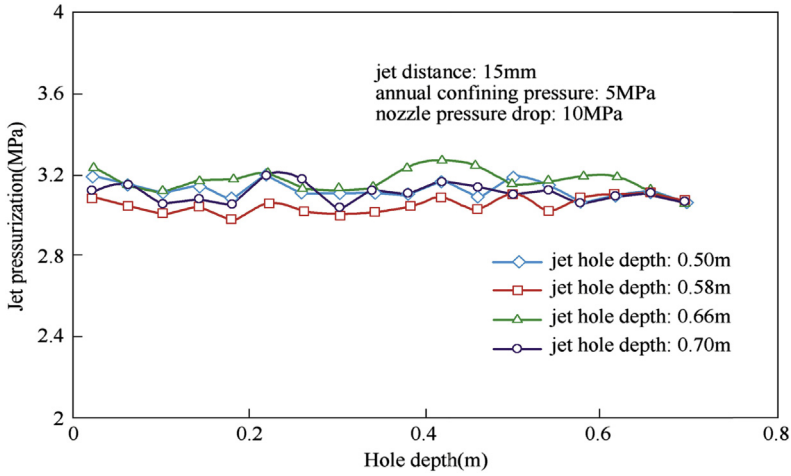

Figure 3.36 Effect of the hole depth on jet pressurization.

respectively. With the increase in the perforation depth from 0.50 to 0.70 m, the hole pressure and jet supercharging are almost unchanged, the pressure in the hole is approximately 8.1 MPa, and the supercharging pressure is approximately 3.1 MPa.

3.2.2.2 Pressurization Formula in the Jet Hole

Numerical simulation and experimental results indicate that the jet pressurization of nozzles with different diameters under different nozzle pressure drops is linear.

As shown in Fig. 3.37, the *x*- and *y*-axes show the nozzle pressure drop and jet pressurization, respectively, and the data points represent the nozzle

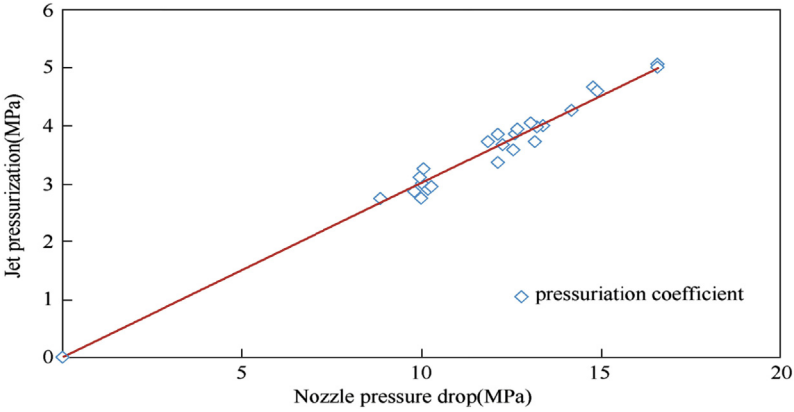

Figure 3.37 Pressurization curve with a diameter of Φ5.5-mm nozzle jet.

pressure drops with the diameter of Φ5.5-mm nozzle under different jet pressurization values. From the figure, the data show a linear distribution. A linear regression is performed to those points, and a straight line passing the origin is obtained, with a slope of 0.3033.

By defining the ratio of jet pressurization and nozzle pressure drop as the supercharging index, the slope of the line in the figure corresponds to the supercharging index value for the nozzle with a 5.5 mm diameter. The supercharging index is essentially the conversion efficiency of the jet fluid from kinetic energy into the static pressure energy. According to the experimental data, the supercharging index of six types of nozzles with various nozzle diameters was subjected to regression analysis.

Fig. 3.38 shows the curves of jet pressurization and nozzle pressure drop after the linear regression of nozzles with different diameters. As can be observed from the figure, the diameter of Φ5.0-mm nozzle corresponds to the largest supercharging index (Tian, Li, Huang, Niu, & Xia, 2008). The diameter of Φ6.5-mm nozzle corresponds to the minimum supercharging index. Hence, no obvious rules are available between the supercharging index and the nozzle diameter. In fact, the supercharging index is related to the nozzle inlet ratio. The greater the inlet ratio, the higher the supercharging index.

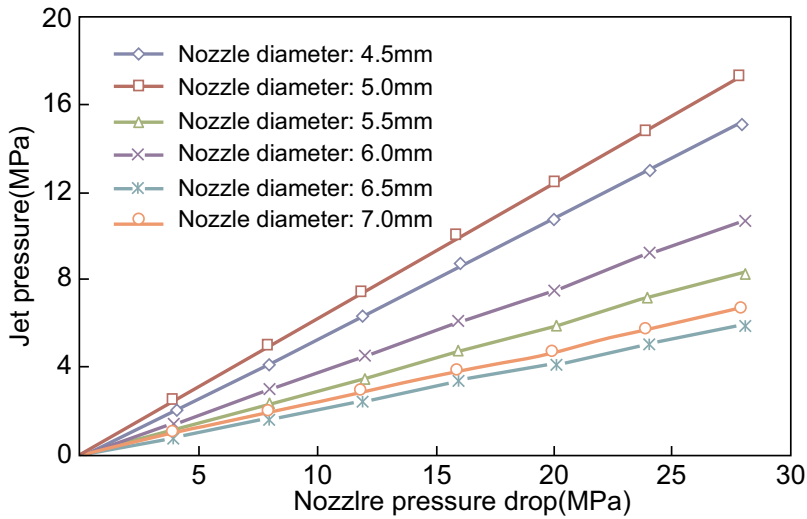

Figure 3.38 Injection curve of jet with different diameters.

The jet pressurization formula can be obtained according to the nozzle pressure drop formula. Taking the diameter of Φ4.5-mm nozzle as an example, the hole pressurization value is expressed as follows:

$$\Delta P = 0.5441 P_b \tag{3.1}$$

where P_b is the nozzle pressure drop in MPa.

By substituting the nozzle pressure drop formula into the previous equation (Wang et al., 1991),

$$\Delta P = 0.5441 \times 513.559 \frac{\rho Q^2}{C^2 A^2} \tag{3.2}$$

where Q is the displacement in L/s, ρ is the fluid density in g/cm^3, A is the total nozzle area in mm^2, and C is the nozzle orifice coefficient, generally taken to be 0.9.

For the diameter of Φ4.5-mm nozzle, the nozzle area in Eq. (3.2) is known; hence, the expression for jet pressurization (Hwang & Irons, 2012) for the diameter of Φ4.5-mm nozzle is expressed as follows:

$$\Delta P = 1.1047 \frac{\rho Q^2}{C^2} \tag{3.3}$$

Similarly, the correlation for the change in the other nozzle jet pressurization with variation of the flow rate can be obtained (Table 3.6).

Fig. 3.39 shows the relationship between the jet pressurization and the flow rate variation for nozzles with different diameters. As can be observed from the figure, using the same nozzle diameter, when the flow rate increases, the jet pressurization also increases. Under the same flow rate condition, when the nozzle diameter increases, the jet pressurization decreases.

Table 3.6 Jet pressurization formulae for different diameter nozzles

Nozzle diameter (mm)	Jet pressurization formulae
4.5	$\Delta P = 1.1047 \frac{\rho Q^2}{C^2}$
5	$\Delta P = 0.8258 \frac{\rho Q^2}{C^2}$
5.5	$\Delta P = 0.2759 \frac{\rho Q^2}{C^2}$
6	$\Delta P = 0.2464 \frac{\rho Q^2}{C^2}$
6.5	$\Delta P = 0.1010 \frac{\rho Q^2}{C^2}$
7	$\Delta P = 0.0839 \frac{\rho Q^2}{C^2}$

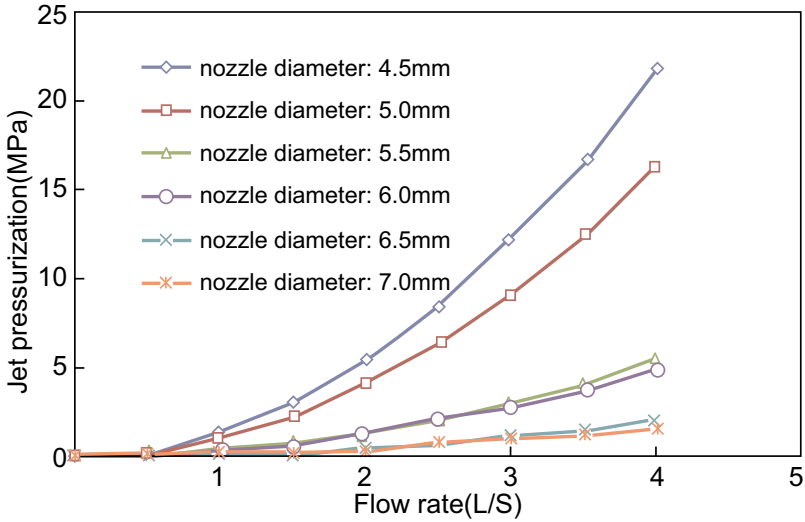

Figure 3.39 Jetting pressurization versus the flow rate variation with different diameter nozzles.

REFERENCES

Gong, J. F., Huang, Z. W., Li, G.-S., & Nie, J.-L. (2007). Auxiliary fracturing and sand pack mechanism of hydraulic abrasive perforation and its field test. *Journal of Oil and Gas Technology, 29*, 136–139.

Han, Z. Z., Wang, J., & Lan, X. P. (2004). *FULENT fluid engineering simulation calculations and application*. Beijing: Beijing Institute of Technology Press.

Huang, Z., Li, G., Niu, J., & Luo, H. (2008). Application of abrasive water jet perforation assisting fracturing. *Petroleum Science and Technology, 26*(6), 717–725.

Huang, Z., Li, G., Tian, S., Shen, Z., & Luo, H. (2008). Mechanism and numerical simulation of pressure stagnation during water jetting perforation. *Petroleum Science, 5*(1), 52–55.

Hwang, H. Y., & Irons, G. A. (2012). A water model study of impinging gas jets on liquid surfaces. *Metallurgical and Materials Transactions B, 43*(2), 302–315.

Li, G., Huang, Z., Tian, S., Niu, J., Qu, H., & Sheng, M. (2010). Investigation and application of multistage hydrajet-fracturing in oil and gas well stimulation in China. In *International Oil and Gas Conference and Exhibition in China*. Society of Petroleum Engineers.

Li, G., Huang, Z., Tian, S., & Shen, Z. (2010). Research and application of water jet technology in well completion and stimulation in China. *Petroleum Science, 7*(2), 239–244.

Qu, H., Li, G., Huang, Z., & Tian, S. (2010a). Boosting mechanism in hydrajet-fracturing cavity. *Zhongguo Shi You Daxue Xuebao/Journal of China University of Petroleum: Edition of Natural Science, 34*(5), 73–76.

Qu, H., Li, G., Huang, Z., & Tian, S. (2010b). The boosting mechanism and effects in cavity during hydrajet fracturing process. *Petroleum Science and Technology, 28*(13), 1345–1350.

Tian, S.-C., Li, G.-S., Huang, Z.-W., Niu, J.-L., & Xia, Q. (2008). Hydrojet-fracturing technology with coiled tubing. *Natural Gas Industry, 8*, 020.

Tian, S., Li, G., Huang, Z., & Shen, Z. (2008). Research on hydrajet fracturing mechanisms and technologies. *Oil Drilling and Production Technology, 1*, 019.

Wang. (2004). *Principle and application of CFD software for computational fluid dynamics analysis (in Chinese)*. Beijing: Tsinghua University Press.

Wang, Cui, et al. (2006). *Fuild mechanics (in Chinese)*. Beijing: Petroleum Industry Press.

Wang, Han, et al. (1991). *Encyclopaedia of fluid mechanics (in Chinese)*. Beijing: Beijing University of Aeronautics and Astronautics Press.

Xia, Q., Huang, Z.-W., Li, G.-S., Zhao, Z.-F., Fu, G.-D., & Tian, S.-C. (2009). Experimental study on the law of jetting boost pressure in hydrajetting. *Fluid Machinery, 37*(2), 1—5.

Ya, Z., & Wang, B. (2005). Application of the reynolds stress model to the calculation of three-dimensional turbulent flow-field. *Journal of Aerospace Power, 20*(4), 572—576.

CHAPTER FOUR

Influence of Jetting Hole on Fracture Initiation and Propagation

Contents

Abstract

Jetting hole geometry parameters definitely influence the fracture initiation and propagation in materials. This chapter introduces the numerical simulation and true triaxial fracturing experiments on hydra-jet fracture initiation and propagation. The Rock Fracturing Process Analysis software was used to calculate the fracture crack pressure and propagation. The investigated key parameters included perforation diameter, perforation depth, and the angle between perforation axis and the maximum horizontal stress. The results showed that the initiation pressure decreased as both perforation depth and diameter rose. The initiation pressure increased with increase in the angle. To quantify the complex fracture geometry, the fractal theory was employed and the fractal dimension was calculated.

Keywords: Fracture initiation; Fracture propagation; Fracturing experiments; Jetting hole geometry; Numerical simulation.

Abrasive Water Jet Perforation and Multi-Stage Fracturing
ISBN: 978-0-12-812807-7
https://doi.org/10.1016/B978-0-12-812807-7.00004-2

4.1 NUMERICAL SIMULATION OF FRACTURE INITIATION AND PROPAGATION

Hydraulic fracturing crack and propagation is a complex none equilibrium and nonlinear evolution process (Yongquan, 2003). Investigation of hydraulic fracturing crack and propagation plays an important theoretical guidance in fracturing design and productivity evaluation (Yishan & Yequan, 2006). Meanwhile, the inhomogeneous and opaque rock mass formed during investigations made specimen crack and failure observation challenging. Even when it is simplified to homogeneous materials, the classical fracture mechanics analytical solution could be difficult to achieve. As a result, for solving crack propagation problems one often turns to numerical methods (Zhou, Guo, Zhao, & Deng, 2002). In this section, the Northeastern University Rock Fracturing Process Analysis software was selected and used to calculate fracture crack pressure and extension at various hydraulic perforating parameters to determine their roles. The resulting data may theoretically guide in current and future hydraulic jet fracturing design and operation.

4.1.1 Geometric Model and Boundary Condition

The base data of the numerical study are as follows:

Number of meshes: 200 × 200
Size of model: 1200 × 1200 mm
Compressive strength of rock: 100 MPa
Tensile strength of rock: 20 MPa
Modulus of elasticity: 50,000 MPa
Poisson's ratio: 0.25
Static pressure in perforation: 1500 m water
Loading rate: 90 m water/step
Frictional angle: 30 degrees

During testing, the standard fracture crack states that the first unit begins to damage. At this point and according to the Kaiser effect, the initiation fracture pressure might be determined using the acoustic emission figure.

4.1.2 Model Results

4.1.2.1 Influencing Factors of Crack Pressure

Relationship between perforation diameter and crack pressure

Fig. 4.1 shows the model of cross-perforation under different perforation diameters (12, 24, 30, 36, and 42 mm) and boundary conditions (respective

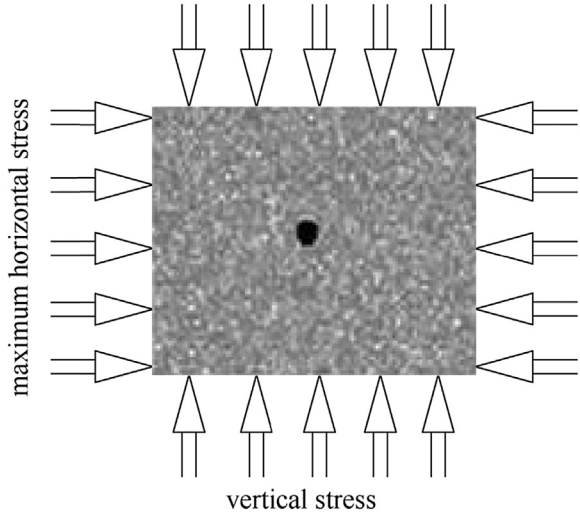

Figure 4.1 Scheme of the numerical study model I.

loading of maximum horizontal stress and vertical stress situations, and so on) (Pearson, Bond, Eck, & Schmidt, 1992). The relationship between the perforation diameter and crack pressure is depicted in Fig. 4.2. The acoustic emission graph of fracture crack and propagation at a perforation diameter of 24 mm is illustrated in Fig. 4.3.

As shown in Fig. 4.2, the fracture initiation pressure decreased quasilinearly as the perforation diameter gradually rose. When the perforation

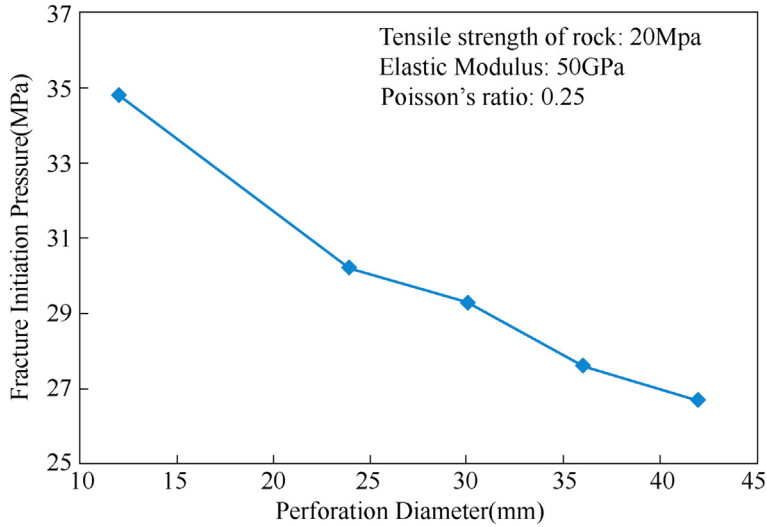

Figure 4.2 Variation of crack pressure as a function of perforation diameter.

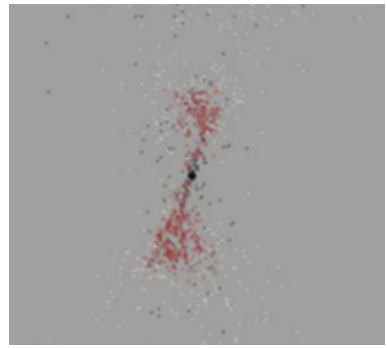

Figure 4.3 Acoustic emission graph at perforation diameter of 24 mm.

diameter increased from 12 to 42 mm, the crack pressure reduced from 34.8 to 26.7 MPa, equivalent to a 23% decline. Fig. 4.3 also revealed that the direction of fracture crack was perpendicular to the minimum principal stress.

Relationship between perforation depth and crack pressure

Fig. 4.4 shows the geometry of the computational model utilized. The diameter of perforation was set to 20 mm. The direction of perforation axis was consistent with the maximum horizontal stress. The perforation depths were set to 0.3, 0.5, 0.7, 0.9, 1.1, 1.3, and 1.5 m.

It will be noted that the crack pressure significantly reduced as the perforation depth rose (Fig. 4.5). When the perforation length increased from 0.3 to 0.3 m, the pressure was reduced by 19.5%. In conventional shaped charge shooting, an increase in the perforation depth from 0.5 to 0.9 m should induce a drop in crack pressure by 8.1%. For hydraulic perforation, the perforation depth could be set to more than 1.5 m and reach up to 2−3 m. For hydraulic fracturing in oil and water wells, the crack pressure was expected to reduce by more than 30% relative to conventional perforating, thereby lowering requirements for the ground manifold and the use of fracturing pumps. This, in turn, should reduce the cost and improve safety.

Fig. 4.6 represents the resulting acoustic emission graph at the perforation depth of 0.5 m.

Relationship between the angle (between perforation axis and maximum horizontal stress) and crack pressure

The perforation was ripped cut along the horizontal direction (Fig. 4.7), and the perforation depth was set to 0.5 m. The maximum horizontal stress was

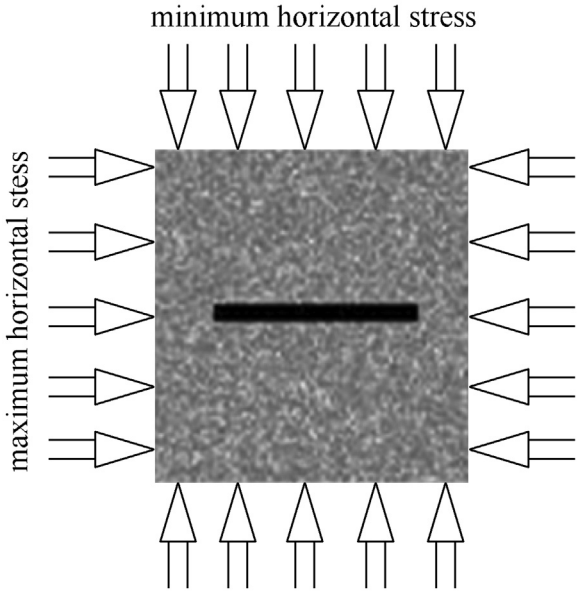

Figure 4.4 Scheme of the numerical study model II.

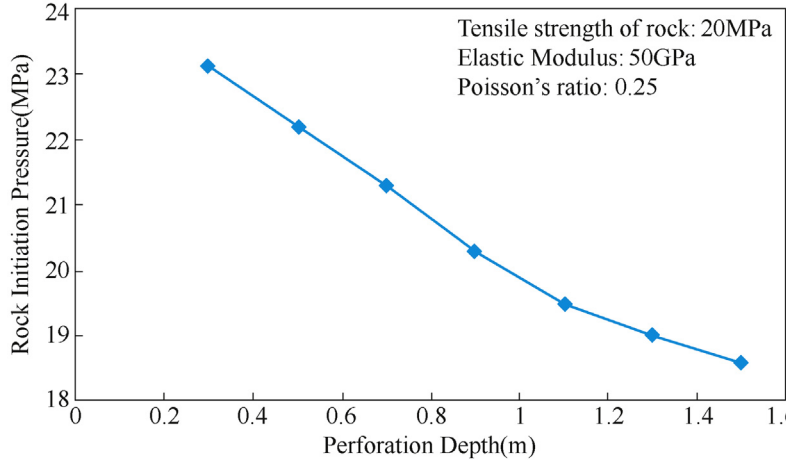

Figure 4.5 Variation of rock pressure as a function of perforation depth.

30 MPa, and the minimum horizontal stress was 25 MPa. The perforation diameter was 30 mm, and the angle α between the perforation axis and the maximum horizontal stress was set to 0, 10, 20, 40, 60, 80, and 90 degrees. The resulting crack pressure at different values of α is shown in Fig. 4.8. The crack pressure increased as the angle α rose from 0 to

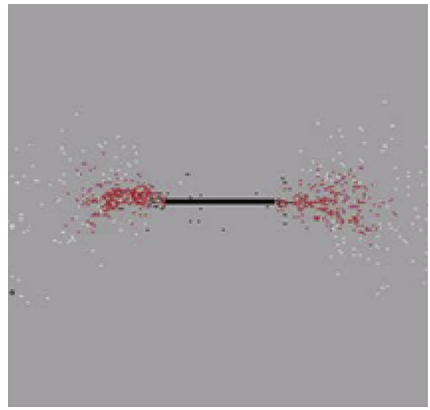

Figure 4.6 Acoustic emission graph for a perforation depth of 0.5 m.

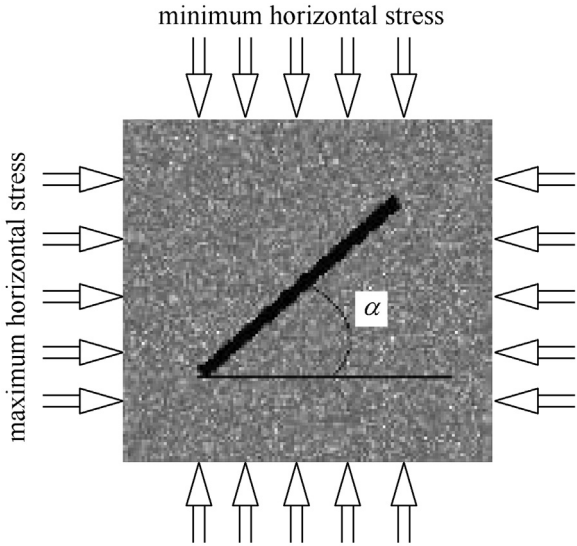

Figure 4.7 Scheme of the numerical study model III.

90 degrees. This variation tendency was consistent with the principle of minimum energy. That is, fractures are always cracking along the minimum energy consumption. Fig. 4.9A–D represents the crack acoustic emission curves at respective α angle fracture values. The principle can be confirmed by the direction of the fracture. In addition, it can be seen that as α angle rose, the crack pressure gradually increased but the crack position remained the same and always ended in the perforation (Fig. 4.9). This phenomenon might be related to the "piston effect" induced during the process of

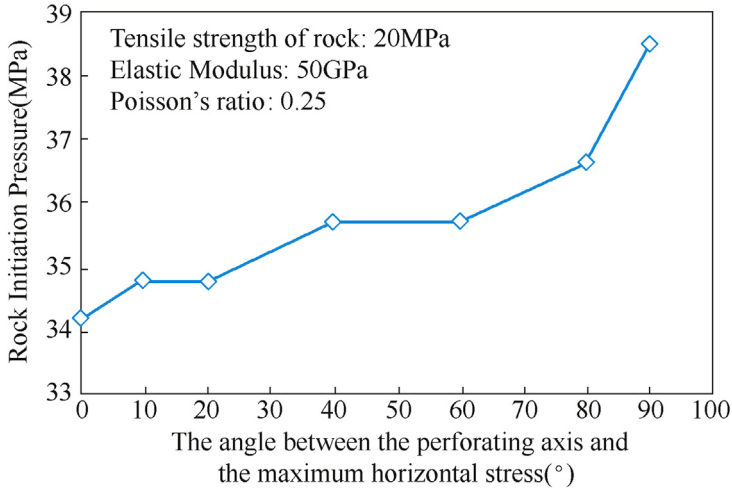

Figure 4.8 Variation of crack pressure with angle α.

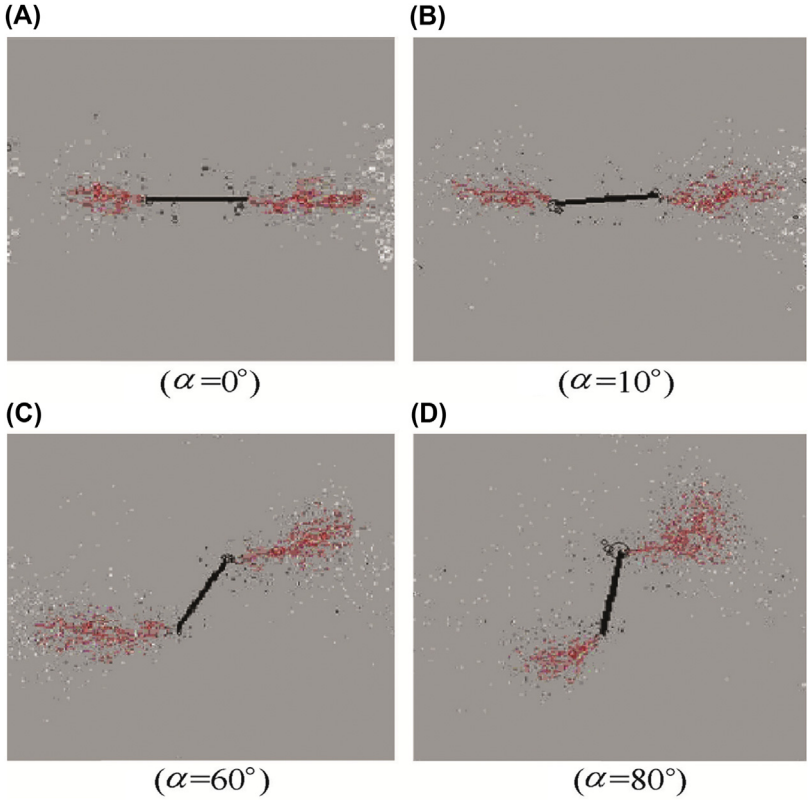

Figure 4.9 Acoustic emission graph under different α.

fracturing. In the narrow approximate round perforation channels, the fracturing fluid inflated the end of the perforationlike piston, resulting in the formation of first cracking at the end followed by propagation of the cracks.

Relationship between the vertical stress and crack pressure

The numerical model is depicted in Fig. 4.10. The perforation diameter was set to 24 mm, and the maximum horizontal stress was set to 20 MPa. The vertical stress values were 20, 25, 30, 35, 40, and 45 MPa. Fig. 4.11 illustrates the curve of crack pressure and vertical stress. It will be noted that the crack

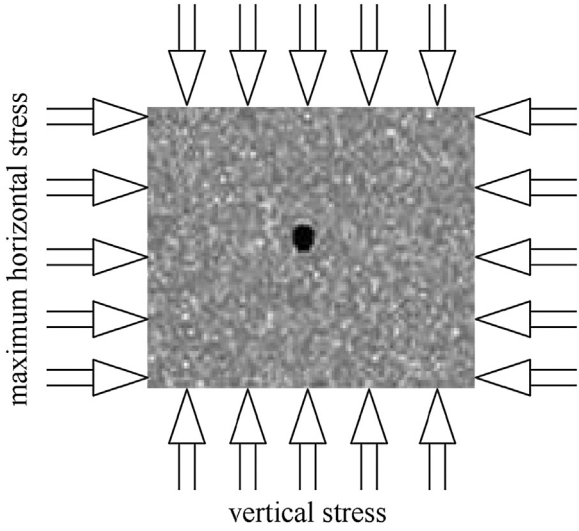

Figure 4.10 Numerical model.

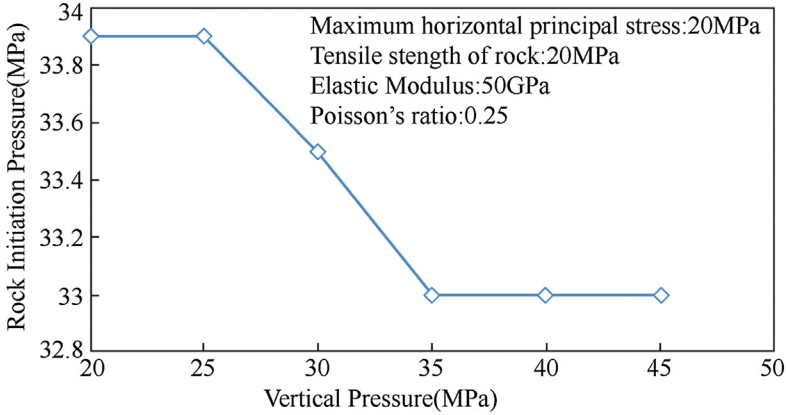

Figure 4.11 Curve of crack pressure versus vertical stress.

pressure declined as the stress ratio increased under biaxial stress. However, the overall change between the two parameters was not obvious. During the test, the vertical stress increased from 20 to 45 MPa and the crack pressure decreased by 0.9 MPa. This tendency suggested that the fracture crack needed only to overcome the constraints induced along the minimum stress direction and that there was little influence on the stress along the other directions. The acoustic emission graphs at horizontal and vertical stresses of 20 MPa are gathered in Fig. 4.12. The results confirmed that despite the significant changes in vertical stress, the resulting effect on crack stress was not significant but a greater influence on the crack propagation direction was noticed. At equal biaxial stress, the direction of crack and the expansion were random.

4.1.2.2 Fracture Morphology

The fracture morphology analyses were mainly performed from the acoustic emission figures. The red part of the acoustic emission represents the acoustic emission phenomenon in rock burst area under the Kaiser effect. It has to be noted that cracks were always extended along the direction of the maximum stress regardless of the changes in perforation parameters (Figs. 4.6, 4.9, and 4.12).

Fig. 4.12 clearly depicted that the direction of fracture expansion was random at equal biaxial stress. At the same time, the cracks were found concentrated at the end of the perforation and had a tendency to spread away from the perforation area.

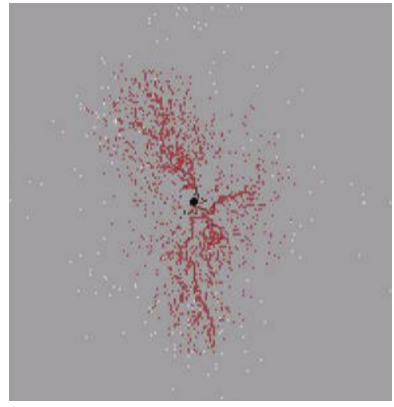

Figure 4.12 Acoustic emission graph.

During fracturing operation, the manager should prevent the spread of cracks to extend the crack propagation distance and avoid fracturing fluid loss (Guangqing, Mian, & YinYouquan, 2003). This was due to the small fracture width after the spread of cracks, which resulted in (1) higher flow resistance and fracture extension pressure, (2) early sand out, and (3) higher leakage rate where larger flow rates were required to continue the operation. Therefore multifractures near wellbore could be prevented or retarded, and the effect of efficient stimulation during fracturing operation could be improved using the hydraulic jet to form deeper perforation.

4.1.2.3 Effect of Model Size

To prevent the influence of model size on the numerical calculations, the effect of the model size was validated, and the physical model is shown in Fig. 4.10. The perforation diameter was set to 30 mm and the model size was set to 0.6 m × 0.6 m, 0.8 m × 0.8 m, 1.0 m × 1.0 m, 1.2 m × 1.2 m, 1.4 m × 1.4 m, and 1.6 m × 1.6 m. The relationship between the crack pressure and model size is illustrated in Fig. 4.13. The change in model size at fixed other parameters induced no effect on the calculation results at the size setting range.

4.2 EXPERIMENTAL STUDY

To gain a better understanding of the mechanism of fracture propagation, fracturing experiment is an important method worth exploring

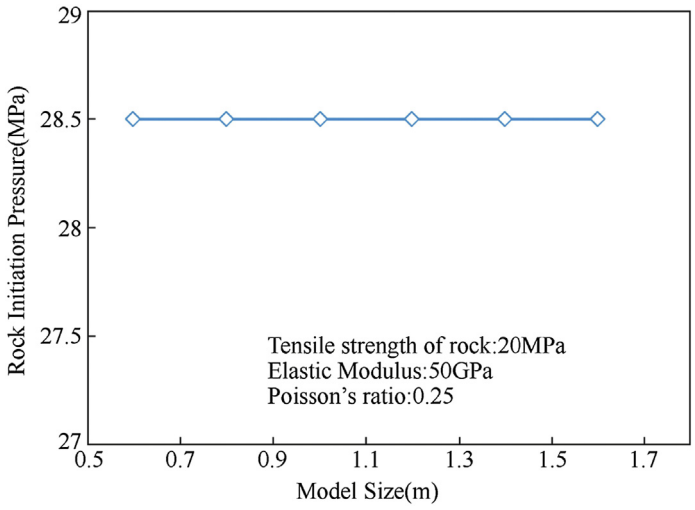

Figure 4.13 Crack pressure versus model size.

(Li et al., 2017). The simulation of fracturing experiments under reservoir conditions should allow monitoring the actual physical processes of fracture propagation and directly distinguish any formed fractures. In addition, various factors affecting the processes of fracture propagation could be studied, with the specific investigation of single parameters. This is of great significance to elucidate the mechanisms of fracture propagation.

In hydraulic fracturing simulations, the current models do not allow to accurately obtain all the parameters needed in crack propagation simulation. Also, it should be hard to grasp how exactly the parameters affect the fracture propagation (Gensheng, Li, Zhongwei, & Jilei, 2006). Thus the precision of the simulations becomes questionable. To circumvent these problems, the effect of most parameters on fracture initiation and extension was studied by means of the physical experiment using a sample size of $300 \times 300 \times 300$ mm.

4.2.1 Experimental Setup and Methods

4.2.1.1 Experimental Setup

The experimental equipment consisting of a large-sized true triaxial simulation system was designed and assembled at the Rock Mechanics Laboratory, China University of Petroleum, Beijing.

The equipment included a large-sized true triaxial experimental system, an MTS servo supercharger, Loca-ATl4 acoustic emission instrument, data acquisition system, voltage stabilizer, oil—water separator, and other auxiliary equipment. The volume capacity of the oil—water separator was 700 mL, and the loading capacity was 60 MPa. Before the experiment, the system was filled with the fracturing fluid, which could simultaneously fracture two rocks. The overall structure of the experimental system is shown in Fig. 4.14, and the physical maps of the liquid voltage regulator are shown in Fig. 4.15.

The experimental frame adopted a flat jack to apply rigid force to the side of the sample and the top surface. According to the characteristics of the hydraulic fracturing shown in Figs. 4.16 and 4.17, three pairs of flat jacks were used in one of the horizontal directions to simulate the crustal stress between the reservoir and both the upper and lower interlayers. Along the two other directions, a pair of flat jacks was placed to simulate the vertical crustal stress and the maximum horizontal crustal stress. Because the multichannel voltage source provided the flat jack with a hydraulic pressure, the pressure in each channel can be controlled and the maximum fluid pressure in each channel could reach 60 MPa. The direction of fracture propagation can artificially be

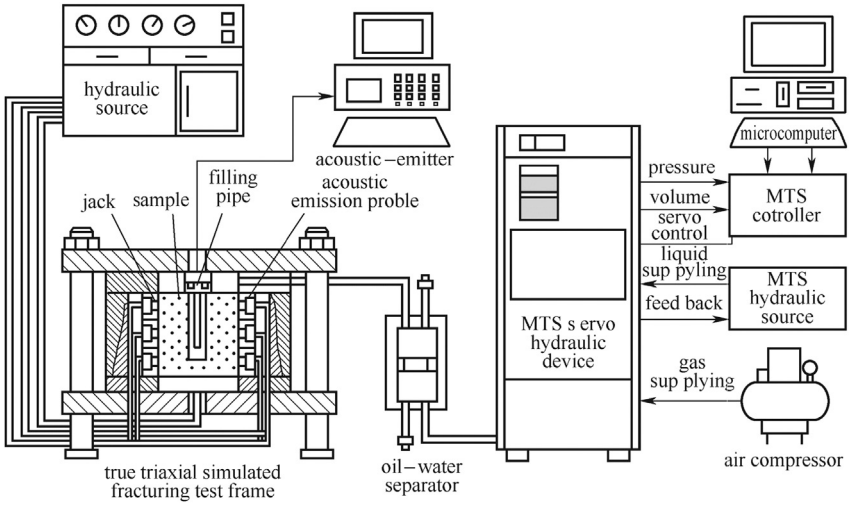

Figure 4.14 Simulation testing device of hydraulic fracturing.

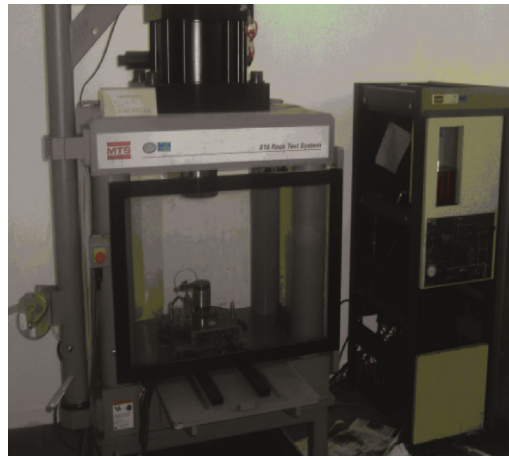

Figure 4.15 Picture showing the hydraulic voltage source.

controlled in the true triaxial loading way to keep the experimental specimen at the actual stress state of rock as much as possible.

In the experimental system, the injection procedure can artificially be controlled by the MTS servo pump and the oil—water separators. The injection can either be accomplished at the constant displacement or using a specific procedure. During the experiment, the data acquisition system can be utilized for recording the pressure and displacement of the fracturing

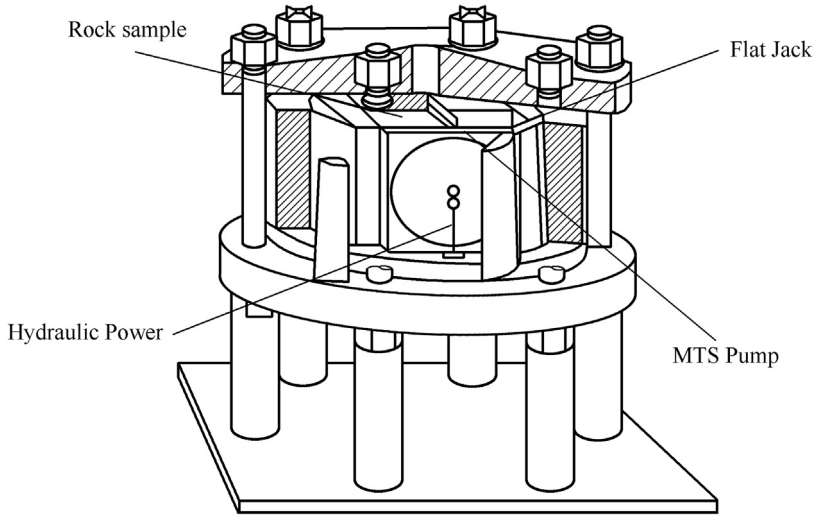

Figure 4.16 Schematic diagram of the true triaxial simulation frame.

Figure 4.17 Picture of the true triaxial simulator.

fluid and other variables. The working fluid in the MTS booster pump consisted of a hydraulic oil. Thus when water (or other fluid) was used as the fracturing fluid, an oil—water separator was required to be set on the pipeline to separate the working fluid of MTS from the fracturing fluid. In this experiment, a slip-on oil—water isolator was employed, and in the thick-walled cylindrical autoclave, an isolating sleeve was used to separate the oil from water.

Furthermore, guar gum with a consistency coefficient of 19.8 Pa s^n and flow index of 0.37 was utilized as the fracturing fluid. To track the final form of fracture, the fracturing fluid was mixed with a red dye. After completion of the experiment, a cement block was cracked using a hammer along the fracture to better observe the fracture.

4.2.1.2 Preparation of Rock Samples

Natural or artificial rock samples could be used for indoor hydraulic fracturing experiments. However, due to limited sources of natural rock and confining processing conditions, concrete specimens were used to simulate the fracturing process in this experiment.

A rigid plate was applied to exert pressure on the rock samples along the triaxial experiment frame, which required a high parallel degree of the end face of the sample of not more than 0.01 mm. The concrete specimens were prepared using the special mold shown in Fig. 4.18.

First, a certain proportion of quartz sand was added to the mold to form cement samples, simultaneously presetting the simulated wellbore in the sample. Second, different steel wires filled with soluble solid particles were added to the bottom of the simulated wellbore. After solidification of the sample, water was injected into the simulated wellbore to melt the solid particles. This formed a hollow hole in the middle of the rock sample. The fracturing fluid could enter the sample through the wire network pore to simulate the hydraulic perforating and fracturing phenomena. The simulation of wellbore and perforation (wire network) are shown in Fig. 4.19A, and the rock sample is shown in Fig. 4.19B. The structure diagram of the

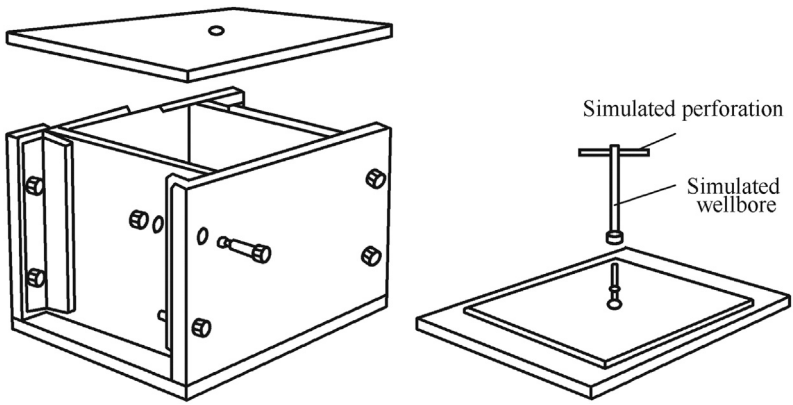

Figure 4.18 Schemes of the sample mold.

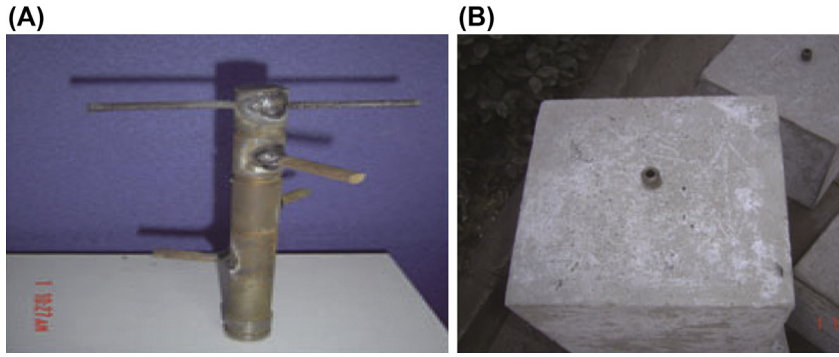

Figure 4.19 (A) Picture of simulated wellbore and perforation. (B) Picture of the artificial rock sample.

rock's size is depicted in Fig. 4.20, where the simulated wellbore and perforation were located in the rock's sample center.

An important factor for simulating the formation condition had to do with the size and distribution of the formation stress. In general, the three formation stresses were equally perpendicular to each other and the horizontal stress of the different layers also differed from each other. For hydraulic fracturing, the direction of crack propagation was determined by the relative size of three principal stresses, where the size and distribution of the minimum horizontal stress were found to affect the geometry of fractures. The usage of true triaxial loading method in the simulation experiments could better reflect the actual stress condition of the formation.

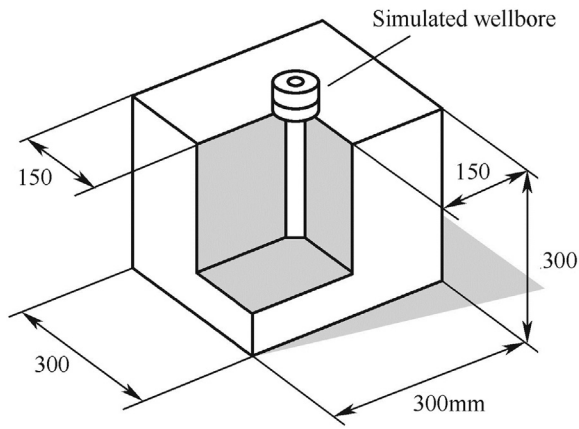

Figure 4.20 The structure diagram of the rock's size.

4.2.1.3 Experimental Methodologies

Similarity criterion in simulation experiment

The similarity theory is often relevant to experiment, which is used for basic layout problems in the experiment like series of experiments to solve differential equations or derivation of empirical formulas. However, due to the developed format of science and technology, similarity theory is mostly employed for guidance in a simulation experiment. In 1992, Dr. De Pater succeeded in deriving the similarity criterion from two-dimensional hydraulic fracturing model using dimensional analysis based on two-dimensional fracturing control model. Gong-hui Liu and Fei Pang from China University of Petroleum, Beijing, further derived the similarity criterion of three-dimensional (3D) hydraulic fracturing model, particularly for 3D simulation control equations. They achieved good results of hydraulic fracturing model experiment according to the similarity criterion. The indexes derived from Victor Fei Pang's model are as follows:

$$c_{\sigma_{zz}} = c_{Ee} = 1, \quad c_T = 1000, \quad c_Q = 10^{-6}$$
$$c_\eta \approx 10^3, \quad c_{K_{ic}} \approx 0.3, \quad c_{K_l} \approx 0.03$$

Under in situ conditions, the samples should own the qualities of good fracture toughness and low permeability in the simulation experiment. Besides, the experiment should be conducted with high viscosity of the fracturing fluid in tiny injection displacement. As free measure unit, the selection of the single-valued conditions should not be singular, and therefore the form of similarity criterion should not be singular as well. The essence should be similar, and meeting the requirements of all the similarity criterion becomes unrealistic. Hence some minor conditions can be ignored to guarantee the feasibility of the experiment, and certain other conditions can only be approximately satisfied. Even so, the similarity criterion and the similarity index should be still relevant for providing the basis for designing the simulation experiment parameters. In this study, the experiment was strictly performed following the guidance of the similarity theory.

In the hydraulic fracturing model experiment, maintaining the stability of the crack propagation is extremely important. All kinds of numerical models are based on the fracture process of quasi-static situations, where the inertia term in the fluid flow equation and crack open process are ignored. In the field of fracturing operations, extensions of fracture processes are similar to quasistatic situations, and thus are complex feedback processes.

The study of crack extension rule according to the requirement of the simulation experiment should importantly guarantee the stability of the crack extension. The injection pressure suddenly showed a large gap at the moment of crack after reaching a peak, indicating the release of strong energy. Compared with smaller experimental models, this sudden rupture of open hole section may produce a quick break through the surface. This would be a great disadvantage for research dealing with rules of cracks expansion, which yet can be solved by improving the confining pressure to control the crack tip extension rate or by prefabricating the fractures to weaken the prefabricated crack force energy released at the moment. Prefabrication of cracks is difficult for natural stone, which is a very strict criterion to the requirement of sample processing at a high cost. The solution consisted of taking the low-strength specimen or improving the viscosity of fracturing fluid to reduce the fracture toughness and influence of crack propagation. This should prevent the appearance of dynamic extension situation of cracking during the process of fracturing experiments, making the cracks for conducting quasistatic expansion (steady-state) extension and consequently controlling the crack extension process within the scope of the ideal scale of time.

Following the similarity criterion, this experiment adopted the cement sample with good fracture toughness and low permeability, as well as the fracturing fluid with high-viscosity guar gum.

Experimental conditions

Specimen size: 300 × 300 × 300 mm
Sample material: cement + fine river and volume ratio 1: 1
Simulation wellbore size: φ20 × 170 mm
Simulation wellbore diameter: φ8 mm
Wellbore wall—simulated perforation diameter: φ5 mm
Simulated perforation number: 2
Simulated perforation position: sample center
Fracturing fluid types: guar gum

Experimental procedure

After putting the sample into the press, the pressure plate and the other parts of the press were installed. To ensure uniform loading of the pressure plate on the sample's surface, a rubber gasket was placed between the pressure plate and the sample. The sample was then loaded and a 3D confining pressure was applied to the sample by a hydraulic constant pressure source. Next,

the fracturing fluid was pumped into the simulated wellbore at selected displacement until the sample was fractured. After the appearance of cracks, the fracture morphology, namely, the trace of the fracturing fluid on the sample surface was observed. Parameters like the pumping pressure and displacement were recorded by the MTS experimental machine during the experiment.

During this study, crack initiation pressure and fracture extension situation of the sample were measured and analyzed by changing the following parameters: (1) perforation diameter, (2) perforating depth, (3) the angle between the hole axis and the maximum horizontal stress, and (4) the horizontal stress ratio.

4.2.1.4 Analysis Results

The load curve was recorded by a microcomputer automating during processing of the experimental results. The initiation pressure was taken as point A in the process of the corresponding value (Fig. 4.21), where the judgment standard had suddenly dropped the point during the process of loading pressure.

4.2.1.4.1 Influence of Perforation Diameter on Rock Crack Stress

The experiments were set between the rock crack stress or the rock crack time and perforation diameter, respectively. For comparative purposes, the perforating depth was set to 50 mm; perforation diameter to 2, 4, 6, and 8 mm; and the triaxial stress on the sample to 12, 15, and 21 MPa.

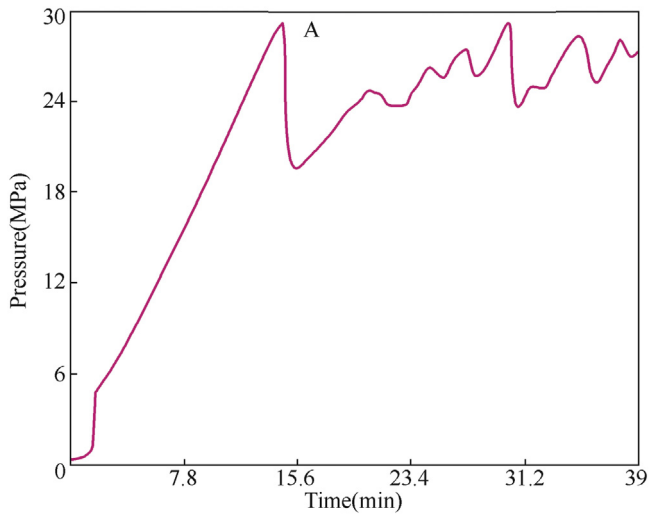

Figure 4.21 Variation of point A of the rock crack stress during the process of loading.

Figs. 4.22 and 4.23 represent the curves between the rock crack stress and the rock crack time and perforation diameter, respectively. The rock crack stress declined rapidly with the increase of perforation diameter (Fig. 4.23). Also, it can be seen that the trend of the curve gradually decelerated as the perforation diameter exceeded 4 mm, whereas the crack pressure decreased by only 0.69 MPa (2.7%) after the double perforation diameter increased from 4 to 8 mm. Thus it could be concluded that crack stress was not sensitive to changes in perforation diameter. However, the crack time increased by raising the perforation diameter only under the same conditions as shown in Fig. 4.23.

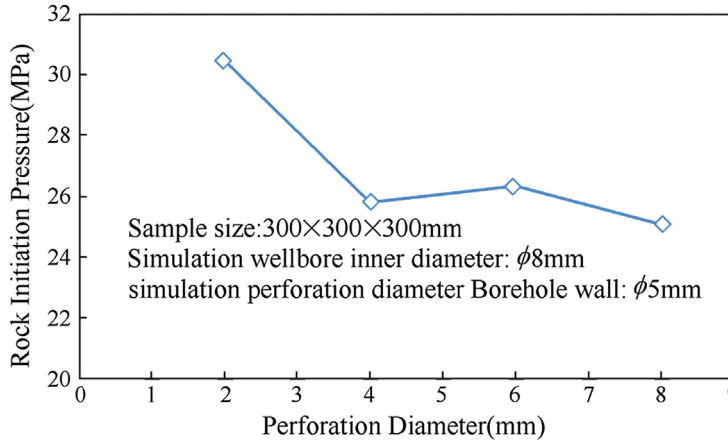

Figure 4.22 Relationship between the rock crack stress and perforation diameter.

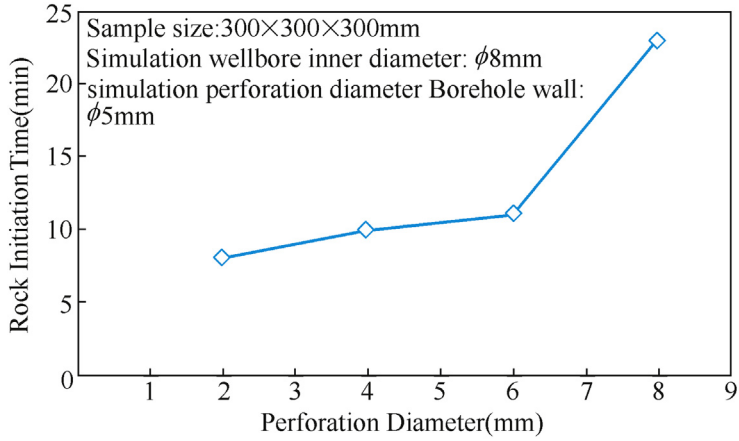

Figure 4.23 Relationship between the rock crack time and perforation diameter.

4.2.1.4.2 Effect of Perforation Depth on Fracture Pressure

In this section, the relationships between the fracture pressure and the fracture time of rock samples and the depth of perforation were studied. According to the physics similarity criterion in principle of similarity, when making rock samples, the diameter of perforation is uniformly set to 4 mm. The perforation depths were set to 30, 50, 70, and 90 mm, and the triaxle stresses to 12, 15, and 21 MPa.

Figs. 4.24 and 4.25 show the curves of the fracture pressure and the fracture time of the rock sample as a function of perforation depth, respectively. It can be observed that as the depth of perforation increased, the fracture pressure of rock sample decreased quasilinearly (Fig. 4.25). The fractured time of the rock sample followed a similar trend. When the depth of perforation changed from 30 to 50 mm (66.7% increase), the fracture pressure decreased from 29.21 to 25.77 MPa (11.8% reduction) and the corresponding fracture time declined by 28.6%.

The reason for this changing tendency was mainly the "piston effect" in the perforation. When the perforated hole was filled with the fracturing liquid subjected to the pressure of the pump, this section of liquid became equivalent to a "liquid piston." Greater perforation depth induced longer length of the "piston," and more energy was contained under high pressure. This made it easier to open the rock samples. Fig. 4.26 shows a cut-away view of the rock sample after the fracturing experiment.

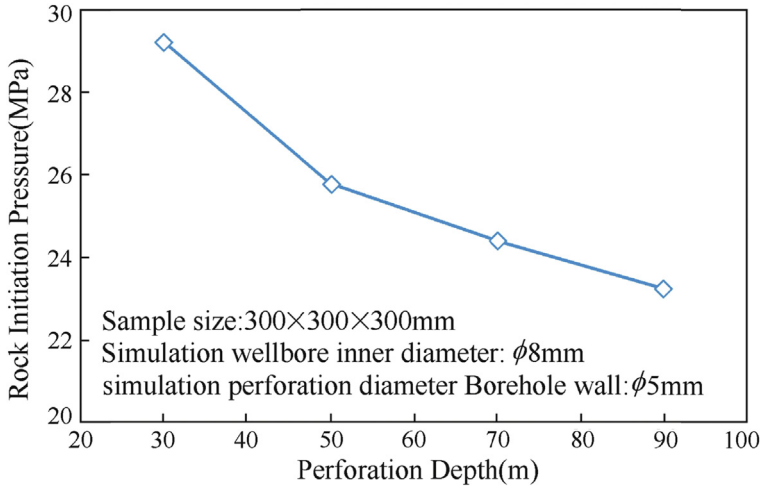

Figure 4.24 Relationship between fracture pressure and perforation depth.

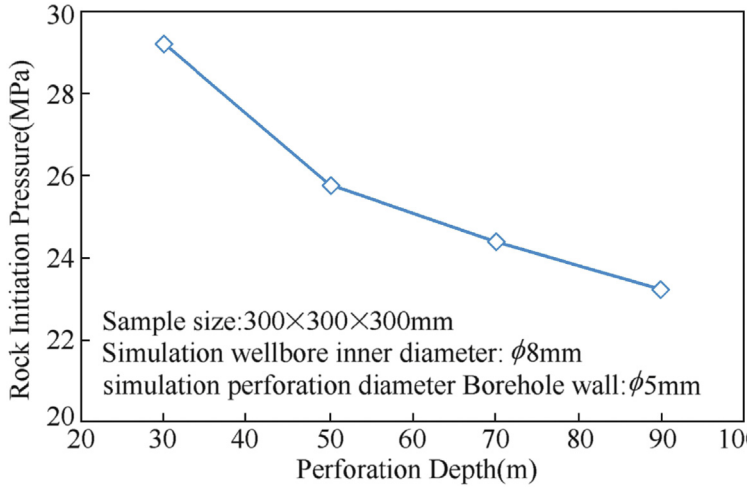

Figure 4.25 Relationship between fracture time and perforation depth.

Figure 4.26 Profile of fractured rock sample.

4.2.1.4.3 Effect of Angle Between Perforation Axis and Maximum Horizontal Principal Stress on Initiation Fracture

The angle between perforation axis and the maximum horizontal principal stress were successively set to 0, 30, 60, and 90 degrees (Fig. 4.27). The hole diameter and hole length were, respectively selected as 4 and 50 mm. The maximum horizontal stress and minimum horizontal stress were 15 and 12 MPa, respectively, and the vertical stress was 21 MPa.

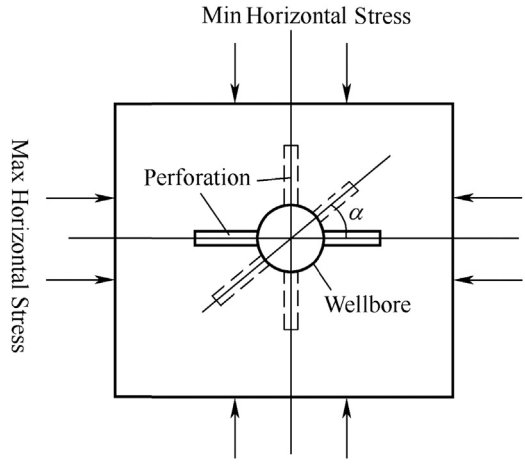

Figure 4.27 Overlooking of the rock cross-section.

Figs. 4.28 and 4.29, respectively, illustrate the breakdown pressure and the breakdown time curves as a function of angle α. Fig. 4.29 confirmed that the perforation direction along the maximum horizontal principal stress ($\alpha = 0$) induced a minimum initial pressure. Also, as the perforation angle rose, the initial pressure increased almost linearly, and the angle α and initiation pressure rose by 10 degrees and 0.7 MPa, respectively. At an angle α of 90 degrees, the initiation pressure reached the maximum value. Correspondingly, the initiation time showed a similar changing pattern. However,

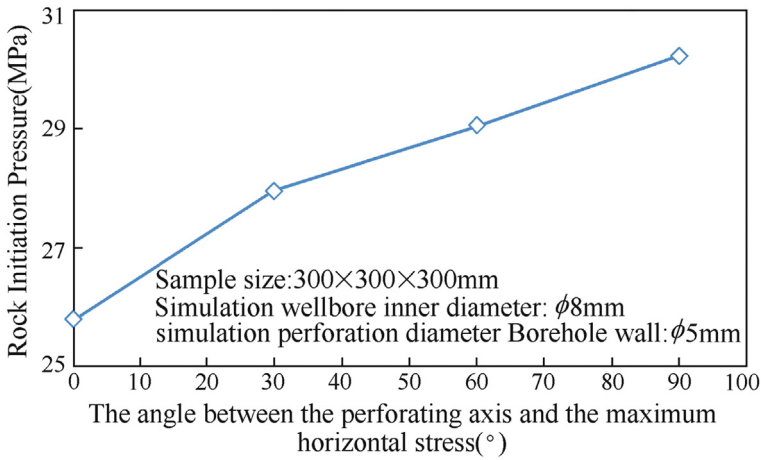

Figure 4.28 Relationship between the crack pressure and the angle α.

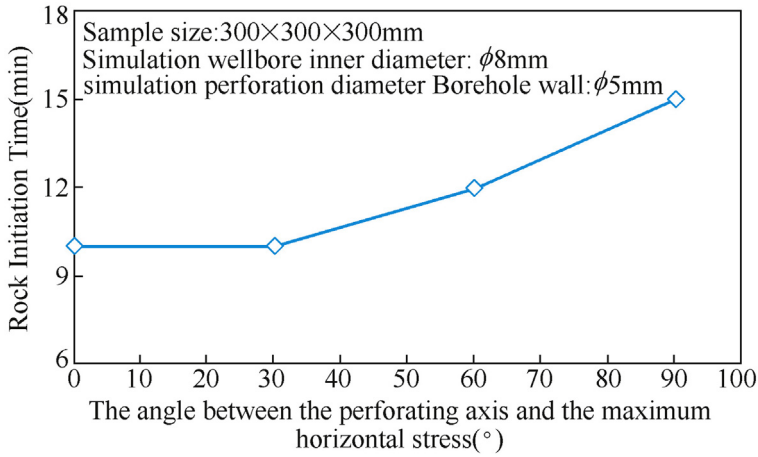

Figure 4.29 Relationship between the fracture initiation time and the angle α.

at an angle α less than 30 degrees, the initiation time did not change and it time began to increase when the angle was above 30 degrees.

The reason for was sample failure, which was consistent with the minimum energy principle. In other words, rock dynamic failure always occurred along the direction of minimum energy consumption.

4.2.1.5 Fractal Characteristic of Fracture

The fractal theory refers to a kind of extremely fragmentary and complex system, with self-similarity or self-affine widespread in nature. It is closely related to chaos theory and reveals the unity of nonlinear systems in order and disorder states and the unity of certainty and randomness. It provides an effective method to study random and irreversible physical phenomena.

The fractal theory is characterized by two important features: self-similarity and scale invariance. Self-similarity means that the characteristics of a structure or process are similar in different spatial and time scales, or the local property or structure of a system is similar to that of the whole.

Scale-invariance means that magnification of any local region of fractals or obtained larger version of figures should display the morphological characteristics of the original figure. As for fractal, the morphology, complexity, irregularity, and other physical properties should remain unchanged whether it is magnified or shrunk. Therefore, scale invariance is also called telescopic symmetry.

According to the characteristics of fractal theory, if the fracture surfaces induced during the fracturing experiments showed fractal features, it could be assumed that the local fracture form induced during the experiment is deeply related to the overall fracture form of the actual fracturing engineering. In other words, using fractal dimension, the fracture area could be predicted according to maximum fracture height and fracture length during the fracturing operation. This could increase the credibility and validity of the experiment results and could be helpful in judging fracture form during the fracturing operation.

4.2.1.5.1 Fractal Criterion

Among the definitions given to fractal dimension, the similarity dimension is easier to understand. Generally, if a graph can be separated into aD similar parts, D can be defined as the similarity dimension. For example, dividing a square into two parts makes one part as half of the original surface. In this case, the similarity dimension of the square is 2. However, the applicability of the similarity dimension is very limited as it is only applicable to strictly self-similar graphs. However, the so-called Hausdorff dimension is more general and applicable to arbitrary graphs including random graphs.

For a line segment having length L, a ruler is utilized to approximate the line segment. The measurement is N, meaning that the line segment can be decomposed into N rulers. Obviously, N is related to the scale of the ruler following Eq. (4.1):

$$N(r) = L/r \sim r^{-1} \tag{4.1}$$

Similarly, if the studied object is dealing with an area, small squares could be employed to reach approximations following Eq. (4.2):

$$N(r) = A/r^2 \sim r^2 \tag{4.2}$$

Smaller *r values* induce more accurate measurements, and the number of the small squares is always proportional to A/r^2.

Thus for a specific geometry, if a ruler with the same dimension as with the geometry of the measuring tool is used, the measurement becomes N. If the dimension of the ruler is smaller than that of the geometry, the measurement becomes infinite. Otherwise, the measurement is zero according to the mathematical Eq. (4.3):

$$N(r) \sim r^{-D_H} \tag{4.3}$$

The logarithm of Eq. (3.3) yields Eq. (4.4):

$$D_H = \ln N(r)/\ln(1/r) \tag{4.4}$$

where D_H is the Hausdorff dimension, which can be an integer or a fraction. If the Hausdorff dimension D_H of an object is a fraction, then D_H becomes the fractal dimension of the object.

With respect to the "ruler," the smaller the r, the more accurate is the obtained fractal dimension. This means that the fractal dimension has uncertainties. The best condition is that the "ruler" tends to zero, but this is almost impossible in actual measurement. The actual fractal has a hierarchy problem, such as fractal fractures formed during earthquakes measured at the macroscopic scale (in kilometers). Also, the fractal structure of the material cross-section is equivalent to the grain size; otherwise it cannot be studied. Therefore the selection principle of the "ruler" states that the length of the unit should be consistent with the existence of fractal scale units.

4.2.1.5.2 Calculation of Fractal Dimension

Fig. 4.30 shows a fractured rock sample under certain conditions during the experiment. Fig. 4.31 represents a plan view of the fracture section obtained from Fig. 4.30. The calculation of fractal dimension can be divided into the following five categories: (1) changing the observation scale, (2) measure relation, (3) correlation function, (4) distribution function, and (5) data based on the spectrum. When combined with the actual situation, only the first two methods were discussed.

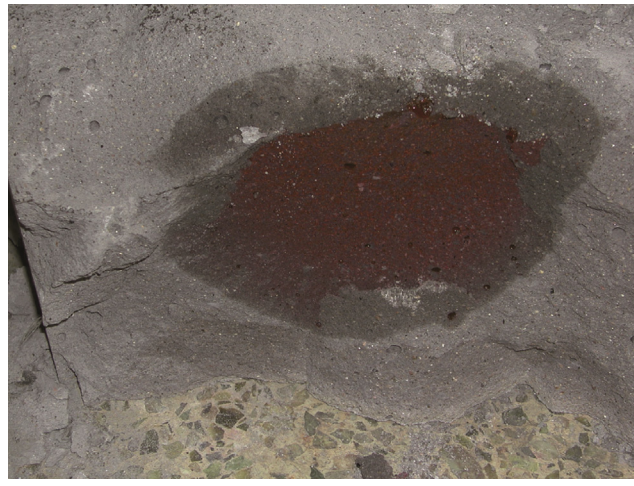

Figure 4.30 Picture of the fractured rock sample.

Figure 4.31 Plan view of the extracted fracture surface.

The basic principle of changing observation dimension of scale relies on the complex curve approximated by a line segment, with the length R being the random curve of fracture plane edge in the picture. One point of the curve was selected as the starting point, and then a circle with a radius R at this point was drawn. The circle was connected to both the point and the starting point of the curve's first intersection, and then a crossing point was made as the new starting point to yield a repeat operation.

As shown in Fig. 4.32, line segments were employed to approximate the edge of the fracture. The total number of the line segments was $N(R)$.

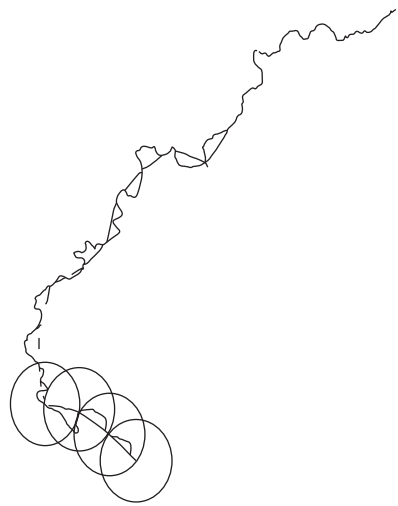

Figure 4.32 Approximation of fracture using line segments.

Changes in the scale will induce variations in $N(r)$. If the formed random curve was straight, the relationship $N(R)/R1$ should exist. For more complex curves, more line segments were required to approximate. Thus the method is overall straightforward and operable, but tedious and time consuming for practical problems.

The basic principle of the dimension of measure relation could be summarized by Eq. (4.5), assuming that L is the length and X is the area or volume.

$$L \propto X/D \tag{4.5}$$

When K enlarges or narrows by folds, X/D should enlarge or narrow by several folds. D is the dimension of the fractal structure. Relatively, the method is simple when compared with the changing observation dimension for scale. Regarding the view of the random curve of fracture edge mentioned here, the aim was to find a solution to the perimeter L and area of a closed edge curve X. Thus the fractal dimension was not hard to determine.

To calculate the area and perimeter of the graph, the graph was input into the software AUTOCAD. By changing the scale, two sets of data, (38.20, 30.91) and (376.00, 98.61), were respectively obtained. Note that the unit was centimeters. Based on Eq. (3.5), the following could be obtained:

$$30.921 \propto 38.204/D \tag{4.6}$$

$$98.612 \propto 376.005/D \tag{4.7}$$

Comparing the two equations yields:

$$\frac{30.912}{98.612} = \left(\frac{38.204}{376.005}\right)^{1/D} \tag{4.8}$$

The logarithm of the equation resulted in $D = 1.971$. The fractal dimension of the fracture surface was estimated to 1.971, meaning that the fracture surface displayed fractal characteristics.

The fractal dimensions of the following three figures were recorded as 1.785, 1.808, and 1.980, respectively. The results were taken from the Zhang's work, as shown in Fig. 4.33A–C. The shape of c appeared very similar with that of Fig. 4.31. Thus, the fractal dimensions should be similar, and the difference was estimated to only 0.009.

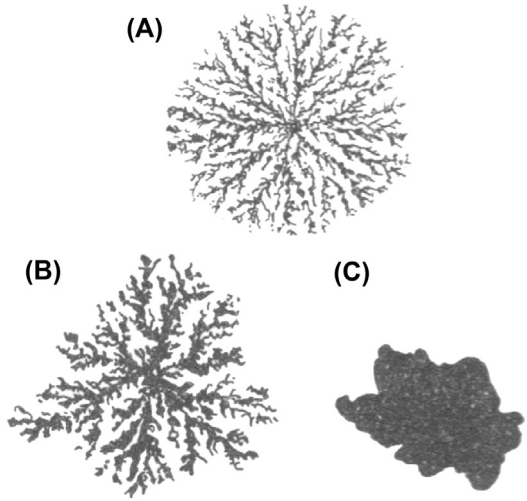

Figure 4.33 The fractal sample.

REFERENCES

Gensheng, L., Li, L., Zhongwei, H., & Jilei, N. (2006). Study of effect of hydraulic perforating on formation fracturing pressure. *Journal of China University of Petroleum, 30*(5), 42−45.

Guangqing, Z., Mian, C., & YinYouquan, S. (2003). Study on influence of perforation on formation fracturing pressure. *Chinese Journal of Rock Mechanics and Engineering, 1*, 6.

Li, Z., Li, L., Huang, B., Zhang, L., Li, M., Zuo, J., et al. (2017). Numerical investigation on the propagation behavior of hydraulic fractures in shale reservoir based on the DIP technique. *Journal of Petroleum Science and Engineering, 154*.

Pearson, C. M., Bond, A. J., Eck, M. E., & Schmidt, J. H. (1992). Results of stress-oriented and aligned perforating in fracturing deviated wells. *Journal of Petroleum Technology, 44*(01), 10−18.

Yishan, L., & Yequan, J. (2006). *Rock mechanics and petroleum engineering (in Chinese)*. Petroleum Industry Press.

Yongquan, H. (2003). Finite element method to calculate fracture pressure of perforated well hydrofrac. *Natural Gas Industry, 23*(2), 58−59.

Zhou, D., Guo, J. C., Zhao, J. Z., & Deng, Y. (2002). Study of fracture initiation of the extended reach wells with openhole completion. *Journal of Southwest Petroleum Institute, 24*(6), 32−35.

CHAPTER FIVE

Flow Behavior and Friction Characteristics of Fluid Flow in Coiled Tubing

Contents

Abstract

The coiled tubing (CT) has many applications in the petroleum industry, which include drilling (CT drilling), cementing, wellbore cleanout, acidizing, and hydraulic fracturing. In contrast, the excessive friction pressure loss, due to the relatively small tubing diameter and tubing curvature (which is believed to cause secondary flow) of CT, often limits the maximum obtainable fluid injection rates. Therefore it is of practical importance to investigate the flow regularity and friction properties in CT. Professor Shah and his research team at the Well Construction Technology Center of the University of Oklahoma have conducted numerous theoretical and experimental studies regarding CT and have reported great achievements.

This chapter primarily introduces the flow analysis of fluids in the helical segment of CT and friction calculations for Newtonian and non-Newtonian fluid flows.

Keywords: Coiled tubing; Friction; Newtonian fluid; Non-Newtonian fluid.

Abrasive Water Jet Perforation and Multi-Stage Fracturing
ISBN: 978-0-12-812807-7
https://doi.org/10.1016/B978-0-12-812807-7.00005-4

5.1 FLUID FLOW BEHAVIOR ANALYSIS IN HELICAL SEGMENT OF COILED TUBING

The coiled tubing (CT) has been utilized in many engineering applications, including heating and refrigeration processes, bioengineering, and chemical reactors. More recently, the CT has gained increased importance due to the corresponding numerous potential applications in the petroleum industry. The majority of these applications involves fluid flow, and requires an accurate assessment of the frictional pressure losses in tubing. Accordingly, the flow through CT has been under extensive investigation, mostly aimed at explaining the corresponding complex nature.

5.1.1 Flow Characteristics

The flow in CT is uniquely different from the flow in a straight pipe, due to the secondary flow pattern induced by the imbalance between forces acting in the radial direction of pipe coil. This secondary flow pattern is composed of counterrotating vortices, commonly called Dean vortices (Dean, 1927), which cause an increase in frictional pressure loss. The central part of fluid will be driven toward the outer wall by centrifugal force, and the fluid consequently entering the boundary layer region will be pushed back along wall toward the inner side by a pressure gradient. At high Dean numbers (i.e., high flow rates and/or small-sized tubing reel), the intensified secondary flow increases the frictional loss significantly over the losses predicted by Poiseuille flow calculation.

An accurate prediction of frictional pressure losses, when fluids are pumped through CT, has remained a challenge in hydraulics design, mainly due to the lack of adequate friction loss correlations and proper understanding of the complex flow phenomena of fluids (especially non-Newtonian fluids) within CT. Since the classical work of Dean, the flow of Newtonian fluids within coiled pipes has been extensively studied; in contrast, the flow of non-Newtonian fluids within coiled pipes has remained relatively unstudied.

The unique feature of fluid flow in CT is the curved flow geometry that results in centrifugal forces and secondary flow. The centrifugal force is the driving force for the sand segregation within CT, whereas in horizontal pipelines, solids (if heavier than the carrier fluid) can settle due to gravity. The flow field within CT is considerably different from that within the straight tubing (ST). The flow within ST is subjected to gravitational and viscous drag forces, whereas in CT, gravitational, centrifugal, and viscous

drag forces are active. In CT flow, the magnitude of centrifugal acceleration is significantly higher than magnitude of gravitational acceleration, causing particle migration toward the tubing extrados.

5.1.2 Flow Behavior Analysis

Based on the research results of previous scholars, Shah and Jain (2008) investigated CT erosion during a hydraulic fracturing slurry flow. The results and discussion are summarized in the following paragraphs.

The contours of velocity magnitude and velocity profile at the tubing cross-section for water flow at 10 bbl/min in both ST and CT are presented in Figs. 5.1 and 5.2, respectively. The Reynolds number at this flow rate and in this tubing size was 6.7×10^5, which indicated that the fluid was in a high-turbulent-flow regime. These plots display unique features of flow within the curved pipe. It could be observed that the profile in CT flow was distorted compared with that in ST. The velocity profile in CT demonstrated that the high-velocity region shifted toward the tubing extrados, due to centrifugal forces. This caused a secondary flow. Similarly, the velocity contours displayed that the contours in CT were distorted and differed from the contours in ST, which are coaxial circles. These observations supported the authors' previous assertion that in CT, the tubing extrados was subjected to significantly severe flow conditions than the tubing intrados.

Figs. 5.3 and 5.4 present the contours of velocity magnitude and velocity profile for 40 lb/Mgal guar fluid flow at 10 bbl/min in straight and CT, respectively. The generalized Reynolds number at this rate was 4.5×10^4, which confirmed that the flow was in a turbulent regime. In case of non-Newtonian fluids, a somewhat flatter profile was observed compared with Newtonian fluids.

As aforementioned, the CFD simulations of the slurry flow in CT were performed with FLUENT (FLUENT Inc., 2006) to study the phenomenon of particle migration in CT. As discussed earlier, the centrifugal force caused particles to migrate toward the tubing extrados. This particle segregation effect was a function of fluid and solid particle properties along with the slurry velocity. The contours and profile of sand volume fraction, when 8 lb/gal of sand in a gel form was pumped at a rate of 10 bbl/min in ST, are presented in Fig. 5.5. It could be observed that the sand particles remained well suspended in tubing. A slight settling at the tubing bottom appeared due to gravity effects, whereas overall the sand concentration remained uniform throughout the entire cross-section. These results demonstrated that the erosion in straight pipe would be significantly less, compared with erosion of CT.

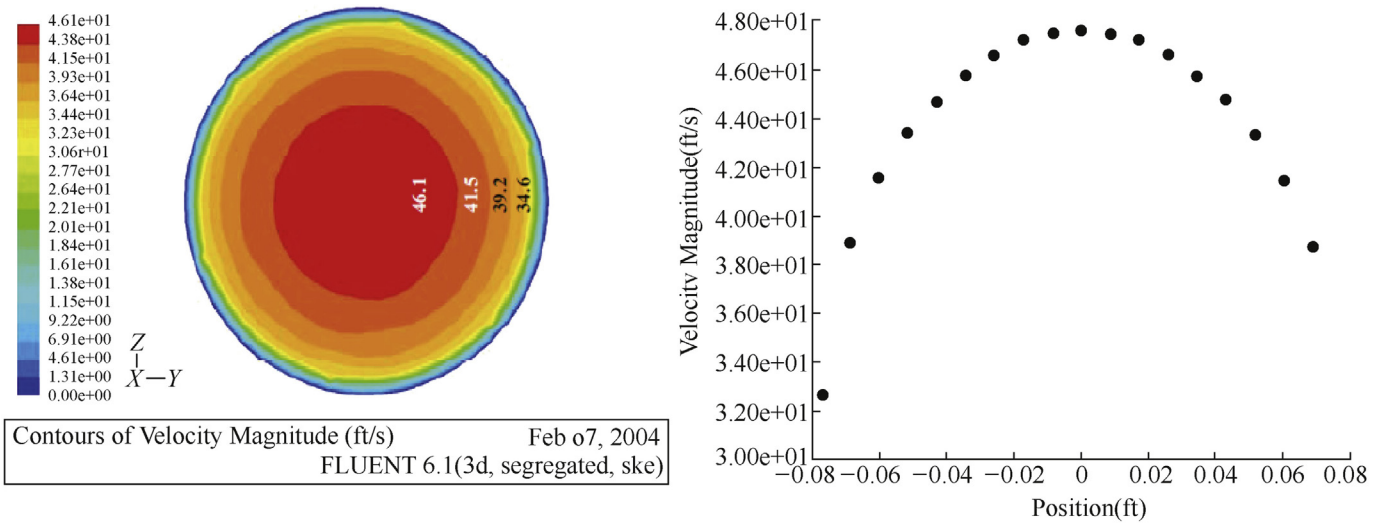

Figure 5.1 Contours and profile of velocity in 2⅜-in. straight tubing for water flow at 10 bbl/min.

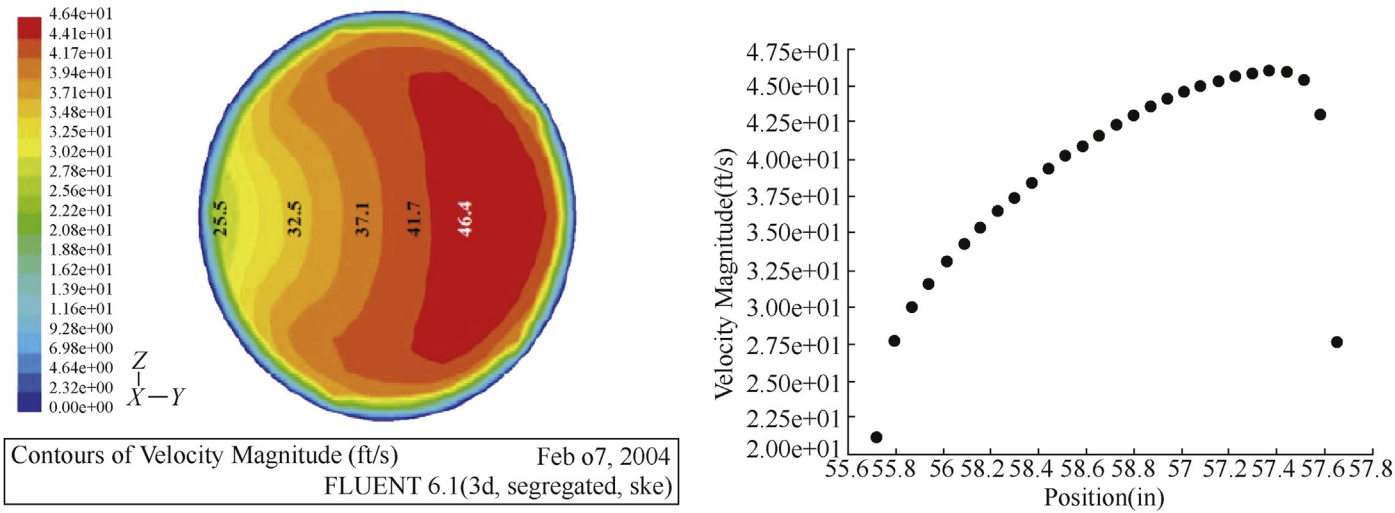

Figure 5.2 Contours and profile of velocity in 2⅜-in. coiled tubing for water flow at 10 bbl/min.

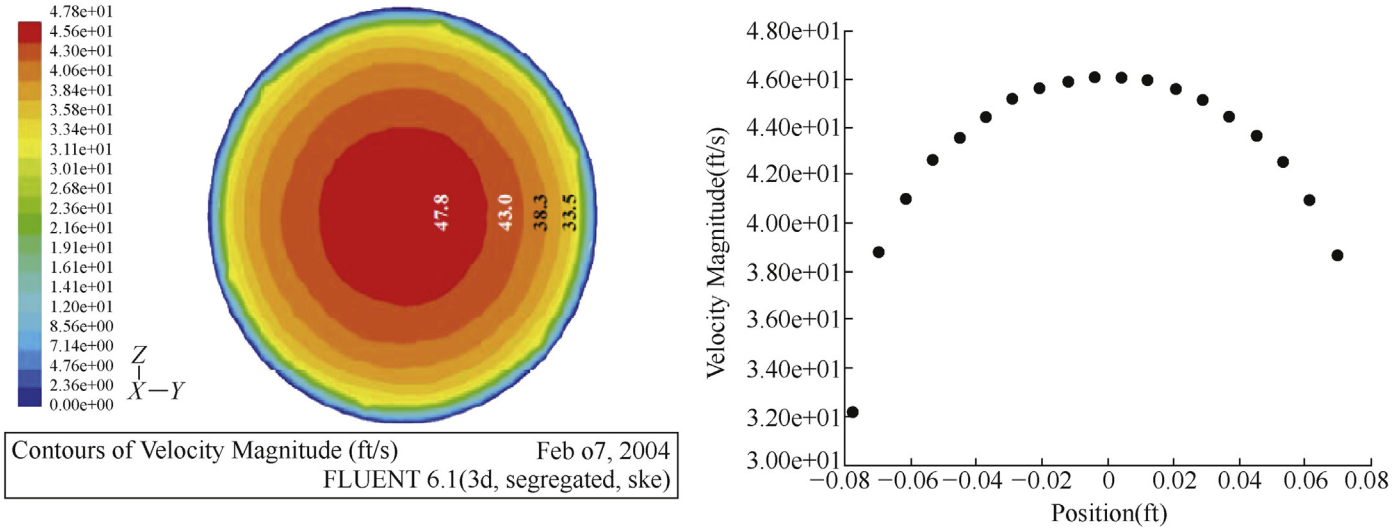

Figure 5.3 Contours and profile of velocity in 2⅜-in. straight tubing for 40 lb/Mgal guar flow at 10 bbl/min.

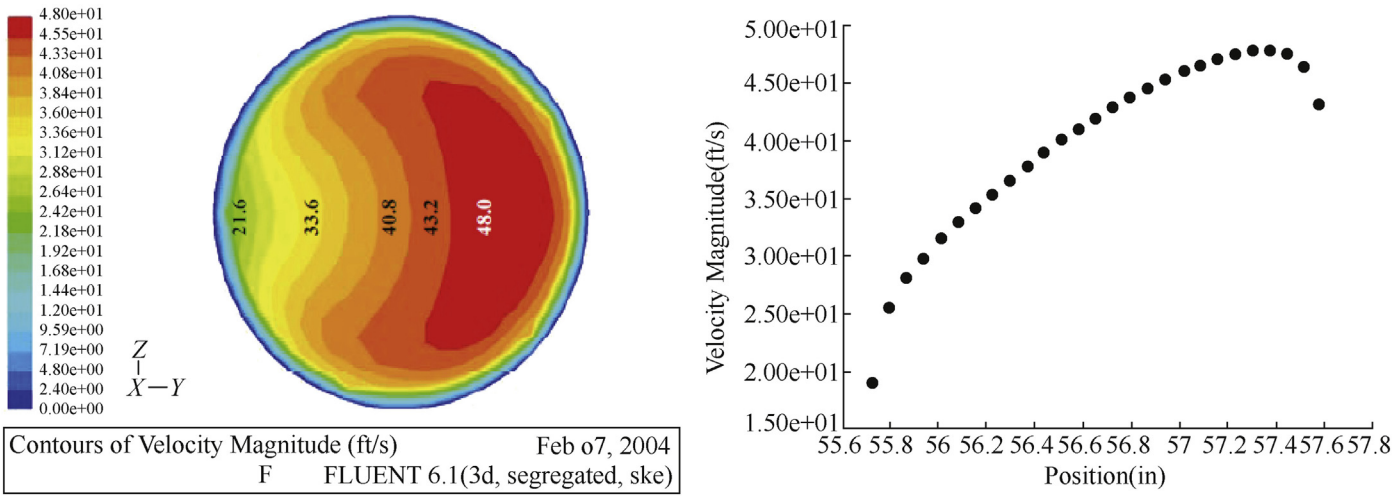

Figure 5.4 Contours and profile of velocity in 2⅜-in. coiled tubing for 40 lb/Mgal guar flow at 10 bbl/min.

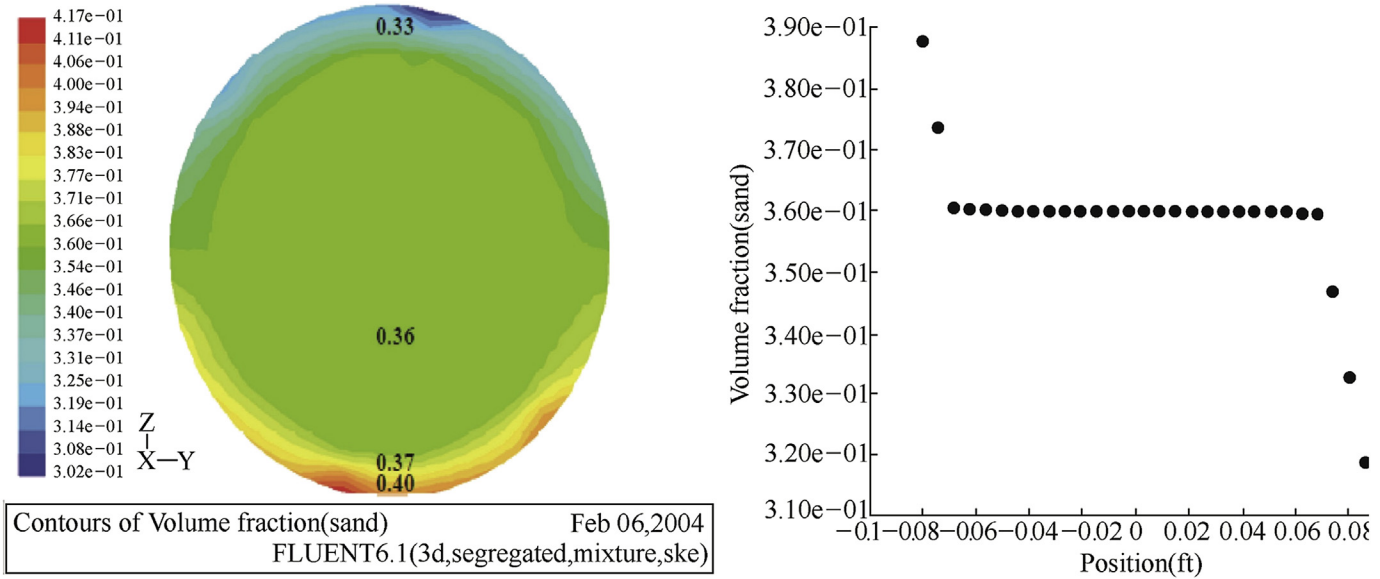

Figure 5.5 Contours and profile of sand volume fraction for 8 lb/gal 20/40 mesh sand in 40 lb/Mgal at 10 bbl/min within 2⅜-in. straight tubing.

The contours and profile of sand volume fraction when 4 and 8 lb/gal sand in guar gel was pumped at a rate of 10 bbl/min within CT are presented in Figs. 5.6 and 5.7, respectively. Similar plots for the flow rate of 15 bbl/min are presented in Figs. 5.8 and 5.9. It could be clearly observed in these figures that in the case of 8-lb/gal slurry the volume fraction of solids were higher than the case of 4-lb/gal slurry. Furthermore, in 4-lb/gal slurry the sand concentration increased linearly, whereas in 8-lb/gal slurry, the sand concentration formed a plateau in the center, which indicated that sufficient quantities of sand were still suspended in slurry. As expected, the sand concentration at extrados in 8-lb/gal slurry exceeded the sand concentration at extrados in 4-lb/gal. Consequently, a higher sand concentration would cause additional erosion, due to higher numbers of particles migrating toward the extrados.

By comparing the flow rate effects on particle migration, it was observed that as the flow rate increased the centrifugal forces tended to produce a quite pronounced effect and particle migration to the extrados increased considerably. This could be observed by comparing the results of Figs. 5.7 and 5.9. At 15 bbl/min the particle concentration reached 63%, whereas at 10 bbl/min it was nearly 58%. This indicated that the erosion rate increased along with flow rate increase, as the particles at higher flow rates impacted the tubing surface with higher velocity.

5.2 FRICTION PRESSURE LOSS CALCULATIONS OF NEWTONIAN FLUID IN STRAIGHT TUBING AND COILED TUBING

The CT units are utilized in a multitude of applications in the industrial arena. This technology due to the corresponding versatility has a range of applications in the petroleum industry including drilling, cementing, cleaning sand from a wellbore, acidizing, scale removal, and formation fracturing. Most of these applications involve pumping of fluids through CT units at significantly high rates. The frictional pressure loss occurrence across the tubing length imposes economic concerns and limits the flow rates that could be achieved through this technique. Since the fluid transport through CT has gained popularity in numerous engineering applications, including the petroleum industry, an accurate calculation of the frictional pressure loss in such tubing is of extreme importance. The accurate estimation of frictional pressure loss plays a crucial role in the determination of horsepower

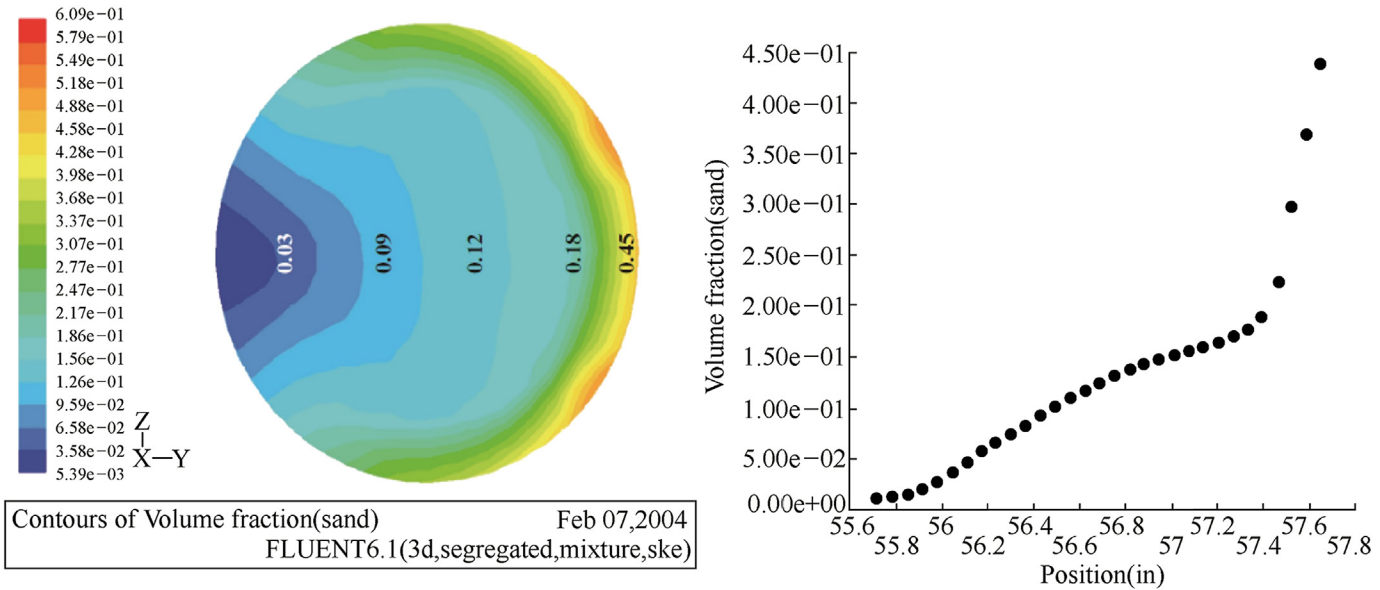

Figure 5.6 Contours and profile of volume fraction of sand for 4 lb/gal 20/40 mesh sand in 40 lb/Mgal guar at 10 bbl/min within 2⅜-in. coiled tubing.

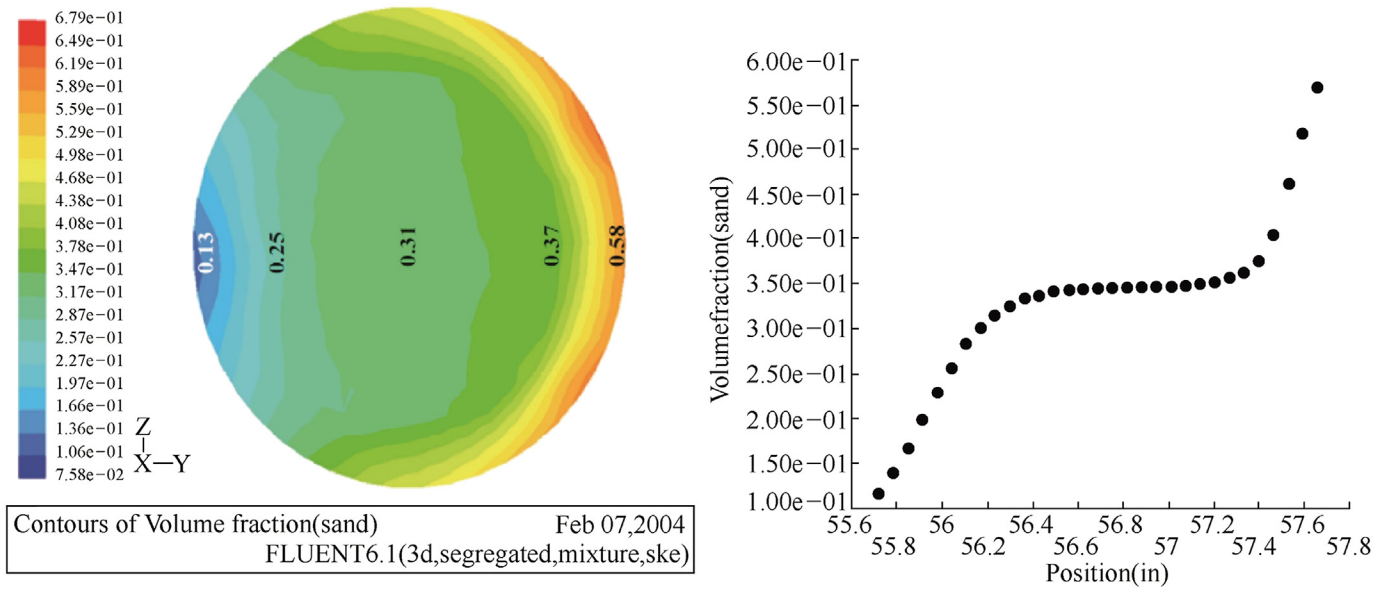

Figure 5.7 Contours and profile of volume fraction of sand for 8 lb/gal 20/40 mesh sand in 40 lb/Mgal guar at 10 bbl/min within 2⅜-in. coiled tubing.

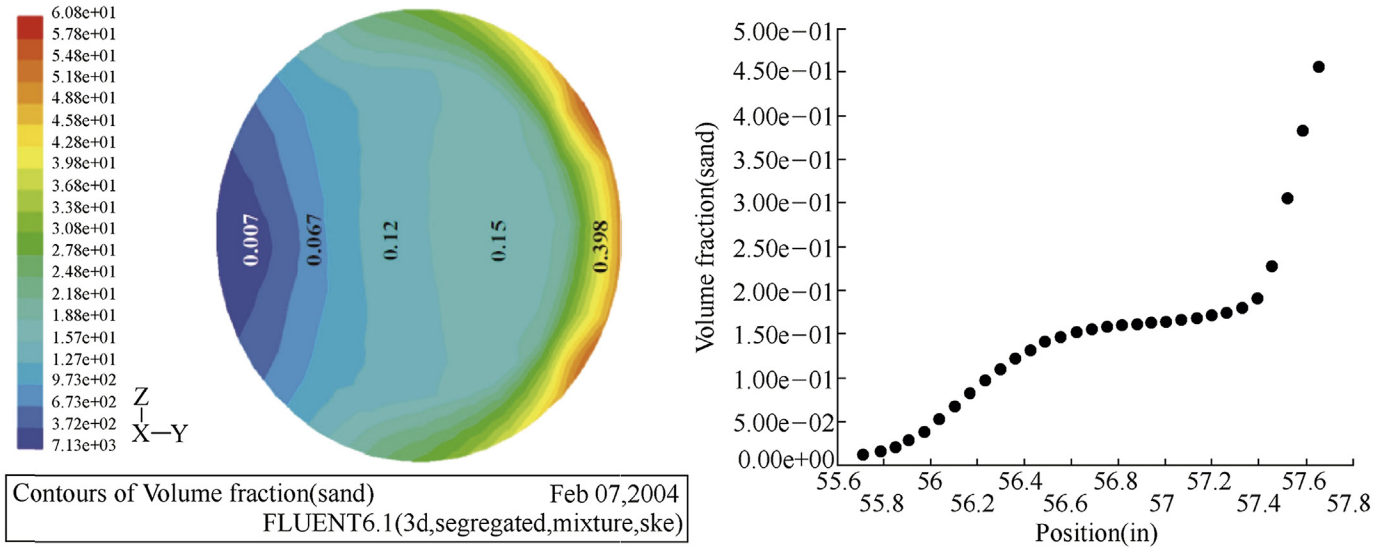

Figure 5.8 Contours and profile of sand volume fraction for 4 lb/gal 20/40 mesh sand in 40 lb/Mgal guar at 15 bbl/min within 2⅜-in. coiled tubing.

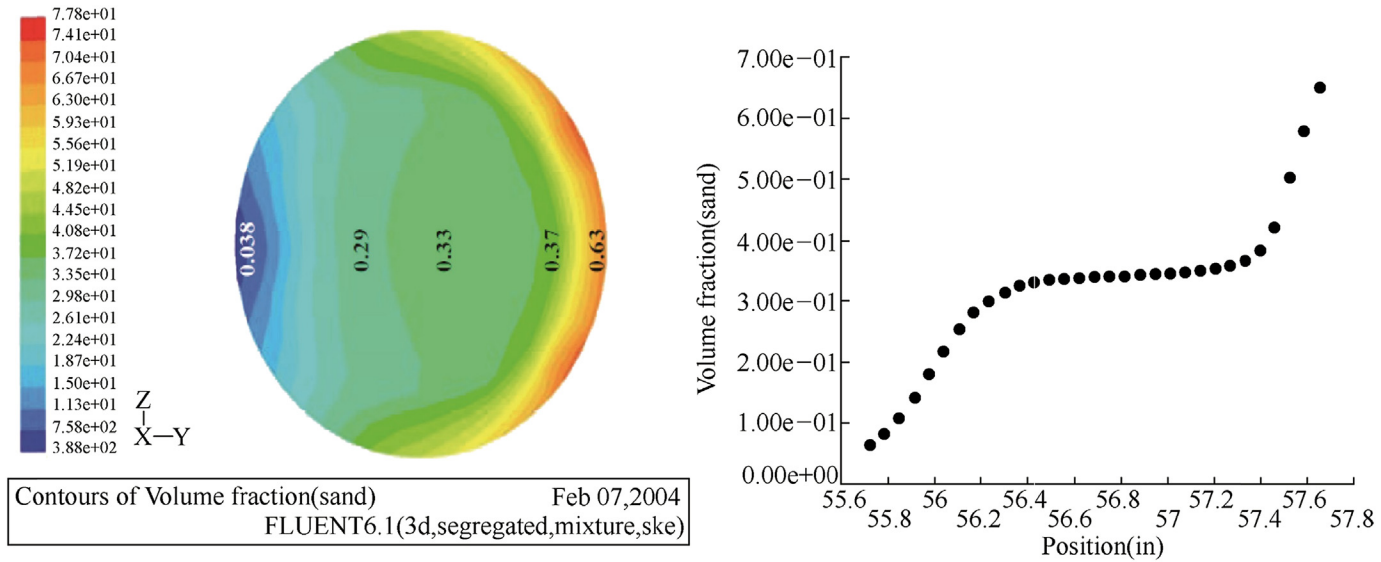

Figure 5.9 Contours and profile of sand volume fraction for 8 lb/gal 20/40 mesh sand in 40 lb/Mgal guar at 15 bbl/min within 2⅜-in. coiled tubing.

requirements for fluid pumping through CT. Furthermore, the friction pressure loss calculations are quite important in the design of any hydraulic fracturing treatment with CT and bottom hole treating pressure estimation, along with maximum wellhead pressure.

The coiled part of tubing during a fracturing operation exhibits significantly higher losses compared with the straight section. Higher frictional losses in coiled geometries are generally caused by increased secondary flow effects that dominate the flow pattern in turbulent flow regime. Even a small increase in the friction pressure gradients can become critical, due to significantly long lengths of tubing involved in a fracturing operation. Certain critical factors in the accurate magnitude determination of friction pressure losses occurring across the tubing lengths are fluid type, fluid flow rate, tubing length, tubing diameter, and tubing curvature. In various experimental approaches the tubing size effects have been investigated. The effects of different fluids have also been studied for common fracturing fluids. In contrast, these studies were limited to the straight conduit. On the other hand, the flow behavior of commonly utilized fluids in CT, where the curvature effects were considered, has scarcely been reported in literature.

In field operations, the CT utilized is wrapped on a spool of different diameters. This variation in spool diameters as well as different tubing sizes utilized on the same spool leads to various degrees of curvature ratio (tubing diameter to reel diameter). This variation in curvature affects the magnitude of frictional losses.

5.2.1 Friction Pressure Loss Calculations of Newtonian Fluids in Straight Tubing

The frictional pressure loss is defined as the energy lost in a fluid transportation through a pipe due to friction between the fluid and pipe wall. Mathematically, the frictional pressure loss can be expressed in terms of Fanning friction factor, f, defined as:

$$f = \frac{\tau_w}{1/2\rho v^2} \tag{5.1}$$

where τ_w is the shear stress at the tubing wall; $\tau_w = \frac{d\Delta p}{4L}$; ρ is the density of fluid; v is the average velocity of fluid; L is the tubing length, across which the differential pressure is measured; d is the tubing diameter; and Δp is the pressure drop.

The Drew, Koo, and McAdams (1932) correlation for smooth pipe is:

$$f = 0.00140 + \frac{0.125}{N_{\mathrm{Re}}{}^{0.32}} \tag{5.2}$$

where f is Fanning friction factor and N_{Re} is Reynolds number. This correlation is applicable in Reynolds number range of $2100 < N_{\mathrm{Re}} < 3 \times 10^6$ and is utilized for Newtonian fluids in turbulent flow in smooth pipes.

The Chen (1979) correlation for a rough pipe is:

$$\frac{1}{\sqrt{f}} = -4.0 \log\left\{\frac{h_r}{3.7065d} - \frac{5.0452}{N_{\mathrm{Re}}} \log\left[\frac{1}{2.8257}\left(\frac{h_r}{d}\right)^{1.1098} + \frac{5.8506}{N_{\mathrm{Re}}{}^{0.8981}}\right]\right\} \tag{5.3}$$

where h_r is the tubing roughness projection and d is the tubing inside diameter (ID). The Chen correlation can be utilized for Newtonian fluids in turbulent flow in straight pipes with roughness. The Chen correlation result is almost identical to Colebrook et al. (1939) equation for the range of N_{Re} from 4000 to 4×10^8 and h_r/d ranging from 0.05 to 5×10^{-7}. Since Chen equation is an explicit equation, it overcomes the drawback of Colebrook equation, which is implicit, and for this a trial-and-error method is required.

5.2.2 Friction Pressure Loss Calculations of Newtonian Fluids in Coiled Tubing

5.2.2.1 Calculations for Fluid Flow in Laminar Flow Regime in Coiled Tubing

The pressure loss in CT is divided into two parts: one part is the pressure loss in the helical segment of CT on the reel and the other is the pressure loss in straight segment of tubing in the well. Many researchers have focused on the down-hole conditions of CT in the field, whereas certain studies emphasized the fluid flow in the helical segment. Li et al. from China University of Petroleum (Beijing) investigated the flow behavior in helical segment of CT through numerical simulations and focused on the effect of secondary flow on the pressure loss (Dongjun et al., 2012).

The continuity equation and the Navier–Stokes equation are discretized by SIMPLEC (Semi-Implicit Method for Pressure Linked Equations-Consistent) algorithm based on staggered grid, whereas the convective term in momentum equation is discretized by the first-order upwind differencing scheme. The velocity inlet, pressure outlet, and wall boundaries are set. To simplify the analysis, the pipe wall was assumed to be hydraulically

Table 5.1 Related parameters of numerical simulation in helical coiled tubing

Outside radius r_o (mm)	Inside radius R (mm)	Drum radius R (mm)	Curvature r/R
38.100	30.1752	1219.2	0.02475
38.100	30.1752	1828.8	0.01650
38.100	30.1752	2489.2	0.01212
38.100	30.1752	2844.8	0.01060
60.325	52.4002	1828.8	0.02865
60.325	52.4002	2082.8	0.02516
60.325	52.4002	5080.0	0.01031

smooth. The wall boundary was set as a stationary wall and a nonslip wall surface. The parameters of helical segment of CT are presented in Table 5.1.

Regarding incompressible fluid, the continuity equation and N—S equation are the governing equations of fluid flow in helical segment of CT. The finite volume method was utilized for discretization. The realizable k—ε model was adopted. To simplify the analysis, the viscosity and density of water were assumed as constant values, and the effect of flow rate change on Dean number was investigated.

Regarding the fluid flow in helical segment, compared with Reynolds number, Dean number was not only quite appropriate in the description of characteristics of the secondary flow and intensity of Dean vortex but also was connected with the helical segment curvature. Therefore the friction coefficient was assumed to be a function of Dean number and curvature of helical segment. The equation (Zhang et al., 2012) was as follows:

$$f = \begin{cases} \dfrac{0.04598}{\mathrm{De}^{0.2}1.755^{A}}, & \text{Turbulent flow} \\ \dfrac{0.8567}{\mathrm{De}^{0.6}5.4^{A}}, & \text{Laminar flow} \end{cases} \tag{5.4}$$

This correlation is applicable in Dean number range of $3 < \mathrm{De} < \mathrm{De}_{cr}$ for a Newtonian laminar flow and $\mathrm{De}_{cr} < \mathrm{De} < 2370$ for a Newtonian fluid in turbulent flow in helical CT. The De_{cr} and A are defined as

$$\mathrm{De}_{cr} = 2100\left[(r/R)^{0.5} + 12(r/R)\right].$$

$$A = \exp\left(-\frac{r/R}{0.01747}\right).$$

where the constant A is used to describe the effects of curvature on friction coefficient. To fully represent the pipe geometry on friction coefficient, Dean number includes both the effect of curvature as well as pipe inner diameter.

To validate the proposed correlation, other correlations (as presented in Table 5.2) were compared with the correlation proposed in Eq. (5.4). The results indicated that, regarding the laminar flow, the proposed correlation had a minimum deviation (0.06%) from the correlation of Srinivasan, and the deviation from the correlation of Mishra and Gupta was at the second place. Regarding turbulent flow, the proposed correlation had a minimum deviation (0.03%) from the correlation of Srinivasan, and the deviation from the correlation of White was at the second place, whereas the deviation from the correlation of Guo was relatively high.

5.2.2.2 Calculations for Fluid Flow in Turbulent Flow Regime in Smooth and Rough Coiled Tubing

The pioneering work of Dean on the theoretical aspect of coiled tube flow problem has been significant. One important contribution of Dean's work was the introduction of nondimensional parameter K, which was called Dean number. The complexity of flow geometries and equations of fluid flow in coiled pipes attracted the attention of theoreticians as well as engineers. Various theoretical methods have been developed, which could be roughly grouped as analytical solutions for a small Dean number, the numerical methods, and the boundary layer methods for high Dean number.

The turbulent flow data analysis of Newtonian fluids in CT with roughness has been a challenge. This is mainly because there is no published correlation on the effect of tubing roughness on friction factor in CT. On the basis of their research work (Zhou and Shah, 2006; Zhou, 2006), the following friction factor correlation for Newtonian fluid flow in CT with roughness was proposed.

$$f_{\text{rough}} = \frac{0.084(a/R)^{0.1} N_{\text{Re}}{}^{0.12}}{(0.125 + 0.00140 N_{\text{Re}}{}^{0.32})} \left[-4.0 \log \left\{ \frac{h_r}{3.7065d} - \frac{5.0452}{N_{\text{Re}}} \log \left[\frac{1}{2.8257} \left(\frac{h_r}{d} \right)^{1.1098} + \frac{5.8506}{N_{\text{Re}}{}^{0.8981}} \right] \right\} \right]^{-2} \tag{5.5}$$

Table 5.2 Compared correlations for friction factor prediction in helical coiled tubing

Scholar	Friction coefficient equation	Scope of application
Srinivasan	$f = \begin{cases} \dfrac{5.22}{\mathrm{Re}^{0.6}}\left(\dfrac{r}{R}\right)^{0.3}, & \text{Laminar flow} \\ \dfrac{0.084}{\mathrm{Re}^{0.2}}\left(\dfrac{r}{R}\right)^{0.1}, & \text{Turbulent flow} \end{cases}$	$30 < \mathrm{Re} < \mathrm{Re}_{cr}$ $\mathrm{Re}_{cr} < \mathrm{Re} < 14000$ $\mathrm{Re}_{cr} = 2100\left[1 + 12(r/R)^{0.5}\right] 0.0097 < \frac{r}{R} < 0.135$
Mishra and Gupta	$f = \frac{16}{\mathrm{Re}}\left[1 + 0.033(\lg \mathrm{De})^4\right]$, Laminar flow	$1 < \mathrm{De} < 3000$
White	$f = \frac{0.08}{Re^{0.25}} + 0.012\frac{r}{R}$, Turbulent flow	$15000 < \mathrm{De} < 100000$
Guo	$\Delta p = \frac{f_c}{4}\frac{n\pi R}{r}\frac{\rho v^2}{2}$, Turbulent flow $f_c = 2.552\mathrm{Re}^{-0.15}(r/R)^{0.51}$	$10^5 < \mathrm{Re} < 4\times10^5$ $n =$ Number of coil turns

where f_{rough} is Fanning friction factor in rough CT, which is dimensionless; a/R is the curvature ratio; a is the radius of CT in in.; R is the reel radius in in.; N_{Re} is Reynolds number, which is dimensionless; h_r is the pipe roughness projection in in.; and d is the pipe inner diameter, in.

The aforementioned correlation was derived based on the assumption that the friction factor ratio in rough to smooth CT was approximately equal to the corresponding ratio in ST. Although the accuracy of this assumption is yet to be verified, the experimental data of the present study appear to indicate that Eq. (5.5) could adequately describe the effect of tubing roughness on friction factor in CT, as discussed later.

Certain correlations are utilized in the turbulent flow data analysis of Newtonian fluid flow in straight rough pipes. One of these correlations was reported by Chen (1979)

$$\frac{1}{\sqrt{f}} = -4.0 \log\left\{\frac{h_r}{3.7065d} - \frac{5.0452}{N_{Re}} \log\left[\frac{1}{2.8257}\left(\frac{h_r}{d}\right)^{1.1098} + \frac{5.8506}{N_{Re}{}^{0.8981}}\right]\right\}, \tag{5.6}$$

where h_r is the tubing roughness projection and d is the tubing ID. The result of this correlation was almost identical to Colebrook equation for the range of N_{Re} from 4000 to 4×10^8 and h_r/d ranging from 0.05 to 5×10^{-7}. Since Chen equation was an explicit equation, it has overcome the drawback of Colebrook equation, which was implicit, and a trial-and-error method was required.

For the turbulent flow of a Newtonian fluid in smooth CT, Srinivasan correlation (Srinivasan, Nandapurkar, & Holland, 1970) could be utilized

$$f = \frac{0.084(a/R)^{0.1}}{N_{Re}{}^{0.2}}, \tag{5.7}$$

where a/R is the CT curvature ratio and a and R are the radii of tubing and reel drum, respectively. Eq. (5.7) is valid for $0.0097 < a/R < 0.135$. The Srinivasan correlation is based on the flow tests of Newtonian fluids (water and oil) in smooth coiled pipes.

Figs. 5.10–5.13 present the plots of Fanning friction factor versus Reynolds number for the flow data of water in 1-, 1½-, 1¾-, and 2⅜-in. ST and CT. Also on the plots are Chen correlation of the friction factor for rough ST and Srinivasan correlation for smooth CT. Several observations could be made and are discussed in the following paragraphs.

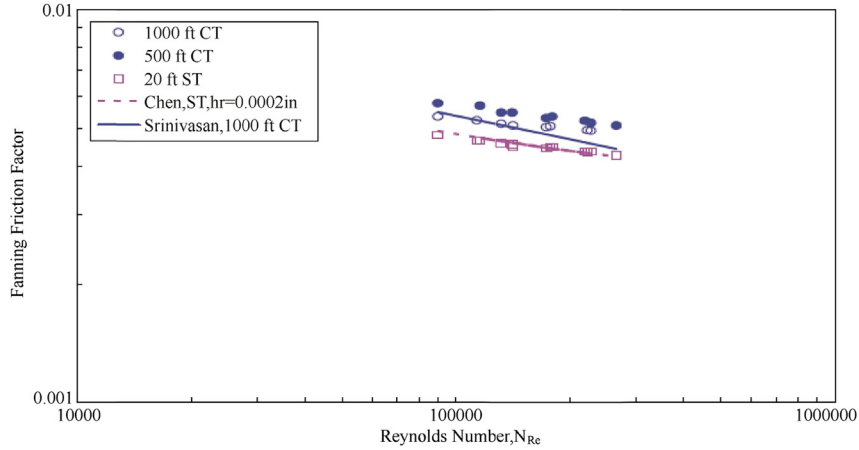

Figure 5.10 Fanning friction factor versus Reynolds number of water in 1-in. straight and coiled tubing (CT).

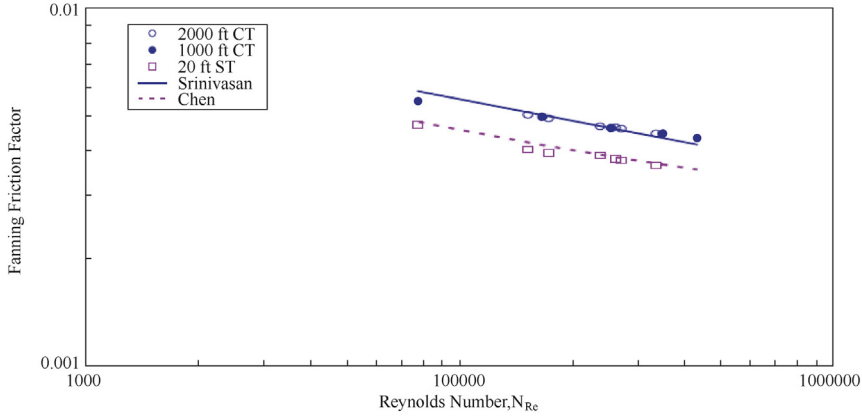

Figure 5.11 Fanning friction factor versus Reynolds number of water in 1½-in. straight and coiled tubing (CT).

First, the friction factor in CT for all tubing sizes (except 1¾-in. tubing reels, which had no corresponding straight sections) significantly exceeded the ST friction factor. The maximum difference in friction factors could be as high as 30%. The extra flow resistance in CT occurred, due to the secondary flow in curved flow geometry. Furthermore, the extent of secondary flow effect was a function of curvature ratio. This was evident by the comparison of friction factors of 500-ft and 1000-ft 1-in. CT, as presented in Fig. 5.10. It was noted that 500-ft CT string was spooled on to a drum of smaller diameter

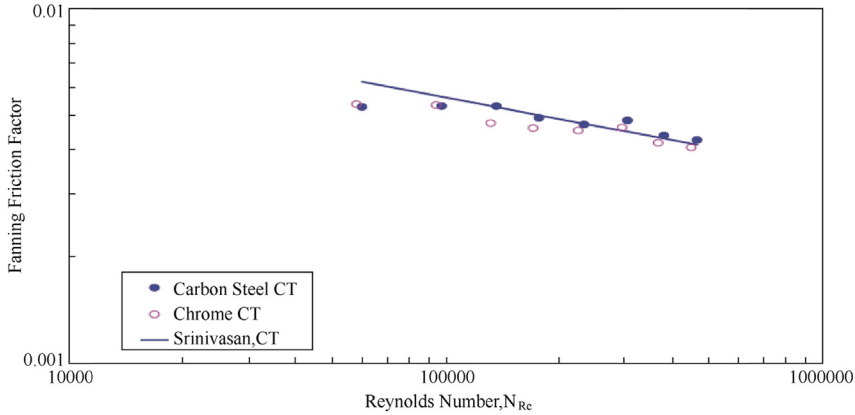

Figure 5.12 Fanning friction factor versus Reynolds number of water in 1¾-in. chrome and carbon steel coiled tubing (CT).

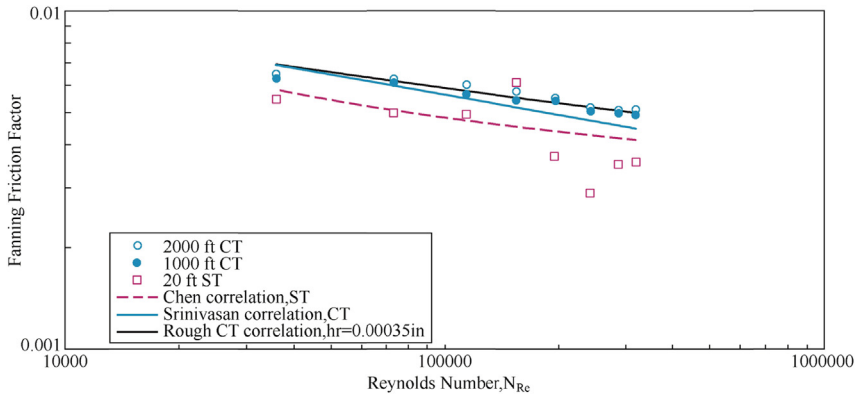

Figure 5.13 Fanning friction factor versus Reynolds number of water in 2⅜-in. straight and coiled tubing (ST and CT, respectively).

(48 in.) than 1000-ft CT string, which was spooled on to a 72-in. diameter drum. The 500-ft CT reel had a higher curvature ratio ($a/R = 0.0169$) than 1000-ft CT reel ($a/R = 0.0113$). The difference in friction factors between 500- and 1000-ft CT reels could be as high as 8%. Also, for the CT reels with same curvature ratio, the corresponding friction factors were approximately the same, as presented in Figs. 5.11 and 5.13.

Second, Figs. 5.10 and 5.13 indicated that the friction factors in 1-in. and 2⅜-in. CT reels were higher than Srinivasan correlation. Therefore, the tubing roughness effect was evident in both CT sizes. To estimate the magnitude of possible tubing roughness, the previously proposed

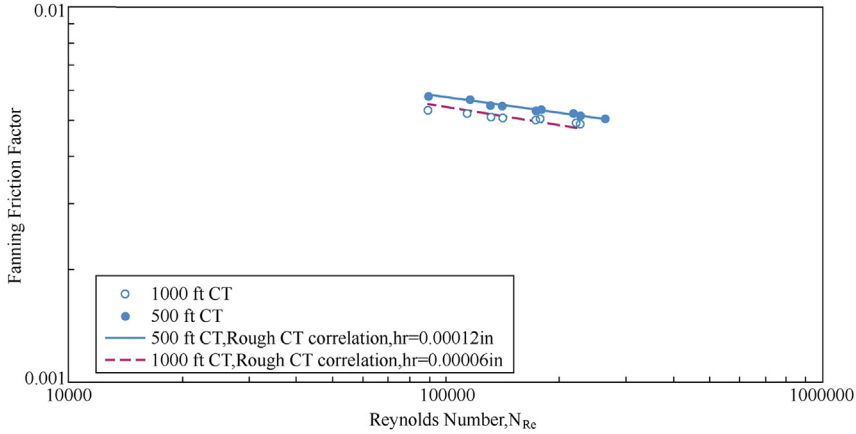

Figure 5.14 Friction factor versus Reynolds number of 1-in. tubing, measured and predicted through proposed rough coiled tubing (CT) correlation.

correlation [Eq. 5.5] was applied to match the friction factor data of 1-in. and 2⅜-in. CT. Fig. 5.14 presents 1-in. CT reel result. It was observed that the proposed correlation was able to match the friction factor data of 500-ft and 1000-ft CT with tubing roughness of 0.00012 and 0.00006 in., respectively. As indicated in Fig. 5.13, a tubing roughness of 0.00035 in. resulted in quite good match of the friction factor data with Eq. (5.5). It was encouraging to find out that these roughness values were quite similar to the roughness data measured by the Tuboscope's Hommel surface roughness meter on similar CT. The measured average roughness for a new carbon steel CT is between 0.000025 and 0.000149 in.

It is important to point out that the newly proposed correlation (Eq. 5.5) not only matched the majority of data on point-to-point basis, but also, more importantly, provided a good match to the data trend. This has been proven for both 1-in. and 2⅜-in. tubing data sets, as presented in Figs. 5.13 and 5.14, respectively. In these plots, it could be observed that Srinivasan correlation had a steeper slope than the correlations of data points, which exhibited flatter slopes. The friction factor behavior of Newtonian fluid in straight pipes was recalled, such as in Moody diagram of the friction factor. The smooth pipe flow or "hydraulically smooth" pipe flow is characterized by steeper slopes than the rough pipe flow, with a slope dependence on the magnitude of Reynolds number. The flatter lines indicated higher dominance of roughness at higher Reynolds numbers. The newly proposed correlation (Eq. 5.5) was seen to be able to effectively adjust the slope of Srinivasan correlation to better match the experimental data of CT with roughness.

It could be observed in Fig. 5.11 that the friction factor data of 1½-in. CT were quite close to Srinivasan correlation. This does not necessarily mean that 1½-in. CT reels were smooth. It was quite likely that the inner diameter of 1½-in. tubing had been changed due to previous usage. Prior to this research project, 1½-in. CT reels had been used extensively for testing fracturing slurries. These previous tests might have altered the tubing inner diameter (enlarged due to slurry erosion). It would be very tempting to have one parameter, either the tubing ID or roughness, independently measured so that the other parameter could be estimated from the water test data through proposed correlation in Eq. (5.5). In contrast, neither measurement was available.

It was interesting to note that the friction factor data for 1¾-in. chrome CT were lower than 1¾-in. carbon steel CT data. It was therefore believed that the chrome tubing had lower roughness effects. The friction factor of the chrome tubing was slightly lower than Srinivasan correlation. Through the new correlation (Eq. 5.5), the roughness in 1¾-in. carbon steel CT was estimated at 0.00005 in.

5.3 PRESSURE LOSS CALCULATION OF NON-NEWTONIAN FLUID IN COILED TUBING

The importance of pressure loss in the design of treatments for various field applications with non-Newtonian fluids necessitates the estimation of pressure loss in the reeled part of CT unit.

By using the fluid mixing system, as presented in Fig. 5.15 (Medjani & Shah, 2000), which consisted of two 50-bbl tanks with paddles and a centrifugal pump to aid the mixing of gels, three polymeric solutions A, B, and C were prepared for this investigation. Three concentrations of polymer solutions A (20, 30, 40 lb/Mgal) and B (10, 20, and 40 lb/Mgal), and two concentrations of polymer solution C (20 and 40 lb/Mgal) were investigated. All fluids were tested in three CT lengths for a given CT size.

The system was composed of 1500 ft of 1-in. CT manifold system allowing the usage of 500, 1000, and 1500-ft tubing. The second set of CT was 5000 ft of 1½-in. CT manifold system, allowing the utilization of 1000, 2000, and 3000 ft of tubing. The third set of CT was 3000 ft of 2⅜-in., allowing the utilization of 1000, 2000, and 3000 ft of tubing.

These CT systems were utilized for fluid friction pressure loss tests. The differential pressure was measured across each coil as well as the spanning 20 ft ST prior to and following the CT reel.

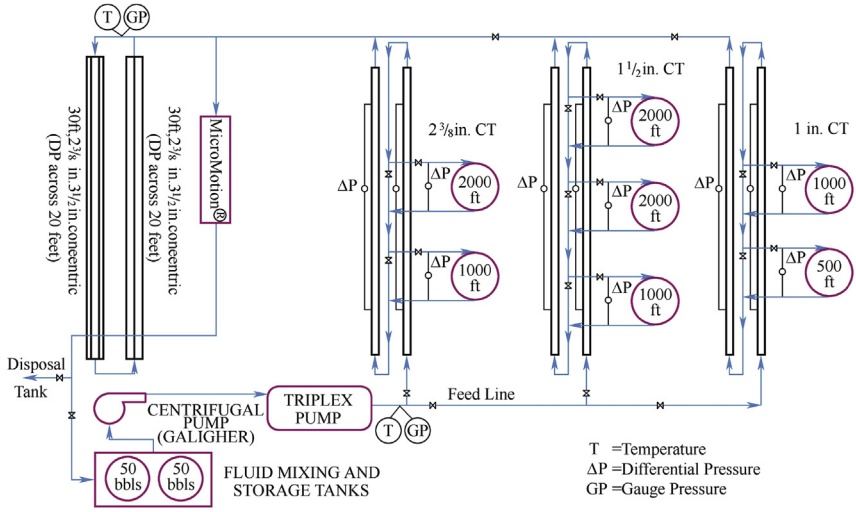

Figure 5.15 Equipment layout.

The viscometer data of polymeric fluids were converted to obtain the wall shear stress, τ_w, and shear rate, γ, data and plotted on a logarithmic paper. The value of slope provided the power law flow behavior index, n, and the intercept at unity shear rate provided the consistency index, K_V. Since the consistency index, K, depends on flow geometry, K_V was converted to K_P to be utilized in CT calculations. The rheological data (n,K) were obtained for all tested fluids.

The plot of calculated friction factors versus generalized Dean number for all three concentrations of solution A in all three CT sizes is presented in Fig. 5.16. The data were fitted with the power law regression curve $Y = a + \frac{b}{(X^c)}$ with $R^2 = 0.84$.

The friction factor versus generalized Dean number data of all three concentrations of solution B in Fig. 5.17 could be well fitted with correlation of the form $Y = a + \frac{b}{(X^c)}$ with $R^2 = 0.98$.

A comparison among friction factors of 20 lb/Mgal solution C in various lengths of 2⅜-in. CT is presented in Fig. 5.18. The results did not demonstrate a significant difference because the curvature ratio in all three cases was almost the same.

The friction factor versus generalized Dean number for two concentrations of polymeric solution C in Fig. 5.19 yielded an excellent correlation of the form $Y = a + \frac{b}{(X^c)}$ with $R^2 = 0.98$.

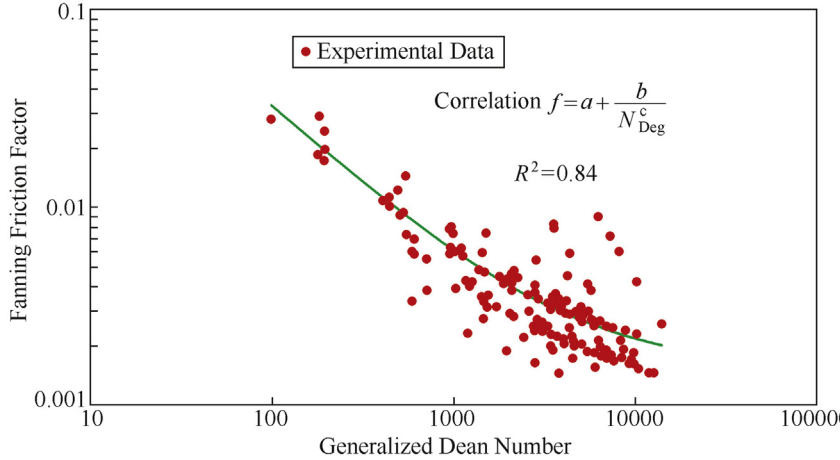

Figure 5.16 Fanning friction factor versus generalized Dean number for 20, 30, and 40 lb/Mgal solution A.

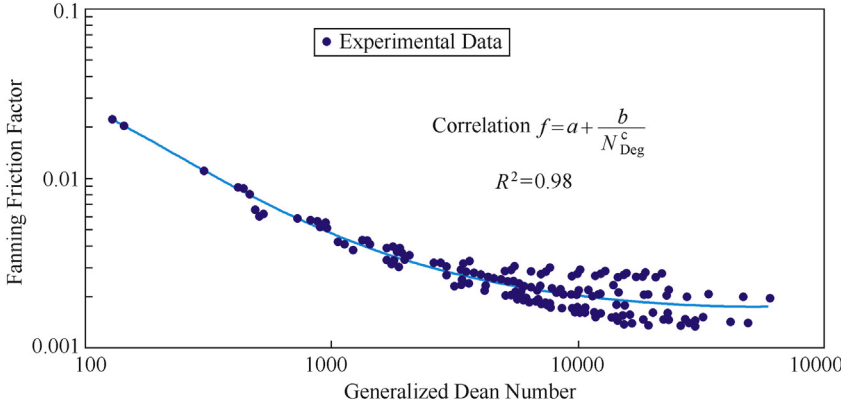

Figure 5.17 Friction factors versus generalized Dean number for 10, 20, and 40 lb/Mgal solution B.

With consideration that the friction factor was a function of generalized Reynolds number, the curvature ratio of CT, and rheological parameters governing the flow, the idea was to suggest a model that governed all these parameters. In this study, a model of the following form was suggested:

$$f = a + \frac{b}{N_{\mathrm{De},g}{}^{c}}, \tag{5.8}$$

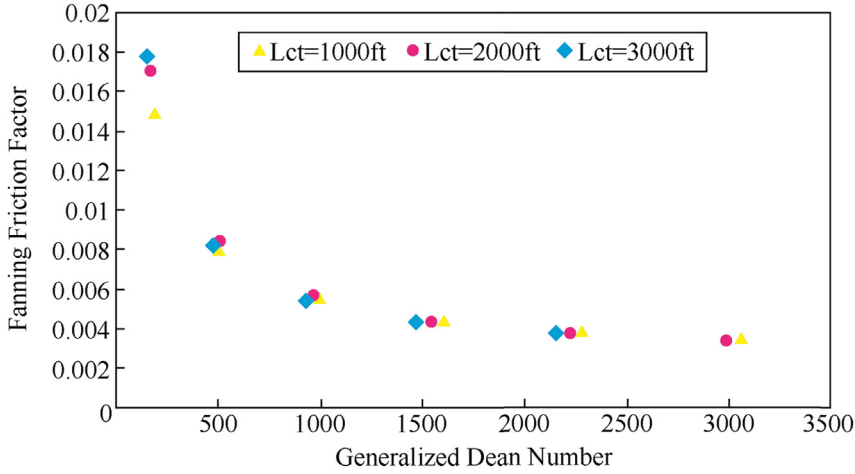

Figure 5.18 Comparison between friction factors of 20 lb/Mgal solution C for various lengths of 2⅜-in. coiled tubing.

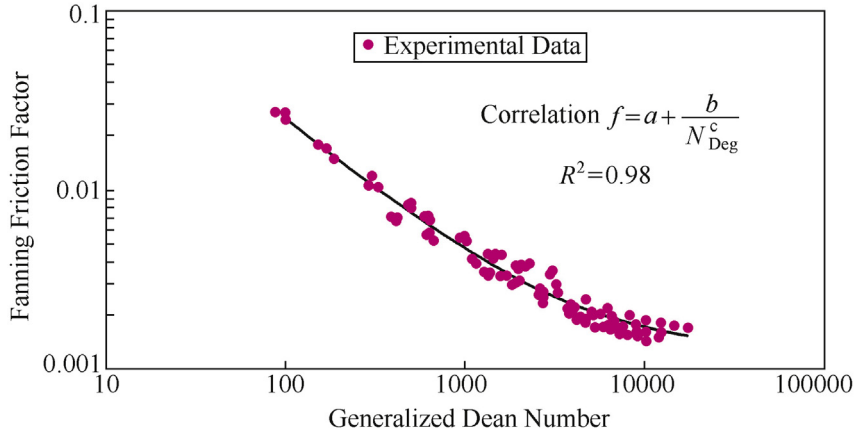

Figure 5.19 Friction factor versus generalized Dean number for 20 and 40 lb/Mgal solution C.

where the constants a, b, and c are defined as:

$$a = a_1(1-n)^{a_2}\left(\frac{r}{R}\right)^{d_1}, \tag{5.9}$$

$$b = 0.079 + b_1(1-n)^{b_2}, \tag{5.10}$$

and

$$c = 0.25 + c_1(1-n)^{c_2} \tag{5.11}$$

where f is Fanning friction factor, which is dimensionless; a, b, and c are constants; R is curvature radius; r is CT radius; n is flow behavior index of power law fluid, which is dimensionless; n_γ is number of wraps; $N_{\mathrm{De},g}$ is generalized Dean number, which is dimensionless; and $N_{\mathrm{Re},g}$ is generalized Reynolds number, where $N_{\mathrm{De},g} = N_{\mathrm{Re},g}\left(\frac{r}{R}\right)^{0.5}$.

The constants were selected in such manner that the friction factor was a function of generalized Reynolds number (for ST) or generalized Dean number (for reeled CT), which included the curvature ratio $\left(\frac{r}{R}\right)$ and flow behavior index, n. The values of 0.079 and 0.25, selected in Eqs. (5.10) and (5.11), respectively, were from the following Blasius equation (Blasius, 1913) for turbulent flow of Newtonian fluid in straight pipes:

$$f = \frac{0.079}{N_{\mathrm{Re}}{}^{0.25}}, \tag{5.12}$$

For Newtonian fluid ($n = 1$) and for the fluid flow within straight pipe, the proposed Eq. (5.8) was reduced to Eq. (5.12), as Blasius equation.

5.3.1 Laminar Flow of Non-Newtonian Fluid in Coiled Tubing

The friction factor in a curved pipe at a given Reynolds number exceeds the factor in a straight pipe because of secondary flow existence, which is caused by the effect of centrifugal forces in curved flow geometry. A recent literature review indicated that the flow of Newtonian fluids in curved pipes has been studied extensively since the pioneering work of Dean (Zhou & Shah, 2004). In contrast, the information on studies of non-Newtonian fluid flow in curved pipes is relatively scarce.

For non-Newtonian fluid in laminar flow, a new correlation was developed through boundary-layer approximation analysis and by numerical solution of the flow equations of a power law model fluid in CT. The correlation is presented in an empirical form for convenience.

Following the approach of boundary-layer approximation and with the assumption of a power law model fluid, Zhou and Shah (2002, 2007) developed the following friction factor correlation for laminar non-Newtonian fluid flow in CT:

$$f_{\mathrm{CL}} = \alpha(2)^{\frac{n}{n+1}} N_{\mathrm{Deo}}^{-1/(n+1)} \left(\frac{a}{R}\right)^{1/2} Y^{-\frac{3n}{n+1}}, \tag{5.13}$$

where

$$Y = c_0 + \frac{c_1}{N_{\mathrm{Deo}}} + c_2 n + \frac{c_3}{N_{\mathrm{Deo}}{}^2} + c_4 n^2 + c_5 \frac{n}{N_{\mathrm{Deo}}}, \tag{5.14}$$

and

$$\alpha = \left[a' + b' \ln(n)^2\right], \tag{5.15}$$

where c_0 through c_5 and α' and b' are correlation constants, n is the flow behavior index of fluid, and Dean number, N_{Deo}, here, is defined as:

$$N_{\mathrm{Deo}} = \frac{(2a)^n v_m^{2-n} \rho}{K} \sqrt{a/R}, \tag{5.16}$$

A generalized Dean number, N_{Deg}, was introduced:

$$N_{\mathrm{Deg}} = N_{\mathrm{Reg}} \left(\frac{a}{R}\right)^{1/2}, \tag{5.17}$$

where N_{Reg} is generalized Reynolds number:

$$N_{\mathrm{Reg}} = \frac{d^n v_m^{2-n} \rho}{K_p 8^{n-1}}, \tag{5.18}$$

It could consequently be presented that

$$N_{\mathrm{Deo}} = 2^{3(n-1)} \left(\frac{3n+1}{4n}\right)^n N_{\mathrm{Deg}} \tag{5.19}$$

where a is radius of CT, R is radius of CT reel, a/R is curvature ratio, N_{Deg} is generalized Dean number, N_{Deo} is Dean number, N_{Reg} is generalized Reynolds number, v_m is mean velocity, K is consistency index of the power law model, and K_P is consistency index determined from pipe viscometer data.

This correlation was developed from the numerical solution flow equations of a power law fluid in curved pipe. According to the simplified flow model, the flow through tubing cross-section was divided into two regions: a central inviscid core and a thin boundary layer adjacent to the tubing wall, as presented in Fig. 5.20.

This new correlation was compared with Mashelkar and Devarajan correlation (Mashelkar & Devarajan, 1976). It was discovered that the new correlation was in closer agreement with the experimental results (Zhou & Shah, 2002). For $n = 1$ (Newtonian fluid), the new correlation matched well with the Ito correlation, whereas the Mashelkar and Devarajan correlation did not.

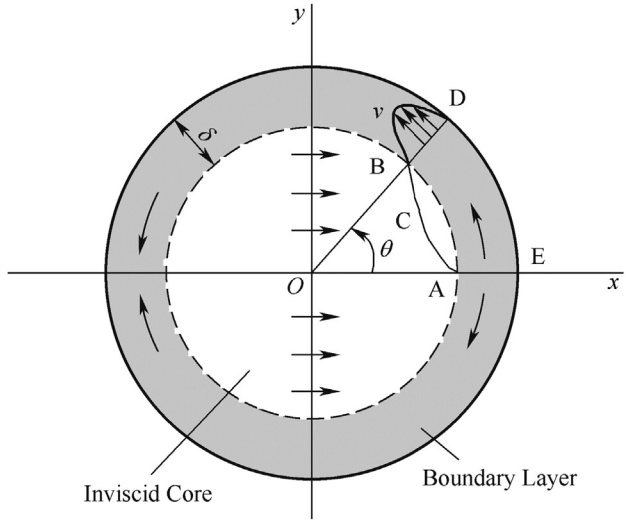

Figure 5.20 Flow model of inviscid core and boundary layer.

5.3.2 Turbulent Flow of Non-Newtonian Fluid in Coiled Tubing

The correlation for non-Newtonian fluids in turbulent flow was developed on the basis of the extensive flow experiments in CT.

Fig. 5.21 (Zhou & Shah, 2006) presents a schematic of the full-scale CT flow loop at the University of Oklahoma. The flow loop consisted of

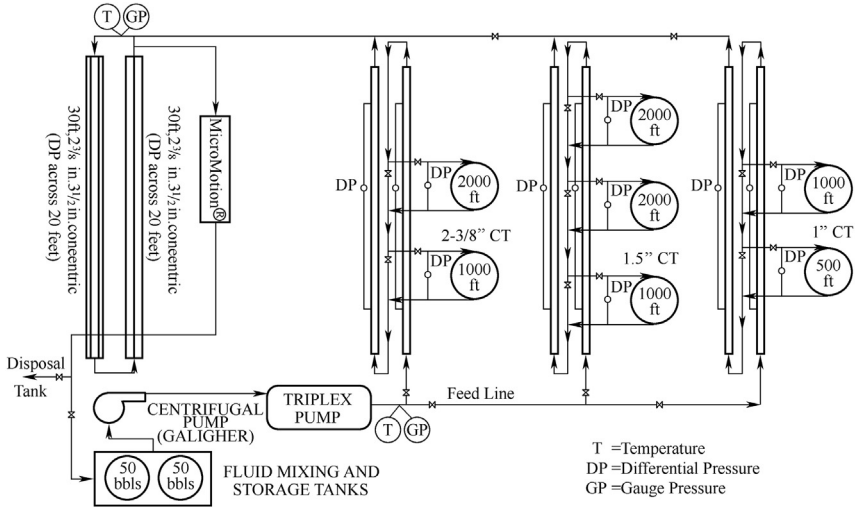

Figure 5.21 Schematic of full-scale coiled tubing test facility.

Table 5.3 Dimensions of coiled tubing reels

Reel no.	Coiled tubing outside diameter (in.)	Coiled tubing inside diameter (in.)	Length (ft)	Reel diameter (in.)	Curvature ratio (a/R)
1	1	0.810	500	48	0.0169
2	1	0.810	1000	72	0.0113
3	$1^1/_2$	1.188	1000	72	0.0165
4	$1^1/_2$	1.188	2000	72	0.0165
5	$1^1/_2$	1.188	2000	72	0.0165
6	$2^3/_8$	2.063	1000	111	0.0185
7	$2^3/_8$	2.063	2000	111	0.0185

several reels of 1-, $1^1/_2$-, and $2^3/_8$-in. CT strings, as well as straight and annular sections. The dimensions of CT reels are given in Table 5.3. It was noted that the reels had four curvature ratios: 0.0113, 0.0165, 0.0169, and 0.0185, depending on the tubing diameter and reel drum diameter.

The fluids tested were typical drilling, completion, and stimulation fluids currently utilized in the industry, including polymeric solutions, drilling mud, and surfactant-based fluids. These fluids were recommended by members of the Joint Industry Coiled Tubing Consortium. Rheologically, the fluids were non-Newtonian and could be described by a power law model within the flow conditions investigated. The fluids utilized for correlation development in this study were all polymer solutions: 20, 30, and 40 lbm/1000 gal guar gum; 20, 30, and 40 lbm/1000 gal hydroxyethyl cellulose (HEC) solution; 10, 20, and 40 lbm/1000 gal xanthan gum; and 20 and 40 lbm/1000 gal partially hydrolyzed polyacrylamide (PHPA) solution.

The primary measured data included the frictional pressure drops across coiled and straight sections of CT at various flow rates, and the rheological properties were measured by CS-50 Bohlin rheometer and Fann Model 35 viscometer. Significant detailed descriptions of the test facility and experimental procedure could be found elsewhere (Shah & Zhou, 2001, 2003).

The measured frictional pressure drops were converted to Fanning friction factor by the following expression:

$$f_c = \frac{\tau_w}{\frac{1}{2}\rho v_m^2}, \tag{5.20}$$

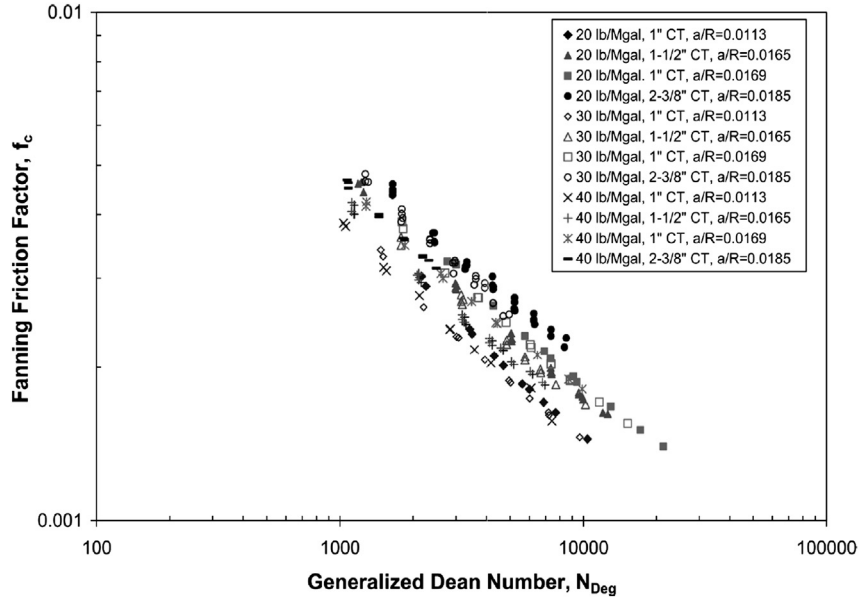

Figure 5.22 Friction factor versus generalized Dean number for guar solutions in coiled tubing (CT).

where

$$\tau_w = \frac{d\Delta p}{4L}, \tag{5.21}$$

The generalized Dean number, N_{Deg}, can be calculated through Eqs. (5.17) and (5.18). A typical plot of f_c versus N_{Deg} is presented in Fig. 5.22 for the guar fluids.

Further analysis of turbulent flow data demonstrated that the following form of correlation for friction factor could be applied for all guar, HEC, and PHPA fluids:

$$f_{\mathrm{CT}} = \frac{[c_1 + c_2 \ln n + c_3(a/R)]\left[c_4 + c_5(a/R)^{1.5}\right]}{{N_{\mathrm{Deg}}}^{\beta}}, \tag{5.22}$$

where c_1 through c_5 and β are correlation constants and are determined separately for guar, HEC, and PHPA fluids.

For xanthan fluids, the following correlation was obtained:

$$f_{\mathrm{CT}} = \frac{[c_1 + c_2(a/R)]}{{N_{\mathrm{Deg}}}^{\beta}}, \tag{5.23}$$

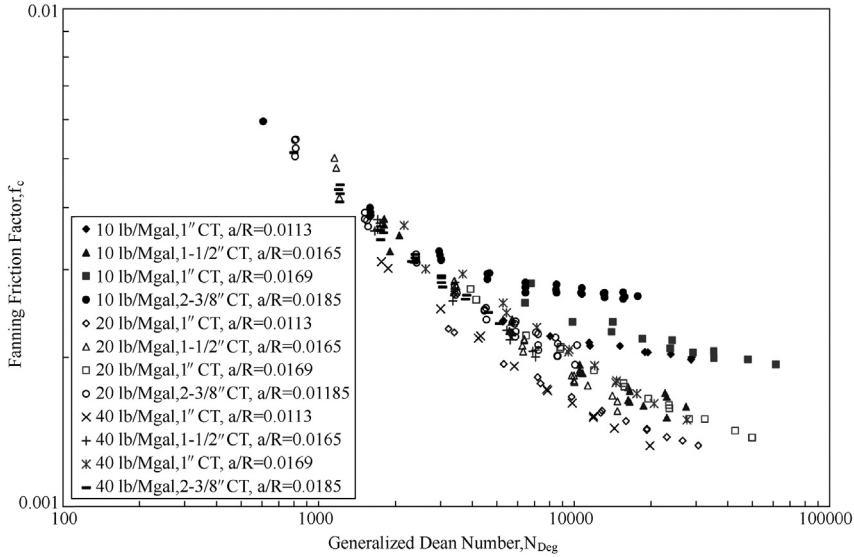

Figure 5.23 Friction factor versus generalized Dean number for xanthan gums in coiled tubing (CT).

In the development of aforementioned xanthan fluid correlation, the data of 10 lbm/1000 gal xanthan were not included, because the flow behavior of 10 lbm/1000 gal xanthan was drastically different from the flow behavior of higher concentrations, as presented in Fig. 5.23.

5.4 DRAG REDUCTION CHARACTERISTICS IN COILED TUBING

Excessive friction pressure loss due to small tubing diameter and curvature (which is believed to cause secondary flow) of CT often limits the maximum obtainable fluid flow rate in most CT operations. A good drag reduction property becomes a desirable quality for drilling, completion, and workover fluids for CT applications. Even so, the drag reduction phenomenon in CT has not been well understood.

It has been observed that the addition of a low amount of specific high-molecular-weight polymers known as "drag reducers" under turbulent pipe flow condition can drastically decrease the friction pressure gradient and consequently, increase the pumping capacity. These drag-reducing fluids include polymers, surfactants, and fibers. The drag reduction phenomenon under turbulent flow in ST has been studied extensively, whereas little information on drag-reducing fluids flowing through CT exists. It is known

that fluids behave differently within ST and CT. In curved pipes, the central part of fluid is forced outward due to the centrifugal force. The slower part along the wall is forced inward, where pressure is lower causing secondary flow right angle to the main flow.

Shah, Kamel, and Zhou (2006) and Shah and Vyas (2010) carried out experiments on the drag reduction performance of commonly utilized drag-reducing agents, high-molecular-weight, anionic AMPS (2-acrylamido-2-methyl propane sulfonate and acrylamide) copolymers (Nalco ASP-820), in ST and CT. The flow loop used consisted of three ½-in. outer diameter (OD) CT reels with curvature ratios of 0.01, 0.019, and 0.031. A ½-in. OD, 10-ft straight section was also included to compare the drag reduction behavior between ST and CT. Various concentrations of the drag-reducing fluid were tested. The optimum concentration was subsequently determined from the results of drag reduction exhibited by fluid. The differential pressure versus flow rate data were reduced in terms of Fanning friction factor and solvent Reynolds number for the estimation of drag reduction characteristics.

The experimental setup, utilized in this study, is presented in Fig. 5.24. The flow loop consisted of the following components:

- A 1000-gal polyethylene tank for fluid mixing and storage.
- A centrifugal feeder pump that fed the fluid to Moyno pump.

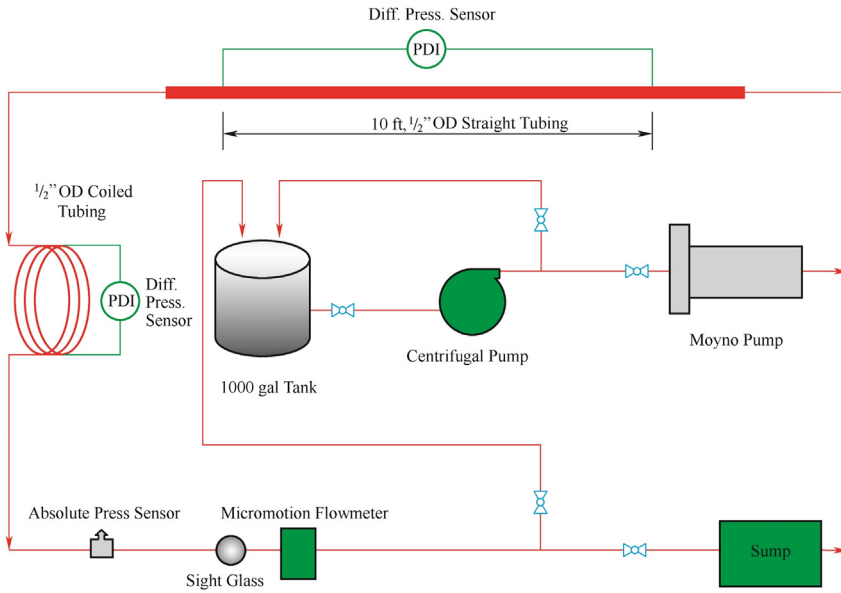

Figure 5.24 Schematic of fluid flow loop.

Table 5.4 Specifications of coiled tubing utilized in flow loop

OD (in.)	ID (in.)	Core diameter[a] (ft)	Ratio (r/R)	No. of tums	Length (ft)
0.5	0.435	3.608	0.010	3	36.14
0.5	0.435	1.878	0.019	3	18.83
0.5	0.435	1.168	0.031	6	23.26

[a]Measured from core center to tubing center.

- A ½-in. tubing was utilized as flow conduit (0.435-in. ID). The flow system had a 15-ft straight section (with 3 and 2 ft as entrance and exit lengths, respectively) and three replaceable CT reels with different curvature ratios. The specifications of the utilized CT reels are presented in Table 5.4. The curvature ratios presented in this table covered the utilized range in field operations.
- Pressure transducers were utilized for the measurement of frictional pressure losses in straight section of tubing and in coils. The measurement range could be selected between 0 and 100 psi.
- An absolute pressure sensor measured the working pressure of system. The maximum working pressure of system was 1000 psi.
- A MicroMotion Elite Model CMF050 Sensor, capable of flow rate in the range of 0−30 gal/min, fluid density with accuracy of ±0.0005 g/cc and temperature with an accuracy of ±1°C or ±0.5% of reading in °C measurements was used.
- The wireless Fluke Hydra data logger system was utilized for data acquisition. The data were transmitted to a personnel computer in control room and were displayed live on the screen. This contributed to the quality control monitoring of the data being gathered during testing.

Correlations have been developed to predict the friction factor values as a function of solvent Reynolds number for both ST and CT with the data of a polymeric fluid with optimum concentration of 0.07%.

A ST correlation predicts the friction factor (f_t) value as a function of solvent Reynolds number (N_{Res}), whereas for CT, it predicts the friction factor (f_t) value as a function of solvent Reynolds number (N_{Res}) and curvature ratio (r/R).

The correlation for ST is

$$f_t = A - \left[\frac{B}{\ln(N_{Res})}\right] + \left[\frac{C}{N_{Res}{}^{0.5}}\right], \tag{5.24}$$

The correlation for CT is

$$f_t = A'\left[\frac{r}{R}\right]^{B'}\left[\frac{1.0}{N_{\mathrm{Res}}{}^{C'}}\right], \tag{5.25}$$

where $A = 0.00907$, $B = 0.12116$, $C = 0.80{,}436$, $A' = 2.17865$, $B' = 0.26465$, and $C' = 0.49391$ (Shah & Ahmed Kamel, 2005; Shah et al., 2006).

The values of correlation coefficient obtained for the aforementioned two equations were quite similar to unity ($R^2 = 0.99$ for ST and $R^2 = 0.99$ for CT), indicating an excellent agreement among the data and correlations.

Both correlations displayed reasonably good agreement with the experimental data from ½-in. ST and CT. The average absolute percentage deviation was 2.3%, with a maximum deviation of 3.9%. These correlations were valid for smooth pipes at the optimum polymer concentration of 0.07% (by vol.) and over the entire range of data [$0.01 < (r/R) < 0.031$ and $22{,}000 < N_{\mathrm{Res}} < 155{,}000$].

Fig. 5.25 presents a comparison between the predicted and experimental Fanning friction factors as a function of solvent Reynolds number, for both ST and CT. It could be observed that a good agreement exists between the

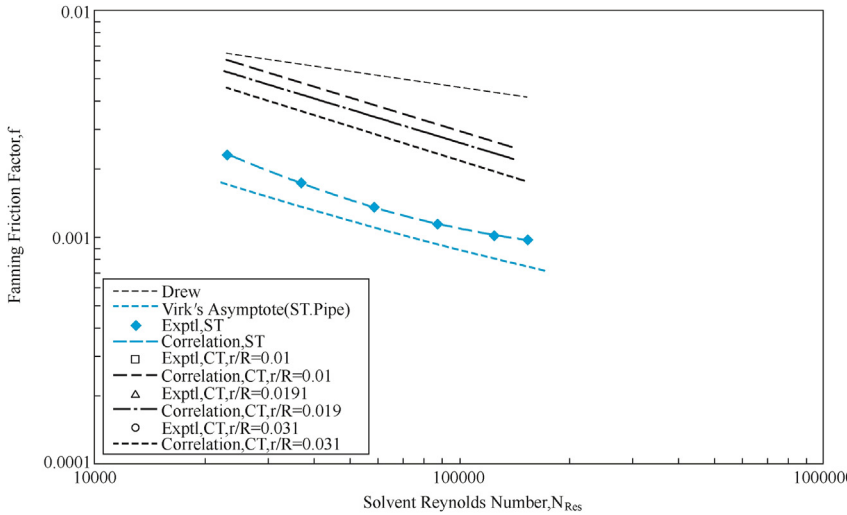

Figure 5.25 Comparison between experimental data and predicted values of Fanning friction factor for 0.07% polymeric fluid in coiled tubing (CT).

experimental and predicted values. The lowest percentage deviation was lower than 3% for 0.01 curvature ratio and the highest was lower than 6% for 0.019 curvature ratio, whereas the percentage deviation was lower than 1% for the ST. It could also be observed that as the curvature ratio increased, the friction factor increased, which meant that the percentage drag reduction decreased. It should be noted here, that 0.07% anionic AMPS copolymer did not exhibit the maximum drag reduction as predicted by Virk's (1975) maximum drag reduction asymptote.

From the preceding results and discussion, it was evident that the correlations developed with ½-in. flow loop data were sufficient to predict Fanning friction factors in large-sized ST and CT within the corresponding application ranges [$0.01 < (r/R) < 0.031$ and $22{,}000 < N_{Res} < 155{,}000$]. Beyond this range, the predictions from correlations deviated significantly from the experimental data. This might be primarily because of the differences in shear field, pipe roughness, and CT curvature ratio. With consideration of these various effects, new correlations (Shah & Kamel, 2010) for a wider range of applications were developed with all the available data. These correlations are as follows:

For the ST

$$f_{DR} = 0.0006189 + 9.6837 \times 10^{-22} {N_{Res}}^3 + 3.88458 \frac{\ln(N_{Res})}{N_{Res}}, \quad (5.26)$$

and for the CT

$$f_{DR} = 2.72687 \left(\frac{r}{R}\right)^{0.448984} \left(\frac{1.0}{{N_{Res}}^{0.445824}}\right), \quad (5.27)$$

The correlation coefficient values obtained for these two correlations were nearly at unity ($R^2 = 0.99$ for ST and $R^2 = 0.98$ for CT), indicating an excellent agreement between the data and correlations. The worst percentage deviation was lower than 7%, whereas the average deviation was lower than 4%.

Figs. 5.26 and 5.27 depict a comparison between the predicted and experimental Fanning friction factors as a function of solvent Reynolds number for ST and CT, respectively. A reasonably good agreement between the experimental and predicted values could be observed. These correlations were valid for the optimum polymer concentration of 0.07 vol% and a wide range of data [$0.0165 < (r/R) < 0.0225$ and $22{,}000 < N_{Res} < 900{,}000$].

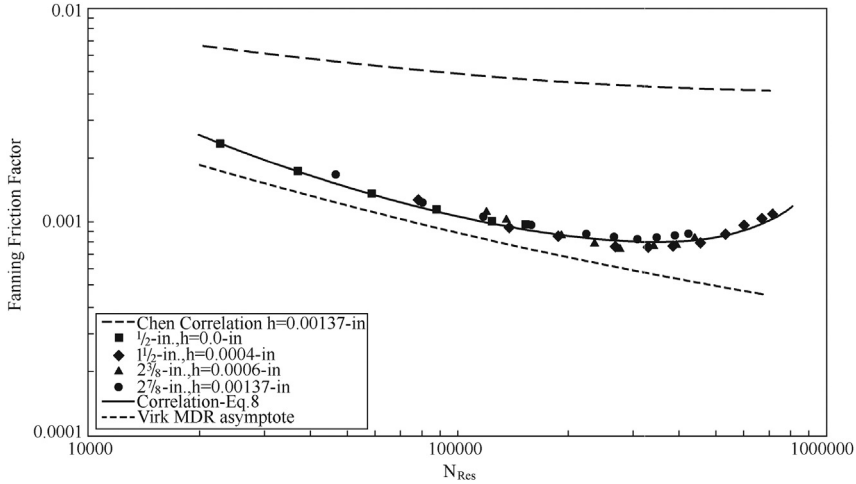

Figure 5.26 Comparison between predicted and measured Fanning friction factors of 0.07% ASP-820 fluid in straight tubing.

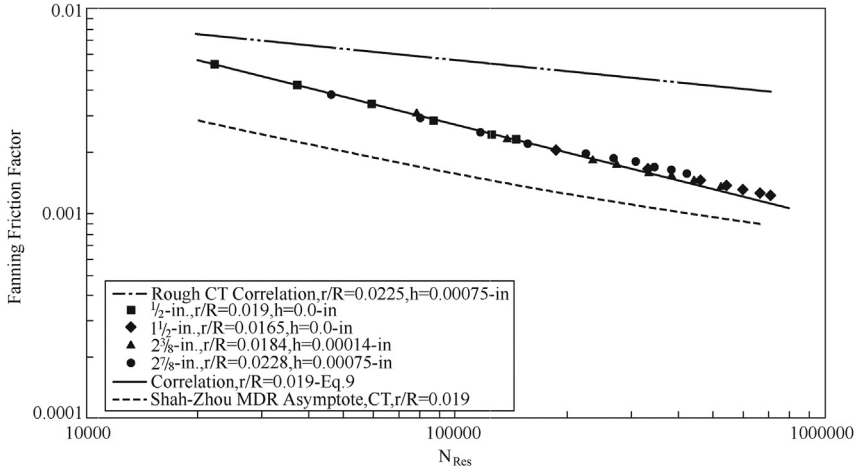

Figure 5.27 Comparison between predicted and measured Fanning friction factors of 0.07% ASP-820 fluid in coiled tubing (CT).

REFERENCES

Blasius, H. (1913). Das ähnlichkeitsgesetz bei reibungsvorgängen in flüssigkeiten. In *Mitteilungen über Forschungsarbeiten auf dem Gebiete des Ingenieurwesens* (pp. 1–41). Springer.

Chen, N. H. (1979). An explicit equation for friction factor in pipe. *Industrial and Engineering Chemistry Fundamentals, 18*(3), 296–297.

Colebrook, C. F., Blench, T., Chatley, H., Essex, E., Finniecome, J., Lacey, G., et al. (1939). Turbulent flow in pipes, with particular reference to the transition region between the smooth and rough pipe laws. *Journal of the Institution of Civil Engineers, 12*(8), 393–422.

Dean, W. (1927). XVI. Note on the motion of fluid in a curved pipe. *The London, Edinburgh, and Dublin Philosophical Magazine and Journal of Science, 4*(20), 208–223.

Dongjun, M., Gensheng, L., Huang, Z., Jilei, N., Cheng, H., Mingjuan, L., et al. (2012). A model of calculating the circulating pressure loss in coiled tubing ultra-short radius radial drilling. *Petroleum Exploration and Development, 39*(4), 528–533.

Drew, T., Koo, E., & McAdams, W. (1932). The friction factor for clean round pipes. *Transactions AIChE, 28*, 56–72.

FLUENT Inc. (2006). F. 6.3 User's Guide. Determining turbulence parameters.

Mashelkar, R., & Devarajan, G. (1976). Secondary flows of non-Newtonian fluids: Part I—laminar boundary layer flow of a generalized non-Newtonian fluid in a coiled tube. *Transactions of the Institution of Chemical Engineers, 54*(2), 100–107.

Medjani, B., & Shah, S. (2000). A new approach for predicting frictional pressure losses of non-Newtonian fluids in coiled tubing. In *Paper SPE 60319 presented at the SPE Rocky Mountain Regional/Low-Permeability Reservoirs Symposium and Exhibition, Denver, CO.*

Shah, S., & Ahmed Kamel, A. (2005). Drag reduction in straight and coiled tubing. In *Paper presented at The University of Oklahoma, Coiled Tubing Consortium Annual Meeting, Houston, TX.*

Shah, S. N., & Jain, S. (2008). Coiled tubing erosion during hydraulic fracturing slurry flow. *Wear, 264*(3), 279–290.

Shah, S. N., & Kamel, A. (2010). Investigation of flow behavior of slickwater in large straight and coiled tubing. *SPE Production and Operations, 25*(01), 70–79.

Shah, S. N., Kamel, A., & Zhou, Y. (2006). Drag reduction characteristics in straight and coiled tubing—an experimental study. *Journal of Petroleum Science and Engineering, 53*(3), 179–188.

Shah, S. N., & Vyas, A. (2010). Temperature and salinity effects on drag-reduction characteristics of polymers in coiled tubing. In *Paper presented at the SPE/ICoTA Coiled Tubing and Well Intervention Conference and Exhibition, Houston, TX.*

Shah, S. N., & Zhou, Y. (2001). An experimental study of the effects of drilling solids on frictional pressure losses in coiled tubing. In *Paper SPE 67191 presented at the SPE Production and Operations Symposium, OKC, OK.*

Shah, S. N., & Zhou, Y. (2003). An experimental study of drag reduction of polymer solutions in coiled tubing. *SPE Production and Facilities, 18*(4), 280–287.

Srinivasan, P., Nandapurkar, S., & Holland, F. (1970). Friction factors for coils. *Transactions of the Institution of Chemical Engineers, 48*(4–6), T156–T161.

Virk, P. S. (1975). Drag reduction fundamentals. *AIChE Journal, 21*(4), 625–656.

Zhang, J.-K., Li, G.-S., Huang, Z.-W., Tian, S.-C., Shi, H.-Z., & Song, X.-Z. (2012). Numerical simulation on friction pressure loss in helical coiled tubing. *Journal of China University of Petroleum (Edition of Natural Science), 2*, 018.

Zhou, Y. (2006). *Theoretical and experimental studies of power-law fluid flow in coiled tubing (Doctoral dissertation).* Norman, OK: University of Oklahoma.

Zhou, Y., & Shah, S. (2002). Non-Newtonian fluid flow in coiled tubing: theoretical analysis and experimental verification. In *Paper SPE 77708 presented at the SPE Annual Technical Conference and Exhibition, San Antonio, TX.*

Zhou, Y., & Shah, S. (2004). Fluid flow in coiled tubing: a literature review and experimental investigation. *Journal of Canadian Petroleum Technology, 43*(06).

Zhou, Y., & Shah, S. N. (2006). New friction factor correlations of non-Newtonian fluid flow in coiled tubing. *SPE Drilling and Completion, 21*(01), 68–76.

Zhou, Y., & Shah, S. (2007). Theoretical analysis of laminar flow of power-law fluids in coiled tubing. *AIChE Journal, 53*(9), 2210–2220.

CHAPTER SIX

Operation Parameters Calculation

Contents

Abstract

In this part, the related hydraulic parameters, including the nozzle numbers, pressure drop, flow rate, pressure loss along the tubing, and the prediction of the surface pump pressure, are presented in detail. The main contents show how to calculate the aforementioned parameters using corresponding equations and methods. According to the calculated results, the operators can determine the bottom-hole assembly, possible maximum pump pressure, and the total fracturing fluid volume, etc. At the end of this chapter, through a practical field case, the calculation procedure and results are listed in a table. Then the operators can clearly know the working steps and the materials consumed in every step.

Keywords: Equation; Nozzle; Pressure drop; Pressure loss; Pump pressure.

6.1 RELATIONSHIP BETWEEN NOZZLE PRESSURE DROP AND FLOW RATE

The nozzle pressure drop and flow rate are important hydraulic parameters for hydra-jet fracturing. Only the nozzle diameter, nozzle number,

Abrasive Water Jet Perforation and Multi-Stage Fracturing
ISBN: 978-0-12-812807-7
https://doi.org/10.1016/B978-0-12-812807-7.00006-6

and nozzle pressure drop are determined; other relevant parameters such as flow rate and surface pressure can be calculated. Based on the experimental and theoretical researches, the nozzle pressure drop is expressed as (Shen, 1998):

$$P_b = \frac{513.559Q^2\rho}{A^2C^2} \tag{6.1}$$

The flow rate of the nozzle is expressed as:

$$Q = \left[\frac{P_bC^2A^2}{513.559\rho}\right]^{0.5} \tag{6.2}$$

where, P_b, Q, ρ, A, and C represent the nozzle pressure drop (MPa), flow rate (L/s), fluid density (g/cm^3), total area of nozzles (mm^2), and the nozzle discharge coefficient (generally equal to 0.9), respectively.

According to Eqs. (6.1) and (6.2), the flow rates were calculated for the nozzle of 6 mm diameter given different numbers and pressure drops. As shown in Fig. 6.1, with the same diameter, setting 6 mm as an example, the nozzle pressure drop was directly proportional to the flow rate. In other words, for the same diameter nozzle, a larger flow rate is required to generate a larger nozzle pressure drop. In addition, the more the number of nozzles, the lower the pressure drop presented. The nozzle with a greater pressure drop can produce a higher velocity jet. In this case, the targeted rock can be impacted by a larger force, thereby being broken

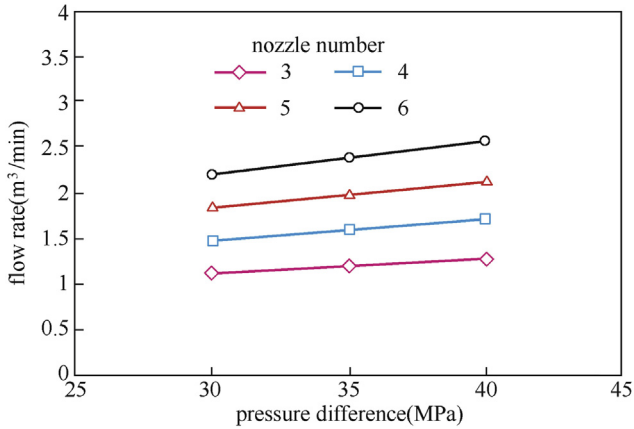

Figure 6.1 Nozzle pressure difference versus flow rate.

more easily. Thus within the pressure-bearing capability of work pipes and surface equipment, the nozzle pressure drop can be improved as high as possible (Tian, Li, Huang, Niu, & Xia, 2009).

6.2 FRICTIONAL PRESSURE LOSS IN WELLBORE

Fracturing fluid, as a viscoelastic fluid, has non-Newtonian shear thinning effect and obvious friction reduction effect (i.e., Toms effect) (Li & Yang, 2000). Due to the complexity of friction reduction mechanisms as well as the diverse influencing factors, there is no unified friction reduction model that can be used to calculate the pressure loss for different fracturing fluids (Hou, 1987; Yu, 1990). At present, many models, such as the S.N Shah model, the Hannah model, and the D.L. Lord model have been proposed to predict the pressure loss of fracturing fluid (Medjani & Shah, 2000; Shah, Zhou, & Goel, 2002; Zhou, 2001; Zhou & Shah, 2002). For the frictional pressure loss in conventional tubing pipe, the method of friction reduction ratio developed by Load et al. is usually used (Lord, 1987). As for the frictional pressure loss in the coiled tubing (CT), a theoretical model was established and then was modified based on the full-size experimental results.

6.2.1 Pressure Loss in Conventional Tubing Pipe

Based on a larger number of friction reduction experiments of hydrophilic polyacrylamide gel (HPG), Lord et al. put forward a concept of friction reduction ratio δ (Lord, 1987)

$$\delta = \frac{\Delta p_{G,p}}{\Delta p_0} \tag{6.3}$$

where $\Delta p_{G,p}$ and Δp_0 represent the frictional pressure losses of fracturing fluid and water, respectively.

In essence, friction reduction ratio is the difference that the Newtonian and non-Newtonian fluids present in the rheological properties. During the flow process, this difference can be characterized by the friction pressure loss. Thus the friction reduction ratio is mainly affected by material and cross-linking characteristics (Fayong, Zhang, & Lu, 2002).

6.2.1.1 Pressure Loss of Clear Water in Tubing Pipe

Based on the relationship of Reynolds number (Re) and friction coefficient, the details of the model can be shown as follows.

6.2.1.1.1 Reynolds Number and Flow Pattern

As early as 1883, based on a large number of experiments, Reynolds found that two different flow patterns existed in the flowing of tubing pipe and then proposed the criterion, i.e., Reynolds number (Re) for these two flow patterns.

For Newtonian fluid, Re can be calculated by the following formula:

$$\mathrm{Re} = \frac{vd\rho}{\mu} \tag{6.4}$$

In general, $\mathrm{Re}_c = 2000$ is regarded as a criterion. If the Re is less than 2100, the flow is laminar, whereas if the Re is greater than 2900, the flow is regarded as turbulent.

6.2.1.1.2 Friction Coefficient

For both Newtonian or non-Newtonian fluids, the friction coefficient can be expressed as follows:

$$f = \frac{a}{\mathrm{Re}^b} \tag{6.5}$$

where a and b are the constants.

For laminar flow, $a = 16$, $b = 1.0$.

As for the turbulent flow, the values of a and b can be determined by the flow index of n:

$$a = \frac{\log_{10} n + 3.93}{50} \tag{6.6}$$

$$b = \frac{1.75 - \log_{10} n}{7} \tag{6.7}$$

For Newtonian fluid, the flow index of n is equal to 1. In the different sections of tubing pipe, the fluids may be in different flow patterns. Thus the flow pattern should be determined before the frictional pressure loss is calculated.

6.2.1.1.3 The Frictional Pressure Loss in Tubing Pipe

According to the Fanning equation, the frictional pressure loss in oil tubing pipe can be expressed as follows:

$$\Delta P_f = \frac{2f\rho v^2 L}{d} \tag{6.8}$$

where ρ is the density of fluid in kg/m^3, v is the average velocity in tubing pipe in m/s, d is the inner diameter of tubing pipe in m, L is the length of

tubing pile in m, f is the Fanning friction coefficient, and ΔP_f is the frictional pressure loss in Pa.

6.2.1.2 Calculation of Friction Reduction Ratio

Friction reduction ratio is the function of the average velocity of fracturing fluid, the gelled agent concentration, and the proppant concentration. Based on the linear regression of 1049 experimental and field data, Lord et al. put forward the following empirical formula to calculate the friction reduction ratio of HPG fracturing fluid (Lord, 1987):

$$\ln\left(\frac{1}{\delta}\right) = 2.38 - \frac{8.024}{u} - 0.2365\frac{C_{\mathrm{HPG}}}{u} - 0.1639\ln C_{\mathrm{HPG}} - 0.028C_p\, e^{\left(\frac{1}{C_{\mathrm{HPG}}}\right)} \tag{6.9}$$

where C_p is the concentration of proppant in kg/m^3, C_{HPG} is the concentration of gelled agent in kg/m^3, and u is the average velocity of fracturing fluid in m/s.

6.2.2 Pressure Loss in Coiled Tubing

As the fluid flows in CT, two mechanisms for pressure loss exist in the pipe: the frictional pressure drop and the pressure loss caused by the helical flow in the spiral pipe (Blanco, Bailey, & Rosine, 2007; Shah, Kamel, & Zhou, 2006). Thus the friction coefficients of straight and spiral pipes should be calculated (Fsadni, Whitty, & Stables, 2016; Liu, Evans, & Barifcani, 2017, pp. 755–772).

6.2.2.1 Pressure Loss Model for Coiled Tubing

The model to calculate the pressure loss of CT is also based on the Fanning equation. Before the calculation, the flow pattern should be estimated. Then the friction reduction ratios in both straight and spiral pipes are calculated.

6.2.2.1.1 Reynolds Number and Flow Patterns

In this model, the fracturing fluid is considered as the power-law fluid. Thus the formula for Re can be expressed as follows:

$$\mathrm{Re} = \frac{\rho v^{(2-n)} d^n}{K8^{(n-1)}}\left(\frac{4n}{3n+1}\right)^n \tag{6.10}$$

In general, when $\mathrm{Re} < (3470 - 370n)$, the fluid is considered as in laminar flow, whereas it is regarded to be in turbulent flow if $\mathrm{Re} > (4270 - 1370n)$.

6.2.2.1.2 Friction Coefficient

When the fluid flows through the CT, the pressure loss consists of two parts: one part is caused by the frictional effect of the pipe wall and the other is caused by the helical flow in the spiral pipe. Thus the friction coefficients in the straight pipe and spiral pipe of CT should be calculated with different formulas.

1. Friction coefficient in straight pipe

   The friction coefficient for both Newtonian and non-Newtonian fluid in CT can be expressed in the following same form:

$$f = \frac{a}{\mathrm{Re}^b} \tag{6.11}$$

where a and b are constants. For laminar flow, $a = 16$ and $b = 1.0$.

For turbulent flow, the parameter a and b depends on the flow index n:

$$a = \frac{\log_{10} n + 3.93}{50} \tag{6.12}$$

$$b = \frac{1.75 - \log_{10} n}{7} \tag{6.13}$$

2. Friction coefficient in spiral pipe

   In 1927, the experimental and theoretical researches on flow characteristics in elbow pipe were conducted by Dean. Followed by his research, a series of studies on the Newtonian fluids flowing in the elbow pipe were performed. Finally, the formulas for the friction coefficients of Newtonian and power-law fluids in the spiral pipe were given by McCann and Islas (1996).

   For Newtonian fluid, the friction coefficient can be expressed as:

$$f = \frac{0.084}{\mathrm{Re}^{0.2}} \left(\frac{d}{D}\right)^{0.1} \tag{6.14}$$

   For power-law fluid, the equation is:

$$f = \frac{1.069a}{\mathrm{Re}^{0.8b}} \left(\frac{d}{D}\right)^{0.1} \tag{6.15}$$

where d is the inner diameter of CT in m and D is the winding drum diameter in m.

6.2.2.1.3 Frictional Pressure Loss

According to the Fanning equation, the frictional pressure loss in CT can be expressed as follows:

$$\Delta P_f = \frac{2f\rho v^2 L}{d} \tag{6.16}$$

where ρ is the fluid density in kg/m^3, v is the average fluid velocity in m/s, d is the inner diameter of CT in m, L is the length of pipe in m, and ΔP is the frictional pressure loss in MPa.

6.2.2.2 Model Correction Based on Experimental Results

Due to the shear thinning effect of fracturing fluid, the friction pressure loss that is calculated by theoretical formula usually has great deviation from the real value. Therefore experimental research on friction and property was performed on Baiqian 110# well in Qionglai City, Sichuan Province, China (Huang & Hong-Mei, 2005).

6.2.2.2.1 Experimental Equipment

- A CT with diameter 50.8 mm (2 in.) and length 2100 m; the permissible flow rate was 2.0 m^3/min and the permissible pressure was 70 MPa.
- The hydra-jet fracturing tool.
- The casing pipe with a diameter of 5 ½ in. and thickness of 36 mm.
- Fracturing fluid of 40 m^3.

6.2.2.2.2 Experimental Process

Step 1: Fracturing base fluid of 8.17 m^3 volume was pumped at a pressure less than 66.13 MPa and flow rate less than 0.92 m^3/min.

Step 2: Cross-link fracturing fluid of 22.37 m^3 was injected. During this process, the pressure and the flow rate were kept below 67.04 MPa and 0.87 m^3/min, respectively.

Step 3: Xanthan gum of 14.85 m^3 volume was pumped. The largest pump pressure and flow rate were 67.37 MPa and 0.88 m^3/min, respectively.

Step 4: Pure water of 6.41 m^3 was pumped at a pumping pressure less than 69.7 MPa and a flow rate less than 1.84 m^3/min.

6.2.2.2.3 Experimental Results Analysis

The frictional pressure losses of different fracturing fluids in CT were tested given different flow rates. The experimental results are shown as follows.

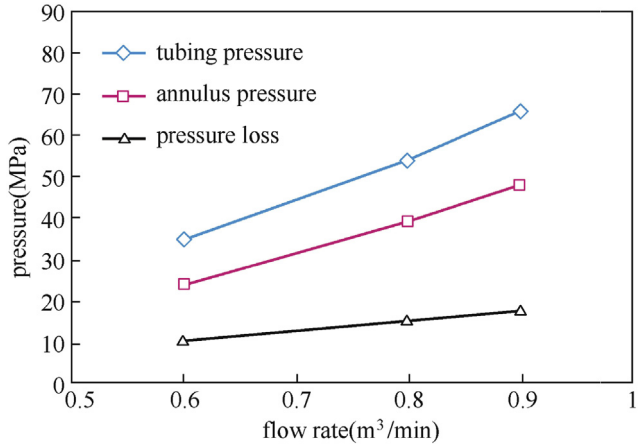

Figure 6.2 Experimental frictional pressure versus the flow rate.

As shown in Fig. 6.2, with CT diameter 50.8 mm and length 2100 m, both the surface pressure and the frictional pressure loss in CT increased with the growth of flow rate. When the flow rate was 0.6 m^3/min, the frictional pressure loss in the spiral pipe of CT was 10.95 MPa. As the flow rate increased to 0.8 m^3/min, the frictional pressures loss was 15.57 MPa, presenting a 33% increase. In addition, as the flow rate increased to 0.9 m^3/min, the frictional pressure loss was 17.63 MPa, indicating a 61% increase. However, the theoretical value of frictional pressure loss that was calculated by Fanning equation was about 41 MPa, given the flow rate of 0.9 m^3/min. This indicated that at the flow rate of 0.9 m^3/min, the theoretical value of frictional pressure loss was about 2.33 times the experimental value. This was because at the shear thinning action of fracturing fluids, the friction pressure loss was weakened with the growth of flow rate, leading to the actual experimental value being less than the theoretical value. According to the experimental results, the calculation formula for the frictional pressure loss of the fracturing fluid used in this experiment was obtained.

According to Figs. 6.3 and 6.4, a similar conclusion can be summarized. The frictional pressure loss increased with the growth of flow rate. However, the larger the flow rate, the smaller was the increment of frictional pressure presented. This was mainly because the increment of the friction coefficient decreased with the growth of the flow rate due to the shear thinning action of the fracturing fluid.

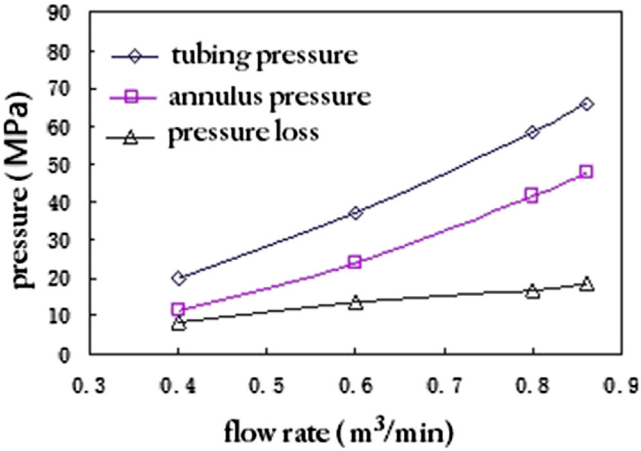

Figure 6.3 Experimental frictional pressure versus the flow rate (for cross-link fluid).

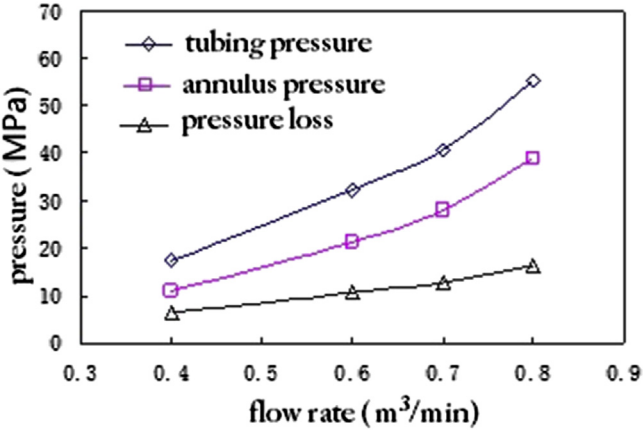

Figure 6.4 Experimental frictional pressure versus the flow rate (for base fluid).

6.2.2.2.4 The Correction of Frictional Pressure Loss in Coiled Tubing

According to the experimental results, the frictional pressure loss regression equations for fracturing base fluid, cross-link fluid, and xanthan gum can be expressed as Eqs. (6.17)−(6.19), respectively,

$$\Delta P = 19.829 Q^{1.1664} \tag{6.17}$$

$$\Delta P = 21.544 Q^{1.0042} \tag{6.18}$$

Table 6.1 Frictional pressure loss of the fracturing base fluid in coiled tubing given different flow rates

Flow rate (m^3/min)	0.6	0.8	0.9	1.0	1.1	1.2
Frictional pressure loss (MPa)	10.95	15.16	17.63	19.83	22.16	24.52

Table 6.2 Frictional pressure loss of the cross-link fluid in coiled tubing given different flow rates

Flow rate (m^3/min)	0.4	0.6	0.8	0.86	0.9	1	1.1	1.2
Frictional pressure loss (MPa)	8.41	13.53	16.84	18.42	19.38	21.54	23.71	25.87

Table 6.3 Frictional pressure loss of the xanthan gum fluid in coiled tubing (CT) given different flow rates

Displacement (m^3/min)	0.4	0.6	0.7	0.8	0.9	1	1.1	1.2
CT pressure loss (MPa)	6.45	10.75	12.93	16.25	18.44	21.17	23.97	26.86

$$\Delta P = 21.166 Q^{1.3069} \tag{6.19}$$

where Q is the flow rate in m^3/min and ΔP is the frictional pressure loss in MPa.

Using the regression equations, the frictional pressure loss of fracturing base fluid, cross-link fluid, and xanthan gum in CT (with 2100 length) can be calculated at different flow rates. The results were as shown in Tables 6.1—6.3.

6.2.2.3 The Frictional Pressure Loss in Annular

In different sections of annular, the fracturing fluid is probably at different flow patterns. Thus the frictional pressure loss should be calculated according to the flow pattern of the corresponding model.

6.2.2.3.1 Frictional Pressure Loss Model for Turbulent Flow

$$P_A = K_1 Q^{K_3} \sum_{i=1}^{M} \frac{L_i}{(D_{hi} - D_{pi})^{K_2} S_i^{K_3}} \tag{6.20}$$

where

$$K_1 = \frac{2aK^b}{12^{b-nb}\rho^{b-1}}\left(\frac{2n+1}{3n}\right)^{nb}; \quad K_2 = nb+1; \quad K_3 = nb-2b+2$$

$$a = \frac{\log_{10}n + 3.93}{50}; \quad b = \frac{1.75 - \log_{10}n}{7}$$

where D_h is the inner diameter of casing in m, D_p is the outside diameter of tubing pipe in m, L is the length of annular section in m, and Q is the flow rate in annular in m^3/s.

Re is calculated as:

$$\mathrm{Re} = \frac{12^{(1-n)}\rho(D_h - D_p)^n V^{(2-n)}}{K\left(\frac{2n+1}{3n}\right)^n} \tag{6.21}$$

6.2.2.3.2 Frictional Pressure Loss Model for Laminar Flow

$$P_A = K_1 Q^n \sum_{i=1}^{M} \frac{L_i}{(D_{hi} - D_{pi})^{n+1} S_i^n} \tag{6.22}$$

where

$$K_1 = 4K\left[\frac{4(2n+1)}{n}\right]^n$$

The model can be simplified as follows:

$$P_A = \frac{0.057503\rho^{0.8}\mu^{0.2}LQ^{1.8}}{(d_h - d_p)^3(d_h + d_p)^{1.8}} \tag{6.23}$$

6.3 SURFACE PRESSURE PREDICTIONS

Predict the surface pressure accurately during the fracturing treatment has great significance for the wellhead selection and pressure control. The surface pressure predictions mainly refer to the tubing and casing surface pressure calculation at the stages of jet perforating and hydra-jet fracturing. According to the flow characteristics of these two stages, the surface pressure can be calculated with different formulas.

6.3.1 Surface Pressure Prediction at the Stage of Jet Perforating

At the stage of jet perforating, the tubing-casing annular is open and the perforating fluid is pumped through the tubing pipe. After the perforation, the fluid flows out and returns to the ground. For this stage, the surface tubing pressure can be expressed as follows:

$$P_{\text{tubing}} = P_b + P_{\text{ftubing}} + P_{\text{fannulus}} \tag{6.24}$$

where P_{tubing} is the surface tubing pressure in MPa, P_b is the nozzle pressure drop in MPa, and P_{ftubing} and P_{fannulus} are the frictional pressure losses in tubing pipe and annular, respectively, in MPa.

6.3.2 Surface Pressure Prediction at the Stage of Hydra-Jet Fracturing

At the hydra-jet fracturing stage, the success conditions for fracturing combined with hydra-jet fracturing mechanism are:

$$P_{\text{annulus}} + P_h + P_{\text{boost}} - P_{\text{fannulus}} \geq P_{\text{fac}} \tag{6.25}$$

Where P_h, P_{boost}, and P_{fac} indicate the hydrostatic pressure in MPa, boost pressure in the perforation cavity in MPa, and the initiation fracture pressure in MPa, respectively.

Among them, the boost pressure increases with the growth nozzle pressure drop. Based on field test data, the boost pressure is about 6.0 MPa if the nozzle pressure drop is kept at 30 MPa.

At the stage of hydra-jet fracturing, the surface tubing pressure and annular pressure equations are as follows:

$$P_{\text{tubing}} = C_a P_{\text{annulus}} + P_b + P_{\text{ftubing}} - P_{\text{fannulus}} \tag{6.26}$$

$$P_{\text{annulus}} = P_{\text{fac}} + P_{\text{fannulus}} - P_h - P_{\text{boost}} \tag{6.27}$$

where C_a stands for the correction coefficient of surface tubing pressure, ranging from 0.4 to 0.6.

The correction coefficient of surface tubing pressure was determined according to the field test data. The field test showed that the increment of surface tubing pressure was equal to 40%—60% of the surface annular pressure. Thus the correction coefficient should be introduced to predict the surface pressure accurately during the hydra-jet fracturing.

REFERENCES

Blanco, I., Bailey, M. B., & Rosine, R. S. (2007). *Comparison of computational fluid dynamics of slurry flow in coiled tubing to field data*.

Fayong, D. U., Zhang, X., & Lu, Y. (2002). The analysis and improvement of friction calculation method in fracturing operation. *Drilling and Production Technology, 25*(5), 41−44.

Fsadni, A. M., Whitty, J. P. M., & Stables, M. A. (2016). A brief review on frictional pressure drop reduction studies for laminar and turbulent flow in helically coiled tubes. *Applied Thermal Engineering, 109*, 334−343.

Hou, H. (1987). *Resistance-reducing mechanics*. Beijing: Science press.

Huang, Y. Z., & Hong-Mei, H. E. (2005). Calculation of pipe string friction during fracturing operation in Chuanxi area. *Special Oil and Gas Reservoirs, 12*(6), 71−75.

Liu, X., Evans, B., & Barifcani, A. (2017). *A comparison of drilling fluid power for coiled tubing drilling of microholes in hard rock: Water versus supercritical CO_2 ICIPEG 2016*. Springer.

Li, G., & Yang, R. (2000). *The new progress of drag reducer in research and production at home and abroad*.

Lord, D. L. (1987). *Turbulent flow of stimulation fluids: An evaluation of friction loss scale-up methods*.

McCann, R. C., & Islas, C. G. (1996). *Frictional pressure loss during turbulent flow in coiled tubing*.

Medjani, B., & Shah, S. N. (2000). *A new approach for predicting frictional pressure losses of non-Newtonian fluids in coiled tubing*.

Shah, S. N., Kamel, A., & Zhou, Y. (2006). Drag reduction characteristics in straight and coiled tubing—an experimental study. *Journal of Petroleum Science and Engineering, 53*(3), 179−188.

Shah, S. N., Zhou, Y., & Goel, N. (2002). *Flow behavior of fracturing slurries in coiled tubing*.

Shen, Z. H. (1998). *Theory and techniques of water jet*. Dongying: Petroleum University Press.

Tian, S., Li, G., Huang, Z., Niu, J., & Xia, Q. (2009). Investigation and application for multistage hydrajet-fracturing with coiled tubing. *Petroleum Science and Technology, 27*(13), 1494−1502.

Yu, S. (1990). *Resistance-reducing technique application in petroleum pipeline of our country*.

Zhou, Y. (2001). *An experimental study of drag reduction of polymer solutions in coiled tubing*.

Zhou, Y., & Shah, S. N. (2002). *New friction factor correlations for non-Newtonian fluid flow in coiled tubing*.

CHAPTER SEVEN

Hydra-Jet Fracturing Bottom-Hole Assembly

Contents

Abstract

As the critical components of this technology, the bottom-hole assembly, including its structure and the material, is very important to guarantee a successful hydra-jet multi-stage fracturing operation. This chapter presents the detailed structure and function of each part of the tool. First, the overall structure and the corresponding function are described in general. Then, the detailed structure of the jet sub and the slide sleeve inside is illustrated considering the possible risks in practical operations, like the pin's strength, sleeve's surface smoothness, and the jet sub or sleeve shoulder wear that results from proppant flowing, etc. Third, as the most important part of the technology, the nozzle inner structure and material are analyzed to get an effective jet for penetrating the casing and formation. A nozzle made of ceramics with a comparatively simple inner structure is adopted. Finally, the accessary parts, including the centralizer and one-way valve, guide, etc. are described briefly.

Keywords: BHA; Jet sub; Nozzle; Slide sleeve; Structure.

7.1 THE BOTTOM-HOLE ASSEMBLY: OUTLINE AND FUNCTIONS

As shown in Fig. 7.1, the bottom-hole assembly (BHA) consists of multi-stage jet guns, whose number and positions are determined by the well bore length, reservoir characteristics, the cost, etc. Considering the risk of sand-sticking, a safety sub should be connected between the tubing string and the BHA. At the end of the BHA, a guide is installed as usual, to lead the tool tripping in smoothly. The screen pipe functions as a filter to prevent solid particles from entering the tool while reverse circulating.

Abrasive Water Jet Perforation and Multi-Stage Fracturing
ISBN: 978-0-12-812807-7
http://dx.doi.org/10.1016/B978-0-12-812807-7.00007-8

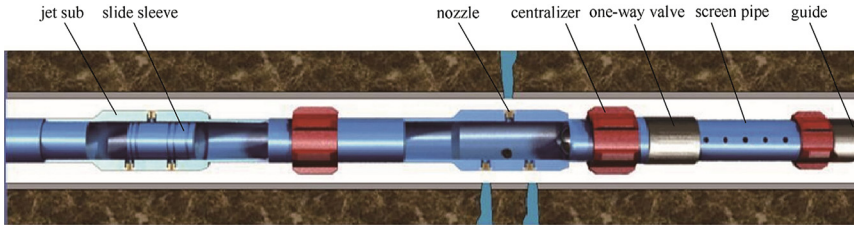

Figure 7.1 The bottom-hole assembly structure.

The centralizer can keep the nozzle's standoff distance equal to the casing. Except for the first jet sub, there is a slide sleeve in each jet sub. Therefore the balls should be bigger to open the corresponding sleeve in practical fracturing performance. For a horizontal well, the operation will start from the toe to the heel stage by stage. The following discussion presents the detailed structure of each component.

7.2 JET SUB AND SLIDE SLEEVE

The jet sub, as shown in Fig. 7.2, is the main part of the BHA. Around the circumstance of the sub, there are distributed several nozzles, whose number is determined by the practical requirement and the pump power. Its maximum diameter determines the nozzle's standoff distance. For

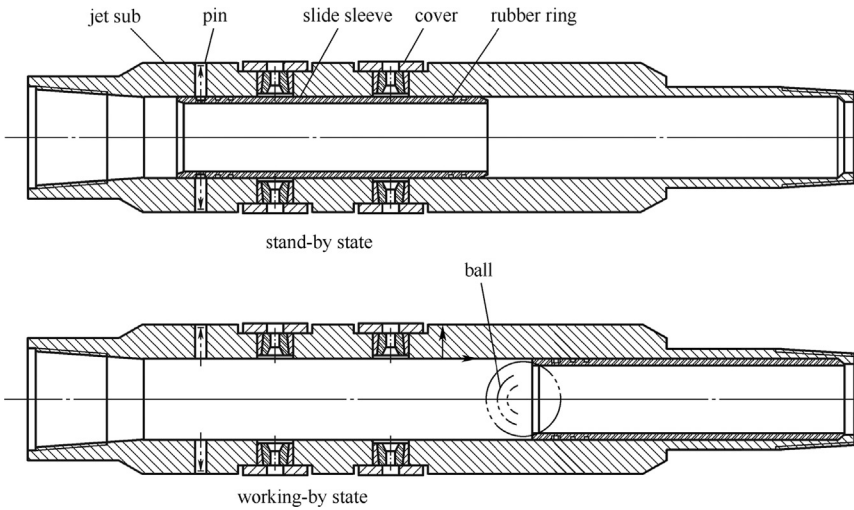

Figure 7.2 The detailed structure of jet sub.

different nozzle structures, this distance will influence the hole diameter jetted by the abrasive water jet (AWJ) on the casing wall. A slide sleeve, fixed by some pins with the sub body, is set inside the sub to seal the nozzles inlet. Once needed, a ball will be cast into the tubing to open the sleeve after cutting off the pins. Then the sleeve will slide to the seat at the downstream end of the jet sub and the nozzles can work normally.

Note that the sleeve outside should be smooth enough and coaxial with the sub inside the hole, to avoid sticking when the sleeve is moving. Also, the pin's strength should be tested ahead of time. If it is too strong, it will be difficult to get cut off; if it is weak, the peak signal transmitted to the surface will be ambiguous and it will be hard to judge whether or not the sleeve is activated successfully. In addition, at the end of the jet sub, there is a shoulder to bear the sleeve when the ball activates it. One fact cannot be neglected, that is, when the proppant volume is big, the shoulder may be worn off. If so, the sleeve will have no support and fall into the tubing string. When this accident happens, the typical phenomenon is that the tubing pressure shows obvious reduction even under the same flow rate as the previous stage. Under this situation, the present stage has to be given up. Another place of possible wearing off is the sleeve mouth, especially for the sleeves close to the heel of a horizontal well. If such wearing happens, the ball will not be able to seal the sleeve's inner hole, showing the same phenomenon as mentioned earlier. In summary, at the inner passage of the tool, any place where the inside diameter varies will have the hazard of wearing. When designing and manufacturing these parts, we should consider the structure and material optimization.

7.3 NOZZLE

The nozzles are the critical parts to generate the AWJ for penetrating the casing and formation, and to pass the proppant-laden fluid in fracturing. Its basic principle is through contraction section along the flow direction to accelerate the fluid, transforming the high-pressure fluid into a high-speed jet. So, the inner passage structure will be very important to get an effective jet, that is, the jet should be able to keep the initial speed as long as possible and reduce the energy loss when fluid passes through it.

Normally, the nozzle inside structure mainly includes the parameters such as inlet contraction angle, inlet section shape, outlet shape, and exit diameter, influencing the jet shape and the impacting force. In this technology, we

need a jet with a longer section keeping the initial velocity to penetrate the casing and formation, and the nozzle material should be strong enough to stand the abrasive wear. In addition, the flow rate coefficient, related with the material matrix, wet-face smooth finish, flow passage profile, etc., should be as high as possible to reduce the fluid power loss. Till date, ceramic composite is the most feasible material, although it is difficult to manufacture. So, the nozzle inside structure should not be very complex for easy fabrication. The frequently applied nozzle inside structures, used in petroleum industry, are cone, cone + straight section, and streamline + straight section, as shown in Fig. 7.3. Considering the aforementioned factors comprehensively, we adopted the nozzle with an inside structure of cone + straight section. As for its detailed design method, there are many professional books that can be referenced. Fig. 7.4 shows the finished nozzles made of ceramic composite.

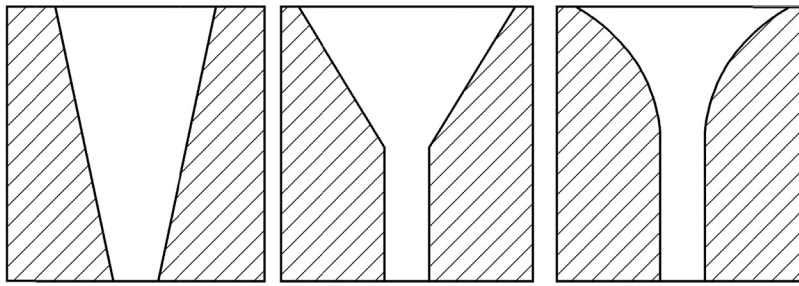

Figure 7.3 The general nozzle structures.

Figure 7.4 Ceramic nozzles.

7.4 THE ACCESSARY PARTS

The accessary parts mainly include the centralizer, one-way valve, screen pipe, and the guide. The centralizer, with a greater diameter than the jet sub, is set on a short tubing sub and can move freely. The reason for such design is to avoid sand-sticking. That is, if there is down-hole BHA sand-sticking, we must try to move the tubing string first. As the centralizers are not fixed with the jet sub, it will be easy to release the BHA when sand-stuck. The one-way valve functions as a reverse circulation passage. When necessary, we can pump fluid from the annulus with a higher flow rate, opening the one-way valve. This operation is mostly to solve BHA accidents. Furthermore, the screen pipe plays the role of filtering bigger particles from entering the BHA under reverse circulation. Naturally, the guide, set at the end of the BHA, leads the tool tripping into a well smoothly.

CHAPTER EIGHT

Field Application

Contents

Abrasive Water Jet Perforation and Multi-Stage Fracturing
ISBN: 978-0-12-812807-7
http://dx.doi.org/10.1016/B978-0-12-812807-7.00008-X

Abstract

This chapter mainly presents the technologies of formation feasibility, operation procedures, bottom-hole assembly damage or failure, possible risks in field performance and the corresponding measures to deal with them, and typical field cases. These contents are summarized according to practical performance. The lessons learned from field operations will be able to provide a valuable reference for potential application. In addition, typical wells are listed to show the feasibility of this technology to different completion categories.

Keywords: Application; Concentration; Feasibility; Procedure; Proppant; Risk.

8.1 HYDRA-JET MULTI-STAGE FRACTURING TECHNOLOGY: FEASIBILITY AND PROCEDURES

8.1.1 Technology Feasibility

Like any other technology, hydra-jet multi-stage fracturing is not universal. According to successful and failed cases completed in over 500 wells, its feasibility can be summarized as follows.

8.1.1.1 Thinner Interbed Formations

For conventional packer multi-stage fracturing, it is difficult to aim for the thinner pay layer for realizing pinpoint fracturing. When applying hydra-jet fracturing, the nozzles can be positioned exactly to the pay zones according to logging results. The interbed can be connected by fractures if the nozzle interval is not very large.

8.1.1.2 Casing-Deformed Well

If a casing-deformed interval above the pay zone exists, then the packer cannot pass to the target formations. Under this condition, it seems that a smaller diameter hydra-jet blasting gun will be the only choice to perform the fracturing work.

8.1.1.3 Liner-Completed Well

For such completed wells, there is no effective method at present to separate different intervals along a horizontal section.

8.1.1.4 Wells With Bad Cement Sheath

In these old wells, most of the cement sheath has been corroded or has even disappeared. So, when the packer is dilated, it will not be able to withstand a higher pressure difference because there is no support outside the casing.

8.1.1.5 Simple Sand Screen-Out Formations

In conventional cement casing and charge perforation wells, the perforation tunnels are smaller compared with those formed by an abrasive water jet (AWJ). When fracturing fluid flows through the tunnels, the pressure drop will be correspondingly higher, easily forming narrow fractures and resulting in sand screen-out. The AWJ perforation tunnel diameters are bigger, reducing the risk of sand screen-out.

8.1.1.6 Packer Failure for Unknown Reasons

In some wells, the casing seems not to deform when measured using a bypass gauge. However, when tripping in the packers to the target intervals, they cannot work normally. After tripping out, it is found that the rubber has been destroyed, as shown in Fig. 8.1. So, under such conditions, hydra-jet fracturing will be a feasible method to avoid packers in the assembly.

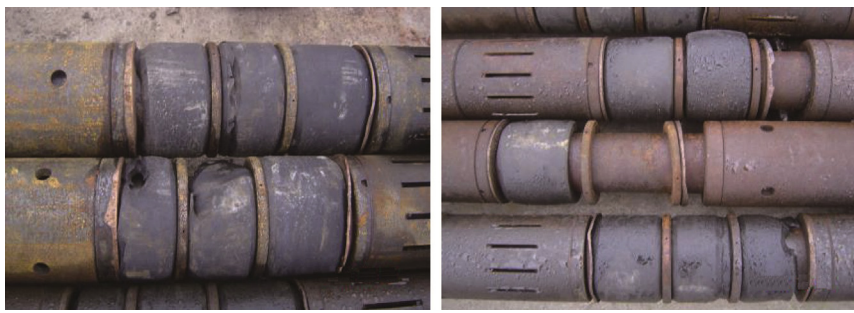

Figure 8.1 Packer rubber damaged (*left*) or falling off (*right*).

8.1.1.7 Larger Difference in Initial Pressure Along the Lateral

According to the mechanism of this technology, if the initial pressure difference exceeds 8 MPa between two intervals, it will be difficult to separate them. Therefore hydra-jet fracturing technology will function well in a homogeneous lateral.

8.1.2 Operation Procedures Utilizing Common Tubing

8.1.2.1 Abrasive Water Jet Perforation Operation

In the newly cemented wells, AWJ perforation will be able to replace the conventional shape charge perforation operation, saving a large amount of capital especially in horizontal wells. When performing AWJ perforating, the abrasive (normally 20–40 mesh sands) concentration will be set at 100–120 kg/m^3, and the nozzle pressure difference at 30–35 MPa, blasting for about 12 min, generally consuming 2 m^2 of sands and 30 m^3 of base fluid.

For conventional wells, this operation always uses 2⅞″ tubing to circulate the base fluid, normally with a viscosity of 30–50 mPa s and a flow rate of 2.6 m^3/min, delivering the sands to the nozzles. Under this condition, the average pressure drop along the tubing string is about 6.0–6.3 MPa/km, equal to the pressure drop of slick water. So, in practical performance, the total pump pressure will be the nozzle pressure difference adding to the pressure drop along the tubing string. For a 3000 m-deep well, the ground pressure is about 50 MPa, which has been approved in practical operations. Because the annulus between casing and tubing is open while AWJ perforating, the used abrasives will flow upward along the annulus. To reduce the amount of perforation fluid returning to ground, once the perforating stage terminates, the annulus will be closed and begin to pump cross-linked pad fluid to initiate and propagate fractures in the formation. Therefore the used perforating fluid in the annulus, containing wasted sands, will be pressured into formations ahead of the pad fluid. Precisely, it will act as a "polishing" fluid to make the fracture surface smooth, reducing the risk of sand screen-out because of fracture "coarseness" in the following procedure.

8.1.2.2 Fracturing Operation

When pumping the pad fluid to the predetermined volume, the proppant will be added to the cross-linked fluid, lifting the concentration from 120 to 700 kg/m^3 in six or seven steps. Assuming that the coincident initial pressure is at the horizontal section, the base fluid will be pumped from the annulus all through the fracturing period at a nearly equivalent pressure.

This will help to avoid base fluid in the annulus entering the previous completed stage fractures, resulting in no proppant near the wellbore. Another function of pumping base fluid from the annulus is to compensate the jet pump sucking effect. That is, when the nozzles, normally six or eight, spray at a high speed (up to 300 m/s), they will generate a "low-pressure" area around the jet just outside the nozzle exit. If no fluid is provided to the annulus, the six or eight jet pumps will suck fluid from the previous completed fractures. Because the fractures have not closed completely, the proppant will return to the wellbore following the fluid, increasing the risk of sticking tubing.

At this stage, we theorized that the ground pump pressure will be much higher than that at the perforation stage. This is reasonable to achieve such a result because just after perforation, the annulus will be closed to initiate the formation. As mentioned earlier, and also for a 3000 m-deep well, assuming the initial pressure is 30 MPa, the pump pressure should be 80 MPa. However, in practical performance, the pressure is not as high as we imagined. Fig. 8.2 shows a well with fracturing curves at the Huabei oilfield. From these curves we can find that the pressure only increased by about 8 MPa, from 40 to 48 MPa, after we closed the annular valve, while the initial pressure in this well was 18 MPa. The pump pressure should be 58 MPa and not 48 MPa if we calculate directly. The reason possibly lies in the perforation stage; the perforating fluid will return to the ground along the annulus,

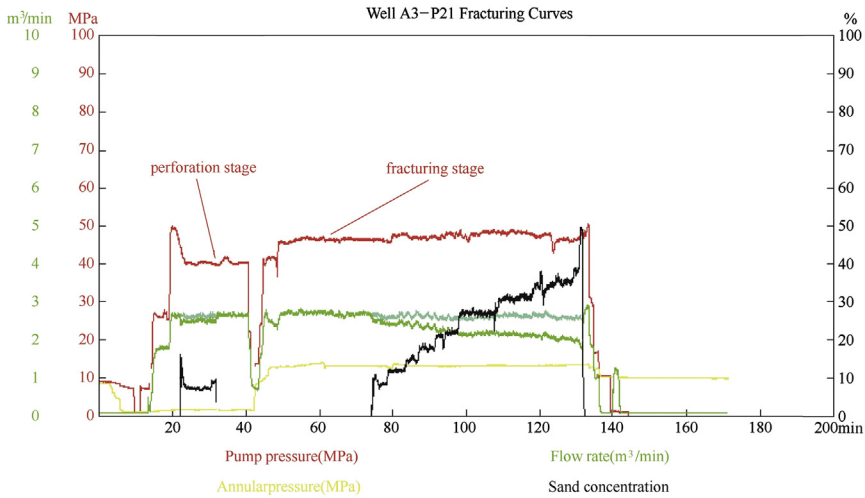

Figure 8.2 Comparison of pump pressure in perforation and fracturing stage.

and the pressure drop in the annulus cannot be neglected, especially when the casing deforms or larger diameter tubing is utilized. However, in the fracturing stage, there is no such pressure drop in the annulus.

As mentioned before, when pumping proppant-laden fluid at this stage, the base fluid will be pumped from the annulus to compensate the sucking effect. Then, in the downhole, the cross-linked fluid will be diluted by the base fluid. Therefore the proppant-laden fluid should be over-cross-linked. The over-cross-linking degree must be calculated according to the flow rate in the tubing and annulus to obtain the correct cross-linking ratio after mixing and before entering the formation. In performance, the flow rate in the annulus should be adjusted according to the annular pressure, equal to or less than the previous stage value. So, the added volume of the linker and delinker should also be changed correspondingly and simultaneously.

Because there is no packer in the string, the transition between the two stages will be critical to avoid the proppant returning from the completed fractures. For a multi-stage fracturing operation in a horizontal well, there is always some time to wait before a fracture closes. Consequently, the proppant in the fracture has not been pressed tightly by the fracture faces. However, in the next stage of the operation, the first step, AWJ perforation, needs an open annulus. How to transit from a pressured wellbore to an open one relates to later production and the risk of tubing sticking. To resolve this problem, we tried the following simple method. After completing one stage, we waited for an hour to let the fracture close partially. Then, we started a pump and simultaneously opened the annular valve step by step. Thereby the higher pressure in the downhole exerted by the ground pump was able to stop the proppant returning from the completed fracture, or at least hinder its movement.

8.1.3 Operation Procedures Utilizing Coiled Tubing

The hydra-jet-assisted fracturing (HJAF) method was the first technique invented that falls under the Bernoulli fracturing class with coiled tubing (CT). Others followed throughout the years, such as the hydra-jet perforating, annular path pumping (HJAP) method, and HJAP with anchor method, which are included in the pinpoint-fracturing class in both vertical- and horizontal-well applications.

8.1.3.1 The Hydra-Jet-Assisted Fracturing Process

The HJAF process was originally created for use in open-hole horizontal wells. It was first implemented in late 1997 in Midland, Texas. While the

well did not produce to an acceptable level, application of the process was a technical success, proving that it was, and still is, a potent process. Granted, many jobs have been performed so far, but this method is currently still in its infancy. Just like the hydraulic-fracturing process in 1964, the industry is still learning what can or cannot be accomplished using this interesting and still-new process. It was found that the HJAF process could be used effectively for other completions as well, such as cased holes, uncemented liners, pre-perforated liners, and even some vertical wells. In 2007, the process was first utilized in gas well BQ-110 in Sichuan, China (Fig. 8.3). Taking advantage of the Bernoulli principle, the process is the first one known that perforates, initiates a fracture, extends the fracture, and places the stimulation medium (sand, slurry, or acid) all in one seamless operation. Because it was much more dangerous when operated in a gas well than in an oil well, an extra blowout preventer, as shown in Fig. 8.4, besides the four blowout preventers grouped with the CT unit, was installed in the wellhead. While sometimes stopping the pump temporarily might be necessary, it is not a requirement imposed by the process. Oftentimes, these stoppages are dictated by safety concerns and/or by equipment limitations.

This process is also the only one that allows each perforation to connect to a fracture. While this might seem unlikely because often only 10% of conventionally created perforations connect to a fracture, it is probable because each perforation is independently pressurized. For an HJAF tool

Figure 8.3 Well BQ-110 field site.

Figure 8.4 Blowout preventer at the wellhead.

with six jets, for example, this functionality is repeated six times, and all six perforations are independently pressurized. In contrast, a 50-perforation section that was perforated conventionally may only have five perforations connected to the fracture. In general, a typical HJAF job is performed by first positioning the tool at a desired fracturing location. This location is usually determined by observing the formation log chart, thus making the decision based on the near wellbore information provided by the logs. Because the logs might not correctly reflect far-wellbore formation qualities, they are only used for vertical wellbores, and because most HJAF jobs are performed in horizontal wells, oftentimes fractures are just placed with equal spacing. After the tool is properly positioned, abrasive jetting fluid is pumped through the HJAF tool to perform the perforating, immediately followed by the "pad" fluid and then the stimulation fluid itself. After all the jet-perforating fluid has passed the jet, the annulus is pressurized to help extend the fracture. Generally, flow into the annulus is minimized so that little or no slurry thinning occurs during the process. However, sometimes it is desired to pump high flow rates into the annulus to purposely thin the fracturing slurry.

Note that downhole mixing with this method is efficient because of the high energy of the fluid flow through the jets. Also note that downhole mixing (using this and other "dual" flow path systems) occurs almost instantaneously. Proppant concentrations can be reduced to nothing within seconds (at the speed of sound), for example, to help avoid a total screen-out. One important aspect to remember is that because stimulation fluid is pumped through tubing, the HJAF process is a good fit for (deep) offshore wells. No proppant touches the costly wellhead cluster. However, this may damage the tubing: the abrasive fluid will wear the inside wall, especially of those tubings at the surface coil. In addition, in one trip, only one tool can be lowered. If more proppant is required, the nozzle material needs much higher strength to withstand abrasive wear. As shown in Fig. 8.5, the nozzles and tool become eroded after passing 36 m^3 of proppant. If necessary, more trips will be required to exchange the downhole assembly, consuming operation time.

8.1.3.2 The Hydra-Jet Perforating, Annular Path Pumping Process

The HJAP process (Fig. 8.6) was originally created for use with CT. With small outside diameter (OD) coil tubing, very limited flow rates can be pumped through the tubing, while flow through the annulus can accommodate very high injection rates. Using small OD CT also reduces the number of jets that can be supported, or smaller inside diameter nozzles, which means fewer or smaller perforations, and most importantly less horsepower

Figure 8.5 Used tool in Well BQ-110.

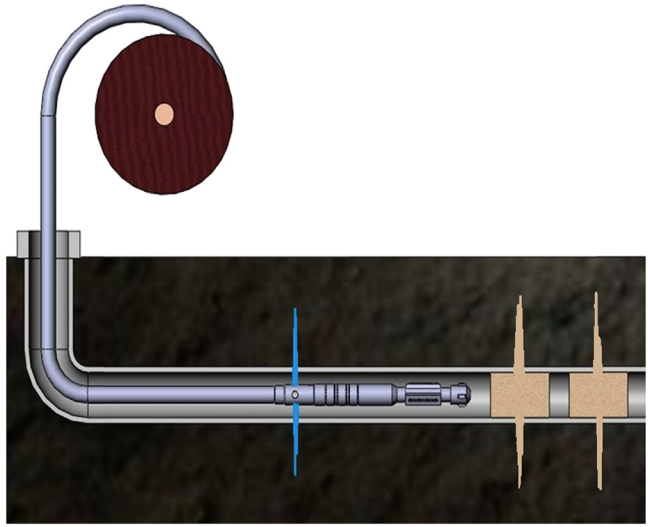

Figure 8.6 Hydra-jet perforating, annular path pumping completion.

can be delivered through the jets. Less jetting horsepower through the jets also means a smaller jet flow-to-annulus flow ratio, which further signifies less effective Bernoulli action. It is therefore important that when fracturing at a second or subsequent wellbore location (operations start nearest the toe and move toward the heel), the previous fracture is somehow isolated or "plugged," and in this way the new fracture extension can be performed conventionally (i.e., without the Bernoulli effect) or the fracture initiation can still be assisted by the Bernoulli effect. Plugging can be accomplished easily using sand (or other proppants) by using ultrahigh concentration slugs so it plugs or covers the previous perforations toward the toe. This will allow fracturing of each individual location, which is not usually possible with conventional processes.

In low-permeability horizontal wells, the notion of "layers" is not commonly valid because the well penetrates only a few layers. Fracture spacing could be just spread out evenly along the wellbore. Filling a long horizontal section with a proppant plug might not be possible, so the sand will form as short plugs. It is also of note that plugs are not square as shown by the artist's conception; in fact, they will be similar to sand dunes—wide on the bottom, with the top only supporting sand dropping from the fracture. The flow rate to create this must be so low that the fluid velocity in the open fracture we are trying to plug is less than the terminal velocity of the fluid going into the fracture. By achieving this, the perforations can be

plugged effectively. Unfortunately, this requires that the flow rate must be sufficiently slow so that proper, strong sand dunes can be created. This is often challenging to attain during the job, and occasionally the process must be repeated. Note that in the HJAF process, downhole mixing can be performed. In this method, after the fracture has been initiated properly, the flow through the jetting tool is reduced to a minimum, and the tool is moved upward. By doing this, the bottomhole pressure can be measured accurately using the coil as a "pseudo-dead string." However, if needed for sufficient fracture extension, the tubing can be used to supplement the flow by pumping clear fluid through it, thus mixing the downhole to obtain the needed mixture.

8.1.3.3 The Hydra-Jet Perforating, Annular Path Pumping With Anchor Process

It is commonly known that CT-deployed hydra-jetting often creates a hole that is irregular, or even a long slot. This irregularity is caused by the tool not being latched in place, or even mechanically centered, and moving within the casing. Also as cool fluid passes the tubing it tends to contract slightly, based on the temperature of the fluid, possibly causing a slot to be created. If this is not desired, an anchor must be used. Generally, an anchor uses slips that expand on actuation and grip to the casing wall when set. The anchor can be deactivated when movement of the bottomhole assembly (BHA) is warranted. Flow around the anchor can occur. Fig. 8.7 is a typical BHA

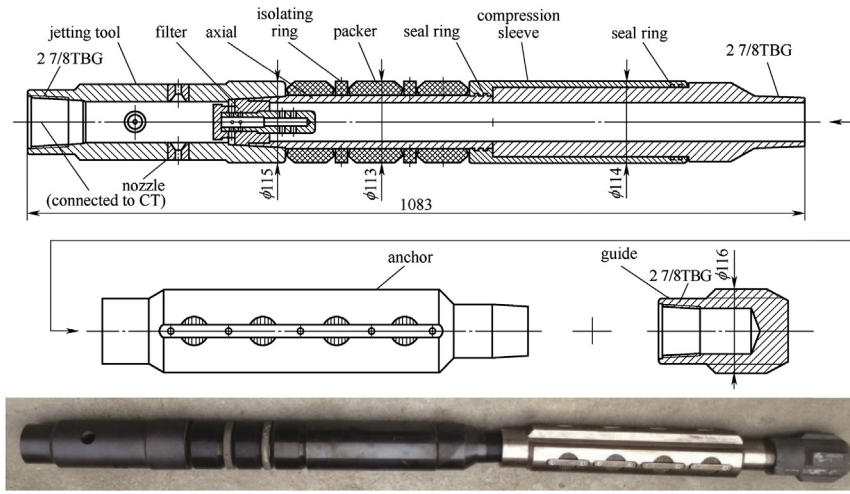

Figure 8.7 Bottomhole assembly structure and photos. *CT*, Coiled tubing.

designed for HJAP. Note that there is a filter between the jetting gun and the packer, which prevents the sands plugging the hole connected to the compression sleeve.

Once the packer is activated, as shown in Fig. 8.8, the axial pulling force will be very large when pumping fluid from the annulus. For a 5½″ casing with 2″CT, when the pressure difference between the packer reaches 25 MPa, the pulling force will be up to 25 t. In this situation, the packer acts just like a piston in the casing. So, the anchor clips must grip the casing wall tightly, or the CT will be cut off under the pulling force. It is necessary to conduct a test to verify how many clips are needed. As shown in Fig. 8.9, this setup can be used to perform such a test. First, pump water into the anchor from the right port and activate the anchor. Then, pump water from the left end to move the piston. The higher the pressure exerting on the piston, the bigger the pushing force. Similarly, the higher the pressure in the anchor, the higher the gripping force on the casing wall. We can measure and record the force by the compression transducer. Fig. 8.10 indicates that when the pressure in the anchor reaches 25 MPa, the pressure difference of the jetting nozzles in practical operation is also 25 MPa, and the anchor with 12 clips can withstand a 70 t pulling force, greatly exceeding the value of 25 t, as mentioned earlier.

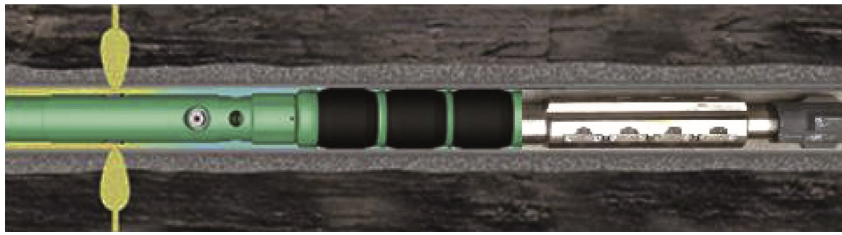

Figure 8.8 Hydra-jet perforating, annular path pumping working process.

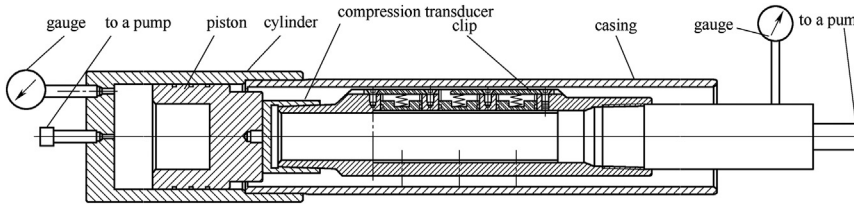

Figure 8.9 Setup of anchor testing.

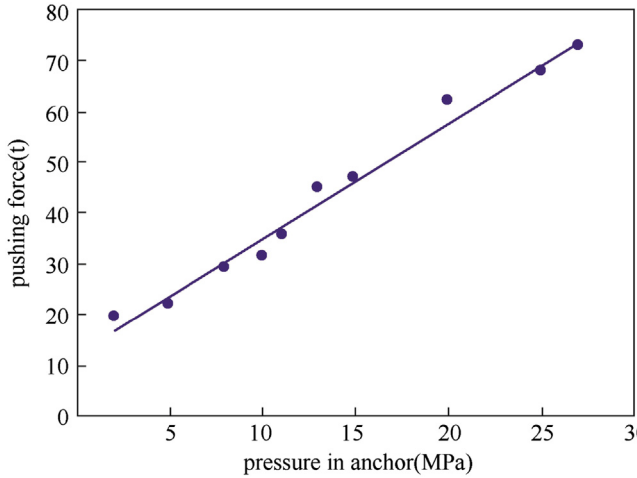

Figure 8.10 Pushing force versus pressure in the anchor.

8.2 TOOL WEAR AND FAILURE

8.2.1 Nozzle Failure

Because all of the proppant passing through the nozzles, a higher wear-resistant material is required to manufacture the nozzles. At present, a compound metal or ceramic composite material is always selected as the nozzle matrix. Normally, under hydra-jet fracturing conditions, the nozzle, made of common ceramics, will increase about by 10% after passing 10 m^3 proppant for each one, or it will damage or fall off, as shown in Fig. 8.11. If keeping a constant flow rate, the pump pressure will be reduced similar to

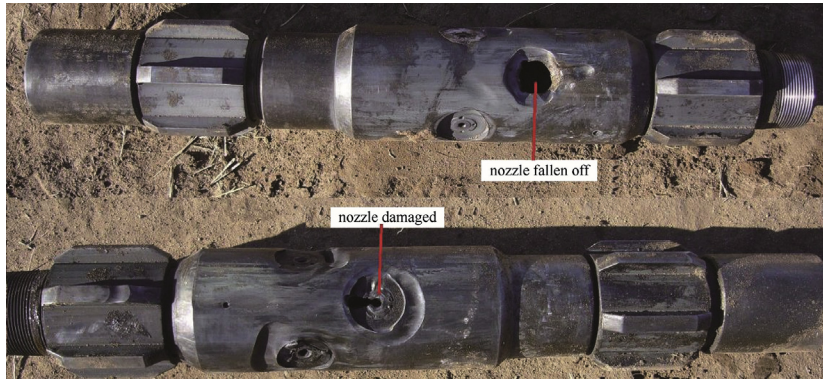

Figure 8.11 Nozzles damaged or fallen off.

the nozzle pressure. Even though the nozzles can work continuously, this will still bring about another practical problem in field performance. There is no packer and anchor in the downhole assembly of this technology; the tubing will lengthen when the pumps begin to pressure fracture the fluid. In addition, the extending degree will be in direct relation to the pressure difference inside and outside the tubing. Once the difference changes, the nozzle positions will also vary along the tubing. Consequently, the AWJ will generate slots on the casing wall, seriously decreasing the casing strength. So, before nozzle failure, it is important to keep a constant nozzle pressure difference to avoid its position changing. The practical operation should be like this: with the nozzle diameter enlarging for AWJ wear, the flow rate has to be raised to fix the blasting position. The bigger the flow rate, the higher the pressure drop along the tubing. So, pump pressure on the ground will also increase.

Besides AWJ wear, there is another factor that cannot be neglected for nozzle failure or even the nozzles falling off. When the fracturing fluid with higher concentration proppant flows along the tubing, it will turn in the direction of the nozzle inlet. Around this area, the flow field may be very complex and the slurry will wear the inside surface of the blasting gun. Once the wear depth is large enough to weaken the nozzle connection thread, the nozzle will fall down, as shown in Fig. 8.12. In this figure, we can observe that at point A, the thread connecting the nozzle has been partially destroyed. In detail, it is recommended that the flow field is calculated with a numerical simulation method.

Therefore to lengthen the nozzle lifespan, it is necessary to enhance the material strength. On the other hand, the blasting gun material, especially around the nozzle inlet, should also be emphasized.

8.2.2 Tubing Failure for the Wrong Blowout Operation After Fracturing

To cut down the operating time in multi-stage fracturing, it always best to conduct a blowout after every stage is completed. This step is critical to keep the proppant fixed in the fractures, reducing tubing sticking risk by returning proppant and ensuring that the tubing will not be broken. For the first point, for continuous flushing, two choke pipes are prepared with different size nozzles attached to them, as shown in Fig. 8.13. A smaller nozzle, normally with 2 mm exit diameter, will be set in line 1, and then flushing can begin. Once the annular pressure decreases to 1 or 2 MPa, the choke in line 1 will be shut down, and line 2, with a bigger nozzle, starts to flush at the same

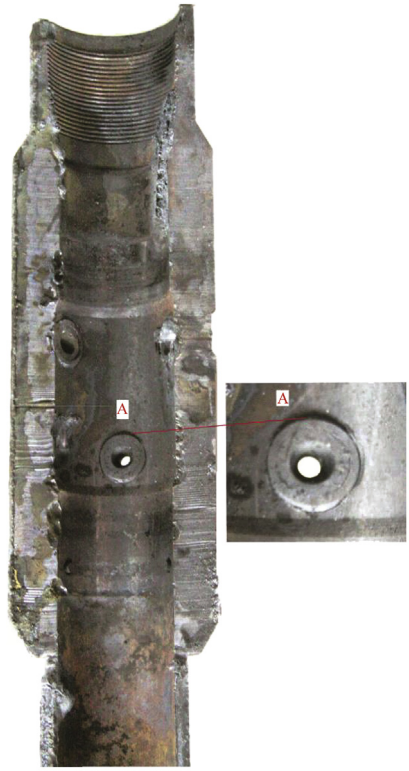

Figure 8.12 Cut-open gun and local enlargement photos.

Figure 8.13 Blowout pipes and nozzles.

time. During downtime of line 1, a new nozzle will be installed to replace the older, smaller one.

For the second point, ensuring the tubing is safe, the choke lines should be connected to the annulus, not the tubing at the wellhead. This is done to avoid the tubing being squeezed and collapsing in the well, as shown in Fig. 8.14. After the fracturing operation is completed, normally the fracture closing pressure is high in the wellbore. Although there is a one-way valve at the end of the downhole assembly, if we open the tubing valve suddenly, the pressure in the annulus will be much higher than in the tubing, and there will be no time for one-way reacting. Consequently, the pressure difference will allow the tubing to be squeezed, deforming or even breaking it. In a deeper well, the tubing string may be cut off for the heavier tubing weight. However, a blowout from the annulus will create another risk whereby the downhole assembly will stick if the supported fractures have not closed thoroughly. In this condition, the proppant may return to the annulus when the choke line valve at the annulus is opened. To compensate, a choice must be made whether or not to flush from the annulus, changing smaller nozzles one by one to try to control the returning proppant.

Figure 8.14 Collapsed tubing.

It should be noted that all of the proppant passes the nozzles at high speed, generally exceeding 200 m/s, requiring the nozzle material to withstand serious erosion and increase its lifespan. Normal erosion along the nozzle discharging passage is unavoidable in field performance, which will urge the operators to lift the pump flow rate to keep a constant jet velocity. So, finding a stronger nozzle material will be the objective of this technology. In addition, because there is no packer between any two stages, transiting from the completed interval to the next standby interval will be a critical step to avoid the tubing sticking because of the returned proppant. According to the author's experience, after about 1 h waiting for supported fractures to close, one pump will be started to circulate base fluid just before opening the annular valve. The purpose of this action is to maintain some backpressure at the bottom to avoid the proppant returning.

8.2.3 Tool Wear for the Detoured Abrasive Water Jet

For the casing cemented and perforated well, one problem cannot be neglected when performing AWJ perforating, that is, the AWJ will detour from the charge perforation tunnels and return to the wellbore, as shown in Fig. 8.15, especially in loose formations or existing fractures between charge perforation and the AWJ tunnel. As a result, the detoured AWJ will generate extra erosion on the AWJ gun or even the tubing surface.

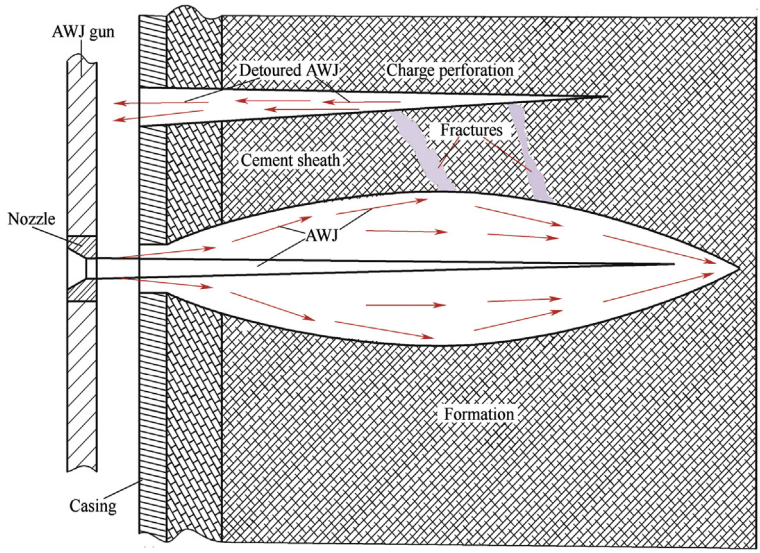

Figure 8.15 Abrasive water jet flows into charge perforation. *AWJ,* Abrasive water jet.

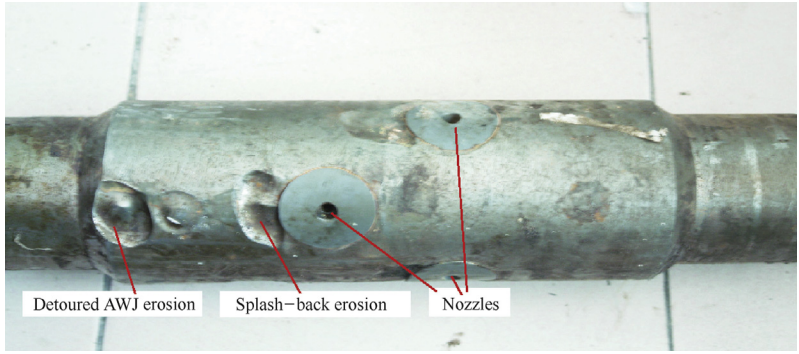

Figure 8.16 Erosion mark on the abrasive water jet gun. *AWJ*, Abrasive water jet.

This phenomenon cannot be observed or measured on the ground. We have sufficient reason to infer the foregoing results from the used downhole tools, as shown in Figs. 8.16 and 8.17. On the gun surface we can find several erosion points, obviously not generated by splashback AWJ. So, in oil wells with charge perforations, possible wear on the tool surface should be considered.

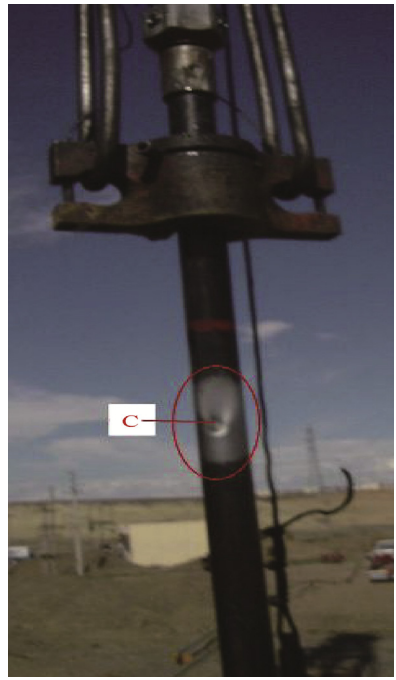

Figure 8.17 Wear on tubing surface (point C).

8.3 RISK AND COUNTERMEASURES

Accidents usually come under four categories: nozzle falling off, tubing breaking, sand screen-out, and sand sticking.

8.3.1 Nozzle Falling Off

If the nozzle falls off when pumping too much proppant, it can be seen that pump pressure decreases sharply and the pumps should be stopped immediately, transferring to pumping base fluid to displace the proppant in the tubing string to avoid the proppant sinking. Subsequently, the assembly should be replaced with a new one.

8.3.2 Tubing Breaking

Under higher pump pressure, the tubing may crack or fall to the bottom. Judged on the basis of pump pressure, a tubing breaking incident is different to the nozzle falling off. When a crack appears in the tubing, the pump pressure will decrease step by step with the crack propagating. If the tubing breaks off completely, the pressure will also fall suddenly by a greater degree compared to the nozzle falling off. If the above accidents happens, the tubing should be tripped out, beginning fishing job if the tubing gets broken down.

8.3.3 Sand Screen-Out

In low-permeability formations, sand screen-out is a serious accident, resulting in complete failure of fracturing. So, when fracturing in such areas, 1 or 2 m^3 of proppant will be pumped along the pad fluid to "polish" the fracture face. If the "polish" operation still does not work, the present interval will have to be given up.

8.3.4 Sand Sticking

The risk of tubing or downhole assembly sand sticking always happens in directional wells, especially with a deviation angle of 45—60 degrees. We implemented three horizontal wells in the Dagang oilfield, China; unfortunately two wells were sticking. Through measurement, both of the wells' sticking points were positioned at the kickoff interval. The reason for such an accident was because the fractures had not closed completely when we began to flush back. So, the proppant flowed back to the wellbore following the delinked fracturing fluid. If the tubing string cannot be tripped out, the recommended step to resolve the problem is to circulate

at higher flow rates, usually with fracturing pumps. If this does not work, the tubing is pulled to the hook load limitation for approximately a day, and then the tubing is released as soon as possible. Long tubing string has spring-like properties. When suddenly released, it will generate a shock force on the sticking sands. If sticking is not serious, sometimes this action can loosen the tubing after several attempts. The last and most effective remedial measure is conventional but expensive and time-consuming: tripping in a milling shoe to clear the annulus sand plug. For the two wells in the Dagang oilfield, the average time to deal with sand sticking was 15 days.

8.4 FIELD CASES

Multi-stage hydra-jet fracturing can perform pinpoint fracturing according to geological conditions without mechanical packers. Under this situation, it uses hydrodynamic isolation to seal fluid flowing into nontarget intervals, saving operating time and lowering sand-stick risk. Therefore this technology can be used to effectively stimulate not only open hole wells, but also screen liner or wells with damaged cementing. More than 600 oil and gas wells have been successfully treated with significant stimulation results since 2007. The following are some typical cases.

8.4.1 Case 1 Well Zheng408-8

8.4.1.1 Basic Information

The Zheng408 block, part of the Wangzhuang oilfield, is located in the west of the Dongying depression. The geological reserve is 1369×10^4 t and the effective reserve is 364×10^4 t. Oil viscosity is 6000—100,000 mPa s (50°C). Because of serious sensitivities, it was difficult to inject water or gas to compensate for the reservoir's pressure. As a result, the reservoir pressure decreased quickly and single well production is less than 1 t/day.

The Zheng 408-8 well structure is shown in Fig. 8.18, and Tables 8.1 and 8.2 present the well's basic data. It was perforated in September 2002 because of low productivity. The asphaltene and colloid in the oil formed a screen belt in the annulus between the metallic cotton liner and the open hole. The dynamic fluid level increased from 500 to 700 m. Then, it was decided to implement abrasive jet perforating and hydra-jet fracturing.

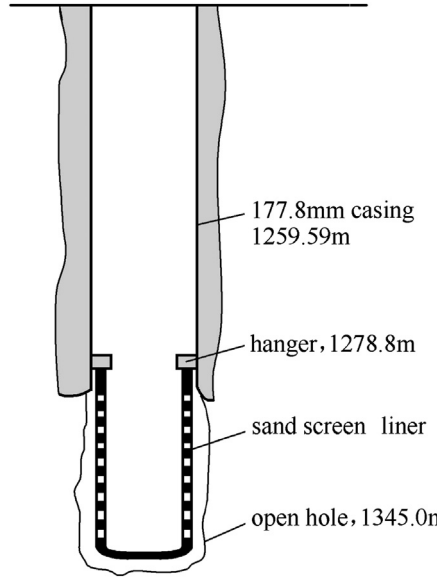

Figure 8.18 Well Zheng408-8 structure.

8.4.1.2 Parameter Design

As shown in Fig. 8.19, the downhole tool mainly includes four parts: jet gun, centralizer, one-way valve, and guide. The OD of the tool is 110 mm, and every gun has three nozzles with a diameter of 4 mm. Because the thickness of the pay zone is 19 m, the space between two guns is 5.5 m (three guns in total). The tubing needs to be trailed upward during the hydra-perforating treatment (perforation space, 0.5 m) to guarantee that the entire target interval is perforated.

Table 8.1 Basic data of Zheng408-8

Completion date	October 22, 1996	Drilled depth	1345.00 m	Artificial bottom hole	1345.00 m
Distance between tubing and bushing	4.20 m	Casing parameter	Φ177.80 mm × 8.05 mm × 1295.59 m		
Maximum hole inclination			1.77 degrees× 425 m		

Table 8.2 Perforation data of small layer

Formation	Electric measurement number	Perforation section (m)	Thickness (m)	Perforation number	Porosity (%)	Permeability 10^{-3} μm^2	Clay content (%)
ES3	013	1318 −1337	19.00	304.00	21.16	93.53	6.65
Total		Thickness of the formation 19.0 m					

8.4.1.3 Fracturing Treatment

The treatment processes are as follows:

1. Trip out the initial pipe and wash out the sand.
2. Trip in the hydra-jet tool, and locate the lowest nozzle at 1337 m.
3. Flush the tubing with 4 m^3 water, and then drop a steel ball to shut down the one-way valve.
4. Pump the sand-laden fluid at a pressure of 30−35 MPa for 10 min.
5. Trail the tubing upward for 0.5 m and repeat step (4) nine times.
6. Stop perforating. Pump 14 m^3 of water to displace the sand-laden fluid in the tubing.
7. Trip out the tubing and tool.
8. Trip in the fracturing pipe for sand packing following the parameters as shown in Table 8.3.

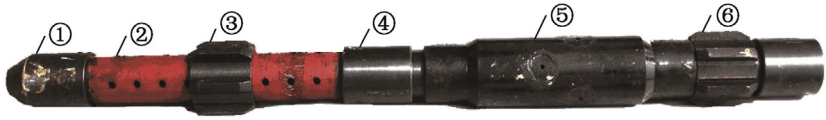

①—guide shoe ②—perforated tube ③—downward centralizer
④—one-way valve ⑤—jet body ⑥—upward centralizer

①−guide shoe ②−perforated tube ③−downward centralizer ④−one-way valve ⑤−jet body ⑥−upward centralizer

Figure 8.19 Hydra-jet tool.

Table 8.3 Frac-packing operation parameters

Pressure (MPa)	Sand (m^3)	Concentration (%)	Fluid
12−24	18	8−30	Guar gum

8.4.1.4 Postfracturing Production

After the operation, both gas and oil production increased. The initial wellhead pressure reached 11.0 MPa with an initial oil production of 8.7 t/day. Because the sand screen liner was damaged, the pay zone was buried and production started to reduce. Production remained at 1.0—2.5 t/day for the following 11 months.

8.4.2 Case 2 Well Wengu2

8.4.2.1 Basic Information

Well Wengu2, as shown in Fig. 8.20, Zhongyuan oilfield, was completed in November 2001. Because there was no production, it was decided to open a new pay zone at a depth of 3542.0 m. Because there are three layers of casing, it would be difficult to penetrate if conventional charge perforation were used. Therefore hydra-jet perforating and fracturing was adopted as an optimized method. The production casing shrank to 96 mm at a depth

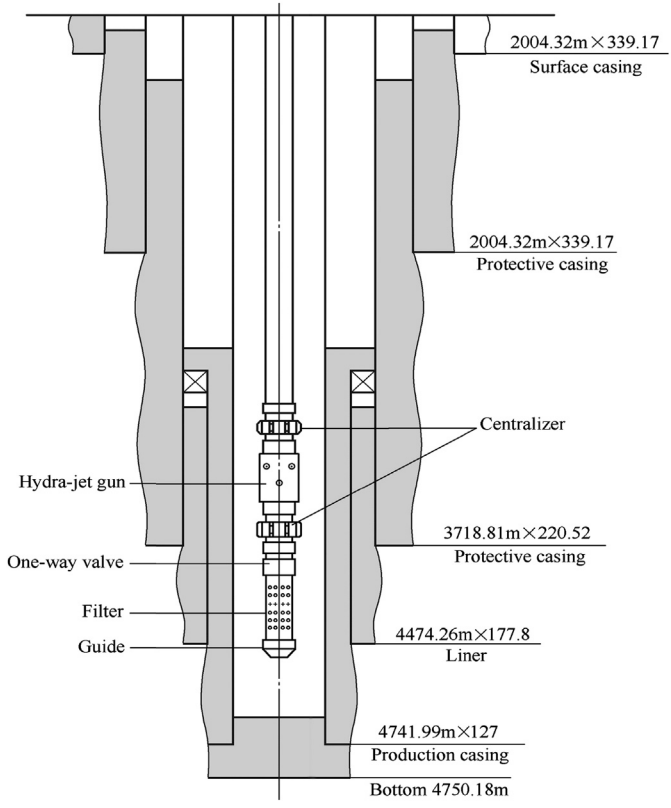

Figure 8.20 Well Wengu-2 structure and hydra-jet gun.

Table 8.4 Jet assembly parameter of Wengu2

Well depth	3542 m	Gun OD	Φ86 mm
Centralizer OD	92 mm	Nozzle assembly	6 × Φ6.0 mm

of 3423.85 m. The downhole assembly, also shown in Fig. 8.12, parameters are presented in Table 8.4.

8.4.2.2 Fracturing Treatment

Hydra-jet perforating and fracturing processes are as follows:

1. Pressure test at 80 MPa for 15 min. It will be qualified if the pressure decrease is less than 0.5 MPa.
2. Pump 20/40 mesh sand-laden fluid at a stable concentration of 6% and a flow rate of 1.9 m^3/min. The total sand volume was set at 3.0 m^3 for the perforation job.
3. Decrease the flow rate to 1.0 m^3/min. Shut down the casing valve and pump 70 m^3 of pad liquid. Inject the base fluid through the annulus at a flow rate of 0.5 m^3/min.
4. Pump 94 m^3 of proppant-laden fluid through the tubing.
5. Pump 11.9 m^3 of base fluid to displace the proppant-laden fluid in the tubing.
6. Stop the pump and wait for the fractures to close. The operating curve is depicted in Fig. 8.21.

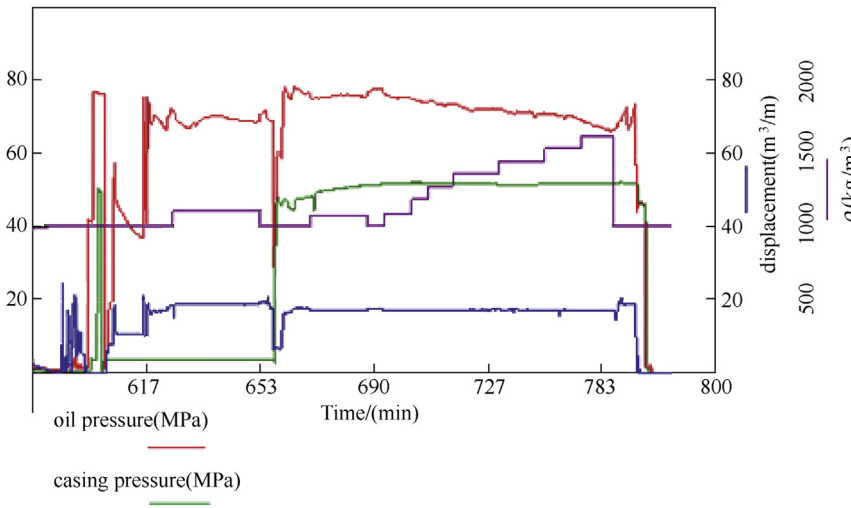

Figure 8.21 Operation curve of Wengu2.

8.4.2.3 Discussions

1. For the first time, this well was perforated with AWJ and hydra-jet fractured in a well pay zone with three layers of casing. It offered a new method to stimulate when conventional charge perforation could not be used.
2. In the hydra-jet fracturing stage, the tubing flow rate reached 1.9 m^3/min and annulus flow rate 0.5 m^3/min.
3. Hydra-jet fracturing can also satisfy complex well structures.

8.4.3 Case 3 Well Baiqian110

8.4.3.1 Basic Information

Well Baiqian110 is a vertical well completed with 5½″ production casing. The depth of the pay zone varies from 602.1 to 1105.2 m with four gas-bearing sections. According to the well-logging data, reservoir engineers found three pay intervals at 1091—1105, 912—926, and 749—760 m as tight sandstones, where fractures and microcracks grew very well. The three layers were chosen to perform multi-stage hydra-jet fracturing with CT equipment, as shown in Fig. 8.22.

8.4.3.2 Parameter Design

The CT, OD 2″, can only be pumped at a flow rate of 1.2 m^3/min considering its pressure limit. To achieve a higher jet velocity, three Φ6 mm

Figure 8.22 Field site.

nozzles were installed with a 120 degree angle. The total length of the jet string was 1980 mm. For every interval, 10 m^3 of proppant will be pumped to support the fracture, with 30 m^3 of 20/40 mesh ceramic proppant added.

8.4.3.3 Fracturing Treatment

This well was first fractured with CT to deliver proppant-laden fluid. It took 2–3 h for each layer to operate, as shown in Fig. 8.23. After the performance, this well produced 140 m^3 of fluid on the second day, with a gas production of 1.33×10^4 m^3/day. Fig. 8.24 shows the tool used after operating for 189 min. The average dilation of the nozzle diameter was approximately 6%. Grooves around the nozzles were a result of abrasive splashback erosion. Up to now, this is the only well being pumped proppant-laden fluid through CT because of concerns about possible wear inside the pipe.

8.4.4 Case 4 Well X5-4HB092

8.4.4.1 Basic Information

X5-4HB092 is a horizontal well located in the Songliao Basin, Daqing oilfield. Its completed depth is 1984.0 m with a horizontal section of 748.6 m and 5½″ production casing perforated. The longest perforation part is 178.0 m. Because of near-wellbore contamination, it was decided to exert hydra-jet three-stage fracturing.

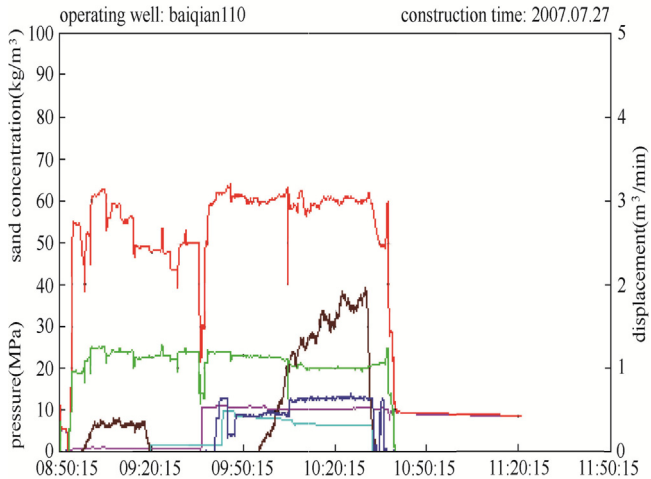

Figure 8.23 Operation curve of Well Baiqian110.

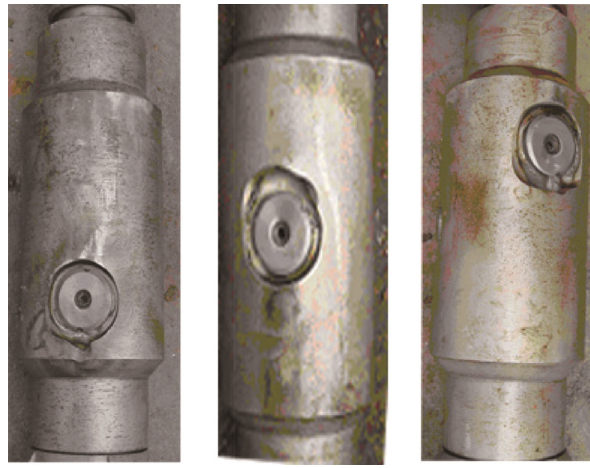

Figure 8.24 Used fracturing tools.

8.4.4.2 Fracturing Operation

Fig. 8.25 shows the three-stage hydra-jet fracturing process, each with four steps: hydra-jet perforation, pad fluid injection, pumping proppant-laden fluid, and displacement.

1. Hydra-jet perforation: Keeping the sand concentration at 6%—7% and flow rate at 2.5 m^3/min, it will consume about 50 m^3 of perforating fluid.
2. Pad fluid injection: In this stage, the flow rate will be reduced to 1 m^3/min to mitigate the possible water hammer when shutting down the

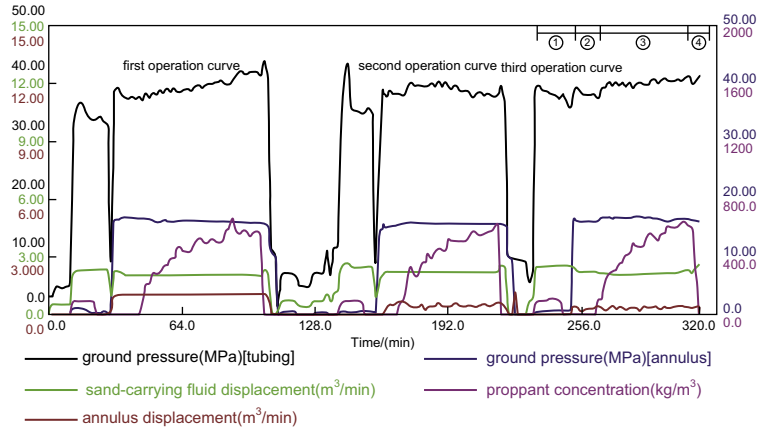

Figure 8.25 Operation curve of X5-4HB092. 1—Hydraulic sand-blasting perforation, 2—Injecting lead liquid, 3—Injecting ladder sand, 4—Replacement.

annulus valve. The pad fluid volume should be at least three times the planned proppant amount to achieve a large enough fracture.

3. Pumping proppant-laden fluid: This step should begin at a lower concentration, normally less than 10% to avoid sand screen-out. At the end, the concentration can be lifted to 40%—50%. Once the pump pressure gradually increases under constant proppant concentration, possible sand screen-out will occur. In this case, pumping should be stopped immediately and the tubing should be displaced with base fluid.
4. Displacement: The displacement volume should be strictly controlled. Generally, the value is set as 1.1 times the tubing string inside volume. This action will guarantee that the proppant will be removed from the tubing thoroughly and there will be no sand-stick risk.

For this well, it took 9 h to perform three-stage hydra-jet fracturing. The total injection fluid was 552 m^3, and 120 m^3 of 20/40 mesh ceramic proppant was placed into the fractures. The average proppant concentrations were 23.2%, 32.2%, and 31.9%, respectively.

The fracturing result was monitored in real time using microseismic technology. Using many geophones in different directions to receive microseismic waves, azimuth, fracture length, and fracture height information can be collected and analyzed. The results are shown in Table 8.5 and Fig. 8.26.

8.4.4.3 Stimulation Results

After the operation, oil production rose from 1.0—1.6 to 5.4 t/day. The water content decreased from over 90% to 81.3%—82.3%, which meant the fracturing effect was obvious. Also the results attained from real-time microseismic monitoring technology showed clearly that there were three fractures in the horizontal section, which dismisses doubt regarding the hydraulic isolation effect between two stages.

Table 8.5 Explanation of microseismic monitoring Well X5-4HB092

Project	StageI (1905.4 m)	StageII (1805.8 m)	StageIII (1315.0 m)
Length of half wing (m)	89.1	85.9	101.3
Azimuth (degrees)	46.5	40.5	44.9
Fracture height (m)	29.5	14.5	14.2
Occurrence	Vertical	Vertical	Vertical

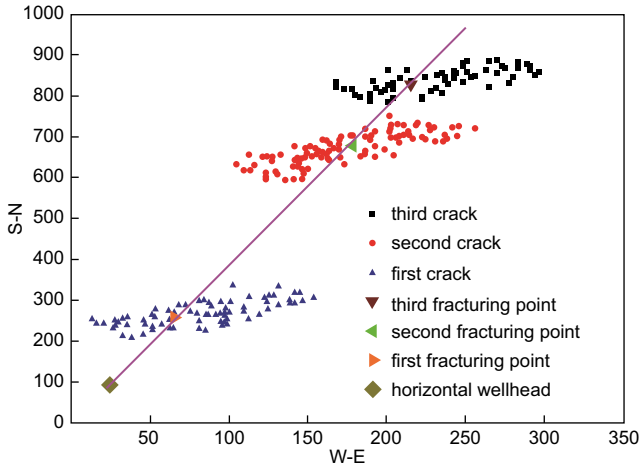

Figure 8.26 Explanation of fracture position and length of the three-stage fractures.

8.4.5 Case 5 Well Aer3-21

8.4.5.1 Basic Information

Well Aer3-21 is a horizontal well, with a horizontal section of 398 m, in the Aer depression, Erlian oilfield. To maximize potential production, an eight-stage hydra-jet fracturing operation was planned to stimulate the well.

8.4.5.2 Parameter Design

According to the well structure, the tool assembly, with seven slide sleeves, is as shown in Fig. 8.27. The planned sand amount for perforation was 18 m^3, the pad fluid was 722 m^3, the proppant-laden fluid was 1260 m^3, and the proppant was 330 m^3.

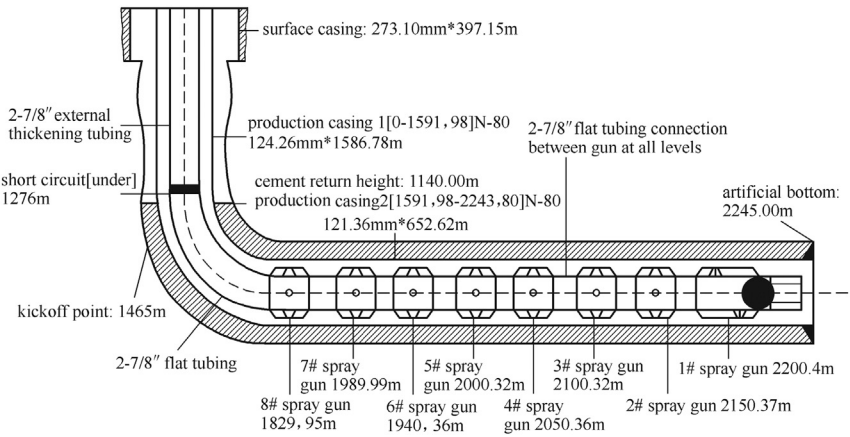

Figure 8.27 Tool assembly in Well Aer3-21.

Figure 8.28 Tripping in the tool.

8.4.5.3 Fracturing Treatment

The stimulation process is similar to the steps mentioned in Case 4. Figs. 8.28 and 8.29 show the field operation site. Fig. 8.30 shows a typical operation curve, displaying such information as tubing pressure, annulus pressure, proppant concentration, etc. The only difference lies in the

Figure 8.29 Field site.

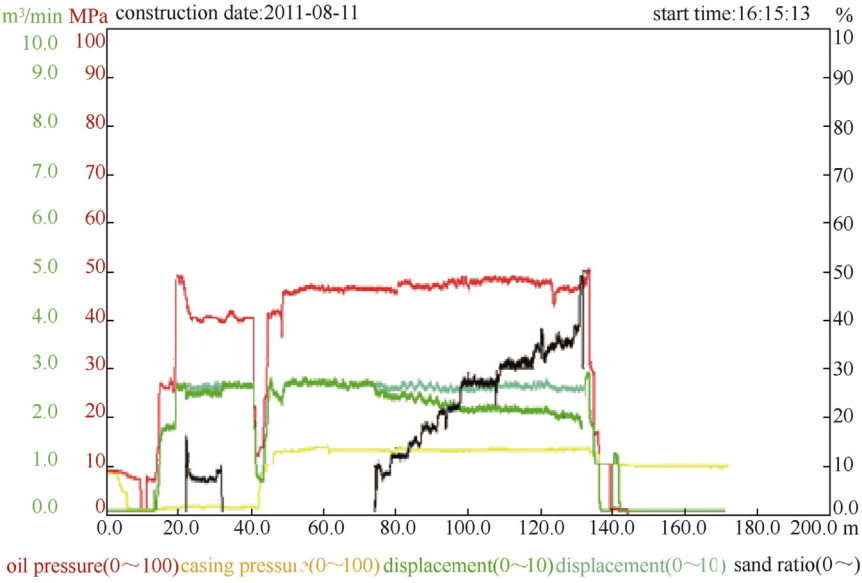

Figure 8.30 One-stage operation typical curve.

number of balls needed to shear the pins fixed to the corresponding slide sleeves. Naturally, because the treating sequence is from the toe to the heel, the ball's size will increase accordingly. For such wells with many stages and a comparatively large amount of proppant, two potential risks cannot be neglected: the slides close to the heel may become seriously worn, resulting in the ball not being able to fit the sleeve seat and failing to shear the pin, and there may be wear of the shoulder inside the gun, which functions as a support to the sleeve after being sheared. If there is no such shoulder, the slide sleeve will move down below the gun, giving rise to failure of the present-stage stimulation.

8.4.6 Case 6 Well Xinsha-311H

8.4.6.1 Basic Information

This gas well, with permeability of 0.18—0.32 mD, is a horizontal well completed with slotted liner in the horizontal open hole. In such a wellbore it is difficult to deploy mechanical packer assemblies to isolate between two stages. So, the hydra-jet fracturing method seems to be the only way to perform pinpoint fracturing at present. This is the first case applied to slotted liners in China. Basic data of this well are shown in Table 8.6 and Fig. 8.31.

Table 8.6 Basic data of Xinsha311H

Measured depth (m)	True vertical depth (m)	Horizontal section length (m)	Completion type
3010.0	2450.0	590.0	5½″ liners

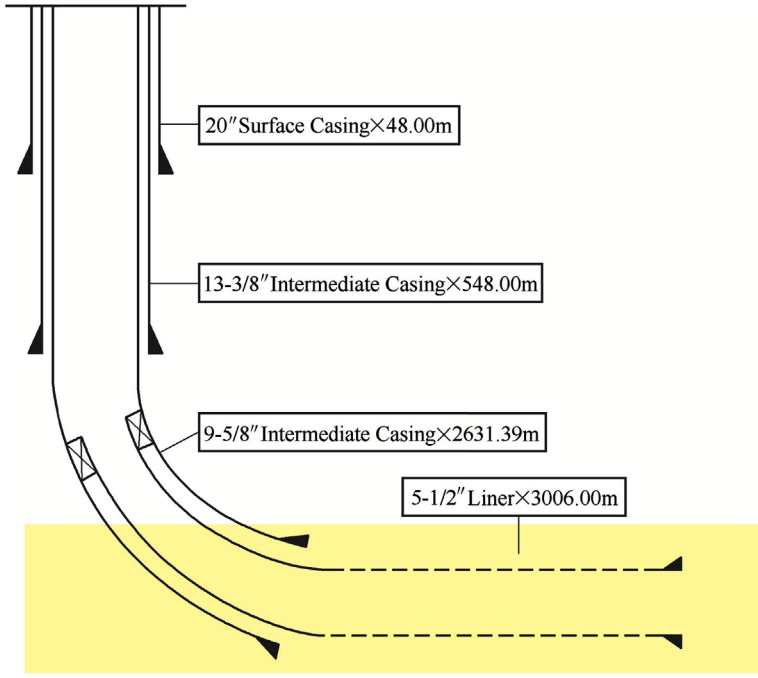

Figure 8.31 Well structure of Xingsha311H.

8.4.6.2 Parameter Design

Three jet guns were planned to perform pinpoint fracturing at 2962.0, 2791.0, and 2647.0 m. Compared to stimulated cemented-casing wells, the leakage of fracturing fluid will be serious in the slotted liners section. Therefore the annulus complement flow rate was adjusted from 1.2 to 1.5 m^3/min. Moreover, the gelled fluid should have a strong antishear ability to resist high-speed shear from the nozzles. This characteristic means the gel has good suspending abilities at high shear conditions. Three stages will be placed at 40, 30, and 30 m^3 of proppant, respectively. After calculation, the total injected fluid will be up to 997.7 m^3. The flow rate in the tubing will be set from 3.0 to 3.3 m^3/min, and the highest concentration will be 700 kg/m^3.

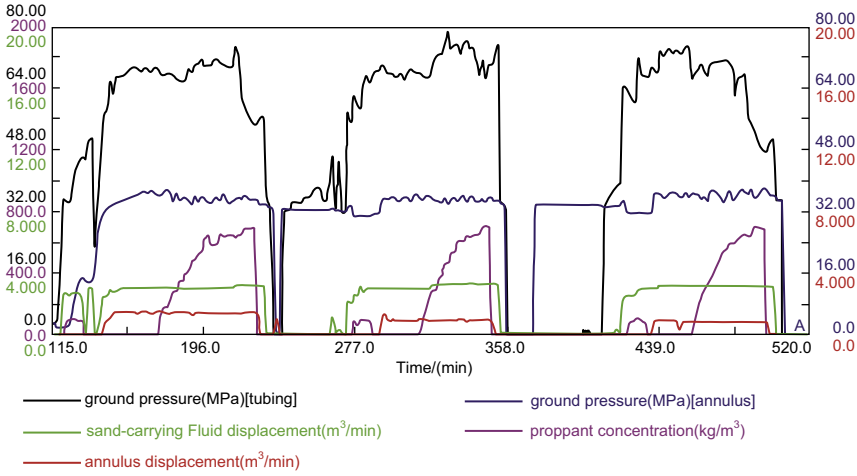

Figure 8.32 Operation curve of Xinsha311H.

8.4.6.3 Fracturing Treatment

It took about 9 h to finish the operation, with tubing pressure fluctuating from 65 to 76 MPa and annulus flow rate from 0.9 to 1.5 m^3/min. As Fig. 8.32 illustrates, it is critical to make sure that the annulus pressure should be lower than the extension pressure of the previous stage. During first-stage fracturing, the annulus rate was about 1.6 m^3/min, and the annulus pressure varied from 33 to 35 MPa. Therefore in the following fracturing stages the annulus pressure was controlled under 34 MPa, and the annulus rate was kept around 1.6 m^3/min. This action can ensure that the correct amount of fracturing fluid flows into the nontarget stages. Gas production increased from 0.3×10^4 to 16.1×10^4 m^3/day, proving its feasibility and effectiveness in such completed wells.

CHAPTER NINE

New Fracturing Fluids and Fracturing Methods

Contents

Abrasive Water Jet Perforation and Multi-Stage Fracturing
ISBN: 978-0-12-812807-7
https://doi.org/10.1016/B978-0-12-812807-7.00009-1

Abstract

A fracturing fluid is typically a water-based fluid that requires several chemical additives that may harm the environment. When the fracturing fluid enters a formation, it causes damage and reduces the oil and gas production. After the fracturing process, a part of the used fracturing fluid returns to the surface. This can contaminate the environment for a second time. To mitigate these problems, a waterless fracturing fluid is urgently needed. This chapter discusses three new fracturing fluids that have the potential to replace water-based fluids: supercritical carbon dioxide, liquid nitrogen, and thermal fluid.

Keywords: Damage; Fracturing fluid; LN_2; SC-CO_2; Thermal fluid.

9.1 CHARACTERISTICS OF SUPERCRITICAL CARBON DIOXIDE JET

9.1.1 The Thermophysical Properties of Liquid Supercritical CO_2

CO_2 is common in nature. Under normal conditions, CO_2 has no color or odor. After dissolving in water, the solution becomes slightly acidic. Furthermore, CO_2 cannot burn, but it can be liquefied easily. The volume fraction of CO_2 in the atmosphere is currently about 0.03%—0.04% and increases with the development of industry.

Fig. 9.1 shows the phase diagram of carbon dioxide. The triple point is at −56.56°C, and 0.52 MPa, with a critical point at about 31.1°C, and 7.38 MPa.

A supercritical fluid is different from gas and liquid, with many unique physical and chemical properties. In its supercritical state, CO_2 has a density

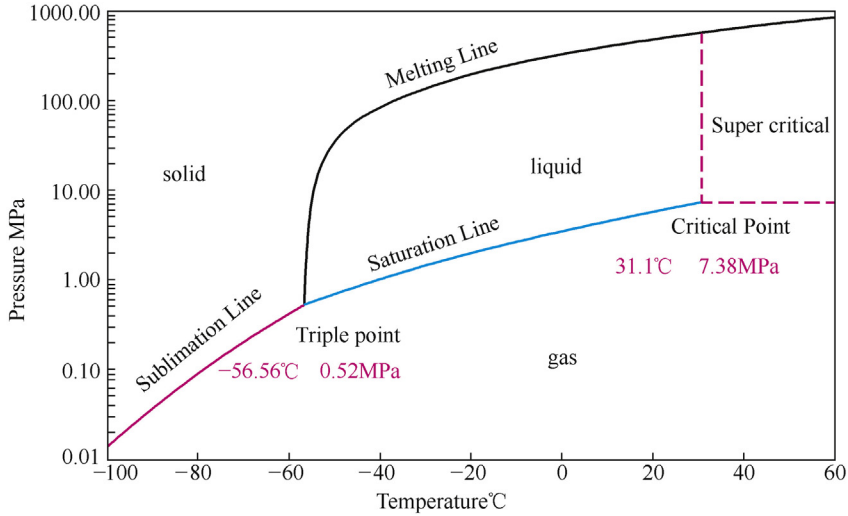

Figure 9.1 Phase diagram of carbon dioxide.

similar to that of a liquid but its viscosity and diffusivity are closer those of a gas. Table 9.1 shows the comparison of three important physical properties between supercritical fluid, gas, and liquid.

9.1.2 Computational Fluid Dynamics Model

The flow fields of an SC-CO_2 jet differ from other fluid jets because supercritical CO_2 (SC-CO_2) has many unusual thermal and physical properties. However, they can be simulated using computational fluid dynamics (CFD). Furthermore, the effect of several parameters on both pressure and velocity fields of an SC-CO_2 jet were studied and compared with a water jet.

Table 9.1 Comparison of important physical properties between supercritical fluid, gas, and liquid

Physical property	Gas (normal temperature and pressure)	Supercritical fluid	Liquid (normal temperature and pressure)
Density/(g/cm^3)	0.0006−0.002	0.2−0.9	0.6−1.6
Viscosity/(mPa s)	10^{-2}	0.03−0.1	0.2−3.0
Diffusion/(cm^2/s)	10^{-1}	10^{-4}	10^{-5}

9.1.2.1 Flow Field

Fig. 9.2 shows a two-dimensional geometric model of an SC-CO_2 jet flow field using a cylindrical polar coordinate system. The model consists of two parts: the internal space of the nozzle (including a conical and a cylindrical section) and the jet region. This model is vertically symmetrical with respect to the nozzle axis (bd). We used the same structure parameters for the conical nozzle of the SC-CO_2 jet as reported in other studies for water jets (Wagner & Kretzschmar, 2008). These parameters are nozzle inlet diameter (al = 16 mm), nozzle outlet diameter (hj = 6 mm), conical section length (bc = 20 mm), cylinder length (ci = 12 mm), standoff distance (id = 28 mm), and flow field height (me = 100 mm).

SC-CO_2 flows through the nozzle inlet (al) to the jet region, while applying pressure on the wall (me). It then flows away from the region (past the lines fg and kn). The nozzle inlet (al) was set as the pressure inlet boundary, while the flow field outlets (fg) and (kn) were set as pressure outlet boundaries (confined pressure). Other boundaries (fe, em, nm) were set as no-slip wall boundaries.

9.1.2.2 Model Details

Because SC-CO_2 jet fracturing involves heat transfer and a compressible fluid, the energy equations, as well as mass and momentum equations,

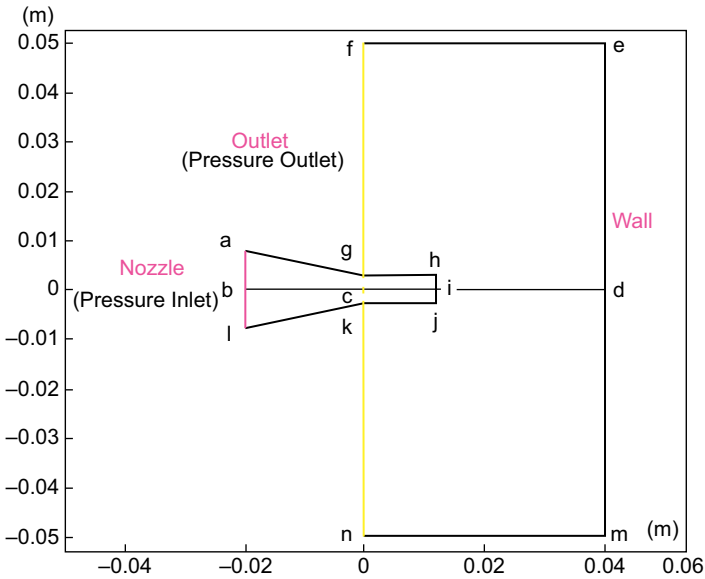

Figure 9.2 Geometry model of the flow field.

should be solved. The SC-CO_2 jet is turbulent and flows with high-speed liquid CO_2, gravity was ignored, and the standard k-ε model was adopted in this study for turbulence closure. The governing equations are as follows (Hualin, Gensheng, & Can, 2005):

The mass equations are

$$\mathrm{div}(\rho\overrightarrow{v}) = 0 \tag{9.1}$$

where ρ represents density (kg/m^3) and $\overrightarrow{v}$ is the velocity vector (m/s).

In the cylindrical polar coordinate system, the momentum equations are

$$\frac{1}{r}\frac{\partial}{\partial x}(r\rho v_x v_x) + \frac{1}{r}\frac{\partial}{\partial r}(r\rho v_r v_x) = -\frac{\partial p}{\partial r} + \frac{1}{r}\frac{\partial}{\partial x}\left[r\mu\left(2\frac{\partial v_x}{\partial x} - \frac{2}{3}(\nabla\cdot\overrightarrow{v})\right)\right] + \frac{1}{r}\frac{\partial}{\partial r}\left[r\mu\left(\frac{\partial v_x}{\partial r} + \frac{2}{3}\frac{\partial v_r}{\partial x}\right)\right] + F_x \tag{9.2}$$

$$\frac{1}{r}\frac{\partial}{\partial x}(r\rho v_x v_r) + \frac{1}{r}\frac{\partial}{\partial r}(r\rho v_r v_r) = -\frac{\partial p}{\partial r} + \frac{1}{r}\frac{\partial}{\partial x}\left[r\mu\left(\frac{\partial v_r}{\partial x} + \frac{\partial v_x}{\partial r}\right)\right] + \frac{1}{r}\frac{\partial}{\partial r}\left[r\mu\left(2\frac{\partial v_r}{\partial r} - \frac{2}{3}(\nabla\cdot\overrightarrow{v})\right)\right] - 2\mu\frac{v_r}{r^2} + \frac{2}{3}\frac{\mu}{r}(\nabla\cdot\overrightarrow{v}) + p\frac{\overrightarrow{v}_z^2}{r} + F_r \tag{9.3}$$

where x is the axial coordinate, r is the radial coordinate in m, v_x is the axial velocity, v_r is the radial velocity, v_z is the swirl velocity in m/s, μ is dynamic viscosity in Pa s, p is the pressure in Pa, F_x and F_r are components of body forces in kg/(m s).

The energy equations are

$$\mathrm{div}(\rho\overrightarrow{v}T) = \mathrm{div}\left(\frac{k}{C_p}\mathrm{grad}\,T\right) + S_T \tag{9.4}$$

where C_p is the isobaric specific heat in J/(kg K), T is the temperature in K, k is the heat transfer coefficient in W/(m K), and S_T is the term for viscous dissipation in K s^2/m^2.

9.1.3 Flow Field Comparison Between Supercritical CO_2 Jet and Water Jet

9.1.3.1 Conversion Between Velocity and Pressure

The velocity and pressure along the axis were compared between SC-CO_2 and water jet. As shown in Fig. 9.3, when SC-CO_2 and water flows through the conical section of nozzle, the fluid velocity increases gradually, whereas the pressure decreases. This indicates that pressure energy was converted into kinetic energy. After SC-CO_2 and water entered the cylinder section of the nozzle, both pressure and velocity remain constant, indicating no conversion between pressure energy and kinetic energy. When SC-CO_2 entered the jet region and hit the wall, velocity decreases sharply, whereas the pressure increases, indicating the conversion of kinetic energy into pressure energy. Finally, velocity becomes zero and pressure increases to a value, which is slightly lower than the nozzle inlet pressure. The results indicate that also for the water jet, both velocity and pressure of SC-CO_2 jet can be converted into each other.

According to fluid mechanics theory, the impact pressure imposed on the wall by high-speed fluid is

$$P_{\text{impact}} = P_{\text{confining}} + \frac{1}{2}\rho v_{\max}^2 - P_f \tag{9.5}$$

where P_{impact} is the impact pressure in MPa, $P_{\text{confining}}$ is the confining pressure in MPa, P_f is the pressure loss in MPa, ρ is the fluid density in

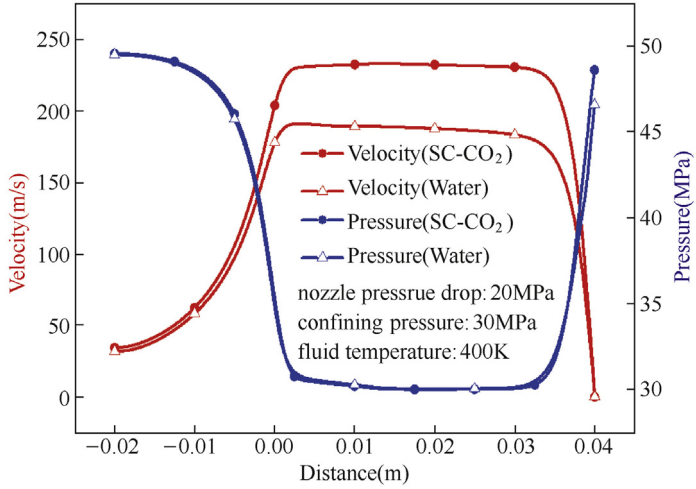

Figure 9.3 Velocity and pressure curves of the two jets.

high-speed jet region in kg/m^3, and v_{max} is the maximum velocity of the fluid in high-speed jet region in m/s.

9.1.3.2 Comparison of Pressure Fields

As shown in Fig. 9.4, with three different nozzle pressure drops (10, 20, 30 MPa), the axial pressures of two jets coincide with each other largely. The main difference is that the axial pressure of the SC-CO_2 jet is slightly higher than that of the water jet at the right end. This indicates that the SC-CO_2 jet has a stronger impact pressure than the water jet. This result may be one reason that the SC-CO_2 jet has a smaller threshold pressure and stronger rock-breaking capacity than the water jet. The other reason is that the penetration capability of fluid SC-CO_2 is stronger because of its lower viscosity and surface tension. Hence the impact pressure of SC-CO_2 jet can be transmitted to the micropores and fractures easily (Potter & Tester, 1998). In other words, the stronger impact pressure of the SC-CO_2 jet is advantageous for rock breaking and can increase the rate of penetration of SC-CO_2 jet drilling.

The relation between pressure loss ratio and nozzle pressure drop is shown in Fig. 9.4. The pressure loss ratio R_{PL} is defined as

$$R_{PL} = \frac{P_{in} - P_{impact}}{P_{in}} \tag{9.6}$$

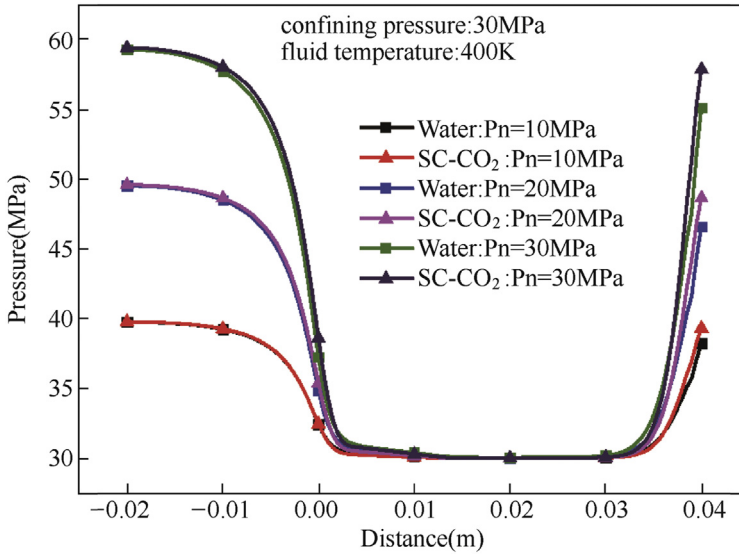

Figure 9.4 Axial pressure comparison of the two jets.

where R_{PL} is the pressure loss ratio, which is dimensionless, and P_{in} is the nozzle inlet pressure in MPa.

As shown in Fig. 9.5, the pressure loss ratio of SC-CO_2 jet is smaller than that of water jet with three different nozzle pressure drops. It indicates that the SC-CO_2 jet undergoes less pressure-energy loss than the water jet under the same conditions. This is mainly because the viscosity of SC-CO_2 is much smaller than that of water ($\mu_{SC-CO_2} = 5-6 \times 10^{-5}$ Pa s, $\mu_{Water} = 20-30 \times 10^{-5}$ Pa s in these cases).

9.1.3.3 Comparison of Velocity Fields

As shown in Fig. 9.6, the maximum velocity of the SC-CO_2 jet reached up to 228 m/s, which is clearly higher than that of the water jet (163 m/s). The reason is that the SC-CO_2 jet has a higher impact pressure than the water jet under the same nozzle inlet pressure and confining pressure, as discussed previously, and the SC-CO_2 density (657–664 kg/m^3) in the high-speed jet region is below the density of water (1000 kg/m^3). Hence according to Eq. (9.5), and because the effect of P_f is negligible, the maximum velocity of the SC-CO_2 jet is higher than that of the water jet. The results indicate that the SC-CO_2 jet has a higher velocity than the water jet under the same conditions, which would increase the perforation speed of an SC-CO_2 jet with abrasives.

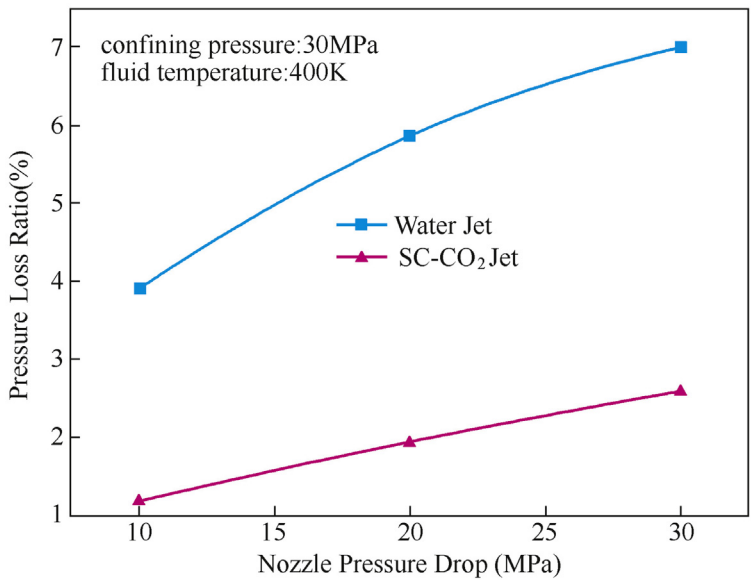

Figure 9.5 Comparison of pressure loss ratio.

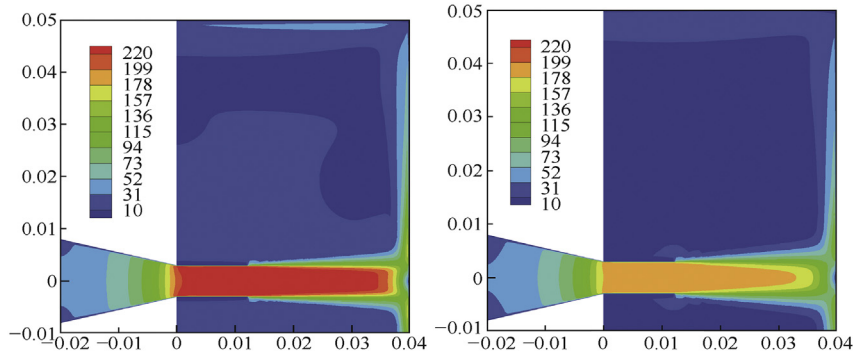

Figure 9.6 Velocity contour plots of the supercritical CO_2 jet and the water jet (unit: m/s).

The axial velocity of two jets under the same conditions is compared as well. As shown in Fig. 9.7, the SC-CO_2 jet has a higher maximum velocity than the water jet under two different nozzle pressure drops (10, 30 MPa).

9.1.4 Parametric Sensitivity Analyses

9.1.4.1 Nozzle Pressure Drop

Nozzle pressure drop is the key parameter determining the kinetic energy of the jet, and the kinetic energy of the jet directly affects the flow field

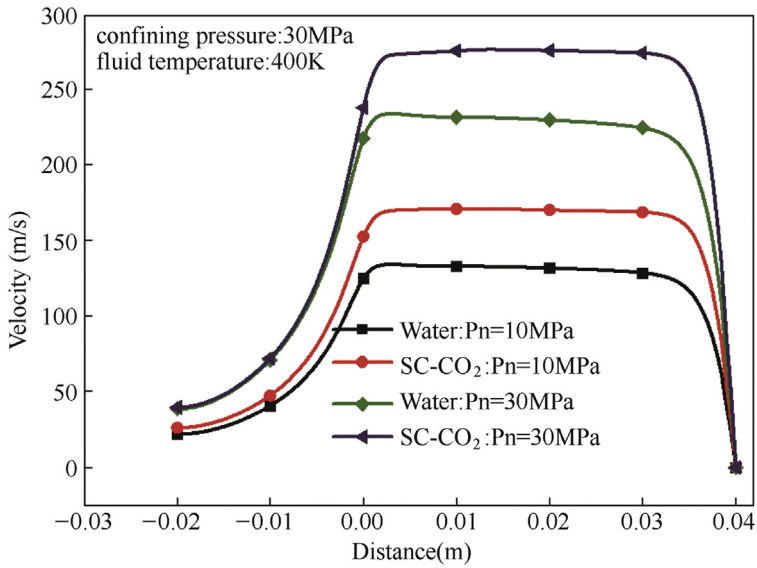

Figure 9.7 Axial velocity comparison of the two jets.

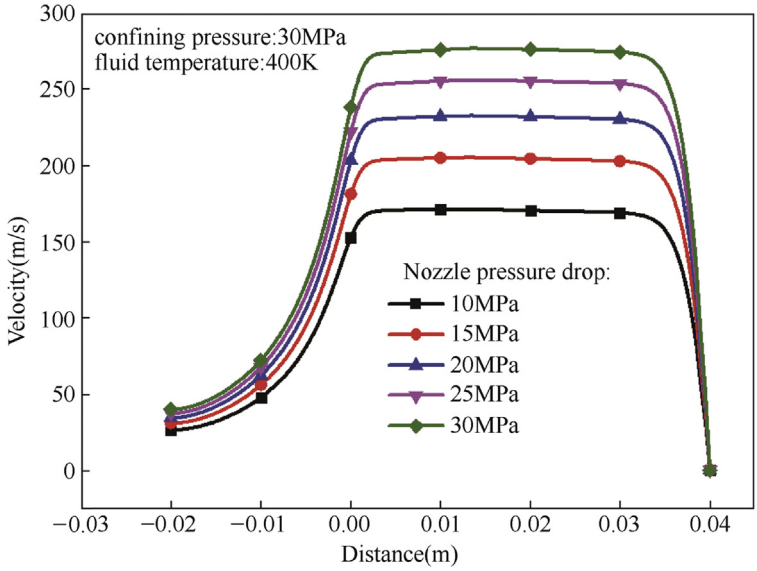

Figure 9.8 Nozzle pressure drop versus the axial velocity.

(Kim, 2003). Therefore the axial pressure and velocity of the SC-CO_2 jet with different nozzle pressure drops were studied. As shown in Fig. 9.8, the maximum velocity of the SC-CO_2 jet increases with increasing nozzle pressure drop.

As shown in Fig. 9.9, the axial pressure of a nozzle cylinder section with five different nozzle pressure drops coincide with each other, which is mainly dominated by confining pressure (30 MPa in these cases). When the fluid SC-CO_2 reaches the nozzle cylinder section, pressure energy is converted into kinetic energy and the axial pressures with different nozzle pressure drops decrease to the confining pressure. At the right end of the flow field, the impact pressure increases with the growth of the nozzle pressure drop because the bigger the nozzle pressure drop, the greater is the kinetic energy and the impact pressure.

9.1.4.2 Confining Pressure

As shown in Fig. 9.10, the impact pressure increases gradually with the growth of the confining pressure, and the respective increment is small. The rate of increase slows down with the growth of confining pressure.

The effect of the confining pressure on the axial velocity of the SC-CO_2 jet is shown in Fig. 9.11. As shown in Fig. 9.11, for the same nozzle pressure

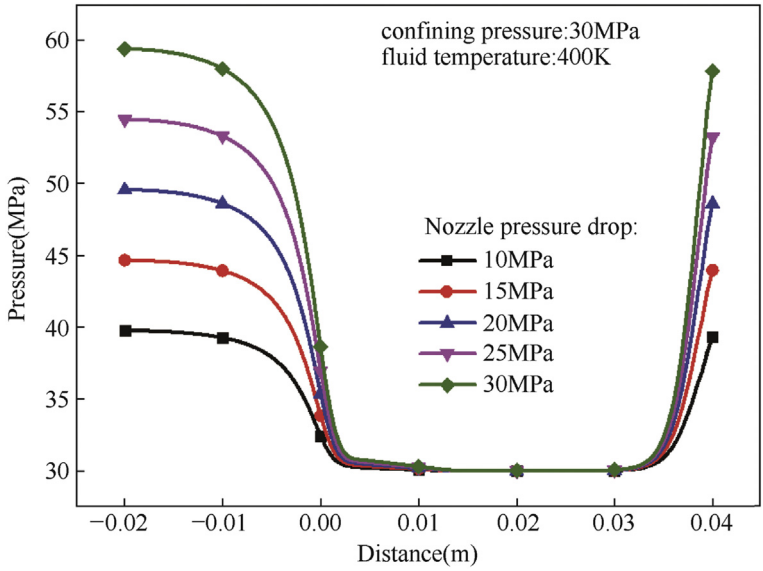

Figure 9.9 Nozzle pressure drop versus the axial pressure.

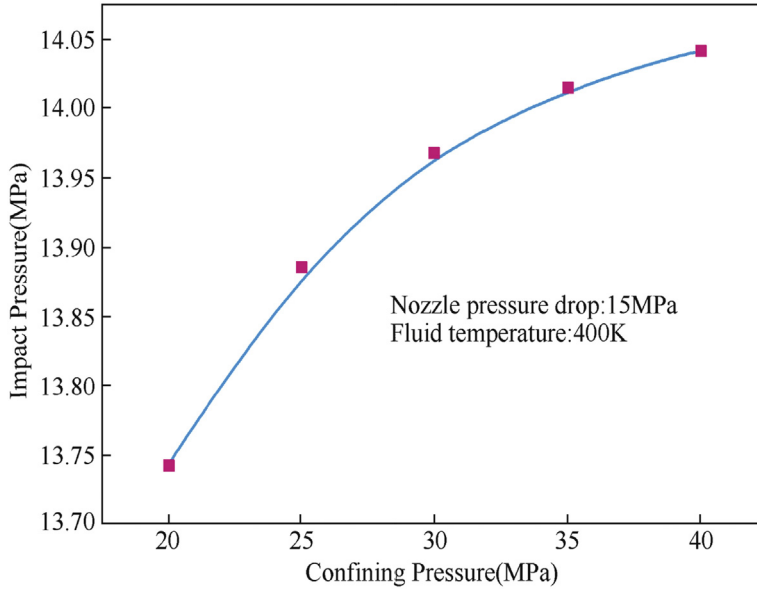

Figure 9.10 Confining pressure versus impact pressure.

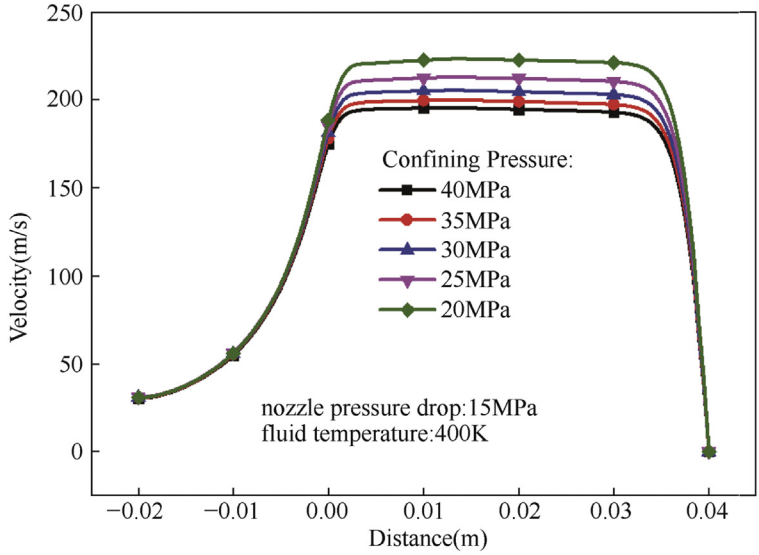

Figure 9.11 Confining pressure versus axial velocity.

drops and fluid temperatures, the velocity in the high-speed jet region increases with growing confining pressure.

9.1.4.3 Supercritical−CO_2 Temperature

The properties of SC-CO_2 fluid are sensitive to temperature, and any change in the property can affect the structural form of the SC-CO_2 jet (Liao & Li, 2006). Therefore the effects of the SC-CO_2 temperature on the axial pressure and velocity of the SC-CO_2 jet were studied.

As shown in Fig. 9.12, the axial pressure of the SC-CO_2 jet was largely the same when the temperature increased from 360 to 420K. This indicates that, for the stimulated condition in this study, the pressure distribution of the SC-CO_2 jet is hardly affected by the temperature change. However, as shown in the enlarged drawings of impact pressure, the impact pressure decreases slightly with increasing temperature. In general, the effect of SC-CO_2 temperature on impact pressure can be neglected in engineering applications.

As shown in Fig. 9.13, the maximum velocity increases with the growth of SC-CO_2 temperature. This is mainly because the fluid density decreases with the increasing SC-CO_2 temperature, while the effect of temperature on impact pressure can be neglected. Hence, according to Eq. (9.5), since the influence of P_f is negligible, the maximum velocity increases with increasing fluid temperature.

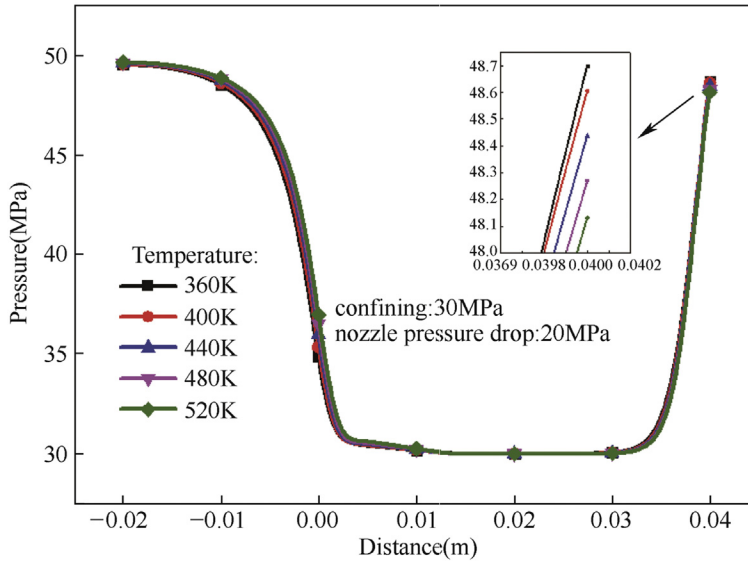

Figure 9.12 Temperature versus axis pressure.

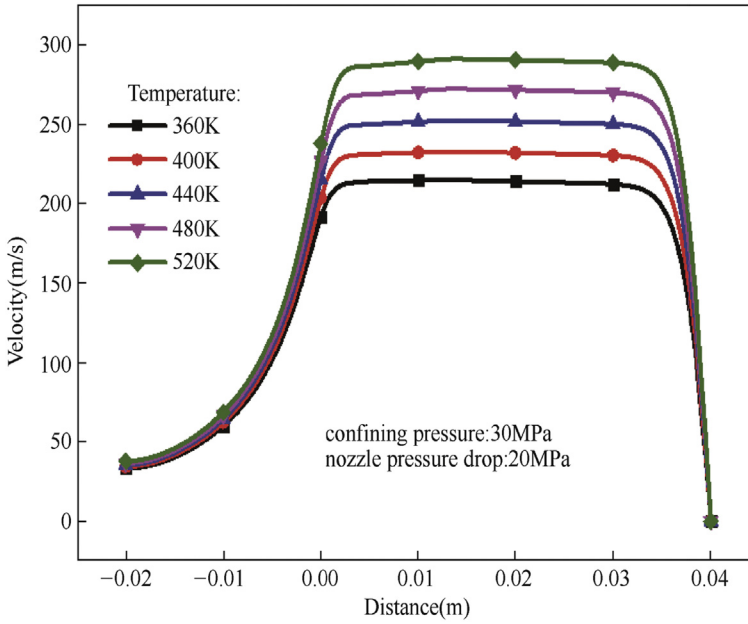

Figure 9.13 Temperature versus axial velocity.

9.1.5 Feasibility Analysis of Supercritical CO_2 Fracturing

9.1.5.1 Advantages of Supercritical CO_2 for Fracturing

SC-CO_2 is a type of nonaqueous fracturing fluid, and there is no need to add other chemical agents. Therefore no pollution will be introduced into the reservoir or the environment.

SC-CO_2 is environment friendly and causes no harm to the human body. Furthermore, because SC-CO_2 is a nonaqueous fracturing fluid, the problem of clay expansion is solved essentially, and the reservoir will be protected effectively. In addition, with a low viscosity and high diffusion coefficient, a fracture network is generated in the reservoir, and the conductivity capacity of the reservoir is improved further. Based on experiments, Li Xiang et al. found that the fracture surface caused by SC-CO_2 is rougher than that caused by water and N_2, and the rough surface helps to improve the fracture conductivity. More importantly, when SC-CO_2 is applied to fracture the shale gas or coal gas reservoir, the adsorbed methane will be replaced. This is because the adsorption capacity of SC-CO_2 is higher than that of methane and the recovery rate of unconventional gas will increase significantly. Therefore SC-CO_2 jet fracturing is expected to become a new type of environment-friendly, efficient, and safe fracturing technique.

With the advantages of multilayer fracturing by one-trip string, no compaction effect caused by bullet perforation and no need to employ a mechanical packer exists. Therefore, coiled-tubing multi-stage hydraulic-jet fracturing is an effective approach to stimulate the reservoir. However, severe challenges need to be overcome with this technique. For example, for a small inner diameter of the coiled tubing, the flow friction is high, and results in deficiency of the down-hole hydraulic energy. Furthermore, the pressure-bearing capacity of the coiled tubing is limited, which could limit the operating pressure (Walsh & Lomov, 2013). Coiled tubing jet fracturing with SC-CO_2 can strengthen the characteristics of coiled tubing fracturing effectively. First, the flow friction of SC-CO_2 in the coiled tubing is smaller, which ensures that the SC-CO_2 jet fracturing contains sufficient energy. Second, for the low rock-breaking threshold pressure of SC-CO_2, jet fracturing by SC-CO_2 can be performed under low operating pressure. Most importantly, SC-CO_2 is a clean fracturing fluid and there is no need to discharge it after operation, which shortens the operation period and reduces the operational costs.

9.1.5.2 Effects of Supercritical CO_2 on Perforation and Pressurization

Hydraulic fracturing includes two processes: hydraulic sandblasting perforation and hydraulic fracturing. Thanks to the high-pressure fracturing fluid flowing through the down-hole jet device, a certain diameter and depth of a perforation hole is formed in the casing and rock. Subsequently, the high-velocity jet continues to flow into the borehole until it stagnates. Then, according to the principle of jet pressurization, the stagnation pressure in the hole is higher than the confining pressure. When the stagnation pressure reaches the fracture pressure, the top of the jet channel will crack and extend. Therefore to facilitate the jet fracturing process, the working fluid must have a certain amount of jet perforation ability and jet pressurization capacity.

The perforation mechanism of the SC-CO_2 jet is similar to that of the water jet, which includes jet impingement and wedge splitting. However, the wedge splitting of SC-CO_2 is particularly prominent (Fig. 9.14). Compared with water, the viscosity of supercritical fluid CO_2 is lower, the diffusion coefficient is larger, and the surface tension is closer to zero. Therefore it is very easy to penetrate the rock micropores and microcracks, and it can effectively reduce the rock strength (Peng & Ma, 2005). As shown in Fig. 9.15, under the differential pressure of 193 MPa, the water jet can only cut the narrow fracture in the Mancons shale, whereas SC-CO_2 can cut the deeper and wider fracture under the differential pressure of 90 MPa. Therefore the use of SC-CO_2 for injection perforation can perforate both casing and rock formation, and form perforation holes under low-pressure conditions.

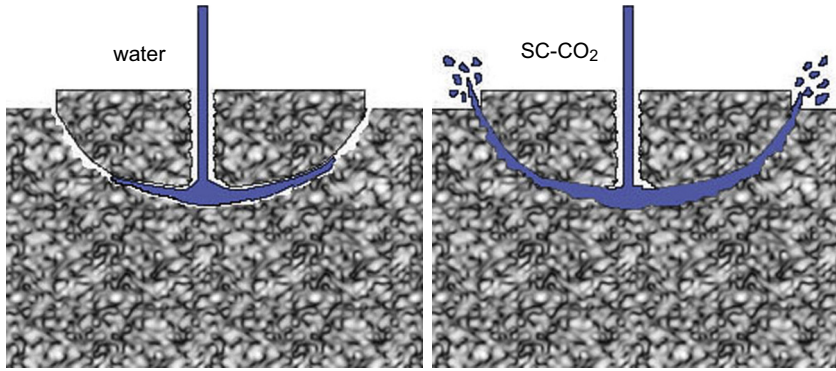

Figure 9.14 Wedging effects of water jet and supercritical CO_2 jet.

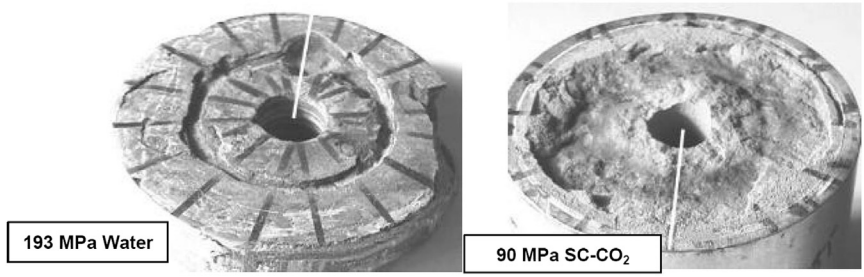

Figure 9.15 Jet erosion effects in Mancos shale with water jet and supercritical CO_2 jet.

To confirm the jet pressurization effect of SC-CO_2, the CFD method was used to simulate the flow field in the hole for the SC-CO_2 injection fracturing process. We then compare the effects of SC-CO_2 with those of injection fracturing and hydraulic injection fracturing. As shown in Fig. 9.16, for three kinds of nozzle pressure drops, the stagnation pressure of SC-CO_2 during injection fracturing in the hole is higher than that of the hydraulic injection under the same conditions. When the nozzle pressure drop is 30 MPa, its supercharging value is 2.4 MPa higher than that

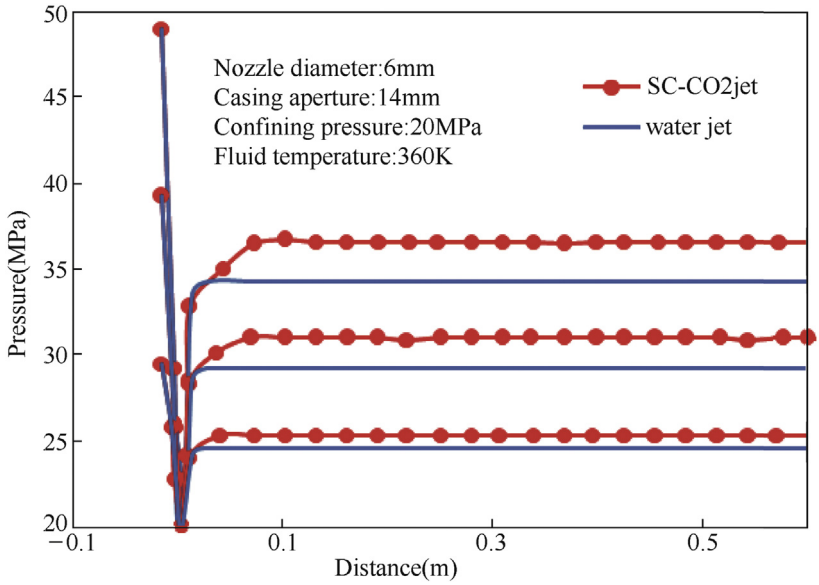

Figure 9.16 Pressure distribution comparison between supercritical CO_2 jet fracturing and water jet fracturing.

of hydraulic fracturing. This shows that SC-CO_2 injection fracturing has a stronger supercharging effect than hydraulic fracturing. Therefore when using SC-CO_2 for jet fracturing, a greater hole pressure can be obtained under the same nozzle pressure drop condition and it is more conducive to the initiation of formation.

In summary, SC-CO_2 jet is more powerful than the water jet and the jet pressurization effect is stronger. Hence jet perforation and fracturing can be realized for lower construction pressure.

9.1.5.3 The Procedure of Supercritical CO_2 Jet Fracturing

Fig. 9.17 is a schematic diagram of SC-CO_2 jet fracturing. As is shown in this picture, liquid CO_2 is stored in a tank. First, sand blast perforation is initiated. Liquid CO_2 is then pumped into the blending equipment and mixed with abrasive sands that are 60—80 meshes in diameter. The mixture is pumped down through coiled tubing. When it flows into the nozzle of the jet fracturing tool, an abrasive SC-CO_2 jet is formed. Then the perforation operation starts, which last about 5—10 min. Subsequently, pure liquid CO_2 is pumped down-hole, carrying the remaining abrasive sands

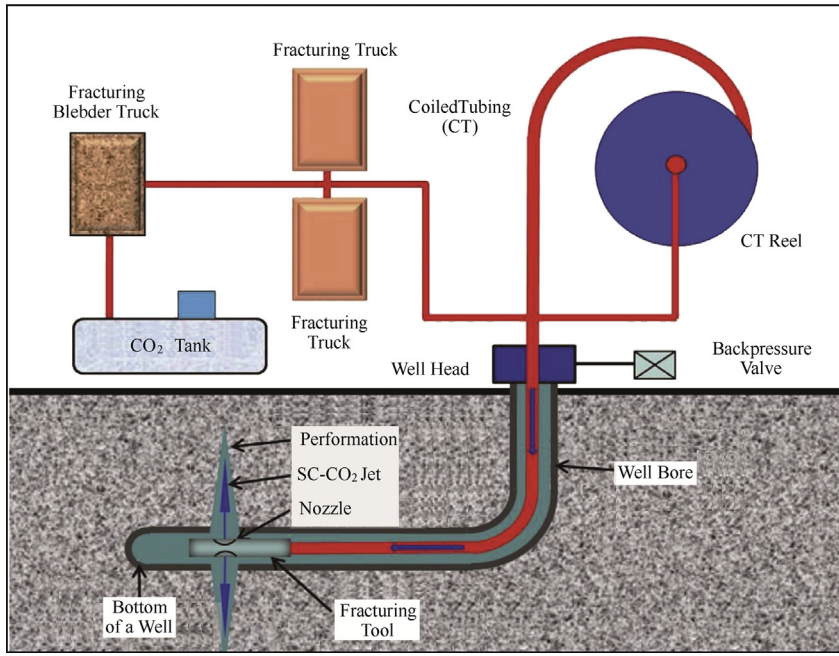

Figure 9.17 Schematic diagram of supercritical CO_2 jet fracturing.

out of the well to avoid blocking a pipe. Then the fracturing operation is carried out. A large amount of pure CO_2 is pumped into the well in liquid form. When the bottom hole pressure exceeds the formation fracturing pressure, CO_2 mixed with proppants is pumped down-hole through coiled tubing, or though the annulus between the coiled tubing and casing simultaneously, to reduce the abrasion with coiled tubing. After that pure liquid CO_2 is pumped into the bottom hole to carry the remaining proppants in the wellbore and out of the well to avoid blocking a pipe. If there is a need to fracture the next layer, coiled tubing and the jet fracturing tool are pulled up to the target layer, and then the second stage of fracturing is started. In a similar way, multi-stage fracturing is conducted. After the fracturing operation, it is recommended to shut the well down for 5−10 days and then open the well to produce without open flow. As described in Section 3, after SC-CO_2 has flown into the reservoir, there are several benefits. For example, the recovery rate is improved further. In addition, if the production is urgent, it is possible to release the down-hole pressure slowly and produce directly.

9.2 LIQUID NITROGEN

9.2.1 Basic Physical Properties of Liquid Nitrogen

Liquid nitrogen is a colorless, tasteless, nonpolluting fluid, which is not only widely used in the fields of aerospace, electronics, food, civil and biology, and others but also plays an important role in petroleum engineering. At the end of the 20th century, it was successfully used as a fracturing fluid to create artificial fractures in formations. As shown in Table 9.2, liquid nitrogen is an extremely cryogenic fluid, whose critical temperature and boiling point (at atmospheric pressure) are −146.9 and −195.8°C, respectively. Thus liquid nitrogen can significantly reduce the temperature of rock when it comes in contact with the hot reservoir. In this case, the significant thermal stress inside the rock will be reduced, which can promote the extension of initial cracks and even produce new cracks. Moreover, liquid nitrogen has excellent compatibility with other fluids in formations and does not take part in any emulsification, thanks to its inertness. Due to the extremely low critical temperature, liquid nitrogen can completely gasify to leave behind nothing in the reservoirs.

Table 9.2 Physical properties of nitrogen

Physical properties	Condition	Parameter
Molecular weight	–	28.013 g/mol
Specific gravity, gas (air = 1.0)	1 atm, 21.1°C	0.9669
Specific volume, gas	1 atm, 21.1°C	0.8615 m^3/kg
Density, gas	1 atm, 21.1°C	1.161 kg/m^3
	Sat at 1 atm	4.604 kg/m^3
Density, liquid	1 atm	808.5 kg/m^3
Critical point	Critical Temperature	−146.96°C
	Critical Pressure	3.396 MPa
Triple point	Temperature	−210.00°C
	Pressure	12.52 kPa
Specific heat, gas	1 atm, 21.1°C	/
	Constant Pressure, C_p	1.04 kJ/(Kg K)
	Constant Pressure, C_v	0.743 kJ/(Kg K)
	Ratio, C_p/C_v	1.40
Dynamic viscosity, gas	1 atm, 21.1°C	1.77×10^{-5} Pa s
Dynamic viscosity, liquid	Sat at 1 atm	1.52×10^{-4} Pa s
Thermal conductivity, gas	1 atm, 21.1°C	2.54×10^{-2} W/m K
Thermal conductivity, liquid	Sat at 1 atm	1.35×10^{-1} W/m K

9.2.2 Effect of Liquid Nitrogen Cooling on the Rock Pore-Structure

To study the effects of liquid nitrogen cooling on the rock pore structure, different rock samples (sandstone, marble, and shale) were cooled by liquid nitrogen under dry and water-saturated conditions, respectively. Using nuclear magnetic resonance (NMR) spectroscopy, characteristics, mechanisms, and factors influencing the rock pore structure were analyzed.

9.2.2.1 Nuclear Magnetic Resonance Theories

NMR is a core testing method commonly used in petroleum engineering. It is used to determine the characteristics of the rock's pore structure according to the transverse relaxation time (T_2) of the fluid in a saturated rock sample. In weak magnetic fields, T_2 is mainly affected by the surface relaxation of rocks, and it is related to the specific surface of the pores. T_2 is defined as (Matteson, Tomanic, Herron, Allen, & Kenyon, 2000):

$$1/T_2 \approx \rho(S/V)_{\text{pore}} \tag{9.7}$$

where ρ is the surface-relaxation intensity (μm/ms) and S/V is the ratio of the surface area (S) to the volume (V), i.e., the specific surface of the pores (μm^{-1}).

In case the pores are spherical, the relationship between T_2 and the radius of the pores is

$$1/T_2 \approx \rho(3/r)_{\text{pore}} \tag{9.8}$$

where r is the radius of the pores (μm).

Using the NMR pore structure tests, the results can be visualized in the form of a T_2 distribution curve (see Fig. 9.18). T_2 is proportional to the radius of the pores. In other words, the larger the radius, the larger is the value for T_2. The signal amplitude corresponds to the number of pores; hence the larger the amplitude, the greater is the number of pores. The integrated area of the T_2 distribution curve is proportional to the volume of the pores (again, the larger the area, the larger the volume of the pores). Thus if the pore structure changes, the distribution characteristic of the T_2 curve changes accordingly.

9.2.2.2 Rock Samples

Three rocks (sandstone, marble, and shale) were used in the experiments. For the NMR tests, four rock samples were drilled for each kind of rock and processed into cylinders (25 mm in diameter and 50 mm in length).

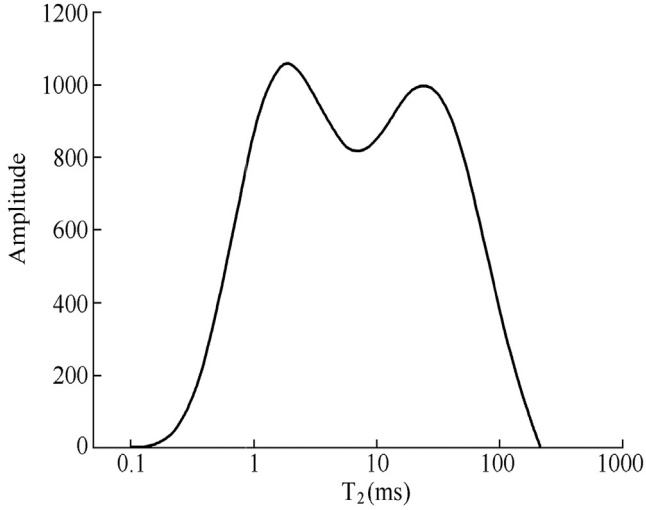

Figure 9.18 A typical T_2 distribution curve.

Table 9.3 The results of physical property tests on the sandstone, marble, and shale

Rock type	Porosity (%)	Density (g/cm^3)	Compressive strength (MPa)	Tensile strength (MPa)
Sandstone	18.33	2.20	75.72	2.35
Marble	0.86	2.88	130.31	5.86
Shale	4.76	2.49	90.62	3.67

Tests were also performed on the used rocks to determine their density, porosity, compressive strength, and tensile strength. The results are listed in Table 9.3.

9.2.2.3 Experimental Equipment

A 10-MHz SPEC-023 NMR spectrometer, designed and manufactured by Beijing Spec T & D Co. Ltd (SPEC), was used to record the NMR data. The magnetic field strength of the permanent magnet is about 0.24 T at room temperature. There are three radio-frequency (RF) probes with different inner diameters of 38, 75, and 111 mm in this spectrometer. The 38-mm RF probe was chosen for this study. A Carr-Purcell-Meiboom-Gill pulse sequence acquires the transverse relaxation time (T_2), and the software in the instrument processes the experimental data. An electronic balance, drying oven, and vacuum saturation vessel were also used in the experiments.

9.2.2.4 Experimental Details

1. The cylindrical rock samples were placed in a saturation device and saturated under pressure in vacuum for 48 h. Then NMR measurements were conducted on the saturated rock samples to obtain the T_2 distribution curves for the rocks in their initial states.
2. Two samples of each rock were cooled by liquid nitrogen for 10−15 min. Previous research (Chen, Yeung, & Mori, 2004) has shown that for a saturated rock sample, which is 30 mm in diameter and 60 mm in length, the pore water is completely frozen after 5 min in liquid nitrogen.
3. The other two samples of each rock were put in the oven and dried at 80°C for 48 h until the weight difference between before and after measurements was less than 0.2%. After cooling down to room temperature, the dried samples were cooled in liquid nitrogen for 10−15 min.

4. After cooling to room temperature, the rock samples cooled in liquid nitrogen were saturated again. Then NMR was performed on them again.

During the NMR tests, the main parameters were set as follows: resonance frequency of 9.38 MHz, echo spacing time of 0.35 ms, waiting time of 3 s, number of sampling being 1024, and number of scans being 16.

9.2.2.5 Experimental Results

9.2.2.5.1 The Effect of Liquid Nitrogen Cooling on the Pore Structure of Marble

Fig. 9.19 illustrates the T_2 distribution curves of dried marble before and after liquid nitrogen cooling. After being cooled in liquid nitrogen, the dried

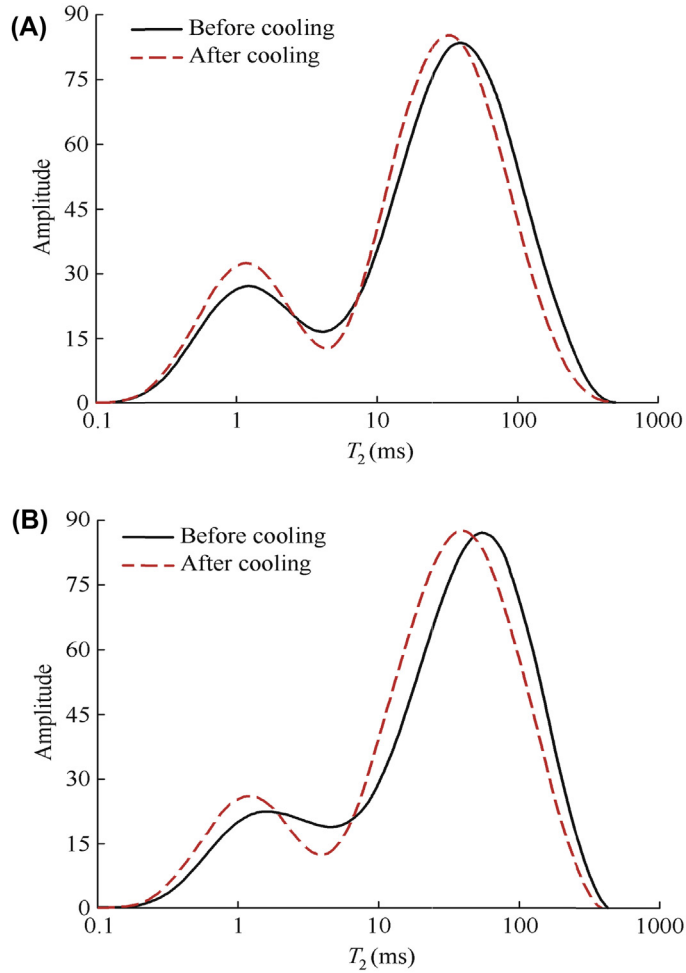

Figure 9.19 Change in the T_2 distribution curves of the dried marble samples after cooling with liquid nitrogen. (A) 1# Marble; (B) 2# marble.

marble's distribution curves show some characteristic changes. These include an increase in the peak amplitudes, an overall shift of the curves toward lower T_2 values, and an increase in the integrated area under the curves. The T_2 peak on the left shifts from 1.29 to 1.08 ms. The amplitudes of the left peaks also increase (by 18.6% and 15.8% for marble samples 1# and 2#, respectively). The peaks on the right in the two samples move from 41.60 to 34.65 ms, and their amplitudes also increase (by 1.6% and 0.3%, respectively). The integrated areas of the T_2 distribution curves increase by 10.3% and 0.9% for the 1# and 2# marble samples, respectively. The results confirm that liquid nitrogen cooling changes the pore structure of the marble. The main changes shown are an expansion of the microfissures (micropores) and an increase in pore volume.

Fig. 9.20 shows the T_2 distribution curves of the saturated marble samples before and after cooling in liquid nitrogen. The main changes are the left shift of the curves and the increase in the peak heights. This is also similar to the changes observed with the dried samples. The results indicate that the pore structure is damaged with an expansion of the micro-fissures and an increase in pore volume. This is mainly because marble is a very compact rock with a porosity of merely $\sim$0.9%, therefore even saturated marble samples contain very little water. In addition, marble has strong internal cementing forces, and thus the freezing of the pore water inflicts limited damage on the rock structure. After cooling in liquid nitrogen, the peak amplitude did not change for marble sample 3#, whereas the maximum T_2 value moved from 372.75 to 215.44 ms. The left-hand peak of marble sample 4# moved from 1.29 to 1.08 ms, whereas the location of the right-hand peak did not change. In other words, an overall left shift is demonstrated in the T_2 distribution curves of the two samples. The amplitude of the peak on the left increased by 5.9%, and the integrated area increased by 5.6% for marble sample 3#. For marble sample 4#, the amplitude of the left-hand peak increased by 1.8% and the integrated area increased by 4.2%.

9.2.2.5.2 The Effect of Liquid Nitrogen Cooling on the Pore Structure of Sandstone

The T_2 distribution curves of dried sandstone samples before and after liquid nitrogen cooling are displayed in Fig. 9.21. Distinct changes are observed. The amplitudes of the left-hand peaks of sandstone samples 1-1# and 2-1# decrease by 7.6% and 4.1%, respectively. The amplitudes of the right-hand peaks decrease by 4.8% and 4.5%, respectively. Furthermore, the integrated areas of the T_2 distribution curves are reduced as well. For

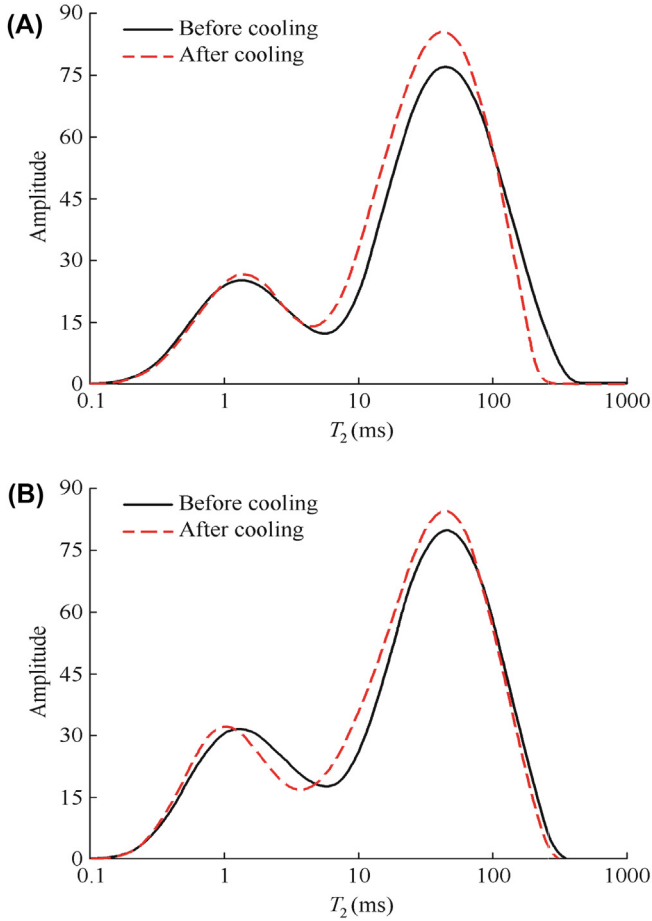

Figure 9.20 The change in the T_2 distribution curves of the saturated marble samples after liquid nitrogen cooling. (A) 3# Marble; (B) 4# marble.

the 1-1# sandstone sample, the integrated area is reduced by 7.9%, and there is a 5.6% reduction in the 2-1# sandstone sample. These results indicate that the major change in the pore structure of the dried sandstone after liquid nitrogen cooling is a reduction in number and volume of the pores. This is significantly different from the behavior of the marble.

As shown in Fig. 9.22, the T_2 distribution curves of saturated sandstone samples, which have been cooled in liquid nitrogen, generally move to the right (i.e., higher T_2 values) and the maximum T_2 values increases. The maximum T_2 value of sandstone sample 3-1# increases from 215 to 3341 ms. For sandstone sample 4-1#, the maximum T_2 value increases

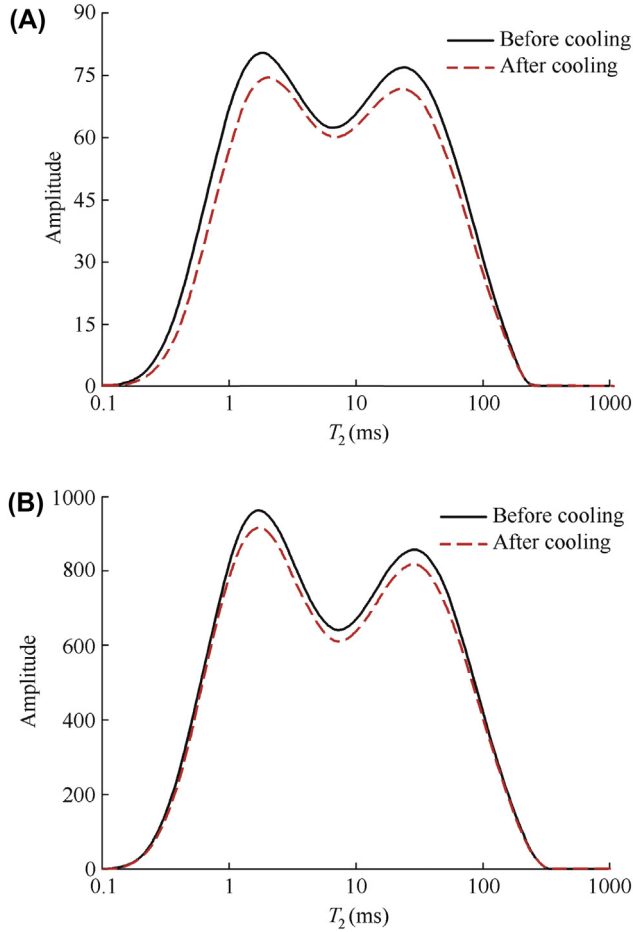

Figure 9.21 The change in the T_2 distribution curves of the dried sandstone samples after liquid nitrogen cooling. (A) 1-1# Sandstone; (B) 2-1# sandstone.

from 215 to 5780 ms and a new peak appears. These changes reveal that liquid nitrogen cooling damages the pore structure of the saturated sandstone samples significantly. It expands the large pores and increases the overall size of the pores. After liquid nitrogen cooling, the integrated areas of sandstone samples 3-1# and 4-1# increase by 1.7% and 6.3%, respectively. As shown in Fig. 9.23, there are also macrocracks visible on the surfaces of the two samples. All these observations prove that the freezing pore water in the rocks intensifies the damage done to the pore structure.

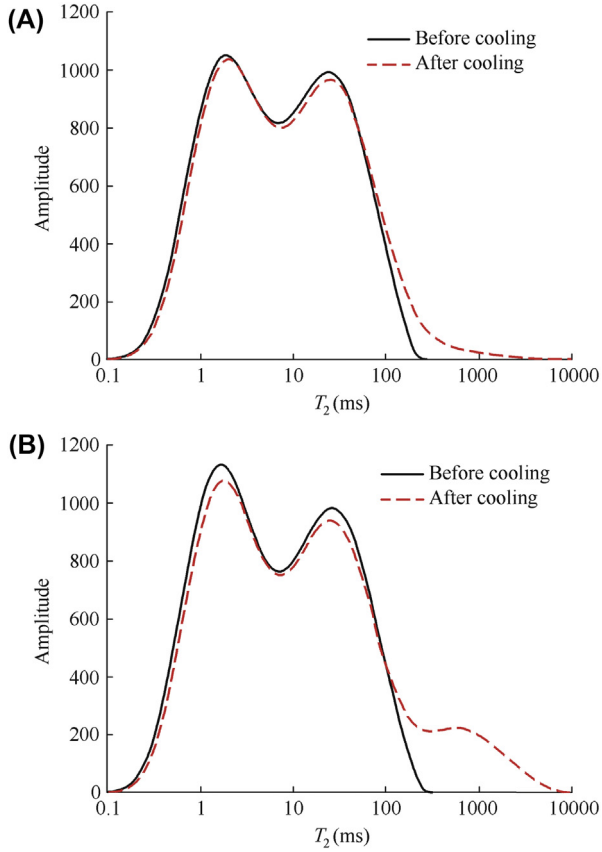

Figure 9.22 The change in the T_2 distribution curves of saturated sandstone samples after liquid nitrogen cooling. (A) 3-1# Sandstone; (B) 4-1# sandstone.

9.2.2.5.3 The Effect of Liquid Nitrogen Cooling on the Pore Structure of Shale

The T_2 distribution curves of dried shale, before and after liquid nitrogen cooling, are shown in Fig. 9.24. After cooling, the main changes are an increase in the peak amplitude and an increase in the integrated area under the curves. The amplitudes of the peaks in the T_2 curves of shale samples 1# and 2# represent a 6.4% and 6.5% increase, respectively. The integrated areas of the T_2 distribution curves increase by 13.7% and 9.9% for 1# and 2# shale samples, respectively. This shows that liquid nitrogen cooling can change the pore structure of shale, the main changes being an expansion of the microfissures and an increase in pore volume.

Figure 9.23 Sandstone samples after liquid nitrogen cooling.

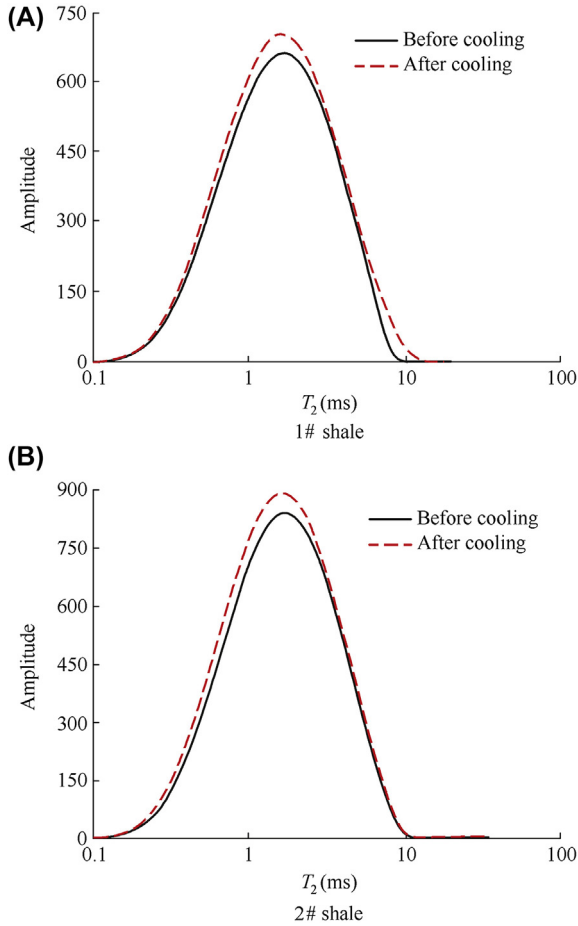

Figure 9.24 The change in the T_2 distribution curves of dried shale samples after liquid nitrogen cooling. (A) 3# Shale; (B) 4# shale.

The T_2 distribution curves of the saturated shale samples before and after being cooled in liquid nitrogen are shown in Fig. 9.25. The changes in the T_2 distribution lead to an increase in peak amplitudes as well as an increase in the integrated area. After liquid nitrogen cooling, the peaks of shale samples 3# and 4# increase by 7.1%. The integrated areas increase by 14.4% (3#) and 15.1% (4#). The increments in the peak heights and integrated areas of the saturated shale samples are slightly larger than the corresponding changes in the dried samples. This is because the pores inside the shale are

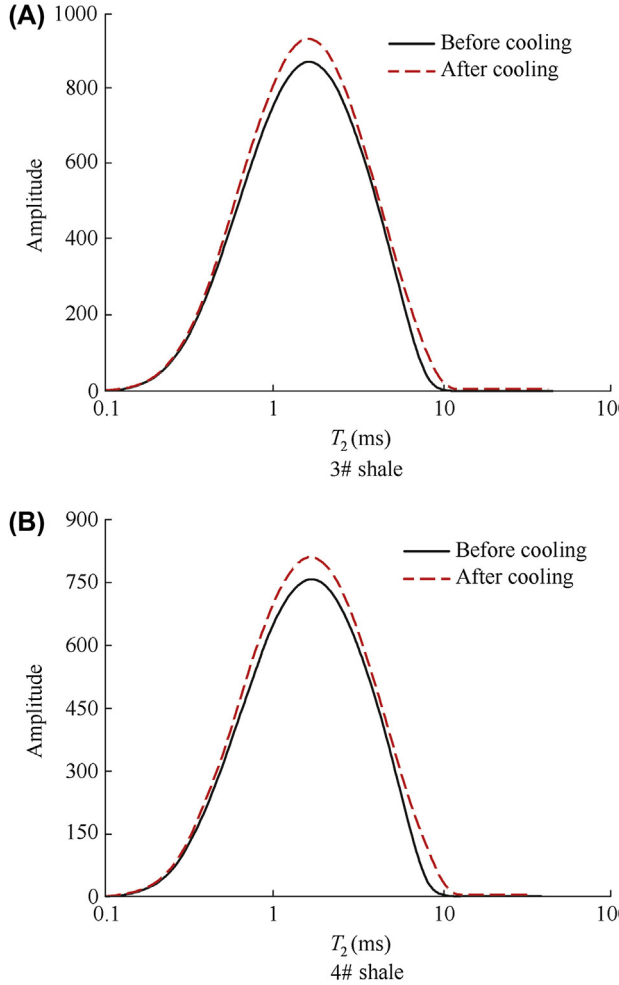

Figure 9.25 The change in the T_2 distribution curves of the saturated shale samples after liquid nitrogen cooling. (A) 3# Shale; (B) 4# shale.

mainly micropores. Therefore each pore can only contain a limited amount of water. In addition, the freezing of the water also has a limited effect on the pore structure.

9.2.2.5.4 Analysis of the Effect of Liquid Nitrogen Cooling on the Pore Structure of Rock

When the temperature decreases, the mineral grains inside a rock shrink and deform. This then generates thermal stress in the cementing areas. When the thermal stress exceeds the cementing strength, the intergrain cementation breaks and cracks are generated. In addition, when the surrounding temperature changes, these local stress concentrations are generated in the grains, pores, and microfissures of low strength inside the rocks under thermal stress. Thus more fractures are induced inside the rocks.

The shrinkage of the mineral grains at low temperature not only increases the number of microfissures but also results in reduction in the number and volume of preexisting pores. For instance, the quantity and volume of the pores in the dried sandstone samples decrease after liquid nitrogen cooling. This is mainly because the pores inside the rocks are formed by the surrounding grains. When the grains shrink, the size of the pores enclosed by the grains is reduced accordingly. Most importantly, the shrinkage of the grains still accelerates the expansion of the inner fractures. Therefore the characteristic of the pore structure changes depends on the dominant acting factor. In the experiments with dried marble and shale with their compact grains and little initial cracking, the pore structure mainly shows an expansion of microfissures (micropores) after liquid nitrogen cooling. For sandstone, on the other hand, because of its porous structure, there is a reduction in both the quantity and volume of the pores.

In the presence of pore water, the frost force produced as the pore water freezes also affects the rock's pore structure. This is because the water expands when it freezes to form ice. In fact, the volume expands by about 9% (Hori & Morihiro, 1998), and a large extrusion force is thereby exerted on the walls of the pores. Subsequently, the intergrain cement is frozen and damaged. Even the overall structure of the rock is damaged and macrocracks are produced (see Fig. 9.23).

Based on the aforementioned analysis, the mechanism responsible for the damage caused to the pore structure of the rock by cooling with liquid nitrogen has two main aspects: (1) shrinkage and deformation of mineral grains at low temperature produces thermal stress inside the rocks and (2) the frost force generated by the freezing of pore water intensifies the damage to the

rock's pore structure (i.e., it increases the expansion of the microfissures or the overall scale of the pores, and even damages the macroscopic structure of the rocks).

9.2.3 Rock Cracking Effect due to Liquid Nitrogen Cooling

9.2.3.1 Rock Cracking Phenomenon due to Liquid Nitrogen Cooling

The most distinct feature of the liquid nitrogen fracturing method is that the rock temperature sharply decreases when the liquid nitrogen is injected. Due to the rapid lowering of temperature, thermal stress is induced in the rock. Moreover, when the stress intensity factor of microfractures is larger than the fracture toughness, these microfractures will extend. Grundmann, Rodvelt, Dials, and Allen (1998) indicated that the rock face will be cracked under the action of thermal stress during liquid nitrogen fracturing. McDaniel, Grundmann, Kendrick, Wilson, and Jordan (1997) observed that coal samples broke into smaller cubical units when they were cooled by liquid nitrogen. In this study, laboratory experiments were performed to investigate the cracking effect of liquid nitrogen cooling on rocks. Coal and shale were selected as the rock samples, which were submerged in liquid nitrogen (about −196°C) for sufficient cooling. As shown in Figs. 9.26 and 9.27, many thermal cracks were generated on the surfaces of the shale and coal samples after liquid nitrogen cooling. It indicates that liquid nitrogen can cause shrinkage deformation of the rock matrix, inducing the expansion of preexisting cracks or generating new cracks. These cracks would further

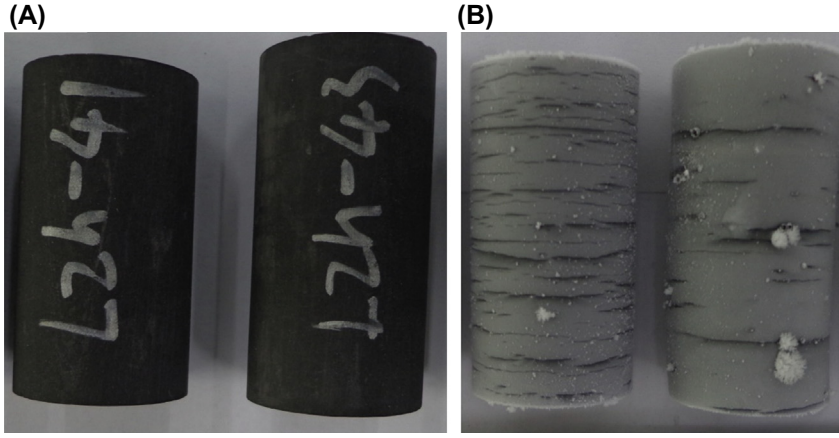

Figure 9.26 Cracking effect of shale samples due to liquid nitrogen cooling. (A) Before cooling; (B) after cooling.

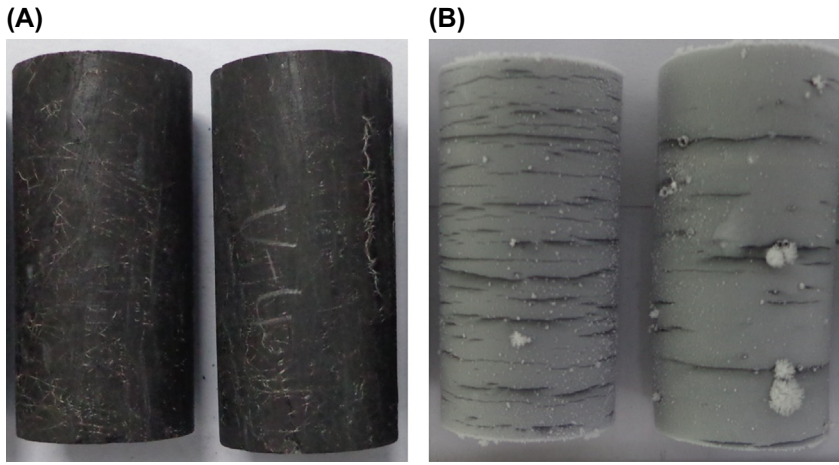

Figure 9.27 Cracking effect of coal samples due to liquid nitrogen cooling. (A) Before cooling; (B) after cooling.

propagate under the action of thermal stress, forming large cracks. Zhang et al. (Chunhui, Weilong, Xizhao, Laigui, & Hewan, 2015) found that the microcrack area of coal sample increased by about 1.8 times after liquid nitrogen cooling.

9.2.3.2 Effect of Liquid Nitrogen Cooling on Wave Velocity and Permeability

Ultrasonic test is an important method used to detect and evaluate the characteristics of rock damage. For the same type of rock, wave velocity is mainly controlled by the distribution of microcracks. In other words, the rock with more microcracks usually presents a smaller wave velocity. Permeability is a parameter that describes the capability of rocks to transmit fluids; it is affected by the size and shape of pores and the connectivity of the pore structure. The rock with better connectivity between pores and fractures usually presents a higher value of permeability. Therefore the damage characteristics of coal induced by liquid nitrogen cooling can be evaluated based on the changes in wave velocity and permeability.

9.2.3.2.1 Materials and Methods

In this work, coal and shale were used as the experimental samples and were processed into cylinders with 25 mm diameter and 50 mm height. To minimize the effect of rock heterogeneity on the experimental results, all samples were drilled from the same block. The samples with regular shape and intact

structure were selected. The density test was conducted to select the samples with similar physical properties. Figs. 9.28 and 9.29 show a few of the shale and coal samples.

Fig. 9.30 illustrates the scanning electron microscopic (SEM) images of shale sample in its initial state. The mineral grains of the shale are arranged very compactly, so the grain distribution and initial fractures can hardly be observed even after magnifying 5000 times. Fig. 9.31 shows the SEM images of the coal sample in its initial state. The mineral grains are 0.03–0.09 mm in diameter. The grains have an extremely irregular shape and present an

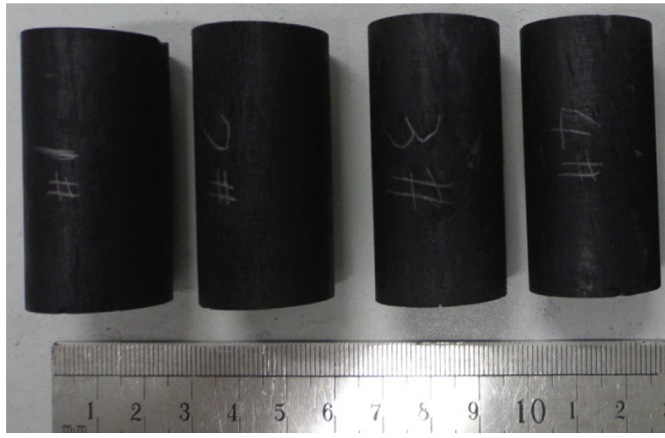

Figure 9.28 Partial coal samples.

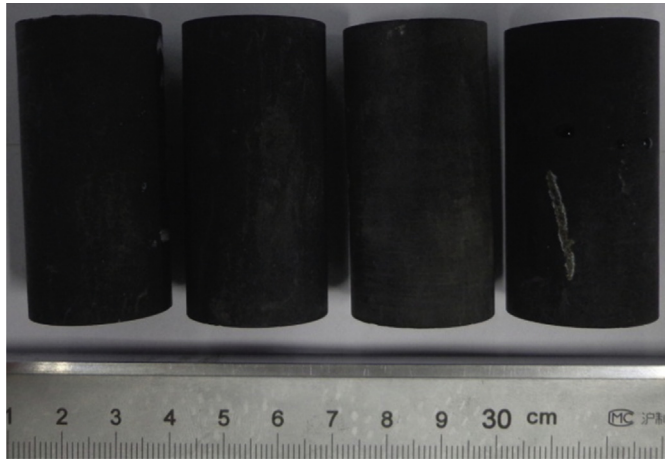

Figure 9.29 Partial shale samples.

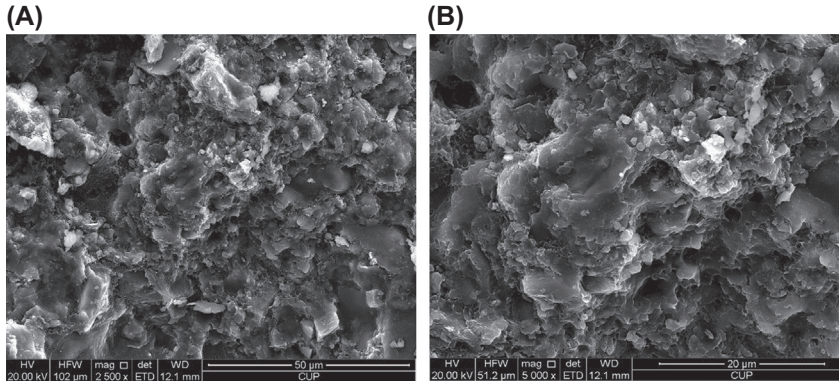

Figure 9.30 SEM images of shale. (A) 2500×; (B) 5000×. *SEM*, scanning electron microscopic.

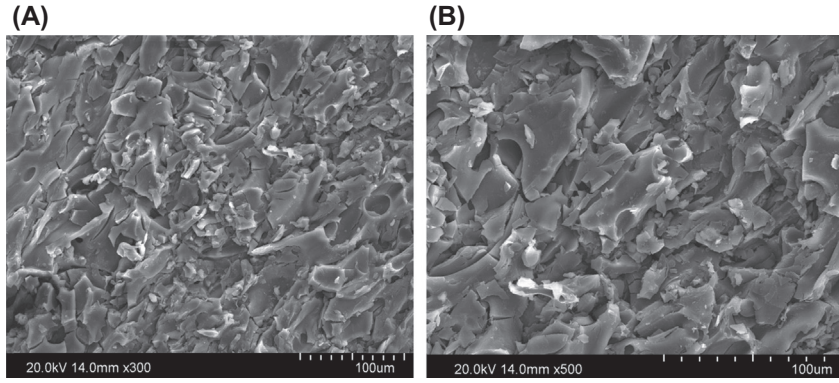

Figure 9.31 SEM images of coal. (A) 300×; (B) 500×. *SEM*, scanning electron microscopic.

interlaced distribution. Thus the grains of coal are loosely arranged such that vast initial microfissures exist in the intergrain.

Before the ultrasonic and permeability tests, preliminary tests were conducted on a few samples to measure their density, porosity, and compressive strength. The results are shown in Table 9.4.

Table 9.4 Key physical properties of shale and coal samples

Rock sample	Density (g/cm^3)	Porosity (%)	Compressive strength (MPa)
Coal	1.24	12.28	22.25
Shale	2.49	4.76	90.62

The experiment consisted of three parts: sample cooling in liquid nitrogen, ultrasonic test, and permeability test. The purpose of ultrasonic and permeability tests was to determine the wave velocity and permeability of the same sample before and after cooling in liquid nitrogen. Before the experiments, the rock samples were dried at 60°C for 8 h. The gas permeability testing device used nitrogen gas to measure the permeability of rock. In the permeability test, the pressure difference between the inlet and outlet of samples was determined by pressurizing the gas, after which the permeability of sample was calculated by using the Darcy formula based on the gas flow rate. During the permeability test, the inlet pressure was 0.25 MPa, whereas the limiting pressure was 2.25 MPa. The outlet flow rate was not measured until the inlet pressure remained stable for at least 30 min.

9.2.3.2.2 Change in Wave Velocity

Figs. 9.32 and 9.33 show the P wave velocity (V_p) of the shale and coal samples before and after liquid nitrogen cooling. It can be seen that the wave velocity of shale samples decreased by 2.69%–3.53%. Shale sample 1# presented the largest decrease, whereas shale sample 4# presented the smallest decrease. As shown in Fig. 9.33, the wave velocity of coal samples decreased by 9.86%–10.43% after liquid nitrogen cooling. This finding indicated that the cryogenic cracking effect occurred because of liquid nitrogen cooling,

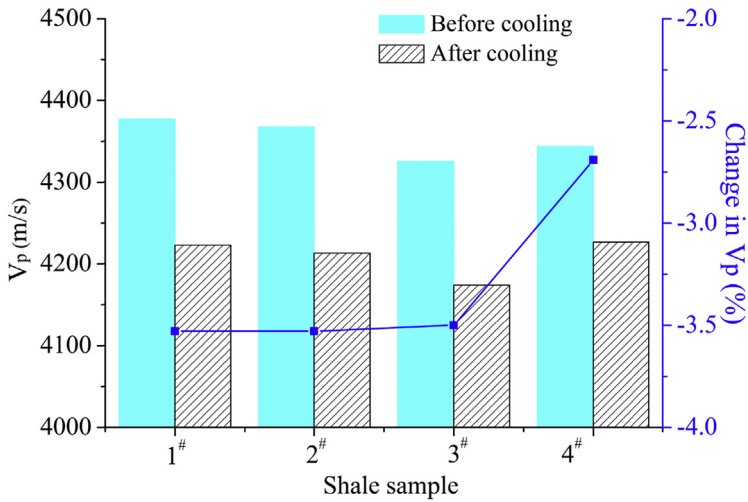

Figure 9.32 P-wave velocity of shale samples before and after cooling.

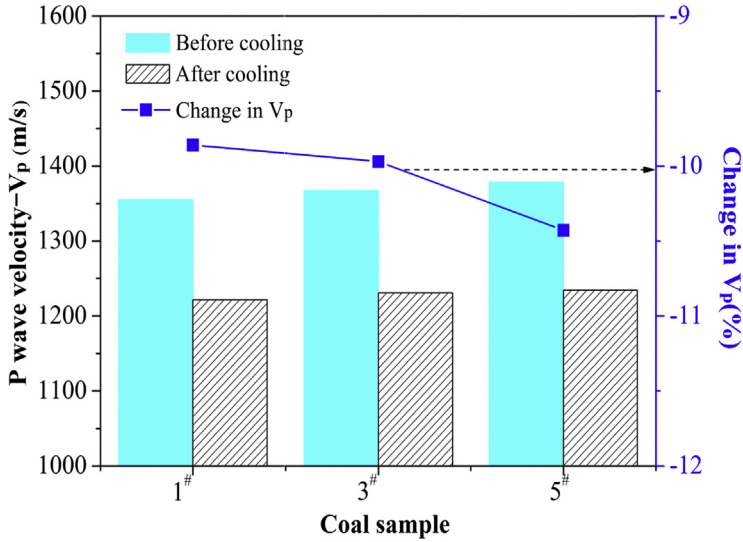

Figure 9.33 P-wave velocity of the coal samples before and after liquid nitrogen cooling.

leading to an increase in the number of cracks. From the mesoscopic view, rock damage is presented as the growth of microcracks. Thus the change in damage degree of rock is mainly caused by the change in the proportion of microcracks. If the microcracks grow and expand after liquid nitrogen cooling, the damage degree will increase accordingly. As the acoustic wave propagates more slowly in air than in solids, the reduction in wave velocity confirms the growth of microcracks. These results indicate that liquid nitrogen cooling aids in cracking the rock and promotes the growth of microcracks.

9.2.3.2.3 Change in Permeability

Fig. 9.34 shows the permeability of shale samples before and after liquid nitrogen cooling. As shown in this figure, the permeability increased by 11.55%—177.27% after liquid nitrogen cooling. Shale sample 3# had the greatest increase, whereas shale sample 4# presented the smallest increase in permeability. As shown in Fig. 9.35, the permeability of the coal rocks increased by 48.89%—93.55%. Coal sample 5# exhibited the largest increase, and coal sample 1# exhibited the smallest increase. The difference in the increment of permeability may be caused by the different pore structure characteristics and natural fracture distributions of the samples. If more

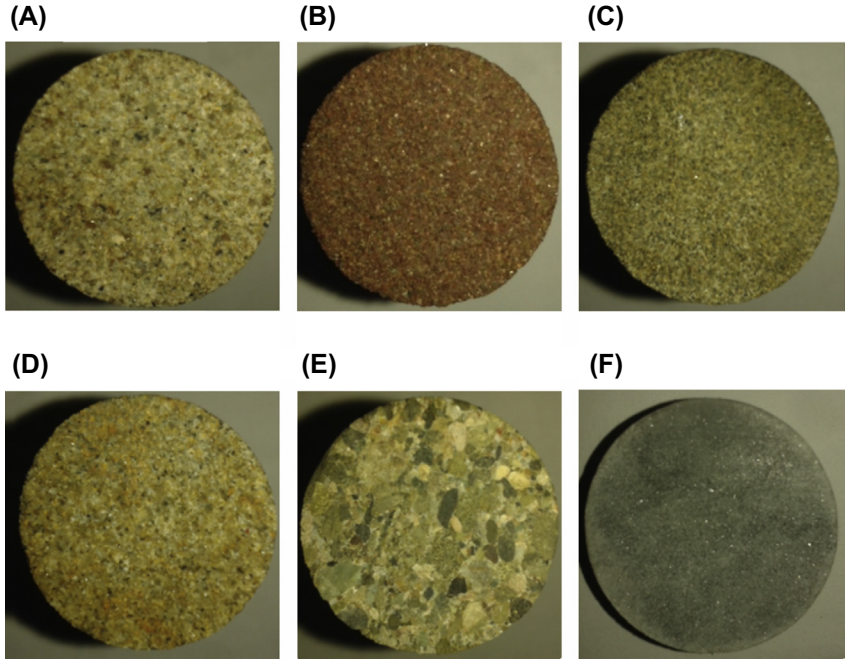

Figure 9.34 Rock samples for tensile tests. (A) Sandstone A; (B) sandstone B; (C) sandstone C; (D) sandstone D; (E) granite; (F) marble.

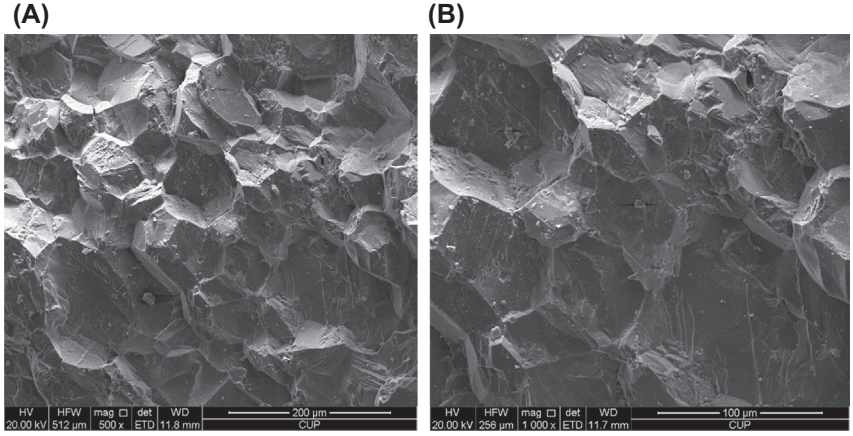

Figure 9.35 Marble scanned by SEM in its initial state. (A) 500×; (B) 1000×. *SEM*, scanning electron microscopic.

closed fractures along the axial direction of cylindrical sample were opened during liquid nitrogen cooling, the permeability of the sample would present a larger increase after cooling. Thus shale sample 3# and coal sample 5# likely exhibited the largest increase in permeability because they had more closed natural fractures distributed along their axial direction than the other two samples. On the other hand, shale sample 4# and coal sample 1# might have the least number of closed fractures along the axial direction, so their permeability presented the smallest increase.

As previously mentioned, an increase in crack damage means the growth of micropores (microfissures) inside rocks (Wang, Schubnel, Fortin, Guéguen, & Ge, 2013). As the samples were cooled in liquid nitrogen, thermal stress was generated due to the shrinkage of the mineral grains. Thermal stress could cause the cracking of intergrain cementation and generate local stress concentration at the tip of preexisting cracks. New cracks were created in this situation, and the preexisting cracks were expanded further. With the growth of cracks inside coal, the connectivity of the pore structure was improved, which eventually resulted in an increase in permeability. As the samples came into with liquid nitrogen, thermal stress was induced because of the shrinkage of rock matrix. When the thermal stress exceeded the strength of intergrain cementation, new microcracks were created. Besides, the preexisting cracks could be expanded further. Consequently, the connectivity and the damage degree of rock pore structure were increased.

9.2.3.3 Effect of Liquid Nitrogen Cooling on Tensile Strength

9.2.3.3.1 Materials and Methods

To analyze the effect of liquid nitrogen cooling on rock strength, different types of rocks were selected for testing their tensile and compressive strengths. In tensile strength tests, marble, granite, and four different types of sandstone were used as shown in Fig. 9.34. These six rock samples were processed into thin cylinders with diameter 25 mm and height 7 mm. To distinguish the samples clearly, all samples were numbered in the format "X-Y" where "X" represents the rock type and "Y" represents the status of sample. Samples with regular shape and intact structure were selected.

The experiments mainly involved two parts, namely, sample cooling with liquid nitrogen and uniaxial compression tests. During the experiment, a few of the samples were submerged in liquid nitrogen for more than 30 min to cool the samples sufficiently. After the cooled samples recovered to laboratory temperature, the uniaxial compression tests were conducted on

all the thin cylinder samples. Then the change in tensile strength was determined from the experimental results. Vernier caliper, electrical drying oven, liquid nitrogen container, electronic balance, and TAW-1000 electrohydraulic servo load tester were used in the experiments. The TAW-1000 electrohydraulic servo load tester can apply a maximum axial load of 1000 KN. The minimum scale and accuracy of load were 10 N and 1%, respectively. The full scale of displacement was 100 mm, and the accuracy of displacement was less than 0.5%.

9.2.3.3.2 Change in Tensile Strength

As rock is a type of porous media, it usually contains many natural fractures, which have a significant effect on the mechanical properties. According to damage mechanics, the damage degree of the material is positively related to the proportion of micropores (microfissures). For the same type of rock, the rock with greater proportion of micropores (microfissures) usually presents a smaller strength. As indicated by the experimental results, the microcracks inside the rock expanded and propagated after liquid nitrogen cooling, which led to the decrease in wave velocity and the increase in permeability. These phenomena indicate that the damage degree of rock increased and the mechanical properties of rock deteriorated after being cooled with liquid nitrogen. Table 9.5 demonstrates that the tensile strengths of all samples decreased by 1.38%—30.43% due to liquid nitrogen cooling. The sample sandstone A presented the smallest decrease, whereas the granite sample presented the largest decrease. It suggests that the liquid

Table 9.5 Results of tensile strength tests

Rock type	Label	Status	Tensile strength (MPa)	Decrease in tensile strength
Sandstone A	A-1	Initial state	4.33	/
	A-2	Cool-treated	4.27	1.38%
Sandstone B	B-1	Initial state	2.35	/
	B-2	Cool-treated	1.98	15.74%
Sandstone C	C-1	Initial state	7.06	/
	C-2	Cool-treated	5.34	24.36%
Sandstone D	D-1	Initial state	4.38	/
	D-2	Cool-treated	3.67	16.21%
Granite	E-1	Initial state	6.90	/
	E-2	Cool-treated	4.80	30.43%
Marble	F-1	Initial state	5.86	/
	F-2	Cool-treated	4.39	35.83%

nitrogen cooling effect increased the initial damage degree of rock and resulted in partial loss of strength.

9.2.3.4 Effect of Liquid Nitrogen Cooling on Compressive Strength

9.2.3.4.1 Materials and Methods

In this work, three types of rocks (sandstone, marble, and coal) were used in the experiments. For the compressive strength tests, two samples were drilled from each kind of rock and processed into cylinders with diameter 25 mm and height around 50 mm. To differentiate the samples expediently, the samples were also labeled in the format "X-Y#" as mentioned in Section 9.2.3.2. The first symbol "X" represented the rock type and the second symbol "Y" represented the serial number. In the experiments, the labels "S," "M," and "C" corresponded to sandstone, marble, and coal, respectively. Finally, six samples were selected and labeled as S-1#, S-2#, M-1#, M-2#, C-1#, and C-2#. Samples S-2#, M-2#, and C-2# were cooled with liquid nitrogen, whereas the other samples were not cooled. Before the compressive strength experiments, preliminary tests were also performed on the rocks to measure their density, porosity, and permeability. The results are shown in Table 9.6.

The experiment consisted of two parts: sample cooling in liquid nitrogen and uniaxial compression test. Before the experiments, the rock samples were dried at 60°C for 8 h. The main experimental steps were as follows. (1) Samples S-2#, M-2#, and C-2# were sufficiently cooled in liquid nitrogen. (2) After the cooled samples recovered to room temperature, uniaxial compression tests were performed on all samples. (3) The stress and strain were recorded using the axial and lateral strain gauges installed on the sample surface. In the experiments, an electronic balance, vernier caliper, liquid nitrogen container, and TAW-1000 electro-hydraulic servo load tester were employed.

9.2.3.4.2 Change in Compressive Strength

The mechanical properties of rock are significantly influenced by the initial defects present in it, such as microcracks. From the macroscopic viewpoint,

Table 9.6 Key physical properties of rocks used

Rock type	Porosity (%)	Density (g/cm^3)	Permeability (mD)
Sandstone	18.33	2.20	10.23
Marble	0.86	2.88	—
Coal	12.28	1.24	0.71

rock damage represents the deterioration of mechanical properties. Thus rock damage can be evaluated on the basis of the change in mechanical parameters, including permeability, wave velocity, and strength. Table 9.7 presents the compressive strengths of all samples in the experiments. As shown in this table, the strengths of the cooled samples were smaller than those of the original untreated samples by 4.45%–40.53%. The decrease in compressive strength suggested that the damage degree in the cooled samples was more serious than that in the original ones.

For the same type of rock, the strength of rock is mainly determined by the distribution of microcracks. In other words, the rock with more microcracks usually presents lower strength. Thus to investigate the mechanism of the effect of liquid nitrogen cooling on rock strength the SEM technique was adopted. In this experiment, the marble sample was used as an example. Fig. 9.35 illustrates the SEM image of the marble sample in its initial state. The sizes of the grains are in the range 0.04–0.09 mm, which are lower than the grain sizes in sandstone. To observe the mineral grain distribution, SEM had to be performed at a magnification of at least 500. Due to the compact arrangement of the mineral grains in the marble with its good intergrain cementation, the initial factures could not be observed even at a magnification of 1000 times.

Fig. 9.36 shows SEM images of dry marble slices that had been cooled by liquid nitrogen. Using magnifications of 500 and 1000, microfissures can be observed between adjacent grains. This indicates that the thermal stress generated during liquid nitrogen cooling breaks the granular cementation and produces new cracks. This finding indicates that the cryogenic cracking effect occurred because of liquid nitrogen cooling, leading to the increase in the number of cracks and the decrease in strength.

9.2.4 Rock Cracking Effect due to Nitrogen Vaporization

When liquid nitrogen is injected into the reservoir, the heat in the rock will quickly transfer to liquid nitrogen, leading to the rapid cooling effect on rock. Moreover, the liquid nitrogen will expand, thereby causing the increase in gas pressure. To investigate the cracking effect due to nitrogen vaporization, the experimental setup shown in Fig. 9.37 was designed. The sample used here was shale, which was processed into cylinders (100 mm diameter and 200 mm length) with a center hole (60 mm diameter). The shale sample was placed in the center of the cement block, which was a 300 × 300 × 300-mm cube. In the experiments, liquid nitrogen at

Table 9.7 Results of compressive tests

Rock type	Label	Status	Compressive strength (MPa)			Decrease in compressive strength	
Marble	M-1#	Initial state	130.31			/	
	M-2#	Cool-treated	111.52			4.45%	
Sandstone				S-1#	Initial state	41.99	/
				S-2#	Cool-treated	39.03	40.53%
Coal				C-1#	Initial state	23.70	/
				C-2#	Cool-treated	19.48	17.81%

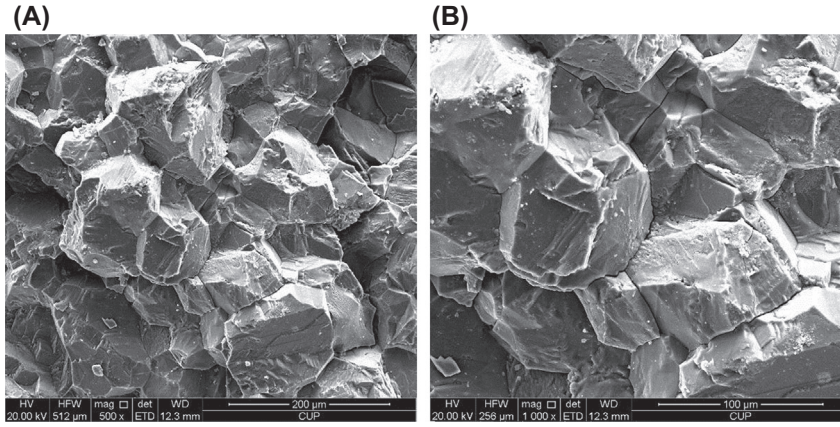

Figure 9.36 SEM images of a dried marble sample scanned after being cooled in liquid nitrogen. (A) 500×; (B) 1000×. *SEM*, scanning electron microscopic.

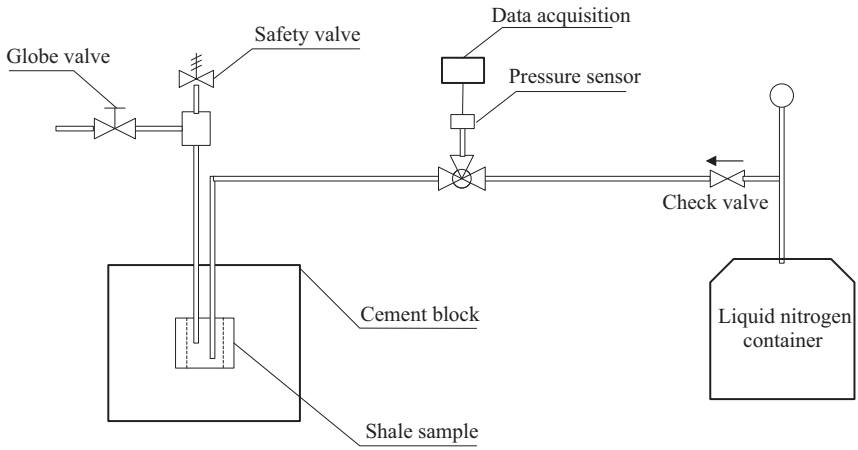

Figure 9.37 Schematic diagram of liquid nitrogen vaporizing experiments.

about −196°C was pumped into the sample through the steel pipe. During this process, the globe valve was open and the liquid nitrogen or nitrogen gas could be released through the left pipe. When the sample was sufficiently cooled, liquid nitrogen instead of nitrogen gas would escape from this pipe. At this time, all the valves were shut off and the liquid nitrogen injection was stopped. With the vaporization of liquid nitrogen, the pressure data was recorded by a pressure sensor and data acquisition system.

Fig. 9.38 shows the pressure−time curve recorded during the experiment. When the globe valve was shut off (191 s), the pressure rapidly

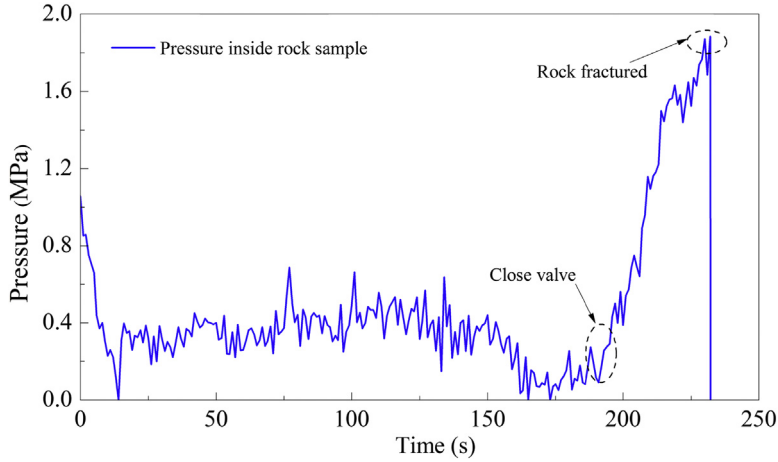

Figure 9.38 Pressure—time curve during liquid nitrogen vaporization.

increased from 0.088 to 1.973 MPa within 38 s (191—229 s). Because no confining pressure was imposed, the gas pressure exceeded the tensile strength of rock, leading to drastic rupture of the shale sample. As shown in Fig. 9.39, the cracks presented a netted distribution. So it can be inferred that the liquid nitrogen vaporization will be able to fracture rock and enhance stimulation reservoir volume (SRV) effectiveness.

9.2.5 Analyzing the Prospects of Liquid Nitrogen Fracturing

9.2.5.1 Advantages of Liquid Nitrogen Fracturing

Liquid nitrogen fracturing is a waterless fracturing technology that uses liquid nitrogen as a fracturing fluid. This technique allows liquid nitrogen to be pumped into a well or rock formation at a typical flow rate and pressure, and then artificial fractures are created in the rock. Due to its relative inertness, liquid nitrogen has an excellent compatibility with other fluids in formations and also does not take part in any emulsification. Thus liquid nitrogen does not induce the expansion of clay minerals or changes in formation water saturation during fracturing. On the contrary, it can reduce the water block damage that occurs during drilling and completion treatments, thereby improving the rock permeability and seepage channels.

After fracturing, the liquid nitrogen in the reservoirs can completely gasify because its critical temperature is extremely low (about −146.9°C). The gasification of liquid nitrogen could reduce the pressure in the well and increase the pressure difference between the reservoir and wellbore. As a result, the fracturing liquid can flow back without any additional

Figure 9.39 The fractured sample.

swabbing or gas lift treatment. During liquid nitrogen fracturing, thermal stress will be generated when liquid nitrogen flows in the main fractures, resulting in tensile or shear damage on the main fracture surface, which then leads to the formation of secondary fractures orthogonal to the main fracture plane. Additionally, the decrease in temperature could cause the shrinkage of mineral grains in the rocks, which may lead to opening of the closed natural fractures. All these factors can promote rock cracking and fracture network formation during the fracturing process. Liquid nitrogen is harmless to groundwater and drinking water because it contains no added chemical components, such as friction reduction agent, bactericidal agent, etc., which are generally added into conventional fracturing fluids. It is mainly nitrogen gas that flows back to the ground after fracturing. Therefore this treatment is expected to be a preferred stimulation method in arid and fragile ecological areas.

9.2.5.2 Technical Difficulties of Liquid Nitrogen Fracturing

With the rapid development of horizontal well technology, multi-stage fracturing has become the key technology for reservoir stimulation. As the rubber packer and bridge plug components can easily fail to work under the

extremely cryogenic conditions, multi-stage fracturing with liquid nitrogen is very challenging. So conventional liquid nitrogen fracturing presents considerable difficulties in controlling the fracture initiation location and creating multiseparated fractures along the wellbore. In conventional liquid nitrogen fracturing, the isolation method, which is called "frozen water" diverter, involves injecting 0.5−0.8 m^3 of water to seal the fracture zone. However, the new fractures will only initiate above the frozen zone, which is a technical bottleneck when applying this method.

Another type of stimulation method is hydra-jet fracturing, which is a combination of jetting perforation, fracturing, and isolation. With hydra-jet fracturing, the fracture initiation location can be controlled and the wellbore can be isolated effectively using the pressure boosting effect in the perforation cavity and the hydrodynamic sealing effect in annular region. Once the fracture is formed, the high-speed jet will continuously pump into the perforation cavity and formed fracture. The jetting system, composed of the nozzle, annulus, cavity, and fracture, behaves as a jet pump (Surjaatmadja, McDaniel, & Sutherland, 2002). According to Bernoulli principle, a low-pressure area around the high-speed jet is formed. Due to the pressure difference between the jet and surrounding fluid, this "jet pump" can draw the annulus fluid into other fractures outside of the fractured zone. Thus the difficulty in controlling the fracture location and the challenges in isolation of the wellbore can be solved perfectly by using liquid nitrogen jet fracturing, which combines the benefits of the liquid nitrogen jet and liquid nitrogen fracturing.

9.2.5.3 Application Prospects of Liquid Nitrogen Fracturing

In recent years, unconventional gases have played a significant role in the global energy supply. However, due to the low reservoir quality and water issues involving these unconventional gases, there are higher technical requirements for the fracturing treatment. To protect the water resources and reservoirs, the fracturing fluid should present excellent compatibility with formation fluids and should be nonpolluting to underground and surface water. During the fracturing, the fracture network is created, which is expected to improve the SRV. In arid regions, the fracturing treatment should consume as little water as possible. Moreover, the regulations for hydraulic fracturing are likely to be stricter in the future. To solve these issues, petroleum engineers are paying increasing attention to substitutes for water-based fluids. The stimulation treatment with liquid nitrogen fracturing requires further research to explore the possibilities of creating self-propping

fractures and reducing water usage. As mentioned before, compared with conventional fracturing, liquid nitrogen fracturing displays a more superior performance in the reservoir, environment protection, and improvement of SRV. It is expected to become one of the most significant methods for the efficient stimulation of unconventional gases with proper technology.

9.3 THE CHARACTERISTICS OF HYDROTHERMAL JET

9.3.1 Introduction

With the rapid development in recent years, the petroleum industry has gradually entered the stage of exploration and development of oil and gas resources in deep formations. Global studies on petroliferous basins have found that, at the end of 2010, the recoverable oil reserves in deep (4500—6000 m) and ultradeep (more than 6000 m) reservoirs were as much as 943×10^8 t, accounting for 39.99% of the global total recoverable reserves. Recoverable natural gas reserves were 729×10^8 t of oil equivalent, accounting for 49.07% of the total recoverable reserves (Chengzao & Xiongqi, 2015; Jianli, 2005; Longde et al., 2013).

Hydrothermal spallation technology is a type of rock-breaking method, which was put forward at the end of 20th century and has gradually become an important field. The technique uses the principle of thermal rock cracking and supercritical water oxidation (SCWO) to produce high-temperature fluid in the well, which disintegrates the bottom rock. This technology has two advantages: the first is that there is no contact between the combustion chamber and the rock. This type of noncontact rock breaking can effectively reduce abrasion of the drill bit. The second advantage is that the method is particularly suitable for disintegration of hard brittle rocks. Therefore this method provides a possible way for the efficient and economic development of oil and gas in deep strata (Potter & Tester, 1998; Schuler, Rothenfluh, & von Rohr, 2013a; Serikawa et al., 2002). Augustine (2009) verified the economic viability of the hydrothermal spallation drilling technology. Rothenfluh, Schuler, and Von Rohr (2011) used the optical schlieren method to study the penetration length of a supercritical jet and found it equal to the injector's nozzle diameter. Sierra-Pallares et al. studied the mixing zones between subcritical or supercritical water jets and subcritical coflow environment (José, Pablo, & Francisco, 2012). The results showed that when pressure is well above the critical point, fluid dynamic behavior is more similar to subcritical conditions. Schuler, Rothenfluh, and von Rohr (2013b) determined the Prandtl number in a subcritical

water bath at near-critical pressures by establishing a numerical model and validated it through laboratory experiments. However, hydrothermal spallation technology only uses the thermal cracking effect to break rock, so it is very sensitive to the lithology of rock, which limits its applications to some extent.

Based on high-pressure water jet technology and hydrothermal spallation method, a novel drilling technique called hydrothermal jet drilling has been proposed by our group. The technique uses the coupled effects of thermal spallation and impact force to break the bottom rock. During the process of drilling, there is no contact between the bottom hole assembly and rock surface. Moreover, the entire drill string does not need to rotate, which can effectively prevent abrasion of the drill bit and reduce the tripping time. The method is suitable for the high-efficiency disintegration of hard brittle rock, which is expected to provide a new way for the efficient development of oil and gas in deep strata.

9.3.2 Mechanisms of Hydrothermal Jet Drilling

Hydrothermal jet drilling is based on the mechanisms of supercritical water oxidization, thermal spallation, and high-pressure water jet impact.

9.3.2.1 Supercritical Water Oxidization

Typically, water is present in three common states: steam, liquid, and ice. Liquid water is a polar solvent that can dissolve most electrolytes, including salts. It has high solubility for some gases, but it dissolves organic matter only slightly or not at all. Fig. 9.40 shows the computational region for different states described by divided by The International Association for the Properties of Water and Steam. The shadowed part is the supercritical water region. In this region, once the temperature and pressure reach or exceed the critical point ($T = 374.3°C$, $P = 22.1$ MPa), water exists in a different state from that of liquid or gas, known as supercritical water (Wagner & Kretzschmar, 2008). Supercritical water is different from ordinary water in the aspects of density, dielectric constant, viscosity, diffusion coefficient, conductivity, solubility, etc (Serikawa et al., 2002). There are only a few hydrogen bonds present in supercritical water, which means that the solubility of supercritical water is similar to that of nonpolar organic solvents. Therefore hydrocarbons have high solubility in supercritical water [12].

Supercritical water has been widely used in industrial production because of its unique properties. Supercritical water has good solubility for organic compounds and a variety of gases. SCWO is a new technology for thermal

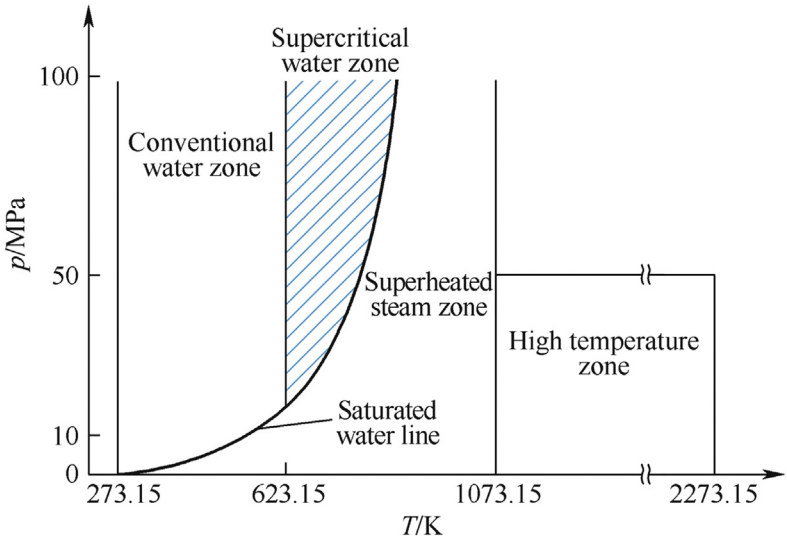

Figure 9.40 States of water and computational region.

oxidation. When oxygen and hydrogen peroxide are used as oxidants in supercritical water environment to react with organic matter, SCWO reaction can be achieved (Peng & Ma, 2005).

Thermal spallation is essentially an SCWO reaction. The injected fuel and oxygen are fully dissolved in the supercritical water, completely mixed and in a homogeneous state. Under these conditions, the organic matter begins to react spontaneously and eventually generates carbon dioxide and water. In the experimental setup, the water reaches a supercritical state mainly through the high-pressure pump unit and fuel reacts with oxygen to produce temperatures of more than 374.3°C and pressure greater than 22.1 MPa.

9.3.2.2 High-Pressure Water Jet Impact

Breakage mechanism of the rock by water jet is complex, so a unified theory has not yet been developed. There are five main theories to explain the mechanism of water jet process, including quasi-static elastic theory, stress wave theory, cavitation damage theory, crack growth theory, and damage and broken theory (Hualin et al., 2005; Kim, 2003; Liao & Li, 2006).

Quasistatic elastic theory: the jet impact force is regarded as a quasistatic concentrated force. The force equals jet stagnation pressure numerically and acts on a semi-infinite elastic body. Based on the elastic intensity theory,

when the jet impact force surpasses the intensity of rock, the rock is destroyed.

Stress wave theory: water jet impact load is considered as a dynamic load and the jet generates a stress wave that is mainly responsible for the rock breakage.

Cavitation damage theory: the cavitation is formed by a negative cavity full of steam or air rupturing on solid surface. According to Rayleigh's theory, the bubble bursting energy focused on one point can generate great pressure, which may be between 680 and 6800 MPa. Crow considers cavitation as the main cause of rock breakage.

Crack growth theory: original cracks exist in the rock naturally, and the growth of these cracks causes the rock to break. According to a different mechanism, this theory is divided into two parts: one is the fracture and broken theory and the other is the stretch-water wedge theory.

Damage and broken theory: the stress wave generated by jet impact load and quasi-static pressure together cause the rock to break, and the stress wave predominates over quasi-static pressure.

9.3.2.3 Thermal Spallation Effect

The rock is composed of a variety of mineral particles. When heated, these mineral particles inside the rock cannot deform freely, thus causing the thermal stress. When thermal stress is more than the ultimate strength of the rock itself, it can lead to expansion of internal cracks and induce the generation and propagation of new cracks. The cracks are then connected with each other to form a network, ultimately resulting in the breakage of rock (Walsh & Lomov, 2013).

The process of thermal spallation rock-breaking, shown in Fig. 9.41, can be divided into three stages:

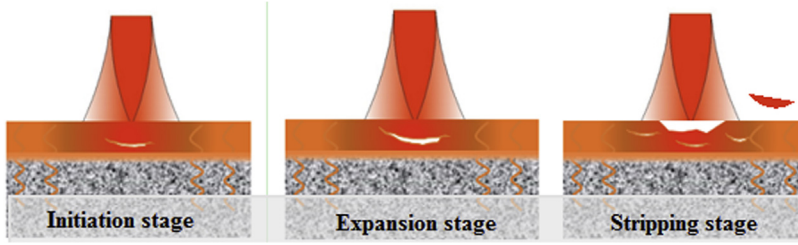

Figure 9.41 Schematic of thermal spallation process.

Initial stage: microcracks occur under the action of nonuniform thermal stresses;
Expansion stage: microfractures and natural fractures accelerate expansion;
Stripping stage: microcracks develop into macrocracks and debris is peeled off from the rock surface, revealing fresh rock surface.

In general, the thermal stress inside the rock mainly arises from the following three factors: (1) stress due to the different expansion coefficients of internal rock matrix grains; (2) stress due to the expansion of pore fluid when heated; although the porosity is very low in granite, stress due to pore fluid expansion cannot be ignored; and (3) stress generated by temperature gradient (Jian, Zhao, & Bing, 2005).

9.3.3 Hydrothermal Jet Drilling Procedures

The steps involved in the hydrothermal jet drilling technique are as follows: fuel, oxygen, and cooling water are injected into the down-hole reaction chamber along different conduits. Then they are ignited to react with each other to build a high-temperature environment. At the depth of more than 2.2 km, the produced water inside the reaction chamber is in supercritical state (temperature greater than 374.3°C, pressure greater than 22.1 MPa) (Fig. 9.42). The fuel, oxygen, and water are completely mixed and exist as a homogeneous phase in the supercritical environment, which helps to accelerate the oxidation process. Therefore supercritical water oxidization occurs in the reaction chamber. The reaction products, including water and carbon dioxide, are discharged to the bottom rock. Finally, cracks are generated inside the rock because of nonuniform thermal stresses induced by the high-temperature jet. With the assistance of the simultaneous impact force, the cracks continue to expand and break the entire rock eventually.

9.3.4 Down-Hole Flow Field in Hydrothermal Jet Drilling

9.3.4.1 Single Orifice Nozzle

Numerical simulation on impact flow field of hydrothermal jet in down-hole cooling environment is carried out. The bottom hole distributions of velocity, temperature, and pressure are investigated. The effects of jet velocity, cooling water velocity, jet temperature, and standoff distance on the flow field are analyzed. Moreover, the cooling effect and carrying capacity of two cooling configurations are compared. Two cooling configurations

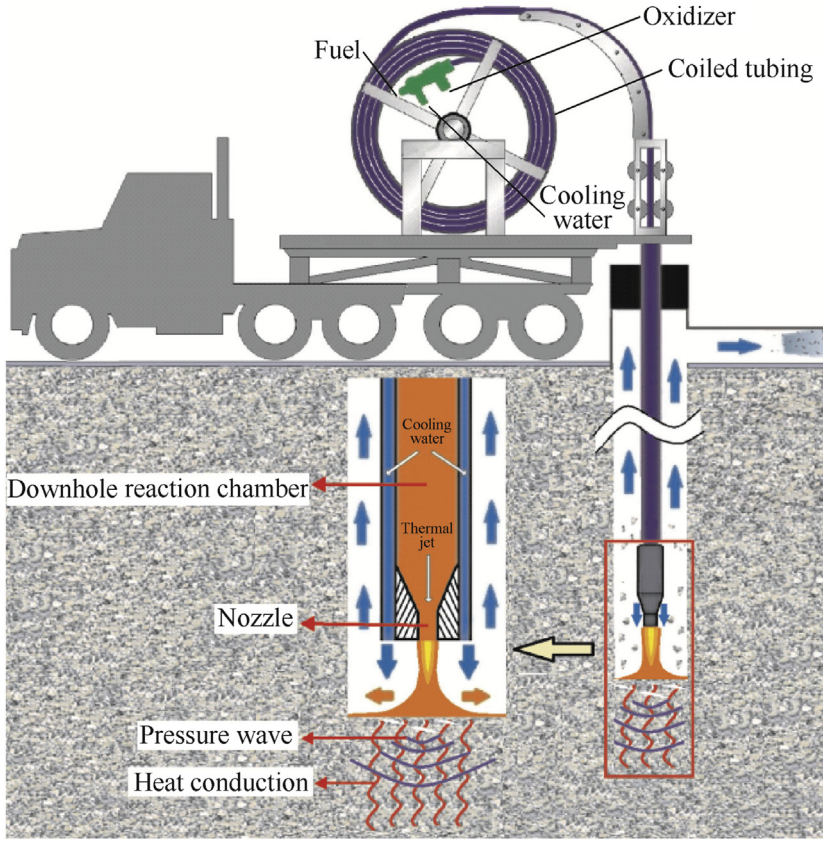

Figure 9.42 Coiled-tubing-deployed hydrothermal jet drilling concept.

are presented, lateral cooling configuration and downward cooling configuration. Figs. 9.43 and 9.44 illustrate the details of the two schemes where the red region represents hydrothermal fluid and the blue region represents cooling water.

Simulated results of wellbore temperature for the lateral and downward cooling configurations with different cooling water velocities (20, 50, and 80 m/s) are illustrated in Fig. 9.45, when the jet velocity is 100 m/s.

The annular temperature (Fig. 9.45) decreases as the velocity of the cooling water increases. In the downward cooling configuration, the flow pattern of the hydrothermal jet remains constant, with the exception of the low-temperature region, which expands with an increase in cooling water velocity. However, in the lateral cooling configuration, the flow

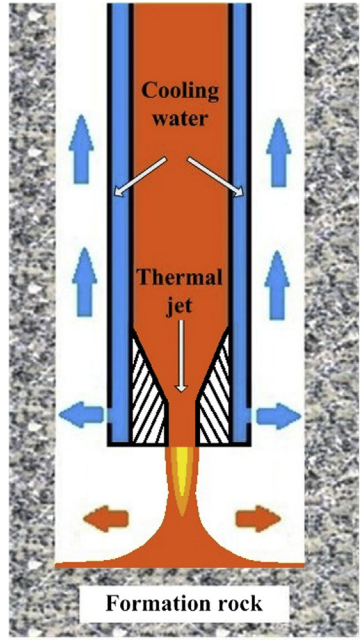

Figure 9.43 Lateral cooling configuration.

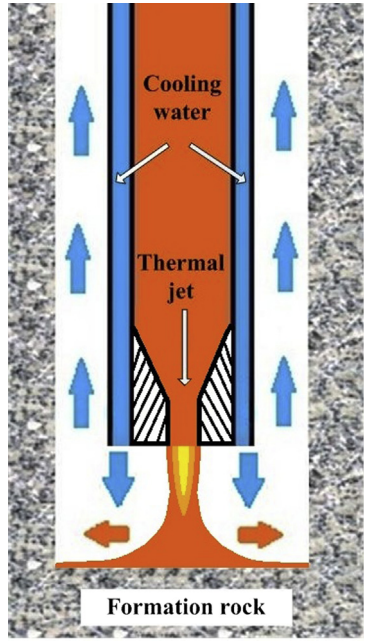

Figure 9.44 Downward cooling configuration.

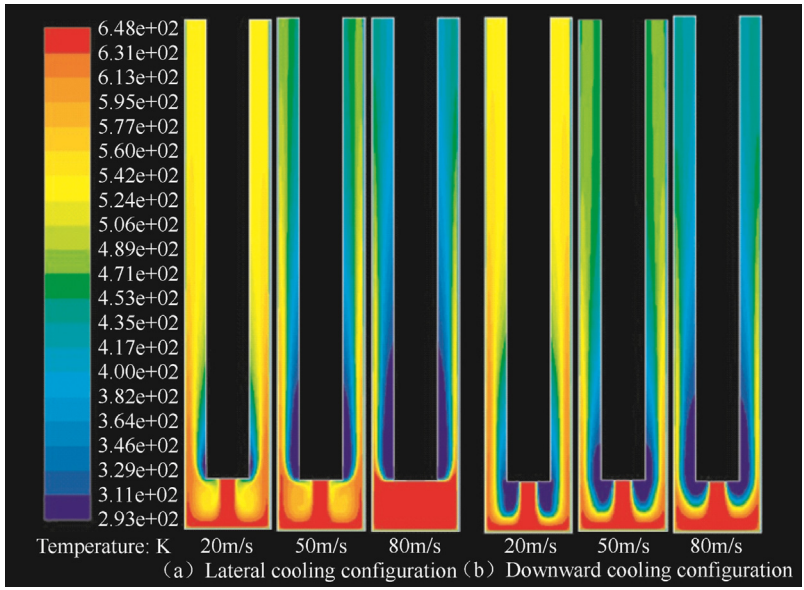

Figure 9.45 Temperature contours of cooling configurations with different cooling water velocities.

pattern of the hydrothermal jet does not generally change at 20 and 50 m/s, but it changes sharply at 80 m/s. The entire bottom hole space becomes a high-temperature region, whereas the annular space remains at a low temperature. This is because the direction of cooling water in the lateral configuration is perpendicular to that of the return fluid in the annulus. The larger the cooling water velocity, the harder it is for the return fluid to flow out, so there is drastic heat and kinetic transfer in the annular inlet. Heat cannot disperse or be carried out by the return flow. Therefore when the cooling water velocity becomes 80 m/s, the down-hole space behaves as if the high-temperature fluid at the hole bottom is sealed off by the cooling water.

In Fig. 9.46, when the cooling water velocity is fixed, the annular temperature decreases as the distance to the bottom increases. Comparing the two cooling configurations, the annular temperature in the downward cooling configuration is lower, which indicates that the downward cooling configuration has a better cooling effect than the lateral cooling configuration. However, the annular temperature remains constant for a short distance in the lateral cooling configuration and then decreases rapidly. It means that the wellbore under the nozzle is exposed to high-temperature

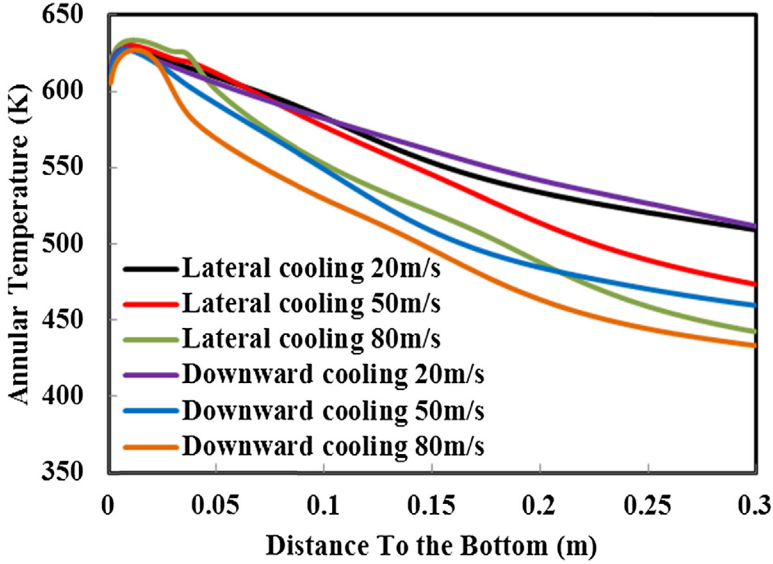

Figure 9.46 Annular temperature distribution of cooling configurations with different cooling water velocities.

fluid, which results in its spallation and enlargement of the wellbore diameter.

Therefore it can be concluded that when reaming is required in hydrothermal jet drilling, it is better to use the lateral cooling configuration because of the high-temperature region in the bottom hole space. When normal drilling is needed, the downward cooling configuration is recommended, because the high-temperature zone in the lateral cooling configuration may cause collapse of the wellbore and bit balling, and also because of its better cooling effect.

9.3.4.2 Multiorifice Nozzle

Hydrothermal jet drilling with a multiorifice nozzle can generate multiple hydrothermal jets to exert force on the bottom hole ambient rocks (Song, Lv, Li, Hu, & Shi, 2016). To simplify the numerical simulation of the asymmetrical circular drilling model, half of the multiorifice model is used to represent the real three-dimensional (3D) situation. The entire 3D hydrothermal jet model can be divided into the fluid part and the solid part. The fluid part includes the flow of hydrothermal jet fluid in the bottom hole and annulus, whereas the solid part represents the wall of wellbore and ambient rocks (Fig. 9.47).

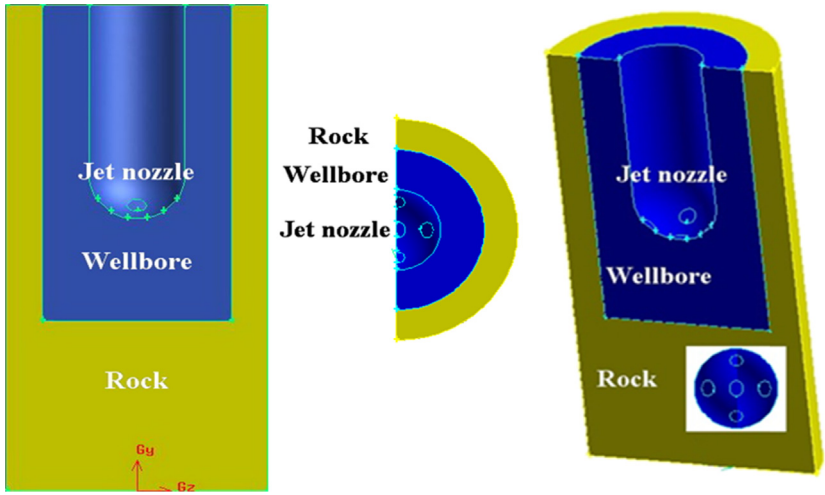

Figure 9.47 Three-dimensional multiorifice nozzle hydrothermal jet model.

There are five orifices in total in the multiorifice nozzle hydrothermal jet model. One orifice is at the bottom center of the bit, whereas the other four orifices are uniformly distributed around the bottom center at an angle of 45 degrees to the gravitational direction. The high-temperature and high-velocity fluid is discharged from the jet orifices in the nozzle to disintegrate the bottom rock.

Fig. 9.48 shows the simulation results of down-hole temperature contours at four different times, 0.0001, 0.01, 0.1, and 1 s. Four central normal sections are illustrated in which the area with high temperature becomes progressively larger as the time increases. At time 0.0001 s, which is the

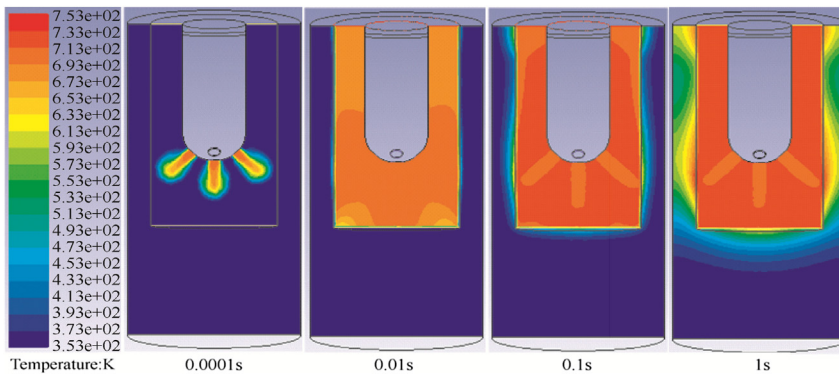

Figure 9.48 Down-hole temperature contours at times 0.0001, 0.01, 0.1, and 1 s.

initial stage for hydrothermal jets discharged from the multiorifice nozzle, three hydrothermal jets are clearly distributed in the wellbore. Then, from 0.01 s, the entire wellbore space is filled with high-temperature fluid and heat transfer between wellbore fluid and ambient rocks begins. When the time reaches 1 s, the average temperature of the rocks is approximately 500K.

Axial temperature distributions in Fig. 9.49 are obtained under the set hydrothermal jet pressure difference of 15 MPa while the jet temperatures are varied. Also, the jet temperature is set as 700K while the pressure difference is varied. Increase in jet temperature and pressure difference can both enhance the heat transfer effect, as shown in Fig. 9.50. In Fig. 9.49, when the jet temperature increases from 650 to 700K, and the pressure difference decreases from 15 to 10 MPa, the final distribution of temperature in the rock becomes higher. Therefore the comparison result shows that the jet temperature has a larger influence on the heat transfer effect than the pressure difference. On the other hand, in Fig. 9.50, the temperature in the rock is more sensitive to the variation in the jet temperature, which indicates that the jet temperature has better heat transfer effect.

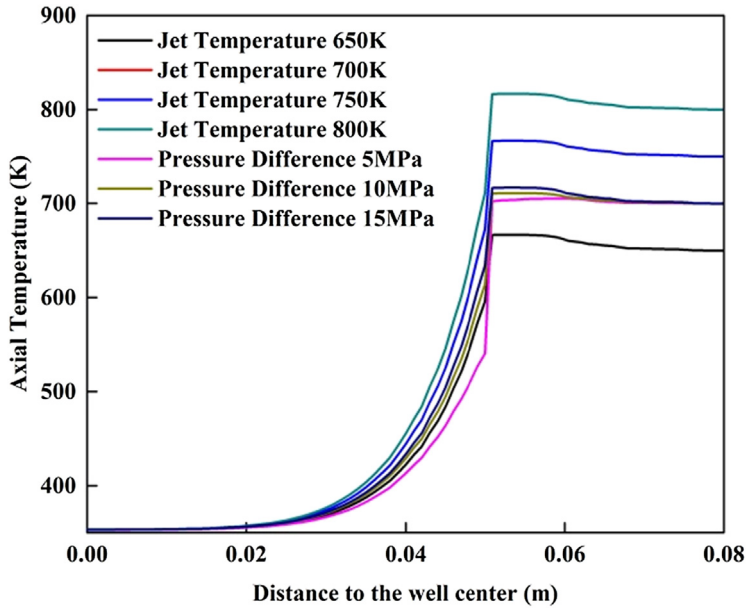

Figure 9.49 Comparison of axial temperature with different jet temperatures and pressure differences.

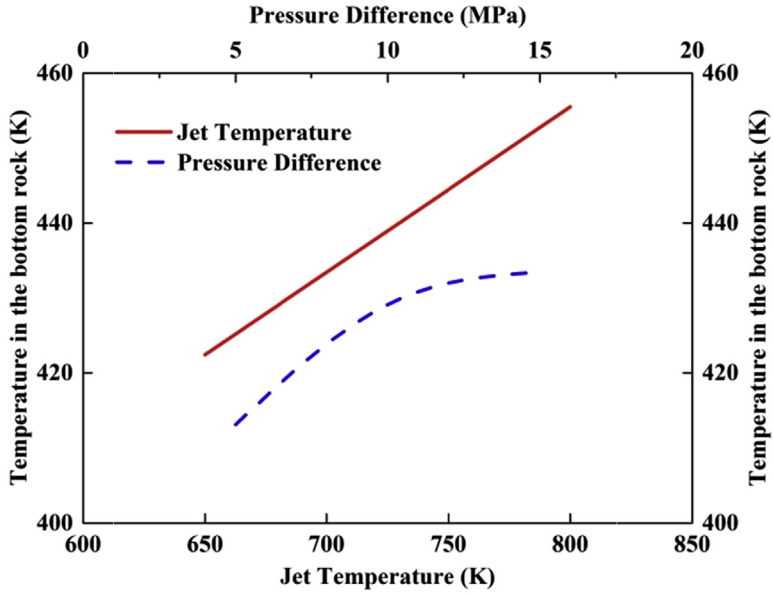

Figure 9.50 Comparison of heat transfer effect with different jet temperatures and pressure differences.

REFERENCES

Augustine, C. R. (2009). *Hydrothermal spallation drilling and advanced energy conversion technologies for engineered geothermal systems*. Massachusetts Institute of Technology.

Chengzao, J., & Xiongqi, P. (2015). Research processes and main development directions of deep hydrocarbon geological theories. *Acta Petrolei Sinica, 36*(12), 1457−1469.

Chen, T., Yeung, M., & Mori, N. (2004). Effect of water saturation on deterioration of welded tuff due to freeze-thaw action. *Cold Regions Science and Technology, 38*(2), 127−136.

Chunhui, Z., Weilong, L., Xizhao, W., Laigui, W., & Hewan, L. (2015). Research of fracturing mechanism of coal subjected to liquid nitrogen cooling. *Journal of Hebei University of Science and Technology, 36*(4).

Grundmann, S. R., Rodvelt, G. D., Dials, G. A., & Allen, R. E. (1998). Cryogenic nitrogen as a hydraulic fracturing fluid in the devonian shale. In *Paper presented at the SPE Eastern Regional Meeting*.

Hori, M., & Morihiro, H. (1998). Micromechanical analysis on deterioration due to freezing and thawing in porous brittle materials. *International Journal of Engineering Science, 36*(4), 511−522.

Hualin, L., Gensheng, L., & Can, Y. (2005). Advance in study on theory of rock breaking under water jet impact. *Metal Mine, 7*, 1−5.

Jianli, Z. Y. L. (2005). Technical status and developmental trend of drilling techniques in deep and ultra-deep wells. *Petroleum Drilling Techniques, 5*, 001.

Jian, K., Zhao, M. P., & Bing, L. (2005). Random solid-head coupled model and numerical tests on hot cracking of rocks. *Rock and Soil Mechanics, 26*(1), 135−139.

José, S., Pablo, S., & Francisco, C. (2012). Numerical modelling of supercritical submerged water jets in a subcritical co-flow. *The Journal of Supercritical Fluids, 65*, 45−53.

Kim, T. J. (2003). *An overview of waterjet fundamentals and applications*. Water Jet Technology Association.

Liao, H., & Li, G. (2006). Numerical analysis of the stress distribution of high pressure water jet impinging solid. In *Paper presented at the Proceedings of the 8th Pacific Rim International Conference on Water Jet Technology.[S. l.]:[sn]*.

Longde, S., Caineng, Z., Rukai, Z., Zhang, Y., Zhang, S., Zhang, B., et al. (2013). Formation, distribution and potential of deep hydrocarbon resources in China. *Petroleum Exploration and Development, 40*(6), 687–695.

Matteson, A., Tomanic, J., Herron, M., Allen, D., & Kenyon, W. (2000). NMR relaxation of clay/brine mixtures. *SPE Reservoir Evaluation and Engineering, 3*(05), 408–413.

McDaniel, B., Grundmann, S. R., Kendrick, W. D., Wilson, D. R., & Jordan, S. W. (1997). Field applications of cryogenic nitrogen as a hydraulic fracturing fluid. In *Paper presented at the SPE Annual Technical Conference and Exhibition*.

Peng, Y., & Ma, C. (2005). *Application manual of super critical fluid technology[M]* (pp. 378–405). Beijing: Chemical Industry Press.

Potter, R. M., & Tester, J. W. (1998). *Continuous drilling of vertical boreholes by thermal processes: Including rock spallation and fusion: Google patents*.

Rothenfluh, T., Schuler, M. J., & Von Rohr, P. R. (2011). Penetration length studies of supercritical water jets submerged in a subcritical water environment using a novel optical Schlieren method. *The Journal of Supercritical Fluids, 57*(2), 175–182.

Schuler, M. J., Rothenfluh, T., & von Rohr, P. R. (2013a). Numerical analysis of penetration lengths in submerged supercritical water jets. *The Journal of Supercritical Fluids, 82*, 213–220.

Schuler, M. J., Rothenfluh, T., & von Rohr, P. R. (2013b). Simulation of the thermal field of submerged supercritical water jets at near-critical pressures. *The Journal of Supercritical Fluids, 75*, 128–137.

Serikawa, R. M., Usui, T., Nishimura, T., Sato, H., Hamada, S., & Sekino, H. (2002). Hydrothermal flames in supercritical water oxidation: Investigation in a pilot scale continuous reactor. *Fuel, 81*(9), 1147–1159.

Song, X., Lv, Z., Li, G., Hu, X., & Shi, Y. (2016). Numerical analysis of characteristics of multi-orifice nozzle hydrothermal jet impact flow field and heat transfer. *Journal of Natural Gas Science and Engineering, 35*, 79–88.

Surjaatmadja, J. B., McDaniel, B., & Sutherland, R. L. (2002). Unconventional multiple fracture treatments using dynamic diversion and downhole mixing. In *Paper presented at the SPE Asia Pacific Oil and Gas Conference and exhibition*.

Wagner, W., & Kretzschmar, H.-J. (2008). IAPWS industrial formulation 1997 for the thermodynamic properties of water and steam. In *International steam tables: Properties of water and steam based on the industrial formulation IAPWS-IF97* (pp. 7–150).

Walsh, S. D., & Lomov, I. N. (2013). Micromechanical modeling of thermal spallation in granitic rock. *International Journal of Heat and Mass Transfer, 65*, 366–373.

Wang, X. Q., Schubnel, A., Fortin, J., Guéguen, Y., & Ge, H. K. (2013). Physical properties and brittle strength of thermally cracked granite under confinement. *Journal of Geophysical Research: Solid Earth, 118*(12), 6099–6112.

FURTHER READING

Cai, C., Huang, Z., Li, G., & Gao, F. (2015). Particle velocity distributions of abrasive liquid nitrogen jet and parametric sensitivity analysis. *Journal of Natural Gas Science and Engineering, 27*, 1657–1666.

Cai, C., Huang, Z., Li, G., Gao, F., Wei, J., & Li, R. (2016). Feasibility of reservoir fracturing stimulation with liquid nitrogen jet. *Journal of Petroleum Science and Engineering, 144*, 59–65.

Cai, C., Li, G., Huang, Z., Tian, S., Shen, Z., & Fu, X. (2015). Experiment of coal damage due to super-cooling with liquid nitrogen. *Journal of Natural Gas Science and Engineering, 22*, 42–48.

Cai, C., Li, G., Huang, Z., Tian, S., Shen, Z., & Wei, J. (2014). Experimental study of the effect of liquid nitrogen cooling on rock pore structure. *Journal of Natural Gas Science and Engineering, 21*, 507–517.

Cha, M., Yin, X., Kneafsey, T., Johanson, B., Alqahtani, N., Miskimins, J., et al. (2014). Cryogenic fracturing for reservoir stimulation – laboratory studies. *Journal of Petroleum Science and Engineering, 124*, 436–450.

Huang, Z., Niu, J., Li, G., Yuan, X., & Liu, Y. (2008). Surface experiment of abrasive water jet perforation. *Petroleum Science and Technology, 26*(6), 726–733.

Huang, Z., Li, G., Shi, H., Niu, J., Song, X., & Shao, S. (2015). Abrasive water jet perforating experiments under ambient pressures. *Atomization and Sprays, 25*(7), 617–627.

INDEX

'*Note*: Page numbers followed by "f" indicate figures and "t" indicate tables.'

A

B

C

D

F

H

I

J

O

P

R

S

T

W

X

Z

Abrasive Water Jet Perforation and Multi-Stage Fracturing

By Zhongwei Huang, Gensheng Li, Shouceng Tian, Xianzhi Song, Mao Sheng, Subhash Shah

The exploitation and development of unconventional oil and gas resources has continued to gain importance, and multi-stage fracturing with abrasive water jets has emerged as one of the three principal methods to recover unconventional oil and gas. Yet there is no one collective reference to explain the fundamentals, operations, and influence of this method. ***Abrasive Water Jet Perforation and Multi-stage Fracturing*** gives petroleum engineers, well completion managers, and fracturing specialists a critical guide to understanding all the details of the technology including materials, tools, design methods, and field applications. The publication will introduce current challenges and give solutions for the problems encountered. Packed with references and real-world examples, ***Abrasive Water Jet Perforation and Multi-stage Fracturing*** equips engineers and specialists with a necessary reservoir stimulation tool to better understand today's fracturing technology.

Key Features

- Understand the fundamentals, design, and application of water jet perforation
- Grasp the pressure boosting assembly in all phases including initiation, hydraulic isolation, and production stage
- Evaluate production analysis, pump pressure predictions, and the latest design software

About the Authors

Dr. Zhongwei Huang, Professor, College of Petroleum Engineering, China University of Petroleum, China

Dr. Gensheng Li, Professor, China University of Petroleum, China

Dr. Shouceng Tian, Associate Researcher, College of Petroleum Engineering, China University of Petroleum, China

Dr. Xianzhi Song, Associate Professor, College of Petroleum Engineering, China University of Petroleum, China

Dr. Mao Sheng, Assistant Professor, School of Petroleum Engineering, China University of Petroleum in Beijing, China

Dr. Subhash Shah, Professor Emeritus, Mewbourne School of Petroleum and Geological Engineering, University of Oklahoma, USA

Related Titles

Hydraulic Fracturing in Unconventional Reservoirs by Hoss Belyadi, Ebrahim Fathi, and Fatemeh Belyadi, 978-0-12-849871-2

Unconventional Oil and Gas Resources Handbook: Evaluation and Development by Y. Zee Ma and Stephen Holditch, 978-0-12-802238-2

Hydraulic Fracturing Chemicals and Fluids Technology by Johannes Fink, 978-0-12-411491-3

Mechanics of Hydraulic Fracturing, Second Edition by Ching Yew and Xiaowei Weng, 978-0-12-420003-6

Energy / Engineering

ISBN 978-0-12-812807-7

9 780128 128077

ELSEVIER

G P P

Gulf Professional Publishing

An imprint of Elsevier

elsevier.com/books-and-journals